Quantum point contact in high mobility graphene

Katrin Zimmermann

Communauté
UNIVERSITÉ Grenoble Alpes

THÈSE

Pour obtenir le grade de

DOCTEUR DE la Communauté UNIVERSITÉ GRENOBLE ALPES

Spécialité : **Physique/Nanophysique**

Arrêté ministériel : 07 août 2006

Présentée par

Katrin ZIMMERMANN

Thèse dirigée par **Serge HUANT**
et codirigée par **Benjamin SACEPE**

préparée au sein **de l'Institut Néel, CNRS**
et de **Ecole doctorale de Physique**

Quantum point contact in high mobility graphene

Thèse soutenue publiquement le **20 juin 2016**,
devant le jury composé de :

Frédéric PIERRE
Directeur de recherche CNRS, Laboratory for Photonics and Nanostructures, Marcoussis, Rapporteur

Bernard PLAÇAIS
Directeur de recherche CNRS, Laboratoire Pierre Aigrain, Paris, Rapporteur

Mark GOERBIG
Directeur de recherche CNRS, Laboratoire de Physique des Solides, Orsay, Président

Dan SHAHAR
Professeur, Weizmann Institute of Science, Israel, Examinateur

Benjamin SACEPE
Chargé de recherche, Institut Néel, Grenoble, Co-Directeur de thèse

ACKNOWLEDGEMENT

First of all, I want to express my sincere thanks to Benjamin Sacépé for his continuous support and advice at all stages of my PhD - from the first steps of device fabrication over the extremely long and exhausting but highly successful measurements to the rigorous data analysis and finishing with the writing and defending of my thesis. I have learned and achieved so much during my thesis which I had not thought possible in the beginning.

I am grateful to Clemens Winkelmann and Hervé Courtois for their helpful advice and valuable discussions throughout my PhD from the preparation of my presentation for the Nanoscience Foundation grant in the beginning to the rehearsals of my PhD defence.

I want to thank Serge Huant for being my PhD director.

Thanks to Bernard Plaçais and Frédéric Pierre for writing the reports to my manuscript. Additionally, I want to thank them as well as Mark Goerbig and Dan Shahar for being a member of the jury of my defence.

During my PhD, I had the opportunity to work on the complete cycle from the device fabrication to measurements at low temperatures and data analysis. This process would not have been possible without the support of several colleagues at the Institute Néel and collaborators. A great thanks goes to the group of Nanofab who have always provided advise and assistance in all manners of device fabrication in the clean room. Especially, I want to thank Thierry Crozes and Thierry Fournier for their help and support with e-beam lithography, first with the LEO and then with the new Nanobeam. Thanks goes to Jean-Luc Thomassin who provided us with the HSQ resist.

I want to thank Kenji Watanabe and Takashi Tanigushi for producing high quality boron nitride crystals which we used for the fabrication of our hBN-graphene-hBN heterostructures.

I want to express my thanks to Zheng (Vitto) Han for introducing me into the fabrication of graphene heterostructures and for always giving me valuable advice. It was always a great pleasure to work with him.

I want to thank Nedjma Bendiab for her time doing Raman spectroscopy on encapsulated graphene with me which turned out to be a bigger challenge than expected. Thanks to Vincent Bouchiat for the interesting discussions. I also want to thank him and Laetitia Marty for their commitment in planning and assembling the new transfer set-up.

For the old and new transfer set-up, we were strongly supported by the pôle ingénierie expérimentale and especially Didier Dufeu, Julien Jarreau and Yves Deschanels whom I want to thank.

Many thanks to Frédéric Gay for setting up the complete measurement system, for always

taking care of the operation of the dilution refrigerator and for his continuous technical support. I also thank Philippe Plaindoux for the technical support of the experimental set-up.

The richness of our experimental results have inspired several exciting discussions about the theoretical interpretation. Here, I want to thank Dmitry Abanin, Thierry Champel, Serge Florens, Mark Goerbig, Leonid Levitov, and Yigal Meir. A special thanks goes to Hermann Sellier for the valuable discussions and collaboration which was essential for the theoretical understanding of our data.

The special time of my PhD would not have been possible without my great colleagues and good friends in our group.

I am especially grateful of having such a great friend and room-mate as Johanna Seidemann. Her spirit enlightened my days even in the hardest and most exhausting times of my PhD.

A special thanks goes to Kévin Le Calvez for all his support in particular for his endless help when I had problems with French speaking administration and insurance. I do not know how I would have managed without him. I find it most impressive that even in the most stressful times, he always stays optimistic and keeps a smile on his face.

I want to thank Louis Veyrat who only joined our group six months ago and has by now become a wonderful friend. I really enjoy discussing with him about science but also about music, films, life etc.

It has been a great pleasure to work with Anna Jordan. Her energy and enthusiasm is inspiring and motivating. I am sure she will do great in her future life outside of science.

Thanks to David van Zanten for always taking the time to discuss and explain the physics and for introducing me into the secrets of the e-beam lithography.

An important part of my life during my PhD has always been my friends outside of daily research.

Here, I am particularly grateful to Jean-Baptiste Decombe. We started the PhD at the same time which allowed us to always support and encourage each other. Over the time of our PhDs, he has become a dear friend.

I am very much grateful for my friendship with Sayanti Samaddar, Sophie Chevalliez, Dipankar Kalita, Farida and Hanno Flentje, Onintza Ros, Cornelia Schwarz and Tobias Bautze who were an integral part of my terrific time in Grenoble.

Die letzten Worte sind meiner Familie gewidmet. Ich bedanke mich von ganzem Herzen bei meinen Eltern für ihre Unterstützung, Kraft und, dass sie immer ein offenes Ohr haben und mir mit Rat und Tat in jeglicher Lebenslage zur Seite stehen. Ein herzlicher Dank geht auch an meine Omas, die mich immer bei all meinen Vorhaben unterstützt haben.

Abschließend möchte ich dem Menschen danken, der schon seit geraumer Zeit einen ganz besonderen Platz in meinem Leben und Herzen eingenommen hat. Ich danke dir, mein geliebter Robert, für deine Liebe, Unterstützung, Verständnis und Kraft und kann unsere gemeinsame Zukunft (an einem Standort) kaum erwarten.

CONTENTS

INTRODUCTIONS

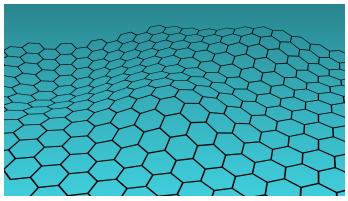

Hexagonal structure of graphene

Since its first isolation in 2004 [1], **graphene** has become one of the most intensively studied materials in solid state physics, reaching from fundamental research to industrial applications. Graphene is a single layer of Carbon atoms arranged in a honeycomb lattice and has some extraordinary properties. A sheet of graphene is almost transparent, inert in air and an exceptionally good thermal and electrical conductor. Being a semiconductor with a zero band gap and a linear bandstructure, its charge carriers behave as relativistic massless Dirac particles which leads to unique transport properties.

The quantum Hall effect is a phenomenon which takes place in a 2-dimensional electron gas (2DEG) when it is subjected to a strong perpendicular magnetic field at low temperature. Its remarkable feature is the quantisation of the electrical conductance in a series of plateaus precisely quantised at multiples of $\frac{e^2}{h}$, the conductance quantum. It was discovered in 1980 [2] and gave rise to an exciting new field in mesoscopic physics.

The Dirac electrons in graphene lead to an anomalous relativistic quantum Hall effect [1, 3]. Due to the four-fold degeneracy of each Landau level in graphene, the conductance is quantised at $2\frac{e^2}{h}$, $6\frac{e^2}{h}$, $10\frac{e^2}{h}$ etc. Additionally, the much larger gap between the Landau levels in comparison to conventional 2DEG systems makes it possible to observe the quantum Hall effect up to room temperature [4].

With increasing mobility in graphene devices, magnetic fields far below 10 T have shown a lifting of the four-fold degenerated Landau levels which gives rise to additional quantum Hall states [5]. Even plateaus of the fractional quantum Hall effect can be observed at such magnetic fields [6].

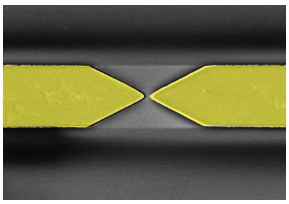

SEM image of a QPC

The **quantum point contact** (QPC) – a narrow and short constriction defined by split gate electrodes in a 2-dimensional electron gas – offers an excellent structure to study many fundamental phenomena of mesoscopic physics [7]. In the quantum Hall regime, the QPC enables the manipulation of one-dimensional quantum Hall edge channels in which the current flows. By controlling the voltage on the split gates, the QPC allows to select the edge channels transmitted through the constriction and those which are backscattered. The QPC is a primary component for electron quantum optics, for instance, in single electron sources, partitioning experiments and quantum Hall interferometer.

In this PhD thesis, we have successfully accomplished a QPC in high mobility graphene. We have studied the effect of the QPC on the propagation of integer and fractional quantum Hall edge channels and the mixing among them.

Chapters 1 to 4 give an overview of the theoretical background of this thesis. **Chapter 1** introduces the quantum Hall effect in conventional 2-dimensional electron gases. In this regime, transport is determined by the dissipationless propagation of electrons through one-dimensional edge channels resulting in a zero longitudinal resistance and a quantised transverse resistance.

Chapter 2 is devoted to the relativistic quantum Hall effect in graphene. The Landau levels are four-fold degenerate due to the symmetries of spin and valley. In high magnetic fields, the Coulomb interaction becomes the dominant energy scale causing the lifting of the degeneracies. The higher the mobility of the graphene device, the lower the required magnetic field to resolve these states.

Chapter 3 presents the theoretical framework of the QPC in the quantum Hall regime and introduces the challenge of realising a QPC in graphene. In conventional 2DEG systems, a negative voltage on the split gates leads to a depletion of electrons underneath them. Therefore, the electrons are transmitted only through the narrow constriction of the QPC. In graphene, due to the absence of a band gap, this approach needs to be adapted. In the quantum Hall regime, the voltage on the split gates can be set so that hole edge channels are localised underneath them while electron edge channels propagate in the bulk.

Chapter 4 discusses the process of equilibration between quantum Hall edge channels at the pn-interface. We will see that this subtlety affects the transport properties of a QPC in graphene.

The quality of graphene, especially its mobility, depends highly on the underlying substrate and the fabrication process. **Chapter 5** presents the van-der Waals pick-up technique which we adapted to fabricate high mobility graphene devices. This transfer technique enables us to encapsulate graphene between two thin flakes of atomically flat hexagonal boron nitride crystals. The graphene flake, which is never exposed to any kind of chemical pollution, remains clean and free of impurities. The encapsulated graphene is contacted only on the edge in the form of one-dimensional contacts.

The following three chapters are devoted to our results on the graphene Hall bar devices equipped with a QPC. **Chapter 6** focusses solely on the transport properties of the graphene devices without a QPC. We measured a high mobility of $250\,000\,\mathrm{cm\,V^{-2}\,s^{-1}}$ and a mean free path corresponding to the distance between neighbouring contacts of $1.8\,\mu\mathrm{m}$. This shows that our device is in the ballistic limit. We study additional signatures of

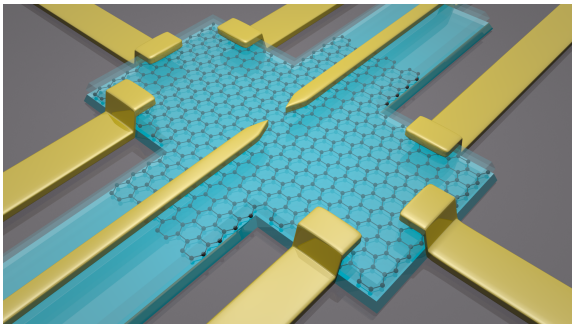

3D model of our encapsulated graphene devices equipped with a QPC

ballistic transport of zero four-terminal resistance and negative non-local resistance at zero magnetic fields as well as electron focusing at low magnetic fields. In the quantum Hall regime, in low magnetic fields, we observe the usual sequence of quantised transverse resistance of $\frac{1}{\nu}\frac{h}{e^2}$ where $\nu = \pm 4\left(n + \frac{1}{2}\right)$. From a magnetic field of 5 T the symmetry of spin and valley is broken and states at all integer values of ν appear. At 14 T, we find several fractional quantum Hall states which are in agreement with the model of composite fermions.

In **chapter 7** the effect of the quantum point contact in our high mobility graphene device is studied in detail. In the quantum Hall regime, we demonstrate that the integer and fractional quantum Hall edge channels can be controlled and selectively transmitted by the QPC. The breaking of the symmetry of spin and valley introduces distinct features of equilibration between quantum Hall edge channels. Our measurements show that equilibration occurs only between states of identical spins and in the case of oppositely charged edge channels, is additionally limited to states within the $N = 0$ Landau level.

In **chapter 8**, we present our results on quasi-particle and fermion tunnelling between fractional edge channels in our QPC device in graphene. We demonstrate that we measured tunnelling of the $\frac{7}{3}$-fractional state for which we study the temperature dependence and energy scale of the tunnelling conductance.

INTRODUCTION – VERSION EN FRANÇAIS

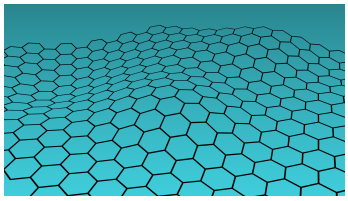

Structure hexagonal du graphène

Depuis sa mise en évidence en 2004 [1], le **graphène** est devenu l'un des systèmes les plus étudiés en physique de la matière condensée, tant en recherche fondamentale que pour ses applications industrielles. Le graphène est une monocouche d'atomes de carbone, agencés en un réseau hexagonal de type nid d'abeille, et présente des propriétés extraordinaires. Un feuillet de graphène est presque transparent, inerte dans l'air et montre des propriétés de conduction électrique et thermique exceptionnelles. De plus, l'absence de bande interdite et la structure de bande linéaire du graphène font que ses porteurs de charges se comportent comme des particules de Dirac relativistes sans masse, engendrant des propriétés de transport uniques.

L'effet Hall quantique est un phénomène qui se produit quand un gaz d'électron bidimensionel (2D-electron gas, 2DEG) à basse température est soumis à un fort champ magnétique transverse. Il se caractérise par la quantification de la conductance électrique en une série de plateaux, dont les valeurs sont des multiples du quantum de conductance $\frac{e^2}{h}$. Cet effet, découvert en 1980 [2], a donné naissance à un très riche nouveau domaine de la physique mésoscopique.

Dans le graphène, la nature relativiste des fermions de Dirac conduit à un effet Hall quantique anormal [1, 3]. Du fait de la quadruple dégénérescence de chaque niveau de Landau, la conductance transverse est quantifiée à $2\frac{e^2}{h}$, $6\frac{e^2}{h}$, $10\frac{e^2}{h}$, etc... De plus, l'espacement entre niveaux de Landau, bien plus grand dans le graphène que dans un 2DEG usuel, rend possible l'observation de l'effet Hall quantique jusqu'à la température ambiante [4].

Grâce à la haute mobilité des dispositifs de graphène, la levée de la dégénérescence quadruple des niveaux de Landau peut s'effectuer à des champs bien inférieurs à 10 T, générant des états Hall quantiques additionnels [5]. Des plateaux Hall quantiques fractionnels peuvent ainsi être observés à ces champs [6].

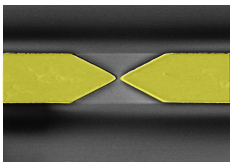

Image SEM d'un QPC

Les contacts ponctuels quantiques (quantum point contact, QPC) – des constrictions courtes et étroites définies dans un 2DEG par des grilles électrostatiques – constituent des structures modèles pour l'étude de nombreux phénomènes en physique mésoscopique [7]. Dans le régime de l'effet Hall quantique, un QPC permet de manipuler les états de bords unidimensionnels qui transportent le courant. En ajustant la tension des grilles électrostatiques du QPC, il est en effet possible de

sélectionner les états de bords transmis ou retrodiffusés au travers de la constriction. Le QPC est un élément de base de l'optique quantique électronique, entre autre pour les sources d'électrons uniques, les expériences de "partitionning" et les interféromètres Hall quantiques.

Au cours de cette thèse, nous avons réalisé avec succès un QPC dans du graphène de haute mobilité. Nous avons étudié l'effet du QPC sur la propagation des états entiers et fractionnaires de l'effet Hall quantique, ainsi que sur leur mélange.

Les chapitres 1 à 4 présentent une vision d'ensemble du cadre théorique de cette thèse. **Le chapitre 1** introduit l'effet Hall quantique dans les 2DEGs conventionnels. Dans ce régime, le transport est régit par la propagation sans dissipation d'électrons par des canaux de bords, qui conduit à une résistance longitudinale nulle et une résistance transverse quantifiée.

Le chapitre 2 est dédié à l'effet Hall quantique relativiste dans le graphène. Du fait de la symétrie de spin et de vallée, les niveaux de Landau sont quatre fois dégénérés. à fort champ magnétique, l'interaction Coulombienne devient l'échelle d'énergie dominante, provoquant la levée des dégénérescences. Le champ nécessaire pour résoudre ces états est d'autant plus faible que la mobilité du graphène est grande.

Dans **le chapitre 3**, le contexte théorique du QPC dans l'effet Hall quantique et le défi présenté par sa réalisation dans le graphène sont présentés. Dans les 2DEGs conventionnels, une tension négative appliquée sur une grille métallique suffit à dépléter le gaz électronique situé en dessous. Les électrons ne se propagent donc qu'au travers de l'étroite constriction du QPC. Cependant, dans le graphène, du fait de l'absence de bande interdite, cette approche peut être adaptée. Dans l'effet Hall quantique, la tension appliquée sur les grilles doit être réglée de manière à ce que des états de bords de type trou soient localisés sous les grilles, tandis que les états de bords de type électron se propagent autour de la grille.

Le chapitre 4 discute le processus d'équilibrage entre les états de bords de l'effet Hall quantique à la jonction p-n résultante. Nous verrons que ce processus affecte de manière subtile les propriétés de transport au travers d'un QPC dans le graphène.

La qualité du graphène, et tout particulièrement sa mobilité, dépendent fortement du substrat utilisé et du processus de fabrication. **Le chapitre 5** présente la technique de "pick-up van-der-Waals" que nous avons adaptée pour la fabrication d'échantillons de graphène de haute mobilité. Cette technique de transfert permet d'encapsuler un feuillet de graphène entre deux fins cristaux de nitrure de bore hexagonal atomiquement plats. Le graphène est ainsi isolé de toute pollution chimique, et reste propre de toute impureté. Le graphène ainsi encapsulé est contacté sur sa tranche par un contact unidimensionnel.

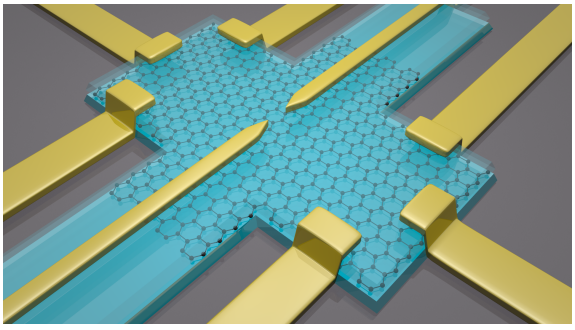

Modélisation 3D de notre dispositif de graphène encapsulé, muni d'un QPC.

Les trois chapitres suivants sont dédiés à nos résultats, obtenus sur des barres de Hall de graphène encapsulées munis d'un QPC. **Le chapitre 6** porte sur les propriétés des dispositifs de graphène sans QPC. Nous mesurons une mobilité de $250\,000\,\mathrm{cm\,V^{-2}\,s^{-1}}$ et un libre parcours élastique moyen de $1.8\,\mu\mathrm{m}$ correspondant à la distance entre contacts voisins. Ceci montre que notre dispositif est dans la limite de transport balistique. Nous avons étudié des signatures additionnelles du transport balistique: la résistance longitudinale quatre-points nulle, la résistance non-locale négative à champ magnétique nulle, ainsi que la focalisation électronique à faible champ magnétique. Dans le régime de l'effet Hall quantique, à faible champ magnétique, nous observons la séquence habituelle des niveaux quantifiés de la résistance transverse en $\frac{1}{\nu}\frac{h}{e^2}$, avec $\nu = \pm 4\left(n + \frac{1}{2}\right)$. Au delà d'un champ de $5\,\mathrm{T}$, les symétries de spin et de vallée sont brisées et des états quantifiés apparaissent pour toutes les valeurs entières de ν. A $14\,\mathrm{T}$, nous observons plusieurs états fractionnaires, en accord avec le modèle des fermions composites.

Dans **le chapitre 7**, les effets du QPC sur notre dispositif de graphène sont étudiés en détail. Dans l'effet Hall quantique, nous démontrons la possibilité de contrôler et de transmettre sélectivement les états de bords entiers et fractionnaires au travers du QPC. La brisure des symétries de spin et de vallée introduit des différences dans l'équilibrage entre états Hall quantiques. Nos mesures montrent que l'équilibrage se produit uniquement entre états de même spin et, dans le cas d'états de charges opposées, uniquement dans le $N = 0$ niveau de Landau.

Enfin, dans **le chapitre 8** nous présentons nos résultats sur l'effet tunnel de quasi-particules et de fermions entre états de bords fractionnaires dans notre dispositif muni d'un QPC. Nous démontrons la réussite de la mesure de l'effet tunnel de l'état fractionnaire $\frac{7}{3}$. La dépendance en température de la conductance tunnel est mesurée et comparée aux prédictions théoriques.

CHAPTER 1

INTEGER AND FRACTIONAL QUANTUM HALL EFFECT

In 1980 von Klitzing et al. made a surprising discovery which gave rise to a new and exciting field in mesoscopic physics. When a high perpendicular magnetic field (B) is applied on a 2-dimensional electron gas (2DEG), well defined plateaus of constant resistance are observed in the transverse resistance R_{xy} versus B while the longitudinal resistance drops to zero. These plateaus are precisely quantised to the value

$$R_{xy} = \frac{h}{e^2 N}$$

with N being an integer. Before having a closer look at the theoretical background of this phenomena, we start by describing the classical motion of an electron in both an electric and a magnetic field. Afterwards we will derive the formation of Landau levels in the density of states which appear under perpendicular magnetic fields. Next, we will see that the

observed plateaus in the transverse resistance are a consequence of the physical boundaries of the sample which leads to the picture of propagating edge channels. Afterwards, we will include the influence of disorder. We will consider the Landau-Büttiker formalism in ballistic conductors and derive the resistivity of a Hall bar. We will finish this section by extending our consideration by including the effect of screening on quantum Hall edge channels.

In 1982, D.C. Tsui, H.L. Stormer and A.C. Gossard made a surprising discovery of a plateau at $\nu = \frac{1}{3}$ which uncovered the realm of the fractional quantum Hall effect [8]. Fractional plateaus can no longer be explained in terms of a one-particle picture as in the integer quantum Hall effect but instead, interactions between electrons become crucial. We will discuss briefly the theories of Laughlin and Halperin as well as the theory of composite fermions. We finish this chapter by introducing fractional states outside of the common series of composite fermions.

1 Integer Quantum Hall Effect

Most of the theories described in this section are based on the books [9–11] and the lecture [12].

1.1 Electrons in a magnetic field

Let us start by having a look at the motion of an electron in an electric and a magnetic field (see Fig. 1.1). The electron with charge e is free to move in the x-y-plane. An electric field $\vec{E}$ which points in the x-direction accelerates the electron in the direction of the electric force. The magnetic field $\vec{B}$ points in the z-direction ($\vec{B} = B\hat{e}_z$) which is perpendicular to the direction of propagation of the electron. Thus, the Lorentz force deflects the electron sideways causing it to move in circles with the cyclotron frequency of

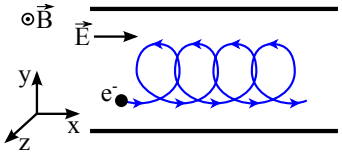

Fig. 1.1: When an electron moves in an electric and a magnetic field, it is accelerated by the electric field, and moves in circles due to the magnetic field.

$$\omega_c \equiv \frac{eB}{m^*}$$

We consider free electrons with effective mass m^* in two dimensions. The motion of the electron in both E and B fields is described by:

$$\frac{m^*\vec{v}_D}{\tau} = e\left(\vec{E} + \vec{v}_D \times \vec{B}\right) \tag{1.1}$$

Here, $\vec{v}_D$ is the drift velocity and τ is the time of momentum relaxation between scattering events. The current density $\vec{J}$ is included in (1.1) by using the relation $\vec{J} = e\vec{v}_D n$ which leads to:

$$\begin{aligned}\begin{pmatrix} E_x \\ E_y \end{pmatrix} &= \begin{pmatrix} \frac{m^*}{e\tau} & -B \\ B & \frac{m^*}{e\tau} \end{pmatrix} \begin{pmatrix} \frac{J_x}{en} \\ \frac{J_y}{en} \end{pmatrix} \\ &= \sigma_0^{-1} \begin{pmatrix} 1 & -\mu B \\ \mu B & 1 \end{pmatrix} \begin{pmatrix} J_x \\ J_y \end{pmatrix}\end{aligned} \tag{1.2}$$

In the second step, we have introduced the quantities $\sigma_0 \equiv |e|n\mu$ and $\mu \equiv \frac{|e|\tau}{m^*}$ which are the Drude conductivity and mobility respectively. The resistivity tensor

$$\boldsymbol{\rho} = \begin{pmatrix} \rho_{xx} & \rho_{xy} \\ \rho_{yx} & \rho_{yy} \end{pmatrix}$$

is defined by

$$\begin{pmatrix} E_x \\ E_y \end{pmatrix} = \begin{pmatrix} \rho_{xx} & \rho_{xy} \\ \rho_{yx} & \rho_{yy} \end{pmatrix} \begin{pmatrix} J_x \\ J_y \end{pmatrix} \tag{1.3}$$

From (1.2) and (1.3), we obtain the longitudinal resistivity ρ_{xx} and the transverse resistivity ρ_{xy} in the form:

$$\rho_{xx} = \rho_{yy} = \sigma_0^{-1} \quad \text{and} \quad \rho_{xy} = -\rho_{yx} = \frac{B}{|e|n} \tag{1.4}$$

We see that ρ_{xx} is constant and independent of the magnetic field while ρ_{xy} increases linearly with B. The relations in (1.4) describe the low magnetic field dependence of the electron's motion, known as the classical Hall effect. For instance, in the measurement of a GaAs quantum well we observe clearly that ρ_{xy} increases linearly with B while ρ_{xx} stays constant up until a magnetic field of about 0.7 T (see Fig. 1.2).

1.2 Landau level quantisation

1.2.1 Discrete energy levels

When we further increase the magnetic field to the point that an electron is able to complete a few circles before loosing its momentum due to scattering ($\omega_c\tau \gg 1$), the quantised circumference of the circular motion of the electron causes its kinetic energy to become quantised. In order to calculate these discrete energy levels, the so-called Landau levels, we need to solve the Schrödinger equation in an external magnetic field. Here, we take

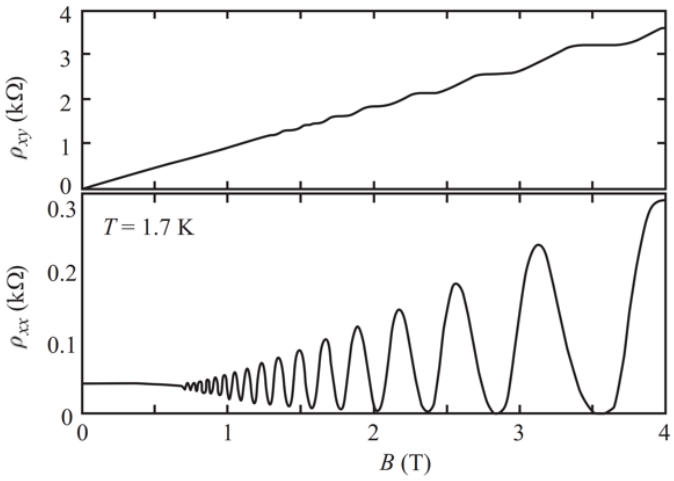

Figure 1.2: Shubnikov-de Haas oscillations measured in a GaAs quantum well are visible in the longitudinal resistance (bottom image) while the transverse resistance still increases linearly with magnetic field (top image). Fig. taken from [9]

into account a conventional 2DEG with a quadratic energy dispersion:

$$\left[\frac{(\vec{p}+|e|\vec{A})^2}{2m^*}\right]\psi(\vec{r}) = \varepsilon\psi(\vec{r}) \tag{1.5}$$

For the vector potential $\vec{A}$, we choose the Landau gauge to be $\vec{A} = -By\hat{e}_y$ which satisfies our chosen magnetic field in the z-direction perpendicular to the motion of the electron (see Fig. 1.1). Since the z-direction does not depend on the magnetic field and as we consider a 2DEG moving in the x-y-plane only, the z-direction can be neglected in (1.5) resulting in:

$$\left[\frac{(p_x - |e|By)^2 + p_y^2}{2m^*}\right]\psi(x,y) = \varepsilon\psi(x,y)$$

We consider a plane wave propagating in the x-direction which leads to the ansatz $\psi(x,y) = \exp(ik_x x)\eta(y)$. The eigenvalue problem takes the form:

$$\left[\frac{p_y^2}{2m^*} + \frac{1}{2}m^*\omega_c^2\left(y - \frac{\hbar k_x}{|e|B}\right)^2\right]\eta(y) = \varepsilon\eta(y) \tag{1.6}$$

Eq. (1.6) describes a one-dimensional Schrödinger equation of a free particle in a quadratic potential which corresponds to the Hamiltonian of an harmonic oscillator in the y-direction with the centre coordinate $y_0 = \frac{\hbar k_x}{|e|B}$. The eigenvalues of (1.6) reveal the spectrum of the quantised energy:

$$\varepsilon_N = \hbar\omega_c\left(N + \frac{1}{2}\right) \tag{1.7}$$

The value $N = 0,1,2\ldots$ indexes the Landau levels. The spacing between neighbouring Landau levels is the cyclotron gap $\hbar\omega_c$ and is, thus, equidistant.

Notice that the energy dispersion (1.7) is independent of the wave vector $\vec{k}$ resulting in a group velocity of

$$v_g = \frac{1}{\hbar}\frac{\partial\varepsilon_N}{\partial k} = 0$$

Therefore, electrons do not move in any distinctive direction, which corresponds to the classical case of closed circular orbits that remain spatially localised[1].

The 2D density of states is constant and independent of the kinetic energy. With increasing magnetic field, the density of states starts to split up into a series of delta-function peaks (dark blue peaks in Fig. 1.3).

While these peaks are not yet fully separated (black line in Fig. 1.3), the oscillations of the density of states cause the resistance to oscillate as a function of either electron density or magnetic field known as the Shubnikov-de Haas effect (see Fig. 1.2). If the magnetic field is further increased so that the spacing of the peaks in the density of states is larger than their width, the minima in the longitudinal resistance drop to zero and the transverse

1 At the moment, we do not consider any applied electric field

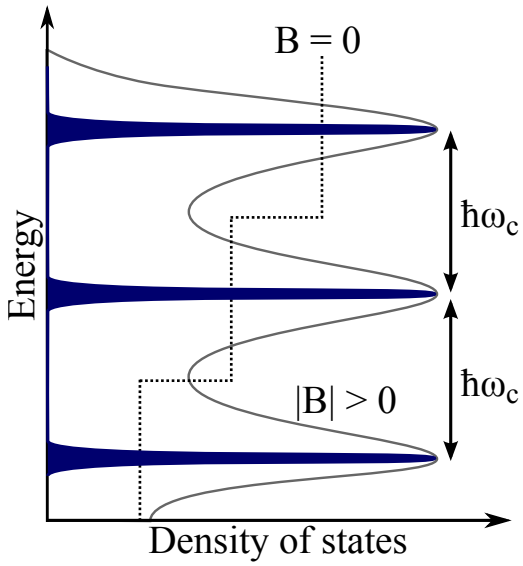

Figure 1.3: At zero magnetic field the density of states follows the dependence $DOS = \frac{m^*}{\pi\hbar^2}\vartheta(\varepsilon - \varepsilon_s)$ which includes the Heaviside step function of ε towards the subband energy ε_s (dashed line). The step-like density of states spits up into a series of delta-peaks with increasing magnetic field, which are separated by $\hbar\omega_c$. The Delta-function peaks in dark blue are broadened for better visibility.

resistance shows precise plateaus at defined value. At this point, we enter the quantum Hall regime. The peaks in the density of states are spaced by $\hbar\omega_c$ and quantised at the value of the Landau level ε_N.

The degeneracy of the Landau levels n_L per unit surface area depends on the centre coordinate y_0 which has to lie within the width W of the sample:

$$n_L = \frac{1}{A}\frac{W}{y_0} = \frac{|e|B}{h}$$

One can define the filling factor which represents the ratio between the number of electrons and the number of flux quanta $\left(\phi_0 = \frac{h}{e}\right)$:

$$\nu = \frac{n_e}{n_L} = \frac{1}{g_s g_v}\frac{n_e h}{|e|B} \tag{1.8}$$

where n_e is the electron density, and g_s and g_v correspond to the spin and valley degeneracy, respectively.

1.2.2 Edges of the sample

The above description of quantised Landau levels assumes an infinite plane without physical boundary. However, quantised plateaus in the transverse resistance as well as the zero longitudinal resistance in the quantum Hall regime are a consequence of the physical size of the sample. Electron density drops to zero at the edge of the sample which introduces a confining potential in the y-direction $V(y)$ in (1.6):

$$\left[\frac{p_y^2}{2m^*} + \frac{1}{2}m^*\omega_c^2\left(y - \frac{\hbar k_x}{|e|B}\right)^2 + V(y)\right]\eta(y) = \varepsilon\eta(y)$$

This confining potential causes the Landau levels to bend upward approaching the edge of sample (see Fig. 1.4).

Bending of the Landau levels is pivotal in the physics of the quantum Hall effect. Let us consider the case when the Fermi energy ε_F lies between two Landau levels. In this situation, the bulk is insulating due to the presence of the cyclotron gap $\hbar\omega_c$. The edges, however, show completely different behaviour. Since each Landau level bends up, it crosses the Fermi level at both sides of the sample. At these two intersecting points, one-dimensional conducting channels emerge at the sample edges (see Fig. 1.4).

When we consider the group velocity for the case of the confining potential, it becomes:

$$v_g = \frac{1}{\hbar}\frac{\partial \varepsilon_N}{\partial k} = \frac{1}{\hbar}\frac{\partial V(y)}{\partial k_x} = \frac{1}{|e|B}\frac{\partial V(y)}{\partial y}\bigg|_{y=\frac{\hbar k_x}{eB}} \tag{1.9}$$

The confining potential causes the group velocity to become non-zero. As we can see in (1.9), the group velocity depends directly on the slope of the confining potential. On both sides of the sample the slope has opposite signs, resulting in chiral edge channels; they are counter-propagating at the opposite edges of the sample with a direction given by B.

Since all the edge channels on one side of the sample propagate in the same direction, backscattering only becomes possible if an electron is transferred to the counter-propagating edge channels at the opposite side of the sample. As both edges are macroscopically separated, backscattering is entirely suppressed in the quantum Hall regime.

1.2.3 Localised states and percolation

The integer quantum Hall effect features precise plateaus in the transverse resistance of $R_{xy} = \frac{h}{e^2 N}$. At these plateaus the longitudinal resistance drops to zero, marking current transport without dissipation. Fig. 1.5 presents the first discovery of the integer quantum Hall effect by K. von Klitzing et al in 1980 [2]. In the following, we have a closer look in how these quantised plateaus emerge and their connection to disorder.

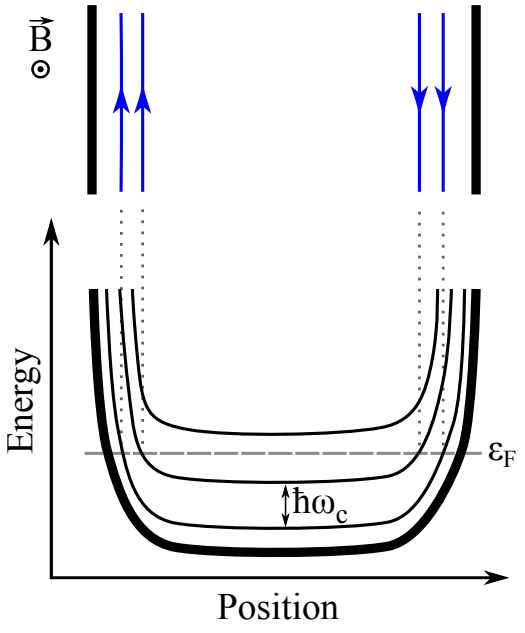

Figure 1.4: The confining potential due to the physical edge of the sample causes the Landau levels to bend up towards the edges. When the Landau levels cross the Fermi level, one-dimensional edge channels emerge (blue lines)

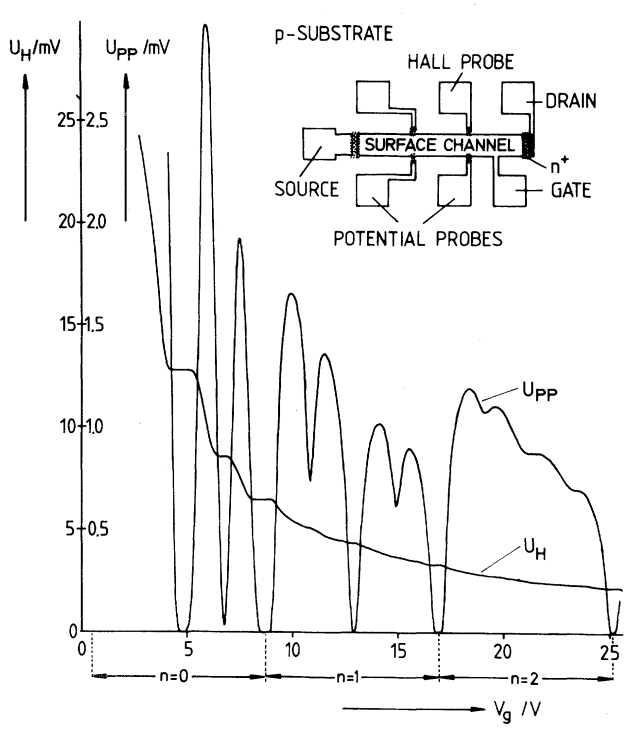

Figure 1.5: First observation of the integer quantum Hall effect. The transverse resistance is quantised at the plateaus while the longitudinal resistance drops to zero. Fig. taken from [2].

The edge channels propagate along the sample's edge carrying the current. So far, we have not considered the impact of disorder on these extended states and on the bulk of the sample in the quantum Hall regime.

Disorder causes the peaks in the density of states to broaden (see Fig. 1.6). As long as the broadening of the Landau levels does not exceed the separation width between Landau levels of $\hbar\omega_c$, quantised plateaus are still observable.

Landau levels in the bulk which so far have been assumed to be flat, exhibit randomly distributed hills and valleys of potential fluctuations (see Fig. 1.7a)[2]. These potential fluctuations can cross the Fermi level and form localised states circulating around potential hills. As long as the localised states remain small, opposite sides of the sample remain isolated and backscattering is suppressed.

When transverse resistance is quantised, edge channels propagate along the sample edge while localised states do not contribute to the current transport. The situation changes in the transition between two quantum Hall plateaus. Consider first Fig. 1.7a, where two edge channels propagate at the sample edge, contributing to the current transport. In this situation, the Fermi energy lies between the third and the fourth Landau level, on a plateau in R_{xy}.

When the magnetic field is increased or the carrier density decreased, we arrive at a situation where the Fermi level lies close to the third Landau level (see Fig. 1.7b). The third counter-propagating edge channel is no longer positioned near the edge of the sample but percolates into the bulk. Therefore, electrons are backscattered between opposite sides

2 Notice that the random potential of the disorder is, in general, weak ($V(\vec{r}) \ll \hbar\omega_c$). Even with some isolated regions of $V(\vec{r}) \gg \hbar\omega_c$, the transport through edge channels stays unchanged as long as the electron scattering rate does not become larger than ω_c [13].

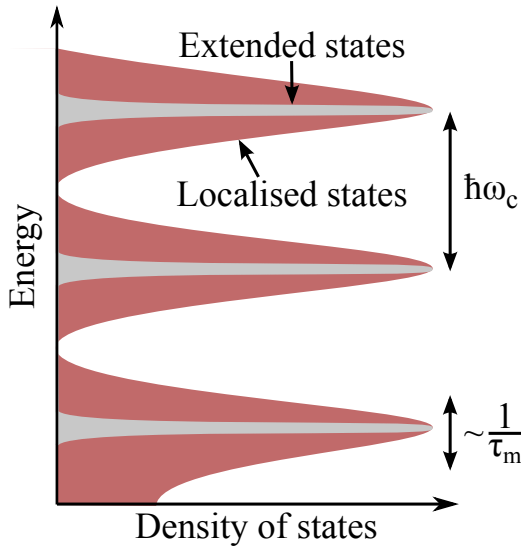

Figure 1.6: The delta-function peaks of density of states in high magnetic fields broadens due to disorder.

of the sample, giving rise to a non-zero longitudinal resistance. In this configuration, the transverse resistance is no longer quantised but in transition between two plateaus.

When the magnetic field is increased or the carrier density decreased even further, the third Landau level is unoccupied and the Fermi level lies between the second and the third Landau level (see Fig. 1.7c). Here, we regain the situation of counter-propagating edge channels (now two) with backscattering completely suppressed. The transverse resistance is quantised again and the longitudinal resistance drops to zero.

1.2.4 Significance of disorder

In order to observe plateaus in the quantum Hall regime, the transverse resistance has to stay constant over a range of magnetic fields and charge carrier density, respectively. In the previous section, we introduced localised states which arise due to randomly distributed hills and valleys of potential fluctuations from disorder in the bulk, causing the peaks in the density of states to broaden. Within these localised states, electrons are trapped on equipotential lines around the potential fluctuations in the bulk and, hence, do not contribute to current transport. We will see in the following that these localised states, and thus disorder, are crucial for observing quantum Hall plateaus. In the absence of disorder, the widths of the quantum Hall plateaus shrinks to zero.

A quantum Hall plateau occurs when the number of extended states which define the current transport stays constant upon varying the magnetic field and charge carrier density. Therefore, the resistance is quantised when the Fermi level is inside the cyclotron gap. However, the Fermi level is always pinned above the last occupied state. In the absence of disorder and, hence, localised states, the Fermi level jumps from one Landau level directly to the next one on changing the charge carrier density or magnetic field (see Fig. 1.8). The Fermi level can only be pinned inside the gap by localised states. Upon varying the charge carrier density or the magnetic field, localised states are filled which does not influence the global current transport and, hence, the resistance is quantised on a quantum Hall plateau.

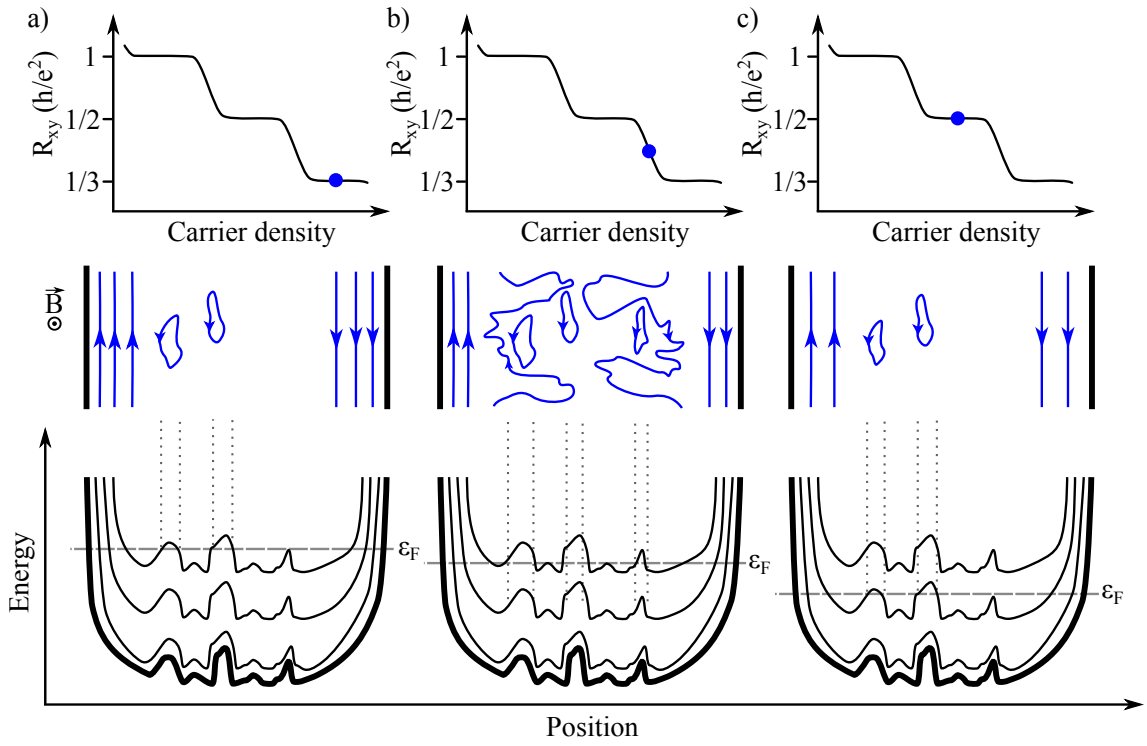

Figure 1.7: Schematic drawing of the evolution of Landau levels and the corresponding situation of channels in the sample at increasing carrier density from a) to c). a) When the Fermi level lies between two Landau levels, edge channels propagate at both sides of the sample, and backscattering is fully suppressed. The resistance is quantised. b) Once the Fermi level is close to a Landau level, edge channels percolate through the bulk connecting both sides of the sample giving rise to backscattering. The resistance is not quantised anymore but transits between two plateaus. c) The Fermi level lies between two Landau levels and the resistance becomes quantised again.

1.3 Transport through edge channels

When the Fermi level lies between two Landau levels in the bulk, current transport is only possible through ballistic edge channels, as seen in 1.2.2. In the following, we give a short introduction to ballistic transport, focusing on the Landauer-Büttiker formalism. Afterwards, we will use this formalism to derive the longitudinal and transverse resistance in the Hall bar configuration.

1.3.1 Ballistic conductors

In the ballistic regime, electrons pass through a device without being scattered and thus changing their momenta. In 1988, the groups of B.J. van Wees and of D.A. Wharam made the interesting discovery that conductance in a ballistic conductor is quantised as a function of its width even in the absence of a magnetic field [7, 14]. This quantisation can be understood by considering that current transport occurs through a specific number of transverse modes M within the Landauer formalism [15]

$$G = \frac{2e^2}{h} M T_r \tag{1.10}$$

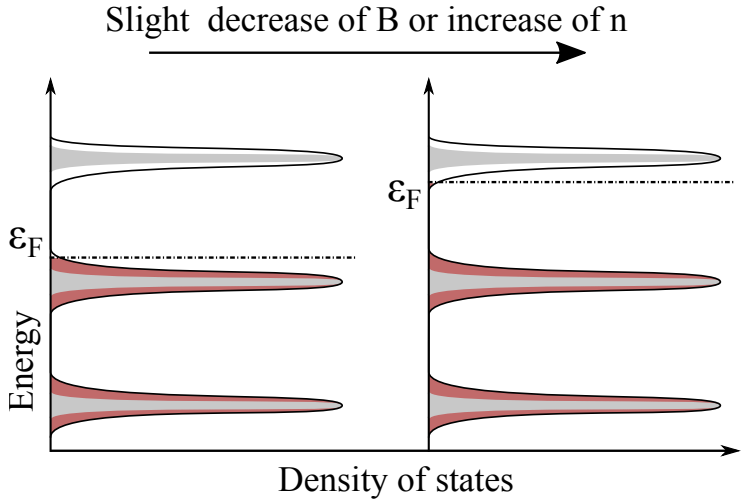

Figure 1.8: Schematic drawing of the density of states of low disorder devices. Low disorder leads to narrower peaks in the density of states. When the Fermi energy ε_F is pinned to the last localised states of the second Landau level, only a slight change in the charge carrier density or magnetic field causes ε_F to jump to the third Landau level. The resulting quantised plateau in the resistance is much smaller than in the case of broader peaks in the density of states.

which includes the transmission probability T_r between the conductor and the contacts. Eq. (1.10) defines the conductance in two-terminal configuration and includes contact resistance. Contact resistance arises from the interface between the contacts and the conductor, where the number of modes is reduced from infinity in the contacts to a few modes in the conductor. If we consider the case of $T_r = 1$, the conductor is fully ballistic and the conductance becomes quantised as

$$G = \frac{2e^2}{h} M \tag{1.11}$$

In this case (1.11) provides the contact resistance directly.

The theory of a two-terminal device has been extended by M. Büttiker to the multi-terminal case (for example the four-terminal device in Fig. 1.9). The total current I_i from lead i is given by the incoming current which is proportional to the number of transverse modes M_i, reduced by the reflected current and by the transmitted current from the other

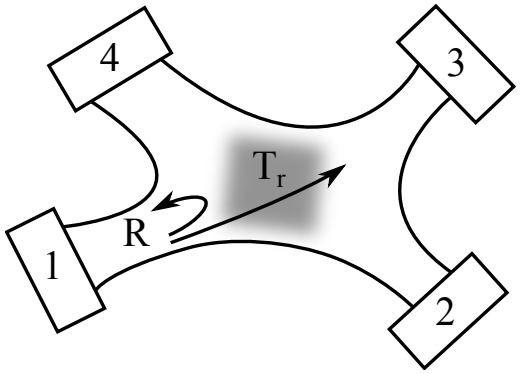

Figure 1.9: Schematic drawing of a four-terminal device. The current from current i is either transmitted to contact j with the probability T_r or reflected back into contact i.

leads [9, 16]:

$$I_i = -\frac{e}{h}\int dE\left[\left(M_i(E) - R_{ii}(E)\right) f_i(E) - \sum_{j\neq i} T_{r_{ij}}(E) f_j(E)\right] \tag{1.12}$$

Here, R_{ii} is the reflection probability from the lead i back into the lead i and $f_{i,j}(E)$ is the Fermi distribution in lead i and j. Büttiker assumes that there is no difference between current and voltage probes [16]. For small potential differences $\Delta\mu = \mu_i - \mu_j \ll k_B T$, equation (1.12) can be linearised in the form:

$$I_i = -\sum_{j\neq i} G_{ij}\left(V_i - V_j\right) \quad \text{with} \quad G_{ij} = -\frac{e^2}{h}\int dE\; T_{r_{ij}}(E)\left(\frac{\partial f_i(E)}{\partial \mu}\right) \tag{1.13}$$

$V_i = \frac{\mu_i}{e}$ is the voltage drop at contact i. For multi-terminal contacts, (1.13) can also be expressed in matrix form as [9]:

$$\begin{pmatrix} I_1 \\ I_2 \\ \vdots \\ I_N \end{pmatrix} = \frac{e^2}{h}\begin{pmatrix} N_1 - R_1 & -T_{r_{12}} & \cdots & -T_{r_{1N}} \\ -T_{r_{21}} & N_2 - R_2 & \cdots & -T_{r_{2N}} \\ \vdots & \vdots & & \vdots \\ -T_{r_{N1}} & -T_{r_{N2}} & \cdots & N_N - R_N \end{pmatrix}\begin{pmatrix} V_1 \\ V_2 \\ \vdots \\ V_N \end{pmatrix} \tag{1.14}$$

1.3.2 Landauer-Büttiker formalism

In the following, we extend the formalism of the previous section to the quantum Hall regime to derive the transverse resistance R_{xy} and longitudinal resistance R_{xx} of a Hall-bar configuration (see Fig. 1.10) [17]. Within this framework, edge states are considered as perfectly ballistic 1-dimensional channels. These channels connect neighbouring contacts in a clockwise direction (with the given magnetic field) with the same potential as the contacts from where they emerge. Fig. 1.10 represents a typical Hall bar with the current source and drain as contacts 1 and 4 respectively. Voltage probes (2, 3, 5 and 6) are assumed to have infinitesimal resistance and therefore not to withdraw any current. Since backscattering is not possible, transmission is perfect $T_r = 1$ between adjacent contacts.

The longitudinal and transverse resistance are obtained by adapting (1.14) to the Hall bar configuration shown in Fig. 1.10:

$$\begin{pmatrix} I_1 \\ I_2 \\ I_3 \\ I_4 \\ I_5 \\ I_6 \end{pmatrix} = \frac{e^2}{h}\begin{pmatrix} \nu & 0 & 0 & 0 & 0 & -\nu \\ -\nu & \nu & 0 & 0 & 0 & 0 \\ 0 & -\nu & \nu & 0 & 0 & 0 \\ 0 & 0 & -\nu & \nu & 0 & 0 \\ 0 & 0 & 0 & -\nu & \nu & 0 \\ 0 & 0 & 0 & 0 & -\nu & \nu \end{pmatrix}\begin{pmatrix} V_1 \\ V_2 \\ V_3 \\ V_4 \\ V_5 \\ V_6 \end{pmatrix} \tag{1.15}$$

The filling factor is directly proportional to the charge carrier density and hence is a real number. In the regime of edge channel transport when the Fermi level lies between two Landau levels, the filling factor ν which we defined in (1.8) becomes an integer and corresponds to the number of propagating edge channels. Since the current flows from

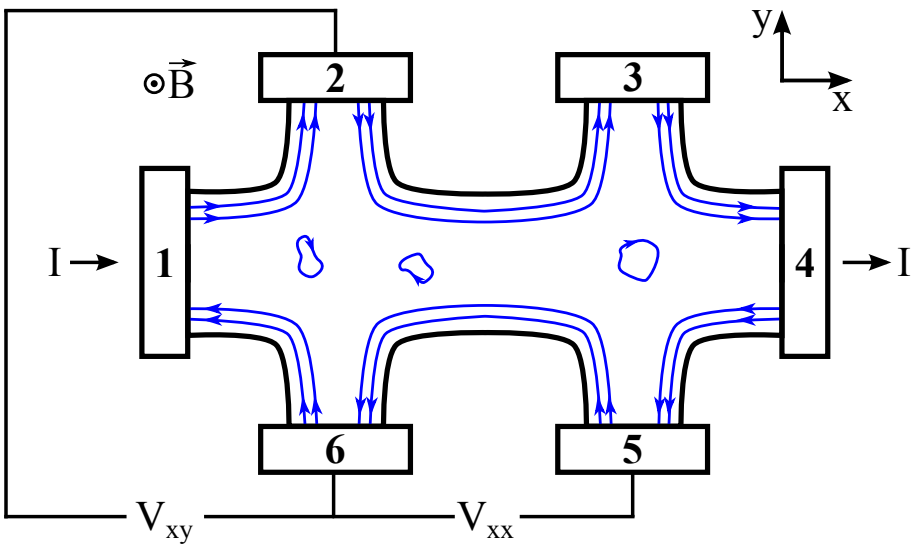

Figure 1.10: In the six terminal configuration of a Hall bar, edge channels circulate in a clockwise direction connecting neighbouring contacts. The current is driven from contact 1 to 4. The transverse resistance can be measured between 2 and 6 or equivalently between 3 and 5. Simultaneously, the longitudinal resistance is determined by the voltage drop between 2 and 3 or between 5 and 6.

contact 1 to 4, I_x takes the values: $I_1 = I = -I_4$ and $I_2 = I_3 = I_5 = I_6 = 0$. These relations simplify (1.15) as $V_1 = V_2 = V_3$ and $V_4 = V_5 = V_6$. This indicates that the voltage is equal along each side of the Hall bar and is determined by the current contact. Therefore, the current across the device is given by:

$$I = \frac{e^2}{h}\nu\,(V_1 - V_4)$$

Longitudinal resistance is measured in a four-terminal configuration. Current is applied between contacts 1 and 4 while voltage is measured between contacts 5 and 6 which results in

$$R_{xx} = R_{14,56} = \frac{V_6 - V_5}{I} = 0$$

As observed in quantum Hall measurements (see Fig. 1.5), the resistance along the same side of the sample vanishes due to the fact that all channels on the same edge have the same chemical potential.

The transverse resistance is calculated equivalently with a voltage measurement between contacts 2 and 6:

$$R_{xy} = R_{14,26} = \frac{V_2 - V_6}{I} = \frac{e^2}{h}\frac{1}{\nu}$$

The resistance between opposite sides of the sample is quantised, as long as the Fermi level remains in between two Landau levels upon varying B or n.

To consider conductivity in the sample, we need to take the tensor form of σ into account:

$$\boldsymbol{\sigma} = \begin{pmatrix} \sigma_{xx} & \sigma_{xy} \\ \sigma_{yx} & \sigma_{yy} \end{pmatrix} = \boldsymbol{\rho}^{-1} \tag{1.16}$$

We obtain the elements of the conductivity tensor by inverting (1.16):

$$\begin{aligned} \sigma_{xx} &= \frac{\rho_{xx}}{\rho_{xx}^2 + \rho_{xy}^2} = \sigma_{yy} \\ \sigma_{xy} &= \frac{\rho_{xy}}{\rho_{xx}^2 + \rho_{xy}^2} = -\sigma_{yx} \end{aligned} \tag{1.17}$$

We see from (1.17), that when the longitudinal resistance ρ_{xx} is zero, the corresponding conductivity is also zero. When ρ_{xx} is zero, both the transverse resistivity ρ_{xy} and conductivity σ_{xy} have a plateau with $\rho_{xy} = \frac{1}{\sigma_{xy}}$.

1.3.3 Edge channel reconstruction

So far, we have only considered non-interacting electrons and completely neglected screening in the 2DEG, which leads to the simple picture of bent Landau levels crossing the Fermi level at a single point at the sample edge (Fig. 1.11a). The singularity of a sudden increase of the charge carrier density is not physically possible. In order to make the model physical, we need to include screening of the confining potential in the one-particle picture [18]. At the spatial locations where the Landau levels intersect the Fermi level, the strongly oscillating density of states is maximal, resulting in strong screening of the confining

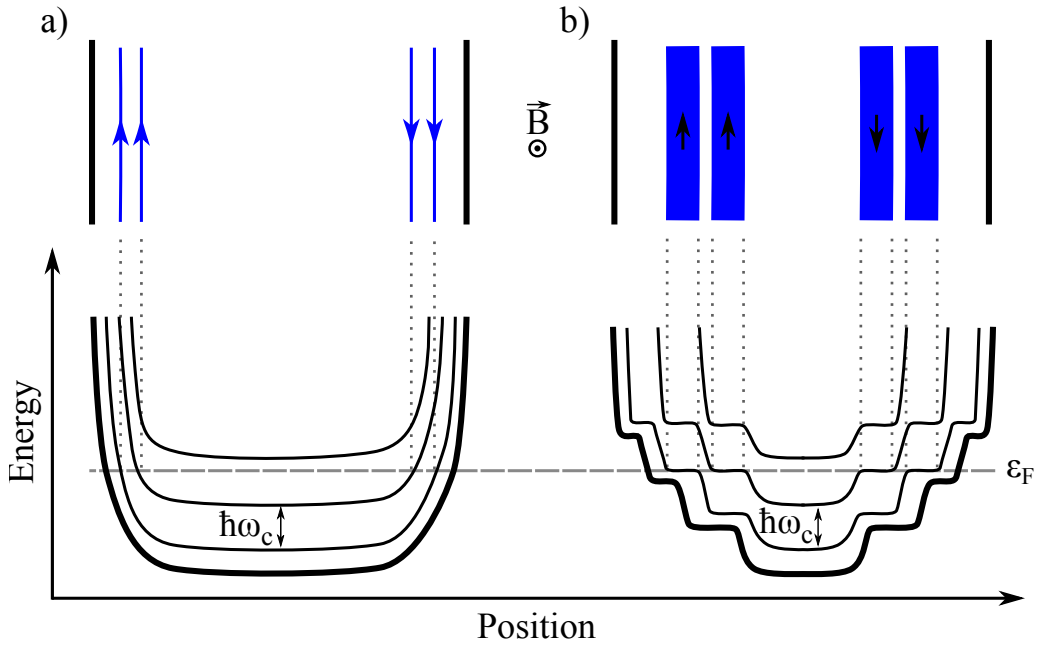

Figure 1.11: a) The one-electron picture leads to infinitesimal narrow edge channels which are physically not possible. b) The screening of a 2DEG in high magnetic field causes the confining potential to stay constant over a spatially extended region. Therefore, the edge-channels obtain a finite width.

potential. The latter is, therefore, flattened leading to the formation of a wide strip (see Fig. 1.11b).

The regions of the flattened confining potential which corresponds to the edge channels form compressible strips. With increasing magnetic field, the compressible strips move further away from the edge towards the bulk of the sample.

Between compressible strips, the Fermi level lies in the cyclotron gap, therefore, there is no screening. These regions are referred to as incompressible strips.

2 Fractional Quantum Hall Effect

In 1982, D.C. Tsui, H.L. Stormer and A.C. Gossard made a surprising discovery of a fractional plateau at $\nu = \frac{1}{3}$ which uncovered the field of the fractional quantum Hall effect [8]. In 1983, R.B. Laughlin provided a theoretical explanation of the fractional plateaus of the form $\nu = \frac{1}{m}$ with m being an odd integer [20]. In his theory, the ground state of the lowest Landau level is composed of an incompressible quantum liquid. Fractional plateaus can no longer be explained in terms of a one-particle picture as in the integer quantum Hall effect. Instead, interactions between electrons become crucial for understanding the fractional quantum Hall effect.

One of the first measurements of H.L. Stormer et al is presented in Fig. 1.12 with the transverse resistance exhibiting quantised plateaus in (a) while the longitudinal resistance has a minimum (b) as a function of the magnetic field.

In order to account for additional plateaus such as $\nu = \frac{2}{5}$ or $\nu = \frac{3}{7}$ which do not fit the $\frac{1}{m}$ series, Laughlin's theory has been extended by Jain who developed the composite fermions picture [21, 22]. until now only fractional plateaus in the form of $\nu = \frac{p}{q}$ with p an integer and q an odd integer had been observed. The detection of even-denominators as $\nu = \frac{5}{2}$ and $\nu = \frac{7}{2}$ was surprising [23]. One of the existing theories explains these fractional

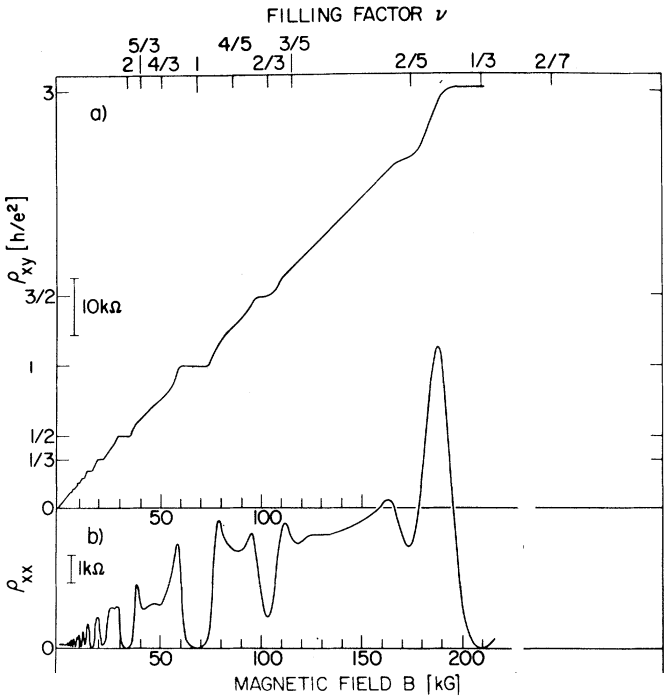

Figure 1.12: One of the first results of the fractional quantum Hall effect by H.L. Stormer et al. Transverse resistance versus magnetic field exhibits plateaus while the longitudinal resistance has a minimum measured at 0.55 K. Fig. taken from [19]

plateaus within the fractional statistics of additional particles called anyons [24, 25].

A short description of each of the theories which are based on the above mentioned articles as well as [9, 11, 12], are presented in the following sections.

2.1 Quantum liquids

Laughlin proposed a many-body wave function of the ground state which conserves the continuous spatial symmetry:

$$\Psi_m = \prod_{j<k} (z_j - z_k)^m \exp\left(-\frac{1}{4}\sum_l |z_l|^2\right) \tag{1.18}$$

Here, $z_j = x_j + iy_j$ is the position of the j^{th} electron. The first term of (1.18) contains the Coulomb interaction between the electrons tending to zero as the electrons approach the same position. The second term is a Gaussian function representing the ground state of non-interacting particles. The integer m must be odd in order to guarantee a change in sign when two electrons are interchanged (Fermi statistics). The filling factor is defined as $\nu = \frac{1}{m}$ which is why only fractional plateaus of the form $1, \frac{1}{3}, \frac{1}{5}$ etc. can be accounted for by the wave function (1.18).

Apart from the previously mentioned plateaus at $\nu = \frac{1}{m}$, additional plateaus of the general form $\nu = \frac{p}{q}$ with q being an odd integer, as $\frac{4}{3}$, $\frac{5}{3}$, $\frac{2}{5}$, $\frac{3}{5}$, $\frac{2}{7}$ have been found [8, 19]. To account for these new plateaus, Haldane and Haperin extended Laughlin's theory to the so-called hierarchical model [27, 28]. In this model, the filling factors extracted from

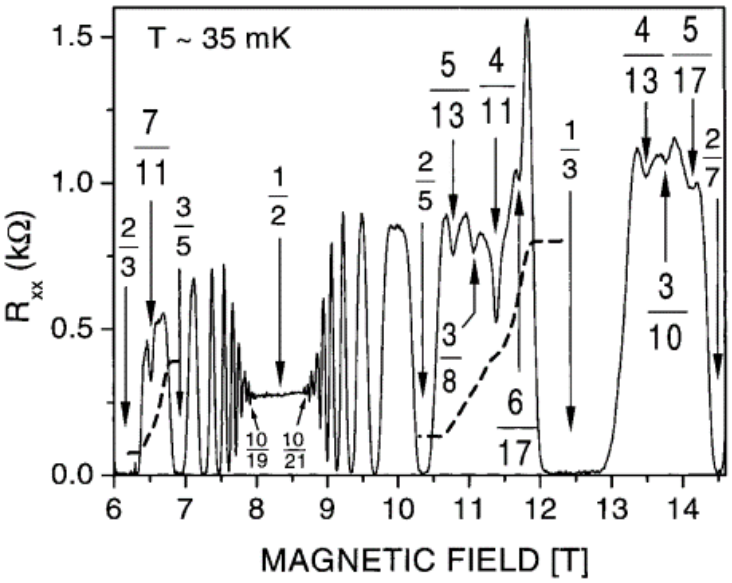

Figure 1.13: In high-quality GaAs/AlGaAs quantum well, the longitudinal resistance R_{xx} as a function of the magnetic field B features pronounced minima at $\nu = \frac{4}{11}$ and $\frac{5}{13}$ which are explained by a fractional quantum Hall effect of composite fermions. Fig. taken from [26]

the Laughlin's theory constitute the "parent" state from which new states are generated:

$$\nu = \cfrac{1}{m + \cfrac{\alpha_1}{p_1 + \cfrac{\alpha_2}{\ddots}}}$$

with $\alpha_j = \pm 1$ and $p_j = 2, 4, 6 \ldots$. In order for the "daughter" state to occur, the Laughlin-type "parent" state must exist. The quasi-particles of the "parent" state condense into the new Laughlin-type "daughter" states due to Coulomb interaction.

2.2 Composite fermions

An alternative approach is the generalisation of Laughlin's theory by Jain [21, 22]. This model provides a theoretical approach to, first, combine the integer and the fractional quantum Hall effect within the same framework and, second, to explain additional plateaus of the form:

$$\nu = \frac{p}{2kp \pm 1} \tag{1.19}$$

in which, k and p are integers.

This form of fractional filling factor can be interpreted as if an average number of magnetic flux quanta $\frac{\phi_0}{\nu}$ is attached to each of the electrons forming non-interacting "composite fermions" in an effective magnetic field [29]

$$B_{eff} = B - B_{\frac{1}{2}} = \frac{hn}{ep}$$

a magnetic field reduced by the field $B_{\frac{1}{2}}$ at $\nu = \frac{1}{2}$. If an even number of flux quanta ($2p$) is attached to an electron, the resulting composite particle is a fermion. The fractional quantum Hall effect is then described by an integer quantum Hall effect of non-interacting composite fermions. Here, the fractional filling factor ν is correlated to the filling factor of the composite fermion ν^* by the relation:

$$\nu = \frac{\nu^*}{1 + 2k\nu^*}$$

While the theory of composite fermions is able to explain many of the observed fractional states, additional fractional plateaus such as $\frac{4}{11}$ and $\frac{5}{13}$ [30] have been observed (see Fig. 1.13) which are not included in the series (1.19). A possible extension of Jain's series is to consider the weak residual interaction between composite fermions resulting in a fractional quantum Hall effect of composite fermions [26, 31].

When we consider (1.19), an interesting case is the even-denominator fraction $\frac{1}{2}$. In order to obtain $\nu = \frac{1}{2}$, p has to go to infinity. Here, the effective magnetic field is zero. The structures in R_{xx} are mirror symmetric with respect to $\nu = \frac{1}{2}$ [21] (see Fig. 1.13). In contrast to the fractional states described so far, the $\frac{1}{2}$-state is a metallic compressible state [32], having neither a plateau in R_{xy} nor a minimum in R_{xx}.

2.3 Even-denominator fractions

So far Laughlin's theory, as well as its extensions, postulate the existence of only odd-denominator fractions to satisfy the antisymmetry of the wave function under the interchange of two particles required to conserve the fermionic statistics. The observation of even-denominator fractions of $\frac{3}{2}$ and $\frac{5}{2}$ came by surprise in 1987 [23] (see Fig. 1.14). Later on, additional even-denominator fractions such as $\frac{7}{2}$ [34] and $\frac{1}{4}$ [35] were observed and in the case of the $\frac{5}{2}$ [33], a highly precise quantisation was measured.

When tilting the magnetic field, the fraction $\frac{5}{2}$ collapses rapidly [36] which had not been observed for any of the odd-denominator fractions. Therefore, it has been assumed that the $\frac{5}{2}$ ground state is a non-polarised spin-singlet state [37]. Another approach is to consider the $\frac{5}{2}$-ground state as a BCS-like pairing of composite fermions into a condensation of bosons [24, 25]. The quasiparticle excitations of this ground state are neither fermions nor bosons but follow the fractional statistics of anyons [38]. Many aspects of the $\frac{5}{2}$-state are still open and under debate.

Summary

In the first chapter, we introduced the basics of the quantum Hall effect in 2DEG systems. We began by describing the motion of an electron in magnetic and electric field which leads to an orbital trajectory. In the quantum Hall regime, the energy is quantised in so-called Landau levels which due to the confining potential bend approaching the edge of the sample. At the crossing of the Fermi level with the Landau levels, one dimensional edge channels emerge. The current is, hence, transferred in these edge channels along the edge of the sample. The chiral nature of the edge channels cause edge channels moving in one direction to propagate along one edge while edge channels in the opposite direction propagating along the opposite edge of the sample. Since these counter-propagating edge channels are distant from each other by the width of the sample, backscattering is suppressed.

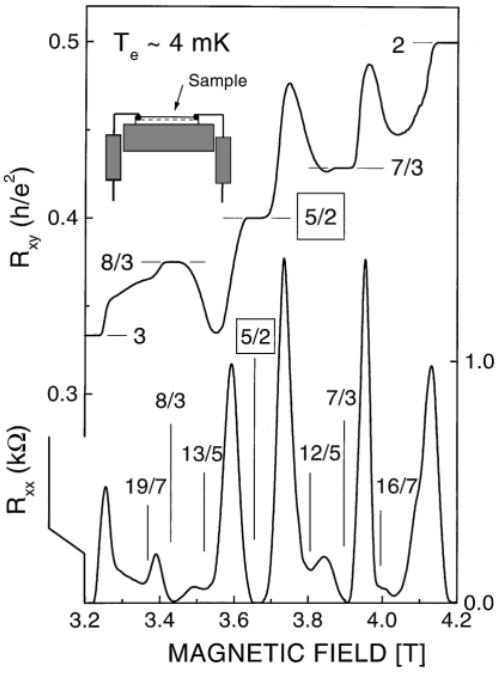

Figure 1.14: Precise quantisation of even-denominator faction $\frac{5}{2}$. Fig. taken from [33]

In this regime, the transverse conductance exhibits precise plateaus at $R_{xy} = \frac{h}{Ne^2}$ while the longitudinal resistance drops to zero. For the complete picture in a Hall bar, we derived the propagation of edge channels in the framework of Landauer-B"uttiker formalism.

In the second part of this chapter, we introduced the fractional quantum Hall effect of highly correlated electrons. We mentioned several theories for explaining and deriving fractional states as Laughlin's theory and the theory of composite fermions.

In the next chapter, we apply these basic principles of integer and fractional quantum Hall effect to the anomalous case in graphene.

CHAPTER 2

THEORETICAL AND EXPERIMENTAL FRAMEWORK ON THE QUANTUM HALL EFFECT IN GRAPHENE

Graphene, a monolayer of carbon atoms arranged in a honeycomb lattice, was theoretically predicted by P.R. Wallace in 1946 [39]. In 2005, K.S. Novoselov et al were successful in isolating a single graphene flake to study its novel transport characteristics [1]. Its peculiar properties stem from its bandstructure which is gapless and has a linear energy-momentum dependence.

In this chapter, we first describe the electronic bandstructure and resulting transport properties of graphene at zero magnetic fields. Afterwards, we add magnetic fields to describe the relativistic quantum Hall regime.

1 Electronic structure of graphene

1.1 Electronic bandstructure

In the following, we give a short overview of the lattice structure of graphene and its resulting energy dispersion relation. We will then focus on the low energy approximation and its consequences on transport properties. It is mainly based on [40–42] where a more detailed description and derivation can be found.

1.1.1 Honeycomb lattice

Due to sp_2-hybridization between the first s-, p_x- and p_y-orbitals, Carbon atoms in graphene are connected through σ-bonds with an average distance of $a = 1.42\,\text{Å}$. The remaining perpendicular p_z-orbital forms covalent π-bonds with its neighbours providing the free electrons which characterise its low energy properties.

The honeycomb lattice can be considered as a triangular Bravais lattice with two atoms A and B per unit cell (Fig. 2.1(a)). The vectors $\vec{a}_1$ and $\vec{a}_2$ represent the corresponding basis of the Bravais lattice. Each atom A is directly connected to an atom B via the nearest neighbour (nn) hopping vectors $\vec{\delta}_1$, $\vec{\delta}_2$ and $\vec{\delta}_3$.

The reciprocal lattice of the honeycomb lattice is composed of hexagons rotated by $\frac{\pi}{2}$ in comparison to the real space lattice. The first Brillouin zone (BZ) with its centre $\vec{\Gamma}$ is spanned by the reciprocal basis vectors $\vec{b}_1$ and $\vec{b}_2$ as shown in Fig. 2.1(b). The corners of the first BZ comprises two inequivalent points $\vec{K}$ and $\vec{K}'$.

1.1.2 Energy dispersion

In order to calculate the energy dispersion of graphene, we need first to consider a wave function which includes the two atoms A and B of a unit cell:

$$\Psi(\vec{r}) = \alpha_{\vec{k}}\Psi^A_{\vec{k}}(\vec{r}) + \beta_{\vec{k}}\Psi^B_{\vec{k}}(\vec{r})$$

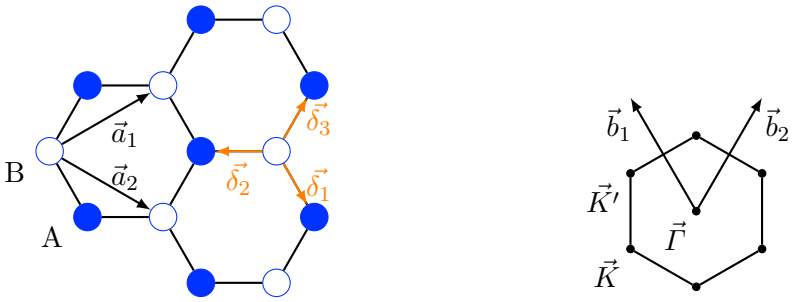

(a) **(b)**

Figure 2.1: a) Real space honeycomb lattice of the graphene spanned by the basis vectors $\vec{a}_1$ and $\vec{a}_2$. The nearest neighbour hopping is expressed by $\vec{\delta}_1$, $\vec{\delta}_2$ and $\vec{\delta}_3$. b) The first Brillouin zone of the reciprocal space is a hexagon spanned by the basis vectors $\vec{b}_1$ and $\vec{b}_2$ and centred around $\vec{\Gamma}$ with the inequivalent corners $\vec{K}$ and $\vec{K}'$.

with α and β being complex functions of the wave vector $\vec{k}$. The Bloch functions $\Psi^A_{\vec{k}}(\vec{r})$ and $\Psi^B_{\vec{k}}(\vec{r})$ of the form:

$$\Psi^j_{\vec{k}}(\vec{r}) = \sum_{\vec{R}_l} \exp\left(i\vec{k}\vec{R}_l\right) \phi^{(j)}(\vec{r} + \vec{\delta}_j - \vec{R}_l)$$

comprise the atomic orbital wave function $\phi^{(j)}$ of $j = A$ or B for the two sublattices. The Bravais lattice vector is $\vec{R}_l$. The energy dispersion is calculated by solving the Schrödinger equation $H\Psi(\vec{r}) = \varepsilon_{\vec{k}}\Psi(\vec{r})$.

The band structure of the π-electrons of graphene is approximated within the tight-binding model [43]. An electron may hop between the nearest-neighbour (nn) and next-nearest-neighbours (nnn) atoms. For the calculation of the energy dispersion, we also need to take into account the nearest-neighbour (nn) overlap corrections. The energy dispersion takes the form[1]:

$$\varepsilon^\lambda(\vec{k}) = 2t'_{nnn} \sum_{i=1}^{3} \cos\left(\vec{k}\cdot\vec{a}_i\right) + \lambda t_{nn} \sqrt{3 + 2\sum_{i=1}^{3} \cos\left(\vec{k}\cdot\vec{a}_i\right)} \tag{2.1}$$

Here, t_{nn} is the (nn) hopping amplitude[2] and t'_{nnn} is the effective (nnn) hopping amplitude[3]. The parameter $\lambda = \pm 1$ represents the two solutions of (2.1) which label the two bands: π (valence band) for a negative λ and π^* (conduction band) for a positive λ.

In undoped graphene, due to the perpendicular p_z-orbital, each carbon atom contributes one π-electron which is either spin-up or spin-down. Each electronic state is occupied by two electrons of opposite spins. Therefore, half of the total number of states is occupied. The valence band is, hence, completely filled with electrons while the conduction band remains empty. The Fermi energy ε_F is located above the last filled state which is at $\varepsilon = 0$. The π- and π^*-bands touch at this point $\vec{k}_D$ which is referred to as the Dirac point. The Dirac point is typically located at the corners of the first Brillouin zone of K and K'.

The energy dispersion (2.1) as a function of the wave vector is plotted in Fig. 2.2a. Only if $t'_{nnn} = 0$, equation (2.1) is symmetric around zero energy. At finite t'_{nnn}, the electron-hole symmetry is broken and the conduction and valence bands are asymmetric.

Since mainly low energy excitations govern the electronic transport properties, the dispersion relation (2.1) can be linearised in the vicinity of the Dirac point ($\vec{k} = \pm\vec{K} + \vec{q}$ with $|\vec{q}| \ll |\vec{K}| \sim \frac{1}{a}$). We obtain in first order approximation:

$$\boxed{\varepsilon^\lambda_{\xi=\pm}(\vec{q}) = \lambda\hbar v_F|\vec{q}|} \tag{2.2}$$

Here, $v_F \cong 1 \times 10^6\,\mathrm{m\,s^{-1}}$ is the Fermi velocity. The energy dispersion (2.2) depends linearly

1 Notice that, (2.1) is already an approximation assuming that $t'_{nnn} \ll t$ which turns out to be justified by comparing this approximation with numerical calculations.

2 $t_{nn} \equiv \int d^2r \phi^{A*}(\vec{r}\Delta V \phi^B(\vec{r}) + \vec{\delta}_2)$ with ΔV being the potential energy of the ions.

3 The effective hopping amplitude of the form $t'_{nnn} = t_{nnn} - s t_{nn}$ contains the (nnn) hopping amplitude $t_{nnn} \equiv \int d^2r \phi^{A*}(\vec{r})\Delta V \phi^A(\vec{r} + \vec{a}_1)$ and the (nn) overlap correction $s \equiv \int d^2r \phi^{A*}(\vec{r})\phi^B(\vec{r} + \vec{\delta}_2)$.

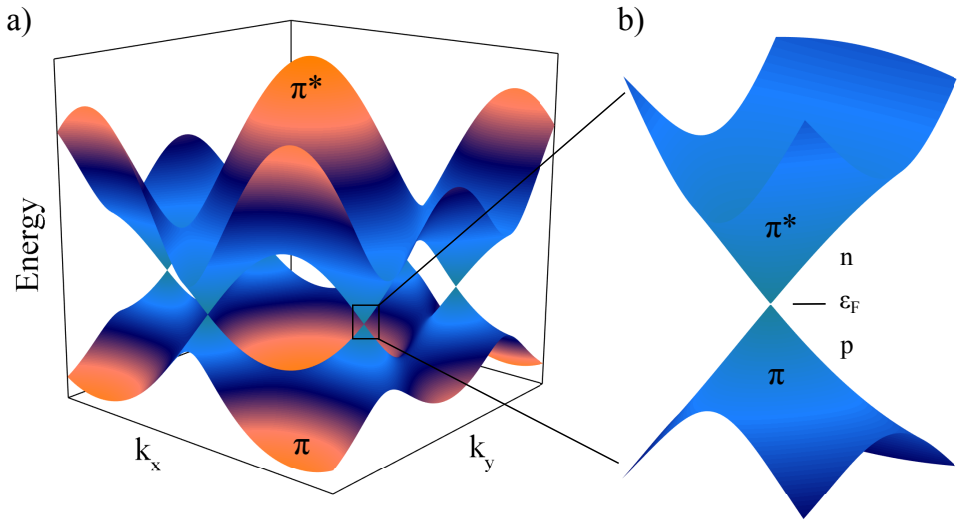

Figure 2.2: a) Energy dispersion given by (2.1) for $t'_{nnn} = 0.1t$ with t =3 eV. The upper band is the π^*- or conduction band and the lower band is the π- or valence band. Both bands touch at the Dirac point where ε_F is located. b) The energy dispersion around the Dirac point can be approximated by a linear $\vec{k}$-dependence.

on the wave vector $|\vec{k}|$ as presented in Fig. 2.2b[4].

We have introduced the parameter $\xi = \pm 1$ in (2.2) which is the valley isospin, present due to the twofold valley symmetry of the points K and K' in reciprocal space. The plus sign corresponds to the K point and the minus sign is linked to the K' point. The linear energy dispersion (2.2) is independent of ξ for which reason K and K' are indistinguishable resulting in a two-fold valley degeneracy.

It is important to distinguish the points K and K' from the two carbon atoms A and B. The points K and K' specify two inequivalent locations at the corners of the first Brillouin zone in reciprocal space. In contrast, the two atoms A and B which form the basis of two sublattices are part of the real space hexagonal structure. The symmetry of the two sublattices lead to the sublattice pseudospin which specifies the location of the electronic density. For instance, the "spin-up" state refers to the concentration of the electronic density at the sublattice A. The electronic density is typically spread equally among both sublattices A and B.

An additional consequence of the linear energy dispersion (2.2) is that the charge carriers in graphene behave like relativistic, massless Dirac fermions with the velocity v_F [1]. The 2D Dirac Hamiltonian $H_D = v_F\ \vec{p}\cdot\vec{\sigma}$ in which $\vec{p} = \hbar\vec{q}$ is the canonical momentum and $\vec{\sigma}$ is the spin, is adapted to the low excitation limit of graphene in the form:

$$H_D^{\xi=\pm} = \xi v_F\ \ (p_x\sigma^x + p_y\sigma^y) \tag{2.3}$$

One important difference to the general Dirac equation is that $\vec{\sigma} \equiv (\sigma^x,\sigma^y)$ in (2.3) are the Pauli matrices of the sublattice pseudospin and not the real spin. Spin-up describes the configuration when the carrier density is concentrated on one sublattice and spin-down

4 In contrast, the energy dispersion of a 2DEG depends on the square of the wave vector ($\varepsilon \sim k^2$).

corresponds to the other sublattice.

For the calculation of the Dirac Hamiltonian in magnetic field, it becomes useful to write (2.3) in matrix notation which directly considers the propagation of the Dirac particles in the x-y-plane:

$$H_D^{\xi=\pm} = \xi v_F \begin{pmatrix} 0 & \vec{\sigma} \cdot \vec{p} \\ \vec{\sigma} \cdot \vec{p} & 0 \end{pmatrix}$$

1.2 Chirality and isospin

Helicity η is defined as the projection of the spin $\vec{\sigma}$ onto the direction of propagation with the momentum $\vec{p}$:

$$\hat{\eta} = \frac{\vec{\sigma} \cdot \vec{p}}{|\vec{p}|}$$

The eigenvalues of $\hat{\eta}$ are $\eta = +1$ (right-handed) if the spin is parallel to the momentum and $\eta = -1$ (left-handed) if the spin and momentum are antiparallel. For instance, neutrinos which are helical particles, are always left-handed while antineutrinos are right-handed.

For massless Dirac particles, as it is the case for electrons in graphene, helicity and chirality are almost equivalent with one deviation. The spin is no longer the true spin of a particle but rather the pseudospin, particularly the valley pseudospin ξ.

Additionally, in the absence of a mass term, the chirality operator commutes with the Dirac Hamiltonian (2.3). Therefore, the chirality is a good quantum number.

The two valleys K and K' have opposite chirality due to time reversal symmetry [44]. Electrons have a positive chirality in the K-valley while they have a negative one in the K'-valley. The relation

$$\lambda = \xi\eta \tag{2.4}$$

shows a direct correlation between the band index λ, the valley isospin ξ and the chirality η (see Fig. 2.3).

The peculiar chirality of graphene due to its massless Dirac charge carriers leads to further interesting consequences which we will discuss in the next section.

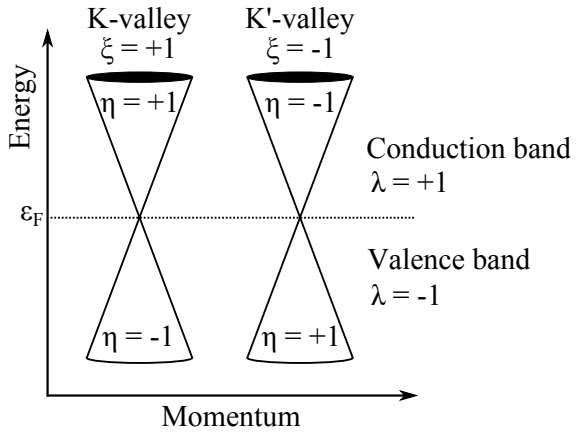

Figure 2.3: The relation (2.4) presents an important correlation between the chirality η, the band index λ and the valley pseudospin ξ.

2 Transport properties at zero magnetic field

In the following, we present some of the special electronic properties of graphene which result from its linear energy dispersion. K.S. Novoselov, A.K. Geim et al were successful in isolating a monolayer of graphene by a simple technique, allowing them to study its unique electronic properties [1]. By placing graphene on an insulating substrate equipped with a backgate electrode (Si^{++}, SiO_2) we are able to change the charge carrier density and, hence, the Fermi level. Fig. 2.4 presents their measured dependence of the conductivity σ on the backgate voltage V_g. The Fermi level is tuned from holes at negative V_g to electrons at positive V_g demonstrating the bipolar behaviour of graphene. The change of polarity from electrons to holes occurs at the charge neutrality point V^{CNP} signalled by the minimum of conductivity.

2.1 Berry's phase

In quantum mechanics, Berry's phase is the phase which is gained by the wavefunction in a cyclic adiabatic process. In graphene, the valley degeneracy leads to a non-zero Berry's phase [45]. When an electron moves in a complete circle which corresponds to a full rotation of the wave vector or pseudospin, the wave function acquires a Berry's phase of π.

The non-zero Berry's phase in graphene is experimentally measurable in Shubnikov-de Haas oscillations and in the quantum Hall regime [3]. Concerning the first point, the Berry's phase causes a phase shift of π in the Shubnikov-de Haas oscillations. We will discuss the second point more in detail when we come to the quantum Hall effect in graphene in the next section. Here, we only mention that the unconventional quantum Hall effect in graphene is also a direct consequence of the non-zero Berry's phase.

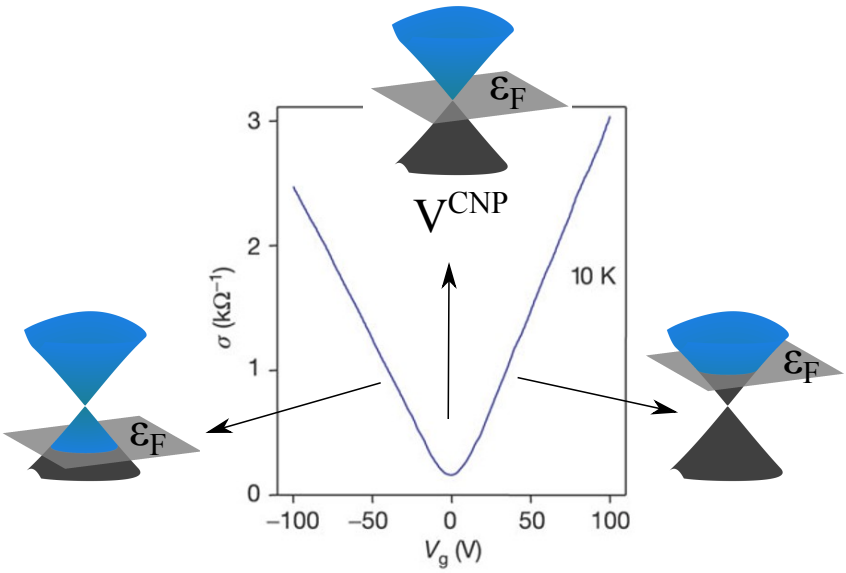

Figure 2.4: Conductance as a function of the backgate voltage showing the electric field effect in graphene. The shift from electrons to holes occurs at the minimum of conductivity at the Dirac point. Fig. taken from [1].

3 Relativistic Quantum Hall effect

The quantum Hall (QH) effect which we have already introduced in the previous chapter, becomes anomalous in the case of graphene. Its linear energy dispersion and the bipolar charge carriers of electrons and holes distinguishes graphene from a conventional 2-dimensional electron gas (2DEG). K.S. Novoselov, A.K. Geim et al [1] as well as Y.B. Zhang et al [3] were able to observe the quantum Hall effect in graphene directly after its discovery in 2005. The results of K.S. Novoselov on the longitudinal resistivity and the transverse conductivity as a function of the charge carrier density are presented in Fig. 2.5. The transverse conductivity exhibits pronounced plateaus while the longitudinal resistivity drops to zero. The intriguing phenomenon of the QH plateaus of graphene is that they occur with the sequence:

$$G_{xy} = \frac{e^2}{h}\nu \qquad \text{with} \quad \nu = \pm 4\left(n + \frac{1}{2}\right) \tag{2.5}$$

The factor of 4 originates from the four-fold degeneracy of each Landau level including the two-fold spin and two-fold valley degeneracies. The sign in the filling factor ν defines the type of charge carrier: plus (minus) sign stands for electrons (holes).

The new zero energy Landau level ($n = 0$) is shared by both electrons and holes. At a filling factor of $\nu = 0$, the number of electrons corresponds to the number of holes resulting

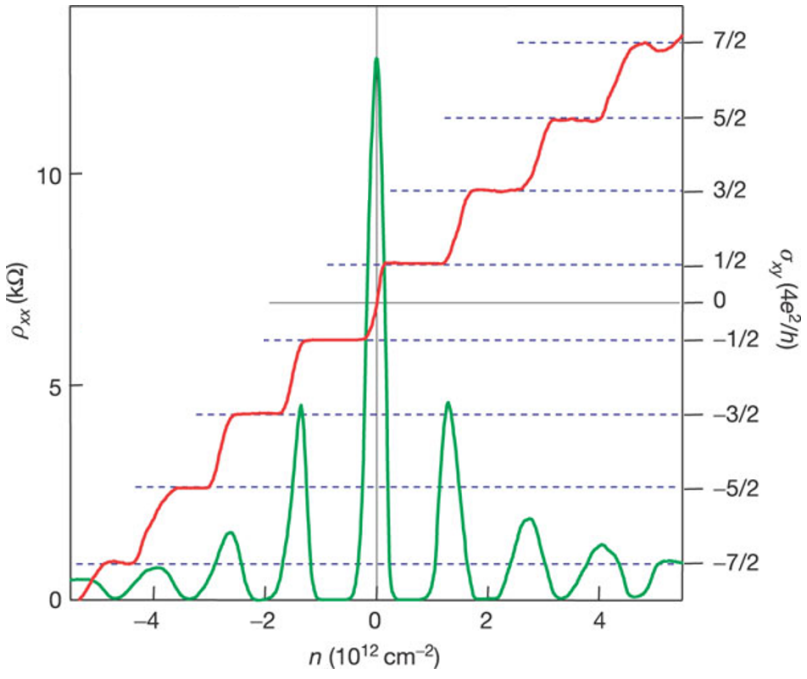

Figure 2.5: Longitudinal resistivity ρ_{xx} (green) and Hall conductivity σ_{xy} (red) with carrier concentration n at B =14 T and T =4 K. The transverse conductivity exhibits quantised plateaus following (2.5) while the longitudinal resistivity drops to zero. Figure taken from [1]

in a half-filled Landau level[5].

The discovery of additional plateaus at $\nu = \pm 1$ and ± 4 outside of the sequence (2.5) by the group of P. Kim was surprising [46]. The group of E.Y. Andrei even observed a plateau at $\nu = \pm 3$ in suspended graphene [47]. more recently in 2011, C.R. Dean developed a technique to place a graphene flake on an atomically flat flake of hexagonal boron nitride (hBN), which opened up the research of high-mobility graphene devices [48]. They observed plateaus at every integer value of the filling factor [5]. The appearance of these plateaus outside of the sequence in equation (2.5) is due to the breaking of the symmetry of spin and valley of the Landau levels. We will consider the possible origin and consequences of the symmetry breaking in the course of this section. Thereby, we will have a closer look at the particular zeroth Landau level. Since it is occupied by electrons and holes, the lifting of the spin and valley degeneracies result in intriguing properties which depend, for instance, on the hierarchy of the symmetry breaking as well as the role played by interactions.

Before addressing the lifting of the degeneracies, we first derive and discuss the degenerate energy dispersion of graphene in magnetic fields which yields the Landau level spectrum.

3.1 Energy quantisation

The Hamiltonian in a magnetic field is obtained by using the Peierls substitution which replaces the canonical momentum $\vec{p} = \hbar\vec{q}$ by the gauge-invariant kinetic momentum $\vec{\pi}$ in the form:

$$\vec{p} \to \vec{\pi} = \vec{p} + e\vec{A}(\vec{r})$$

This substitution is valid as long as the magnetic length $l_B = \sqrt{\frac{\hbar}{eB}}$ is much larger than the lattice spacing a. This is indeed the case for graphene, at least up to a magnetic field of 45 T. The vector potential $\vec{A}(\vec{r})$ is gauge-invariant and introduces a spatial dependence which is why the Hamiltonian is no longer translation invariant and canonical momentum is no longer conserved. The Hamiltonian in magnetic field translates therefore into

$$H_D^\xi = \xi v_F \left(p_x\sigma_x + p_y\sigma_y\right) \to H_B^\xi = \xi v_F \left(\pi_x\sigma_x + \pi_y\sigma_y\right) \tag{2.6}$$

The commutation relations of the canonical momentum $\vec{p}$ and position $\vec{r}$ of $[x,p_x] = [y,p_y] = i\hbar$ and $[x,y] = [p_x,p_y] = [x,p_y] = [y,p_x] = 0$ lead to the commutation relation of the kinetic momentum

$$[\pi_x,\pi_y] = -i\frac{\hbar^2}{l_B^2}$$

As for the derivation of the one-dimensional harmonic oscillator, we introduce the ladder operators:

$$\hat{a} = \frac{l_B}{\sqrt{2}\hbar}\left(\pi_x + i\pi_y\right) \quad \text{and} \quad \hat{a}^\dagger = \frac{l_B}{\sqrt{2}\hbar}\left(\pi_x - i\pi_y\right) \tag{2.7}$$

5 The shift of $\frac{1}{2}$ in (2.5) is due to the Berry's phase of π.

with the commutation relation $\left[\hat{a},\hat{a}^\dagger\right] = 1$. By inverting (2.7), we obtain for the components of the kinetic momentum:

$$\pi_x = \frac{\hbar}{\sqrt{2}l_B}\left(\hat{a}^\dagger + \hat{a}\right) \quad \text{and} \quad \pi_y = \frac{\hbar}{i\sqrt{2}l_B}\left(\hat{a} - \hat{a}^\dagger\right) \tag{2.8}$$

Inserting (2.8) in (2.6), the Hamiltonian takes the form:

$$\begin{aligned} H_B^\xi &= \xi\frac{\sqrt{2}\hbar v_F}{l_B}\begin{pmatrix} 0 & \hat{a}^\dagger \\ \hat{a} & 0 \end{pmatrix} \\ &= \xi\hbar\omega_c'\begin{pmatrix} 0 & \hat{a}^\dagger \\ \hat{a} & 0 \end{pmatrix} \end{aligned}$$

In the second step, we have introduced the parameter $\omega_c' = \frac{\sqrt{2}v_F}{l_B}$ which corresponds to the cyclotron frequency in the case of relativistic particles.

At this point, we are ready to solve the Schrödinger equation $H_B^\xi \Psi_n = \varepsilon_n \Psi_n$ with the spinor

$$\Psi_n = \begin{pmatrix} v_n \\ u_n \end{pmatrix}$$

to calculate the energy spectrum of relativistic particles in magnetic field. We obtain the two coupled equations:

$$\xi\hbar\omega_c'\hat{a}v_n = \varepsilon_n u_n \quad \text{and} \quad \xi\hbar\omega_c'\hat{a}^\dagger u_n = \varepsilon_n v_n$$

Therefore, the equation for the second component of the spinor is given by:

$$\hat{a}^\dagger\hat{a}v_n = \left(\frac{\varepsilon_n}{\hbar\omega_c'}\right)^2 v_n$$

Considering the eigenvalue equation of the number operator $\hat{a}^\dagger\hat{a}\,|n\rangle = n\,|n\rangle$, we can directly derive the energy spectrum of the relativistic Landau levels:

$$\boxed{\varepsilon_n = \pm v_F\sqrt{2\hbar enB}} \tag{2.9}$$

Eq. (2.9) has two solutions which corresponds to Landau levels at positive and negative energies. As in the case of zero magnetic field (2.2), the energy dispersion (2.9) does not contain the valley isospin ξ for which reason the Landau levels are two-fold valley degenerate. So far we have neglected the particles' spin which leads to an additional two-fold degeneracy resulting altogether in a four-fold degeneracy.

Let us have a closer look at (2.9) to emphasize the differences to the usual 2DEG of chapter 1. The relativistic energy dispersion (2.9) has a square root dependence on the magnetic field and the Landau level index (see Fig. 2.6) in contrast to the linear dependence of the conventional 2DEG (1.7). Therefore, the spacing between adjacent Landau levels is

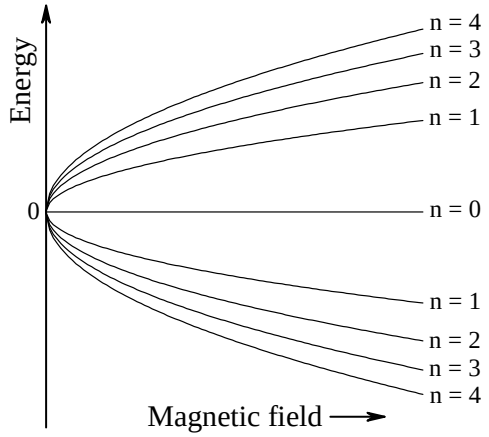

Figure 2.6: Relativistic Landau levels as a function of magnetic field B for various indexes n.

no longer equidistant but varies as:

$$\Delta\varepsilon_n = v_F\sqrt{2\hbar eB}\left(\sqrt{n+1}-\sqrt{n}\right) \tag{2.10}$$

The distance between Landau levels depends on their index n and decreases with increasing index.

Considering (2.10), we see that graphene has a much larger cyclotron gap than conventional 2DEG systems. For instance, the energy gap between the zeroth and the first excited Landau level is in graphene about $420\,\mathrm{K}\cdot\sqrt{\mathrm{B[T]}}$ and in conventional 2DEG systems as GaAs only about $20\,\mathrm{K}\cdot\,\mathrm{B[T]}$. Due to this large cyclotron gap in graphene, the quantum Hall effect has already been measured up to room temperature at 29 T [4].

3.2 Spin and valley degeneracies

In the previous section we derived the Landau levels of graphene in a magnetic field within the one-particle picture, neglecting all kinds of interactions. In the non-interacting picture, each electron has four degrees of freedom due to the two spin projections (SU(2)(spin)) and the two valleys K and K' (SU(2)(valley)) resulting in a four-fold degeneracy of each Landau level with an approximate SU(4) symmetry.

The breaking of the symmetry of spin and valley leads to the experimental observation of plateaus outside of the series $G = \pm\frac{4e^2}{h}\left(n+\frac{1}{2}\right)$. It mainly stems from Coulomb interactions and the Zeeman effect.

The first obvious symmetry breaking that comes to mind is due to the Zeeman effect that could split spin degenerate Landau level. The resulting Zeeman splitting has the usual form

$$\varepsilon_Z = g\mu_B B$$

which includes the Landé factor (g factor) $g \approx 2$ and the Bohr magneton. ε_Z defines the energy gap between spin polarised states. However, magnetotransport measurements in 2DEG systems of silicon surfaces [49] and GaAs/AlGaAs heterostructures [50] as well as in graphene [51] have shown that the gap between spin polarised states is several times larger than expected from the Zeeman splitting. This enhancement of the spin splitting is

attributed to the exchange interaction between electrons [52].

In quantum mechanics, the interchange of the wave functions of two fermions has to be antisymmetric. This exchange gives rise to the exchange interaction which depends on the Pauli principle and is, in the first approximation, of the order of the Coulomb energy

$$\varepsilon_X \propto \varepsilon_C = \frac{e^2}{4\pi\varepsilon_0\varepsilon_r l_B}$$

where the magnetic length $l_B = \sqrt{\frac{\hbar}{eB}}$ is the relevant length scale for interaction within a Landau level. We immediately notice that the Coulomb interaction scales with $\sqrt{B}$ which is different from the linear behaviour of the Zeeman effect. Electrons of opposite spins have no exchange contribution since they are in two different states and the Pauli principle does not prevent them from being at the same place.

On the other hand, the valley symmetry is broken by valley anisotropies induced by lattice distortions which arise from short range electron-electron interaction [53] and electron-phonon interaction [54]. The latter may introduce a so-called Kekulé distortion where both the A and B atoms of the hexagonal lattice have an arbitrary in-plane displacement. Another possible lattice distortion is such that both sublattices A and B vibrate vertically out-of-plane and out of phase. These lattice distortions open a gap which is enhanced by the Coulomb interaction [51, 55] and reads

$$\varepsilon_V \propto \frac{a}{l_B}\varepsilon_C$$

The valley gap increases, therefore, linearly with magnetic fields.

Let us compare these energy scales to get an idea of their influence (see tab. 2.1). The cyclotron gap between the zeroth and the first Landau level is about $\simeq 400 \cdot \sqrt{B[T]}[K]$ which results in a value of 1265 K at 10 T. The Coulomb interaction is approximately $100 \cdot \sqrt{B[T]}[K]$ on SiO_2 leading to 316 K at 10 T. It is, thus, about four times smaller than the cyclotron gap. In comparison to the Zeeman splitting of $1.3 \cdot B[T][K]$ which becomes 13 K at 10 T, and the valley anisotropies of $0.16 \cdot B[T][K]$ which is about 1.6 K at 10 T,

Table 2.1: Relevant energy scales in graphene.

Energy	Equation	Order of magnitude	Value at 10 T
Cyclotron gap $n = 0 \to 1$	$\sqrt{2\hbar eB}$	$\simeq 400 \cdot \sqrt{B[T]}[K]$	$\simeq 1265\,\mathrm{K}$
Coulomb energy	$\frac{e^2}{\varepsilon_r l_B}$	$\simeq \frac{625}{\varepsilon_r} \cdot \sqrt{B[T]}[K]$	$\simeq \frac{1976}{\varepsilon_r}\mathrm{K}$
Coulomb energy (SiO_2)	$\frac{e^2}{\varepsilon_r l_B}$	$\simeq 100 \cdot \sqrt{B[T]}[K]$	$\simeq 316\,\mathrm{K}$
Zeeman energy	$g\mu_B B$	$\simeq 1.3 \cdot B[T][K]$	$\simeq 13\,\mathrm{K}$
Lattice effects (anisotropies)	$\frac{a}{l_B}\varepsilon_C$	$\simeq 0.16 \cdot B[T][K]$	$\simeq 1.6\,\mathrm{K}$

the Coulomb interaction is two orders of magnitude larger than any other terms and is, therefore, the dominant interaction in high magnetic fields.

The lifting of the degeneracies of spin and valley are associated with the spontaneous breaking of the SU(4) symmetry of spin and valley. Two theoretical models have been developed to explain the lifting. The first one is quantum Hall ferromagnetism which focuses on the interactions between electrons of the same Landau level [53, 56–58]. The second branch of theories is called magnetic catalysis and is limited to the case of $\nu = 0$ [59, 60]. We discuss both theories in the following before turning to the particular and rich physics of the zero energy Landau level.

3.2.1 Quantum Hall ferromagnetism

In the simple picture of two electrons, the Coulomb interaction decreases in strength with increasing distance between the two particles. In a system of N-particles, the situation is more complex. Screening between electrons means that the higher the density of electrons, the smaller the distance between electrons and therefore the smaller the Coulomb interaction. One electron no longer feels each individual electron in its vicinity but rather a cloud of electrons with an average Coulomb interaction which is reduced by such screening effects. Therefore, the electrons are highly correlated and, thus, by adding or removing one electron, this "collective" state becomes disturbed.

We have seen in the previous section that the Coulomb interaction increases with increasing magnetic field ($\varepsilon_C \propto \sqrt{B}$). In high magnetic fields, when the Coulomb interaction dominates over disorder, spontaneous symmetry breaking and quantum Hall ferromagnetism becomes possible. Quantum Hall ferromagnetism is interaction-driven and is defined by the spontaneous polarisation of quantum Hall states. The nature of the polarisation depends on the lifting of the degeneracy which can be, for graphene, the spin or the valley degree of freedom[6].

Quantum Hall ferromagnetism leads to plateaus outside of the expected series. In the 2DEG of GaAs/AlGaAs which is two-fold spin degenerate, plateaus of spin degenerate Landau levels are expected at a conductance of multiples of $\frac{2e^2}{h}$. Exchange interaction causes the breaking of the SU(2) spin symmetry and the emergence of additional plateaus at odd-integer quantum Hall states of $\nu = 1, 3, 5\ldots$ [61]. The case of $\nu = 1$ which is fully spin polarised provides an example of perfect quantum Hall ferromagnetism.

In the case of graphene, the theory of quantum Hall ferromagnetism predicts a full lifting of the degeneracies, with plateaus in conductance at integer values of $\frac{e^2}{h}$. Coulomb interaction induces the emerging spin and valley gap, respectively and results in spin and/or valley polarised quantum Hall ferromagnetism [51].

The appearance of quantum Hall ferromagnetism in real samples depends on the level of disorder. A theory of K. Nomura and A.H. MacDonald used the Stoner criterion to predict the critical field at which QH ferromagnetism appears for a given disorder (mobility). The

6 In simple terms, quantum Hall ferromagnetism is a consequence of Coulomb exchange interaction and the Pauli principle, a phenomenon which is based on the Stoner ferromagnetism. The system attempts to reduce the exchange energy by minimising the overlap of the orbital wave functions of the electrons. The reduced overlap is achieved by antisymmetric orbital wave functions and resulting symmetrical spin states. The magnetic ordering of the spins results in fully polarised spin states.

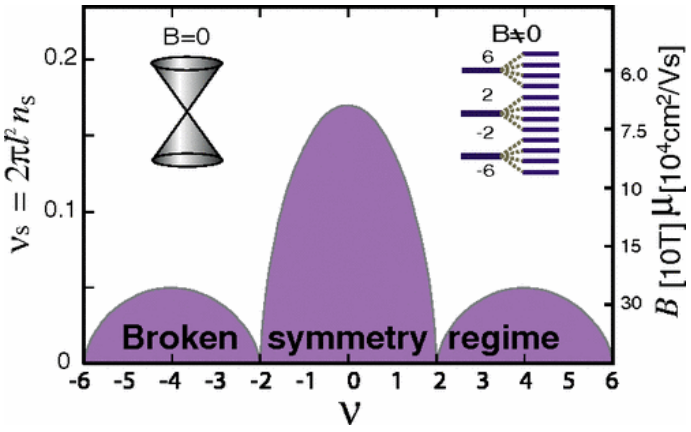

Figure 2.7: The phase diagram of the quantum Hall ferromagnetism links the mobility of a graphene device with the required magnetic field to observe quantum Hall plateaus in the first two Landau levels. The maximal ratio of the density of Coulomb scatterers to the total density of a Landau level in the form of the parameter ν_S is plotted as a function of each filling factor. The required mobility and external magnetic fields which is inversely proportional to ν_S is given on the right axis. Figure taken from [56]

result of this theory is presented in Fig. 2.7 in which the critical magnetic field is plotted as a function of ν and $\mu \cdot B$. According to Fig. 2.7, for graphene devices of a mobility of $5 \times 10^4\,\mathrm{cm^2\,V^{-1}\,s^{-1}}$, the symmetry breaking of $\nu = \pm 1$ is expected at 17 T. The group of P. Kim observed the appearance of the $\nu = \pm 1$ plateau in their graphene devices with the mobility $5 \times 10^4\,\mathrm{cm^2\,V^{-1}\,s^{-1}}$ at 17 T [46] which is in good agreement with the theoretical prediction.

3.2.2 Magnetic catalysis in the zero energy Landau level

In the following, we mention briefly the second branch of theories which are based on magnetic catalysis. An external magnetic field enhances the probability for interactions to break the SU(4) symmetry and to generate a dynamical mass term in quantum field theory for massless fermions, a process which is known as "magnetic catalysis". Various theories for the generation of the mass term of the Dirac fermions in graphene have been studied.

One approach considers the Coulomb interaction between electrons and holes. The special configuration of having both electrons and holes in the $N = 0$ Landau level causes an electron-hole pair to condense into a so-called exciton generating an excitonic gap [59]. This excitonic gap splits the zero energy Landau level leading to a quantum Hall plateau at $\nu = 0$. The degeneracy of higher Landau levels is predicted to be lifted by the Zeeman effect.

The theories of magnetic catalysis predict quantum Hall plateaus at $\nu = 0$, ± 1 and $\nu = \pm 2n$ which is in good agreement with the first observation of the degeneracy lifting in graphene [46, 63]. A quantum Hall plateau at $\nu = 0$ has also been experimentally observed as shown in Fig. 2.8 which is only correctly explained by magnetic catalysis.

Both branches of theories, the quantum Hall ferromagnetism and the magnetic catalysis, imply the breaking of the SU(4) symmetry as the cause for the lifting of the spin and/or valley degeneracy. Quantum Hall ferromagnetism reveals conductance plateaus at integer

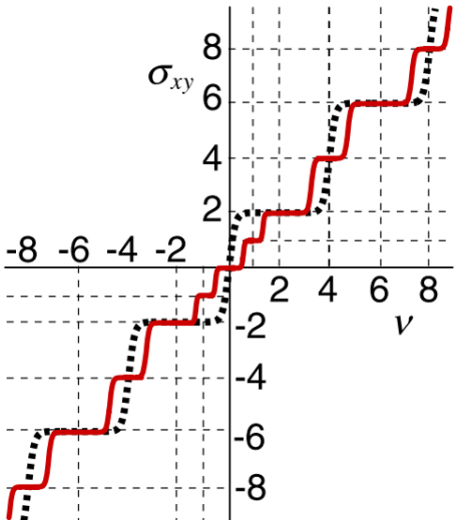

Figure 2.8: QH conductivity in magnetic catalysis theories with the sequence $\nu = 0, \pm 1, \pm 2, \pm 4 \ldots$ (red curve) in comparison to the usual sequence of $\nu = \pm 2, \pm 6, \pm 10 \ldots$ (dotted curve). Fig. taken from [62].

values of $\frac{e^2}{h}$ and magnetic catalysis explains the conductance plateau at $\nu = 0$. E.V. Gorbar et al [64–66] have combined the two branches of theory to the "generalised magnetic catalysis" to understand the full mechanism of the lifting of the spin and valley degeneracies in graphene [67].

With the rise of new generation of high mobility graphene devices, it has been possible to observe systematically the full lifting of the spin and valley degeneracies in all Landau levels. All integer values of the filling factors have been observed (in [5, 47, 48, 51] as well as in our data). The group of P. Kim measured graphene devices on hexagonal boron-nitride (hBN) which has proven to achieve a much higher mobility than when placed on SiO_2 [51]. In Fig. 2.9, we present their results on the longitudinal and transverse resistances plotted as a function of the filling factor (at a perpendicular magnetic field of 12 T for various temperatures). Inspecting this figure, we see that R_{xx} drops to zero at every integer of the filling factor ν while R_{xy} exhibits a quantised plateau at $\frac{h}{\nu e^2}$. The black curve in R_{xx} is taken at the base temperature where the minima always drop completely to zero. We clearly see in this example the four symmetry breaking states for each Landau level.

3.2.3 Special properties of the zero energy Landau level

The zeroth Landau level in graphene defines a special case since it is occupied by both electrons and holes, a configuration which does not exist in conventional 2DEG systems. In experiments, the transverse conductance σ_{xy} features a step-like structure (see Fig. 2.10a). However, neither the transverse resistance ρ_{xy} exhibits a quantised plateau, nor the longitudinal resistance ρ_{xx} possesses a pronounced minimum (Fig. 2.10b). In fact, ρ_{xx} develops strongly insulating behaviour around the charge neutrality point [5, 47, 69–72]. The insulating behaviour which increases with magnetic field (Fig. 2.10e) seems to be an intrinsic property of a perfect graphene flake without defects since the resistance increases with the quality of the samples [54].

The $\nu = 0$ state is determined by the competition between Zeeman splitting and valley anisotropies giving rise to two possible ground states. In both scenarios the bulk is predicted to be gapped. Approaching the edge due to the bending of the Landau level, the situation looks different. The edge excitations can be gapped or not depending on the order of the

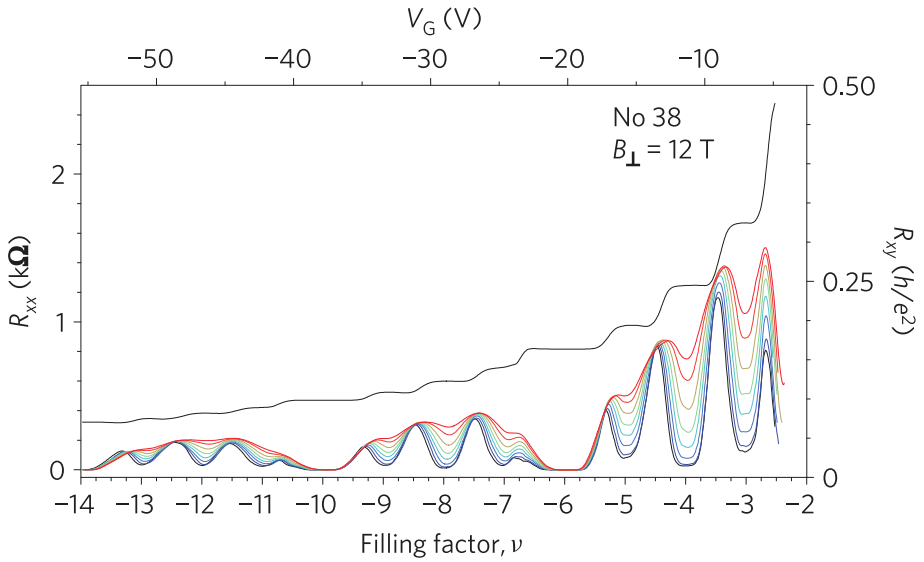

Figure 2.9: Longitudinal and transverse resistances are plotted as a function of the filling factor ν. The lifting of the spin and valley degeneracies lead to plateaus in R_{xy} and minima in R_{xx} at all integer values of ν. With increasing temperature, the minima in R_{xx} become smaller. Fig. taken from [51].

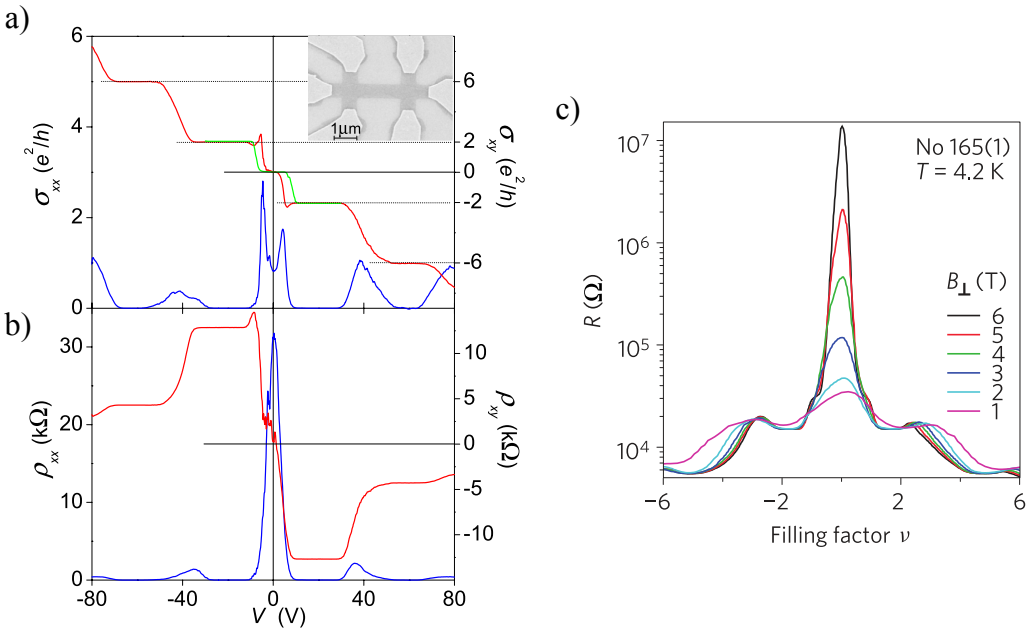

Figure 2.10: a) The transverse conductance σ_{xy} (red curve) features a step-like structure at $\nu = 0$ while the longitudinal conductance σ_{xx} possesses a double-peak structure. b) Neither the transverse resistance ρ_{xy} exhibits a quantised plateau (red curve), nor the longitudinal resistance ρ_{xx} possesses a pronounced minimum (blue curve). c) Resistance R as a function of the filling factor ν around the CNP at various magnetic fields B. The insulating behaviour of R increases with increasing B. Fig. a) and b) taken from [68]. Fig. c) taken from [51].

breaking of the symmetry, if the degeneracy of the spin or of the valley is lifted first.

Quantum Hall insulator - $\Delta_V > \Delta_Z$ When the Fermi level lies within the gap Δ_V at $\nu = 0$, the bulk is insulating. At the edge the electron states of the K valley bend up while the hole states of the K' valley bend down (see Fig. 2.11a). The resulting edge excitation is gapped between the electron and hole states. An additional splitting of the spin induces a gap between the states of differing spins.

The gapped edge excitation explains the insulating behaviour in ρ_{xx} around the charge neutrality point which is observed in transport measurements [5, 47, 69–72]. The plateau-like feature in σ_{xy}, however, cannot be understood within this theory.

Quantum Hall metal - $\Delta_V < \Delta_Z$ Similar to the previous scenario, the bulk is insulating at $\nu = 0$. Approaching the edge, the situation looks different as presented in Fig. 2.11b. The spin-up hole band crosses with the spin-down electron band resulting in two spin-polarised edge channels [68, 73]. These two edge channels have opposite chirality and propagate, therefore, in opposite directions along the same edge (see Fig. 2.12). This configuration leads, therefore, to a spontaneously spin-polarised state [74] similar to that of the quantum spin Hall state observed in HgTe quantum wells [75].

The group of L.S. Levitov predicts that the counter-propagating edge channels lead to a large peak in ρ_{xx} as well as a plateau-like feature in σ_{xy} [68] which has been experimentally observed by themselves and the group of P. Kim [46].

The group of P. Jarillo-Herrero were able to unveil the quantum spin Hall effect in graphene by applying a high in-plane magnetic field [76]. By increasing the in-plane component of the magnetic field, they varied the Zeeman splitting without affecting the valley anisotropies. The gap of the edge excitations becomes continuously smaller until it is closed in the quantum spin Hall state.

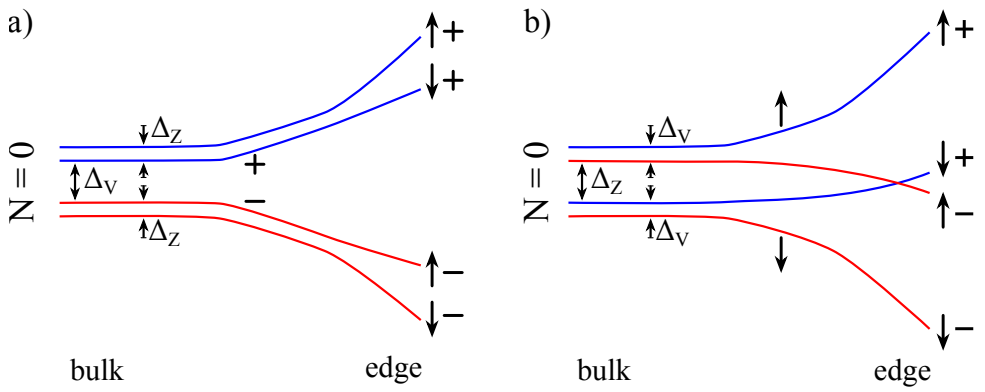

Figure 2.11: Two scenarios for the lifting of the spin and valley degeneracies: a) The valley degeneracy lifts before the spin degeneracy. b) The spin degeneracy lifts before the valley degeneracy. The arrows represent the spin and the plus and minus sign corresponds to the K and K'-valley, respectively.

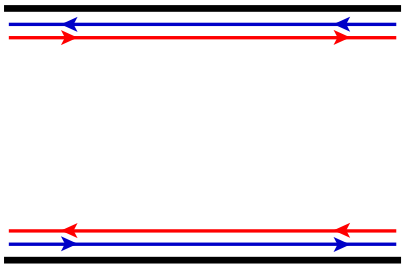

Figure 2.12: The gapless edge excitation is characterised by two counter-propagating edge-channels, of which one contains spin-up polarised electrons while the other is comprised of spin-down polarised holes.

4 Fractional quantum Hall effect in graphene

A couple of years after the discovery of the integer quantum Hall effect in graphene, the increasing quality of graphene devices achieved by leading experimental groups has led to the observation of fractional quantum Hall plateaus for $\nu < 1$ [47, 69] and later on for higher filling factors $\nu > 1$ [5, 6, 77–79].

C.R. Dean et al. were one of the first groups to observe the fractional states of $N + \frac{1}{3}$ and $N + \frac{2}{3}$ for each Landau level N in their device of graphene on hBN. At these fractional states, the pronounced minima in the longitudinal resistance are accompanied by clear plateaus in the transverse resistance (see Fig. 2.13). These features appear, additionally, symmetric in the electron- and hole-doped regime.

In the following, we need to distinguish two kinds of notation for the filling factor. We continue to name the filling factor ν whose zero is set to the half filled $N = 0$ Landau level. This filling factor is the one used in experiments.

In theory, however, a different definition is taken for the filling factor. Theory introduces a new filling factor ν_f which sets the zero-point at $\nu = -2$ to start with an unoccupied $N = 0$ Landau level. The relation between both filling factors is, therefore,

$$\nu_f = \nu - 2 \tag{2.11}$$

In some literature, we also find the relation $\nu_f = 2 - \nu$ [77]. Due to the particle-hole symmetry, this representation is equivalent to (2.11).

One of the first observed fractional plateaus is at $\nu = \frac{1}{3}$ [47, 69]. This state is different from the Laughlin $\frac{1}{3}$ state measured in conventional 2DEG systems as in GaAs [26]. It corresponds to the theoretically predicted state of $\nu_f = 2 + \frac{1}{3} = \frac{7}{3}$. Therefore, two Landau levels are completely filled plus one third of the next sublevel which is a complex SU(4)-spin-valley ferromagnetic state [80].

On the other hand, the theoretical $\nu_f = \frac{1}{3}$ Laughlin state corresponds to the experimental $\nu = \frac{5}{3}$ state[7] which has been observed by the group of Goldhaber-Gordon [6].

In the last section we have already introduced the role of Coulomb interaction on the lifting of the spin and valley degeneracies and the breaking of the SU(4) symmetry which results in fully polarised quantum Hall ferromagnetic states. We extend these considerations to have a look at the fractional quantum Hall effect in graphene within the frameworks of Laughlin's theory and of the theory of composite Fermions.

7 The fractional states $\nu = -\frac{5}{3}$ and $\nu = \frac{5}{3}$ are equivalent due to particle-hole symmetry.

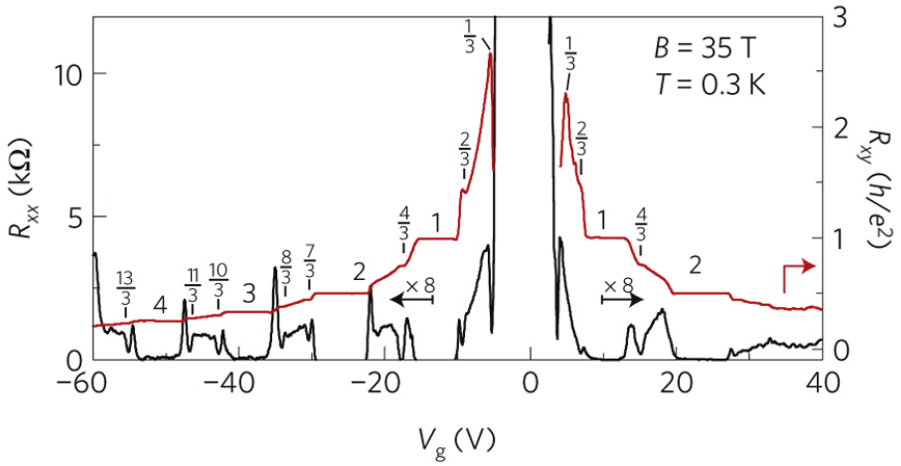

Figure 2.13: Experimental observation of the fractional quantum Hall effect in graphene. Longitudinal resistance R_{xx} and transverse resistance R_{xy} is measured as a function of the backgate voltage at 35 T. Fig. taken from [5].

4.1 Multicomponent fractional quantum Hall effect

Within the framework of ferromagnetic states in the integer quantum Hall effect (sect. 2.3.2.1), we have noted that the orbital wave function is antisymmetric which leads to a symmetric spin and valley degenerate wave function due to the Fermionic nature of the particles. A suitable representation of an antisymmetric orbital wave function is the Laughlin wave function which was introduced in (1.18) of the form

$$\Psi_m = \prod_{j<k} (z_j - z_k)^m \exp\left(-\frac{1}{4}\sum_l |z_l|^2\right)$$

The Laughlin wave function describes fractional quantum Hall states at filling factors $\nu_f = \frac{1}{m}$. In 1983 Halperin generalised the Laughlin wave function to the SU(2) symmetry to account for spin as degree of freedom in the absence of Zeeman splitting. Following Halperin's approach, Laughlin's wave function can be extended to the SU(4) symmetry including the spin and valley degeneracies [81]

$$\Psi^{SU(4)}_{m_1,\ldots m_4} = \phi^L_{m_1,\ldots m_4}\phi^{inter}_{n_{ij}} \tag{2.12}$$

The first term of (2.12) is given by

$$\phi^L_{m_1,\ldots m_4} = \prod_{j=1}^{4}\prod_{k_j<l_j}^{N_j}\left(z^{(j)}_{k_j} - z^{(j)}_{l_j}\right)^{m_j} \exp\left(-\frac{1}{4}\sum_{j=1}^{4}\sum_{k_j=1}^{N_j}|z^{(j)}_{k_j}|^2\right)$$

which is a product of four N_j-particle Laughlin wave functions, one for each of the flavours of spin and valley labelled by m_1, m_2, m_3 and m_4. The correlations between each flavour

is included by

$$\phi_{n_{ij}}^{inter} = \prod_{i<j}^{4} \prod_{k_i}^{N_i} \prod_{k_j}^{N_j} \left(z_{k_i}^{(i)} - z_{k_j}^{(j)} \right)^{n_{ij}}$$

To fulfil the requirement of Fermionic statistics, the exponents m_j must be odd integers. The exponents n_{ij} which define the correlation between the states i and j of different flavours are both even and odd[8]. All of these exponents n_{ij} with $n_{jj} = m_j$ are represented in a 4×4 matrix $M = n_{ij}$ which defines the components of the four filling factors [82]:

$$\begin{pmatrix} \nu_1 \\ \nu_2 \\ \nu_3 \\ \nu_4 \end{pmatrix} = \begin{pmatrix} m_1 & n_{12} & n_{13} & n_{14} \\ n_{21} & m_2 & n_{23} & n_{24} \\ n_{31} & n_{32} & m_3 & n_{34} \\ n_{41} & n_{42} & n_{43} & m_4 \end{pmatrix}^{-1} \begin{pmatrix} 1 \\ 1 \\ 1 \\ 1 \end{pmatrix} = M^{-1} \begin{pmatrix} 1 \\ 1 \\ 1 \\ 1 \end{pmatrix} \tag{2.13}$$

The components 1 to 4 represent a specific spin and valley configuration: $1 = (\uparrow, K)$, $2 = (\uparrow, K')$, $3 = (\downarrow, K)$ and $4 = (\downarrow, K')$. For instance, the component n_{13} defines the correlation within the same valley but opposite spins.

If the matrix M is not invertible, eq. (2.13) does not have a unique solution leaving the filling factors undetermined. Even if some filling factors e.g. ν_1 and ν_2 are not fixed, their sum may still be precisely determined. The total filling factor is obtained by its independent components

$$\nu_f = \sum_{j=1}^{4} \nu_j$$

Let us have a look at some examples based on [82] of possible configurations in order to discuss their resulting fractions. In these examples, we assume that all exponents within a certain spin and valley flavour are the same, $m_j = m$. The exponents describing the correlations between the different components n_{ij} are separated into two groups, those which stay in the same valley ($n_{13} = n_{24} \equiv n_a$) and those operating between differing valleys ($n_{12} = n_{14} = n_{23} = n_{34} \equiv n_e$). We consider examples within the notation $[m; n_e, n_a]$.

$\boldsymbol{[m; n_e = m, n_a = m]}$ When all exponents are identical and set to an odd integer m, the orbital wave function corresponds to that of Laughlin which is completely antisymmetric. The filling factors ν_1 to ν_4 are not individually determined and the total filling factor is fixed to

$$\nu_f = \frac{1}{m} \tag{2.14}$$

$\boldsymbol{[m; n_e = m - 1, n_a = m]}$ The exponents of the intervalley correlation n_e is reduced by one. The filling factors of the same valley are fixed. The 4×4 matrix M is of rank two

8 Since n_{ij} describes the relation between states of different flavour, the Pauli exclusion principle does not apply.

but still not invertible:

$$M = \begin{pmatrix} m & m-1 & m & m-1 \\ m-1 & m & m-1 & m \\ m & m-1 & m & m-1 \\ m-1 & m & m-1 & m \end{pmatrix}$$

Due to the linear dependence of its first and third as well as its second and fourth lines, only the sum $\nu_K = \nu_1 + \nu_3$ and $\nu_{K'} = \nu_2 + \nu_4$, each associated with one valley, can be determined. Therefore, (2.13) can be rewritten as

$$\begin{pmatrix} \nu_K \\ \nu_{K'} \end{pmatrix} = \begin{pmatrix} m & m-1 \\ m-1 & m \end{pmatrix}^{-1} \begin{pmatrix} 1 \\ 1 \end{pmatrix}$$

which has a unique solution. The total filling factor $\nu_f = \nu_K + \nu_{K'}$ is given by

$$\nu_f = \frac{2}{2m-1} \tag{2.15}$$

Theory predicts that the corresponding states are unpolarised in the valley isospin but ferromagnetic spin ordered whose directions may be aligned by the Zeeman effect. An example of this group is the fraction $\nu_f = \frac{2}{5}$ which occurs when $m = 3$.

$[\boldsymbol{m; n_e = m-1, n_a = m-1}]$ Both the exponents of the intervalley and intravalley correlations are reduced by one. The matrix M is invertible which determines completely the filling factors ν_1 to ν_4.

$$\begin{pmatrix} \nu_1 \\ \nu_2 \\ \nu_3 \\ \nu_4 \end{pmatrix} = \begin{pmatrix} m & m-1 & m-1 & m-1 \\ m-1 & m & m-1 & m-1 \\ m-1 & m-1 & m & m-1 \\ m-1 & m-1 & m-1 & m \end{pmatrix}^{-1} \begin{pmatrix} 1 \\ 1 \\ 1 \\ 1 \end{pmatrix}$$

The corresponding total filling factor $\nu_f = \sum_{j=1}^{4} \nu_j$ takes the form

$$\nu_f = \frac{4}{4m-3} \tag{2.16}$$

Theory predicts that the resulting states are SU(4) singlets with no polarisation in either spin or valley. For instance, at $m = 3$, the arising fraction is $\nu_f = \frac{4}{9}$.

4.2 Composite fermions in graphene

In the first chapter (sect. 1.2.2), we introduced the picture of composite-fermions in which a strongly interacting system of electrons in a partially filled Landau level is transferred into a system of weakly interacting composite-fermions. These particles are bound states of an electron and an even number of vortices ($2k$). The $2k$ attached vortices generate a Berry phase which reduces the external magnetic field to an effective magnetic field felt by the composite-fermion particles. Similar to Landau levels, quantised energy levels Λ are subsequently filled by composite fermions with the corresponding cyclotron frequency ω_c^{CP}.

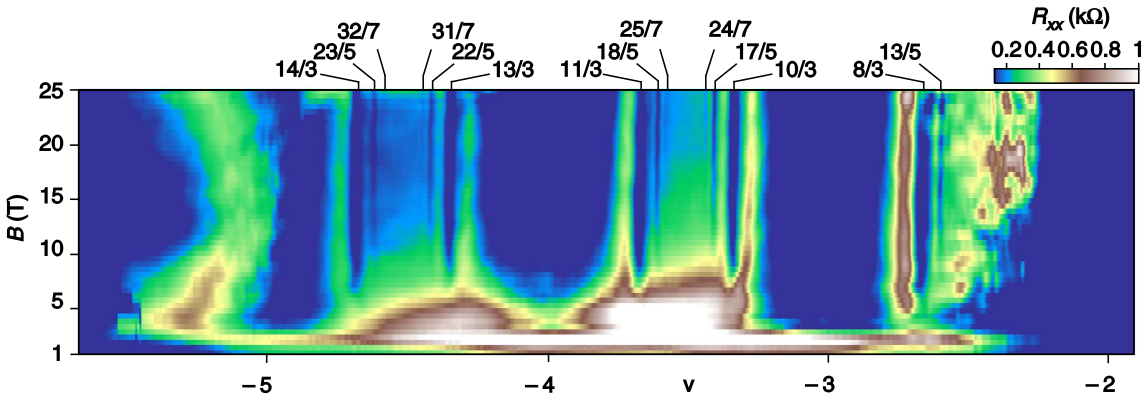

Figure 2.14: Measurement of composite fermions in graphene. The longitudinal resistance is plotted as a function of the filling factor and the magnetic field. The dark blue regions of zero resistance correspond to integer and fractional QH states. Fig. taken from [6].

The $n\Lambda$ filled energy level corresponds to a filling factor of

$$\nu_f = \frac{p}{2kp \pm 1} \tag{2.17}$$

The group of Goldhaber-Gordon were able to measure an elaborated sequence of composite fermions (2.17) in high mobility graphene on hBN ($\mu > 4 \times 10^5\,\mathrm{cm^2\,V^{-1}\,s}$) [6]. They observe the broken symmetry states of $\nu = 1$ and $\nu = 3$ starting at a magnetic field of 1.5 T and fractional states from $B > 5\,\mathrm{T}$. An example of their results is presented in Fig. 2.14 in which the evolution of longitudinal resistance is plotted as a function of filling factor and magnetic field. The blue regions of zero resistance reveal the appearance of each integer and fractional state.

In order to compare the observed fractional states with the sequence of composite fermions (2.17), the table 2.2 lists all theoretically predicted states and the observed states (coloured in blue). The group of Goldhaber-Gordon observe almost all fractional states of the sequence of composite fermions (2.17) of $k = 1$ and $p \leq 4$. The states are built in hierarchical order. If, for instance, the state $\frac{10}{7}$ ($p = 3$ and $k = 1$) was not observed, then the subsequent state $\frac{13}{9}$ ($p = 4$ and $k = 1$) is not observed either.

In the previous section, we have introduced the theories by Laughlin and Halperin of fractional quantum Hall states. Let us compare briefly the fractional states predicted by their theories with the observed fractions. Since the parameters $(m; n_{ij})$ offer a large number of combinations, we focus on the three examples (2.14), (2.15) and (2.16). Table 2.3 lists the predicted fractional states for each of the three examples together with the ones experimentally observed (coloured in blue)[9]. We observe that for $m = 3$, the theoretical predicted states correspond to the observed fractional states. The theoretical states of $m = 5$ have not yet been observed.

9 The parameter m has to be an odd integer due to Fermionic statistics.

Table 2.2: Fractional quantum Hall states with ν filled states following the composite fermion series (2.17) measured in the group of Goldhaber-Gordon [6]. Their observed fractional states are coloured in blue.

$\nu = \frac{p}{2kp+1} - 2$	$p=1$		$p=2$		$p=3$		$p=4$	
	$k=1$	$k=2$	$k=1$	$k=2$	$k=1$	$k=2$	$k=1$	$k=2$
$\nu = 0$	$\frac{1}{3}$	$\frac{1}{5}$	$\frac{2}{5}$	$\frac{2}{9}$	$\frac{3}{7}$	$\frac{3}{13}$	$\frac{4}{9}$	$\frac{4}{17}$
$\nu = 1$	$\frac{4}{3}$	$\frac{6}{5}$	$\frac{7}{5}$	$\frac{11}{9}$	$\frac{10}{7}$	$\frac{16}{13}$	$\frac{13}{9}$	$\frac{21}{17}$
$\nu = 2$	$\frac{7}{3}$	$\frac{11}{5}$	$\frac{12}{5}$	$\frac{20}{9}$	$\frac{17}{7}$	$\frac{29}{13}$	$\frac{22}{9}$	$\frac{38}{17}$
$\nu = 3$	$\frac{10}{3}$	$\frac{16}{5}$	$\frac{17}{5}$	$\frac{29}{9}$	$\frac{24}{7}$	$\frac{42}{13}$	$\frac{31}{9}$	$\frac{55}{17}$
$\nu = \frac{p}{2kp-1} - 2$	$p=1$		$p=2$		$p=3$		$p=4$	
	$k=1$	$k=2$	$k=1$	$k=2$	$k=1$	$k=2$	$k=1$	$k=2$
$\nu = 0$	1	$\frac{1}{3}$	$\frac{2}{3}$	$\frac{2}{7}$	$\frac{3}{5}$	$\frac{3}{11}$	$\frac{4}{7}$	$\frac{4}{15}$
$\nu = 1$	2	$\frac{4}{3}$	$\frac{5}{3}$	$\frac{9}{7}$	$\frac{8}{5}$	$\frac{14}{11}$	$\frac{11}{7}$	$\frac{19}{15}$
$\nu = 2$	3	$\frac{7}{3}$	$\frac{8}{3}$	$\frac{16}{7}$	$\frac{13}{5}$	$\frac{25}{11}$	$\frac{18}{7}$	$\frac{34}{15}$
$\nu = 3$	4	$\frac{10}{3}$	$\frac{11}{3}$	$\frac{23}{7}$	$\frac{18}{5}$	$\frac{36}{11}$	$\frac{25}{7}$	$\frac{49}{15}$

Table 2.3: The fractional quantum Hall states calculated from the theories by Laughlin and Halperin are compared with the observed fractions in the group of Goldhaber-Gordon [6] for each Landau level N.

$\nu = \frac{1}{m} - 2$	$\nu = 0$	$\nu = 1$	$\nu = 2$	$\nu = 3$
$m = 3$	$\frac{1}{3}$	$\frac{4}{3}$	$\frac{7}{3}$	$\frac{10}{3}$
$m = 5$	$\frac{1}{5}$	$\frac{6}{5}$	$\frac{11}{5}$	$\frac{16}{5}$
$\nu = \frac{2}{2m-1} - 2$	$\nu = 0$	$\nu = 1$	$\nu = 2$	$\nu = 3$
$m = 3$	$\frac{2}{5}$	$\frac{7}{5}$	$\frac{12}{5}$	$\frac{17}{5}$
$m = 5$	$\frac{2}{9}$	$\frac{11}{9}$	$\frac{20}{9}$	$\frac{29}{9}$
$\nu = \frac{4}{4m-3} - 2$	$\nu = 0$	$\nu = 1$	$\nu = 2$	$\nu = 3$
$m = 3$	$\frac{4}{9}$	$\frac{13}{9}$	$\frac{22}{9}$	$\frac{31}{9}$
$m = 5$	$\frac{4}{17}$	$\frac{21}{17}$	$\frac{38}{17}$	$\frac{55}{17}$

The results of the group of Goldhaber-Gordon demonstrate the impressive increase in the quality of graphene devices which pave the way to study the rich physics of the fractional quantum Hall effect in this new system.

Summary

Within this chapter, we introduced the first essential ingredient of this work which is graphene. We discussed its particular gapless bandstructure with its linear energy dispersion which leads to its special electronic properties. In the main part of this chapter we focussed on the relativistic quantum Hall effect in graphene which occurs at transverse conductance values of $G_{xy} = \pm 4 \left(n + \frac{1}{2}\right) \frac{e^2}{h}$ due to the four-fold degeneracy of spin and valley. With the rise of a new generation of high mobility graphene devices, plateaus at every integer filling factor have been observed which are a result of the breaking of the symmetries of spin and valley. This symmetry breaking is caused by Coulomb interaction which becomes the dominant interaction in high magnetic fields.

The $N = 0$ Landau level has special characteristics in graphene since it is occupied by both electrons and holes. The lifting of the degeneracies leads to two possible scenarios if either the spin or the valley degeneracy lifts first. When the valley degeneracy lifts first, the edge excitation is gapped leading to insulating behaviour at the charge neutrality point. On the other hand, when the spin degeneracy lifts first, the gapless edge excitation leads to a quantum spin Hall state.

In the last section, we turn to the fractional quantum Hall regime and discussed the adaptation of the theories of Laughlin and Halperin as well as of composite fermions to graphene.

With this framework we can now go on to discuss the quantum point contact in graphene in the quantum Hall regime.

CHAPTER 3

QUANTUM POINT CONTACTS

A quantum point contact - a narrow and short constriction in a 2DEG - presents an ideal system to study many fundamental phenomena of quantum mesoscopic physics. In the quantum Hall regime, the QPC can locally manipulate edge channels by controlling the tunnelling probability between counter-propagating edge channels which introduces backscattering. The QPC enables the selection of specific channels which pass the constriction while others are backscattered. For instance, it can be tuned to be partially open to transmission, making it the electronic analogue of an optical beam-splitter. The QPC offers, therefore, an elementary ingredient to realise electron quantum optics.

In the course of this PhD thesis, we have studied the QPC in high mobility graphene. In the previous chapter, we have introduced graphene and discussed its behaviour in the quantum Hall regime. In this chapter, we turn to the second crucial ingredient, the quantum point contact, and present its theoretical framework in the quantum Hall regime.

1 Conductance quantisation

The quantum point contact (QPC) is a narrow constriction of a quasi one-dimensional channel which is connected to large 2-dimensional reservoirs at each end (see Fig. 3.1). A QPC is usually realised by depositing electrostatic split gates above a 2-dimensional electron gas (2DEG). In 1988, Wharam et al. [7] and van Wees et al. [14] studied the first QPC in the 2DEG of GaAs-AlGaAs at zero magnetic field. The surprising result was that conductance shows step-like quantisation of $\frac{2e^2}{h}$ in dependence of the split gate voltage (see Fig. 3.2a). These step-like features become visible if the transport through the QPC

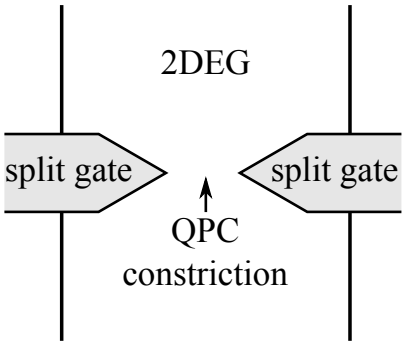

Figure 3.1: Schema of a QPC. The split gates are decoupled from the 2DEG affecting the 2DEG due to electric field effect.

is in the ballistic regime which requires the mean free path of the electrons to be much longer than the length of the QPC.

At zero voltage on the split gates, the 2DEG is spread homogeneously between the Ohmic contacts. When a negative gate voltage is applied, the 2DEG is depleted beneath the split gates. Charge transport is then only possible within the constriction of the QPC. The confinement of the QPC, which can be treated analogously to a particle in a 1D well, causes the 2D density of states to split into one-dimensional modes (or subbands) of quantised energy.

Decreasing further the negative gate voltage, the QPC closes continuously, limiting the number of transverse modes which are transmitted through the QPC. The conductance is

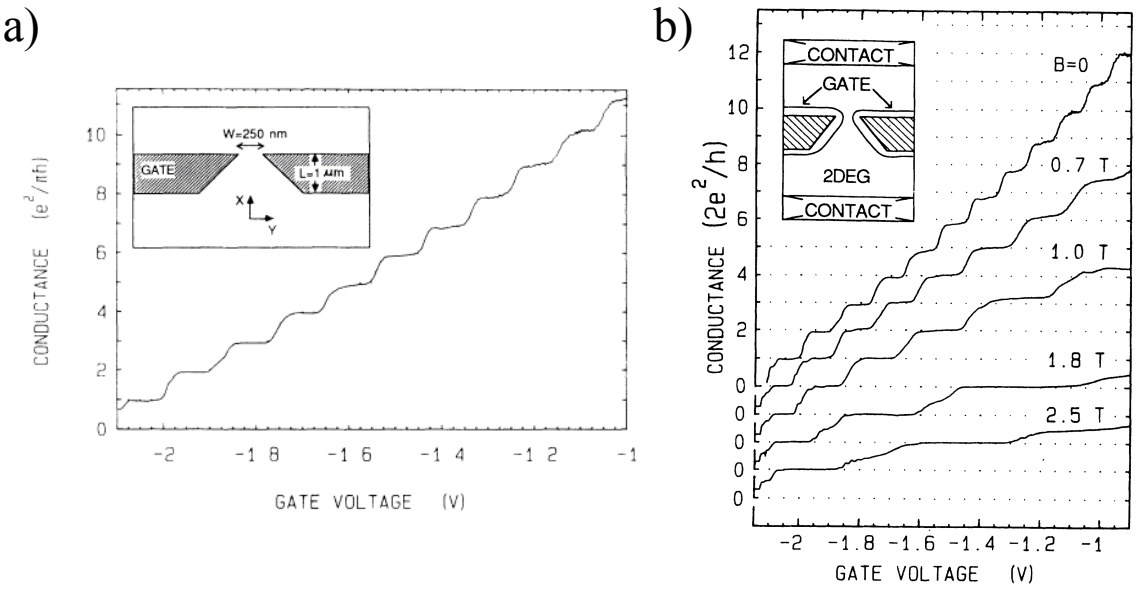

Figure 3.2: The conductance plotted as a function of the applied voltage on the split gate a) At zero magnetic field the conductance exhibits a step-like features with a quantisation at multiples of $\frac{2e^2}{h}$. Inset: Layout of the device with the QPC. Fig. taken from [14]. b) When a perpendicular magnetic field is applied, the conductance plateaus become flatter and broader in the transition to the quantum Hall regime. The lifting of the spin degeneracy in the quantum Hall regime results in additional plateaus at all integers of $\frac{e^2}{h}$. Fig. taken from [83].

directly proportional to the number of transmitted transverse modes M in the form

$$G = \frac{2e^2}{h} M$$

Each time the conductance increases by a step of $\frac{2e^2}{h}$, an additional transverse mode is transmitted through the QPC. This result is a remarkable manifestation of the Landauer formula of perfect transmission which we introduced in 1.3.1.

2 Transition to the quantum Hall regime

At zero magnetic field, the conductance plateaus at multiples of $\frac{2e^2}{h}$ are present due to the lateral confinement of the QPC. By applying a perpendicular magnetic field, the conductance plateaus are observed to flatten and become wider (see Fig. 3.2b). When entering the quantum Hall regime, the observed conductance plateaus are no longer a measurement of the transmitted transverse modes but are due to the formation of Landau levels. The main characteristic of this regime is the propagation of electrons within edge channels which dictates the current transport at the conductance plateaus. The two-fold spin degenerated Landau levels split in magnetic fields, giving rise to additional plateaus at multiples of $\frac{e^2}{h}$ (at about 2 T in Fig. 3.2b).

By changing the gate voltage, the number of transmitted edge channels can be tuned. For instance, let us consider the case of two spin-degenerate edge channels which pass through the QPC. In this case, the conductance exhibits a plateau of $\frac{2e^2}{h}$ (Fig. 3.3a)[1]. When the gate voltage is decreased, the QPC becomes narrower causing each edge channel to get nearer to its counter-propagating partner from the other sample edge. At some point, electrons start to scatter between the counter-propagating inner edge channels which introduces backscattering (Fig. 3.3b). Hence, the conductance is situated between two plateaus. By further increasing the gate voltage, only one edge channel is transmitted

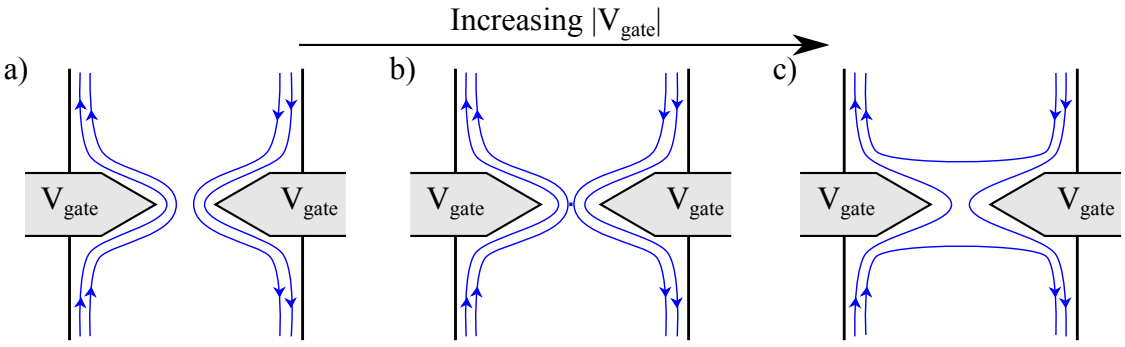

Figure 3.3: The QPC limits the number of transmitted edge channels in the quantum Hall regime. a) Two edge channels pass through the QPC. b) When the gate voltage is increased, the edge channels from one side are brought in closer proximity to their counter-propagating partners. At some point, electrons are scattered between the counter-propagating edge channels leading to backscattering. c) One edge channel passes through the QPC while the other one is fully backscattered.

1 We assume that the spin degeneracy is lifted

through the QPC while the other one is fully backscattered (Fig. 3.3c). The conductance reaches the plateau of $\frac{e^2}{h}$.

2.1 Landauer-Büttiker formalism of a QPC

So far, we have seen that no backscattering takes place in the quantum Hall regime. In this regard, we have derived the longitudinal and the transverse resistance in the framework of the Landauer-Büttiker-formalism (see 1.3.2). At this point, let us apply this formalism to a Hall bar equipped with a QPC which limits the number of transmitted edge channels (see Fig. 3.4). We assume that out of M edge channels, N channels are transmitted through the constriction. Therefore, $M - N$ channels are backscattered.

We adapt (1.14) to calculate the conductance matrix in the configuration of a Hall bar with a QPC:

$$\begin{pmatrix} I_1 \\ I_2 \\ I_3 \\ I_4 \\ I_5 \\ I_6 \end{pmatrix} = \frac{e^2}{h} \begin{pmatrix} M & 0 & 0 & 0 & 0 & -M \\ -M & M & 0 & 0 & 0 & 0 \\ 0 & -N & M & 0 & -(M-N) & 0 \\ 0 & 0 & -M & M & 0 & 0 \\ 0 & 0 & 0 & -M & M & 0 \\ 0 & -(M-N) & 0 & 0 & -N & M \end{pmatrix} \begin{pmatrix} V_1 \\ V_2 \\ V_3 \\ V_4 \\ V_5 \\ V_6 \end{pmatrix} \tag{3.1}$$

Similar to the calculation of the resistances in a Hall bar in 1.3.2, we assume that the current flows from contact 1 to contact 4. Therefore, we set $I_1 = -I_4 = I$ and $V_4 = 0$. The contacts 2, 3 and 5, 6 are considered as voltage probes which implies $I_2 = I_3 = I_5 = I_6 = 0$. We can directly deduce that $V_1 = V_2$ and $V_4 = V_5$. The two remaining voltages V_3 and V_6

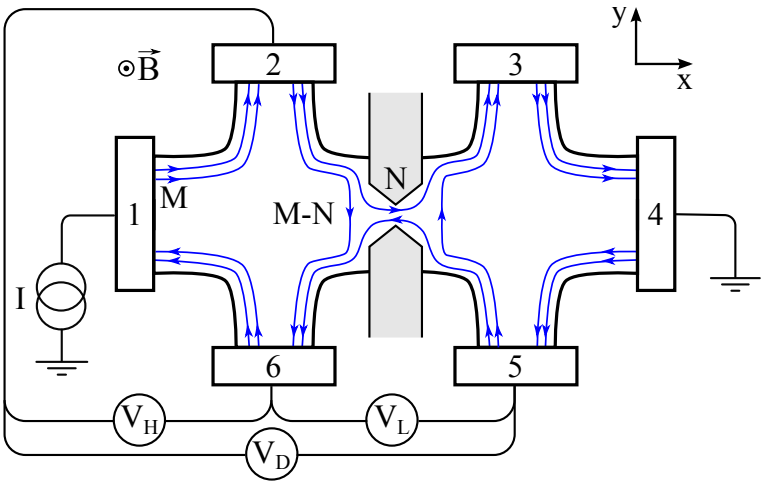

Figure 3.4: Schematic of a Hall bar equipped with a QPC to calculate V_H, V_L and V_D within Landau Büttiker formalism. Out of M edge channels, N edge channels are transmitted through the QPC and $M - N$ edge channels are backscattered.

are calculated as $V_3 = \frac{N}{M} V_1$ and $V_6 = \frac{M-N}{M} V_1$. Hence, (3.1) takes the form:

$$\begin{pmatrix} I \\ 0 \\ 0 \\ -I \\ 0 \\ 0 \end{pmatrix} = \frac{e^2}{h} \begin{pmatrix} M & 0 & 0 & 0 & 0 & -M \\ -M & M & 0 & 0 & 0 & 0 \\ 0 & -N & M & 0 & -(M-N) & 0 \\ 0 & 0 & -M & M & 0 & 0 \\ 0 & 0 & 0 & -M & M & 0 \\ 0 & -(M-N) & 0 & 0 & -N & M \end{pmatrix} \begin{pmatrix} V_1 \\ V_1 \\ \frac{N}{M} V_1 \\ 0 \\ 0 \\ \frac{M-N}{M} V_1 \end{pmatrix}$$

Solving this set of equations leads to the current

$$I = -\frac{e^2}{h} N V_1$$

The longitudinal resistance $R_L = \frac{V_2 - V_3}{I}$ can, therefore, be deduced:

$$\boxed{R_L = \frac{h}{e^2} \frac{M-N}{N \cdot M}} \tag{3.2}$$

In the same manner, the transverse resistance $R_H = \frac{V_2 - V_6}{I}$ is calculated

$$\boxed{R_H = \frac{h}{2e^2} \frac{1}{M}} \tag{3.3}$$

In contrast to the longitudinal resistance (3.2), the transverse resistance (3.3) only depends on the total number of edge channels independent of the actual number of transmitted channels.

In the course of this work, we will make use of the diagonal resistance $R_D = \frac{V_2 - V_5}{I}$ which is given by

$$\boxed{R_D = \frac{h}{2e^2} \frac{1}{N}} \tag{3.4}$$

The diagonal resistance is especially relevant since it provides a direct measure of the number of transmitted edge channels N.

2.2 Filling factors within the QPC

The relations of R_L (3.2), R_H (3.3) and R_D (3.4) can be directly translated into corresponding filling factors. A QPC device is divided into two regions of differing charge carrier densities which result in two different filling factors. The filling factor in the bulk, ν_1, corresponds to the total number of edge channels M. The filling factor within the QPC ν_2 is equal to the number of transmitted channels N. The region below the split gates is assumed to be completely depleted of electrons. Entering the definitions $\nu_1 = M$ and

$\nu_2 = N$ into the equations (3.2) to (3.4) of the resistances, we obtain

$$\begin{aligned} R_H &= \frac{h}{e^2}\frac{1}{|\nu_1|} \\ R_L &= \frac{h}{e^2}\frac{|\nu_1| - |\nu_2|}{|\nu_1| \cdot |\nu_2|} \\ R_D &= \frac{h}{e^2}\frac{1}{|\nu_2|} \end{aligned} \tag{3.5}$$

3 Towards a quantum point contact in graphene

With the rise of the new generation of graphene devices with the graphene layer either suspended or on boron nitride, carrier mobility has continuously improved recently above $10^5\,\mathrm{cm}^2\,\mathrm{V}^{-1}\,\mathrm{s}^{-1}$ paving the way to ballistic transport [84, 85].

We have seen that in conventional 2DEG systems equipped with a QPC, applying a negative voltage to the split gates of the QPC depletes the region underneath the split gates. Full depletion is possible due to the band gap of the semiconductor. The situation is completely different in graphene since its band structure is gapless. A negative gate voltage induces a decrease in the electron density and the doping shifts directly from electrons to holes. By applying a negative voltage on the split gates, the graphene underneath becomes, therefore, hole-doped.

Even though the graphene can be doped of opposite charge underneath the split gates, at zero magnetic field, a QPC as in conventional 2DEG systems is still not possible in graphene. The reason lies within the phenomenon of Klein tunnelling. An electron which encounters a pn-interface with a normal incident angle, is fully transmitted through the hole-doped region. Therefore, the electrons cannot be deflected to pass through the constriction of the QPC and, hence, the conductance is not quantised.

In the quantum Hall regime, electron transport is carried by edge channels which follow the confining potential of the edge of the device. The split gates allows to locally change the charge carrier density to obtain, for instance, a hole-doped region below the split gates while the bulk remains electron-doped. As shown in Fig. 3.5a in this case, the hole-doped edge channels circulate only below the split gates and remain localised. The electron-doped edge channels of the bulk follow the equipotential lines going around these hole-doped regions. In this configuration, the bulk edge channels are forced to pass through the QPC.

In the following, we describe the different configurations of edge channels in the bulk and underneath the split gates depending on the particular polarity of each region. We denote the filling factor in the bulk by ν_b and the filling factor underneath the split gates by ν_g which in both cases define the number of propagating edge channels in those regions.

3.1 Configurations of a QPC in graphene

Bipolar configuration Two different configurations are possible when the graphene is oppositely doped underneath the split gates than in the bulk. We have already mentioned the first one in which hole edge channels are localised underneath the split gates and the bulk edge channels are, hence, forced to pass through the QPC as presented in Fig. 3.5a.

In the second configuration, the hole edge channels underneath the split gates extend

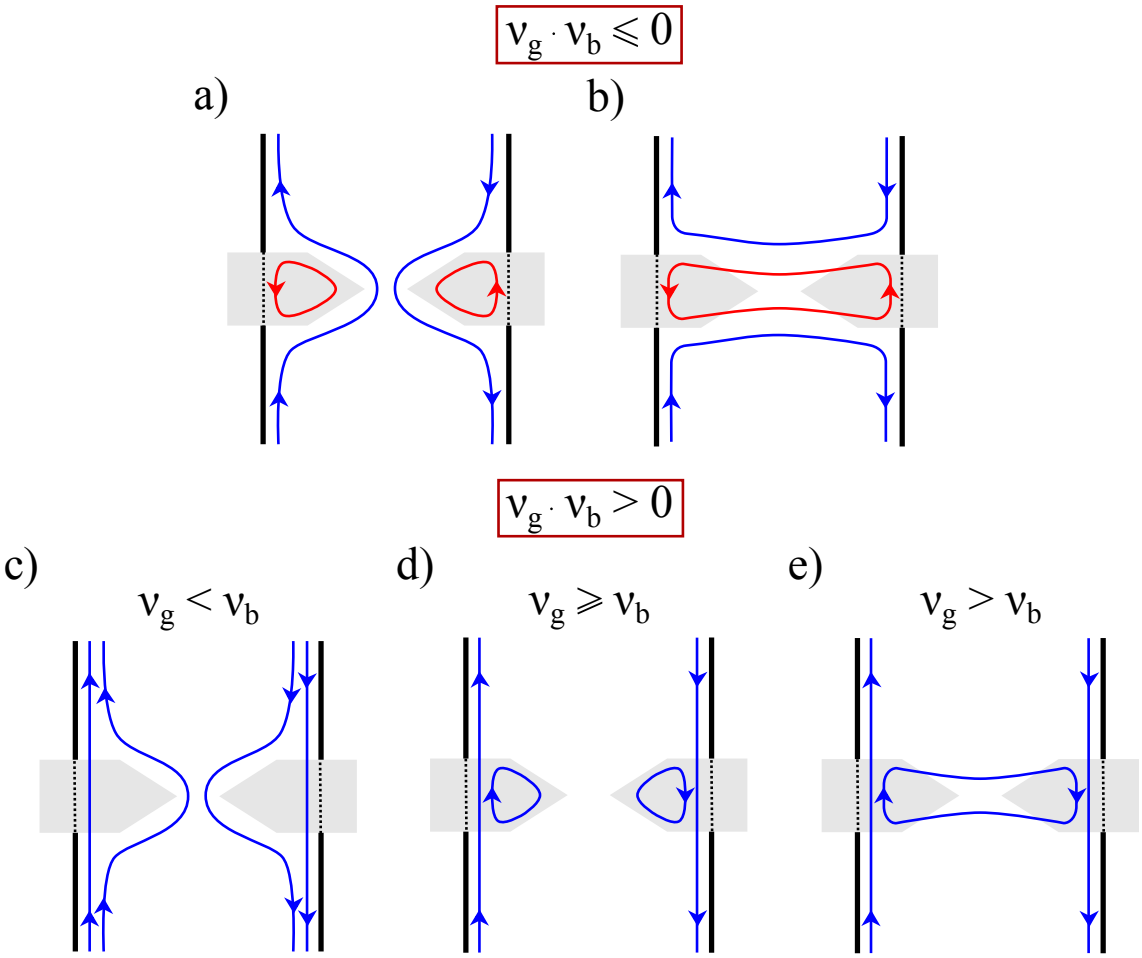

Figure 3.5: Schematic drawing of five configurations of a QPC in graphene. a) $\nu_b \cdot \nu_g < 0$: The charge carriers in edge channels of the bulk have an opposite polarity than the ones underneath the split gates. The bulk edge channels are forced to pass through the QPC. b) $\nu_b \cdot \nu_g < 0$: The hole edge channels from underneath the split gates extend across the QPC circulating between the two edge of the sample. The bulk edge channels are backscattered. c) $\nu_g < \nu_b$: The common edge channels propagate underneath the split gates while the additional bulk edge channel is forced to pass through the QPC. d) $\nu_g \geq \nu_b$: The common edge channels pass beneath the split gates while the additional gate edge channels circulate underneath the split gates. e) $\nu_g > \nu_b$: The edge channels underneath the split gates extend across the QPC and the bulk edge channels pass underneath the split gates.

across the QPC and circulate in between the edges of the sample as shown in Fig. 3.5b. The bulk edge channels can no longer pass across the QPC and are, thus, backscattered. No current is transferred and, hence, the QPC is fully pinched-off.

Unipolar configuration In the unipolar regime, when the polarities in the bulk and underneath the split gates are the same, three configurations are possible. In the simplest case when the filling factors are equal, the edge channels are not deflected and pass directly below the split gates. An increase of the filling factor in the bulk ν_b ($\nu_g < \nu_b$), implies that more edge channels propagate in the bulk than underneath the split gates. The additional bulk edge channels are forced to pass directly through the QPC as shown in Fig. 3.5c.

If instead the filling factor underneath the split gates ν_g ($\nu_g \geq \nu_b$) is increased, the

additional edge channels are localised underneath the split gates without influencing the bulk edge channels which pass below the split gates as presented in Fig. 3.5d.

The states underneath the split gates may not remain localised but extend across the QPC circulating between the two edges of the sample as shown in Fig. 3.5e.

3.2 Short-circuit and backscattering via equilibration

The effect of a QPC in graphene is especially realised in the configurations of Fig. 3.5a and 3.5c in which bulk edge channels are forced to pass through the QPC. In these configurations, by changing the voltage on the split gates, the number of transmitted bulk edge channels can be controlled.

However, in our consideration, we have neglected one important aspect which changes entirely the situation: We need to include equilibration between the edge channels. When the edge channels are equilibrated, current flowing through the edge channels is equally distributed among them. If the current is not equally distributed among the edge channels, inelastic scattering processes cause the current to redistribute to have an equal fraction of current each [86]. Equilibration also takes place between the bulk edge channels and those originating from the split gates independent of their respective polarity.

In three out of the five configurations in Fig. 3.5, equilibration changes the transport properties. When hole edge channels are localised underneath the split gates, the bulk edge channels are forced to pass through the QPC as shown in Fig. 3.5a. The voltage applied on the split gates controls the number of transmitted bulk edge channels. As presented in Fig. 3.6a, the bulk edge channels which are backscattered may still contribute to current transport by equilibrating with the hole states underneath the split gates. Therefore, current is transferred from the backscattered bulk edge channel across the QPC.

The configuration of the fully pinched-off QPC of Fig. 3.5b may not be completely closed. As presented in Fig. 3.6b, equilibration between the backscattered bulk edge channel and the hole states of the split gates leads to current transfer across the QPC.

In the unipolar regime of Fig. 3.5e, the edge channels from the split gates extends across

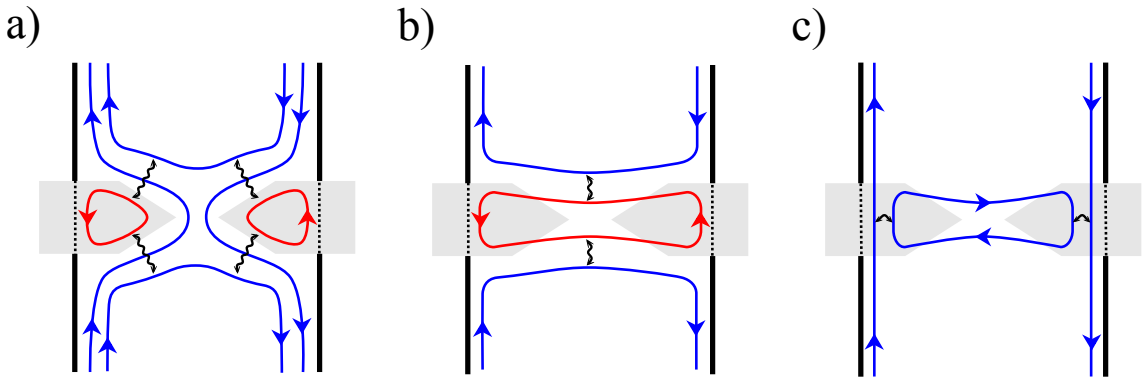

Figure 3.6: Schematic drawing of QPC configurations in graphene including equilibration between edge channels (black wavy arrows). a) $\nu_{bulk} \cdot \nu_{gate} < 0$: When a bulk edge channel is backscattered, it may equilibrate with the localised hole states underneath the split gates. b) $\nu_{bulk} \cdot \nu_{gate} < 0$: The hole edge channels propagating across the QPC equilibrate with the backscattered bulk edge channel. c) $\nu_{gate} > \nu_{bulk}$: The edge channel from underneath the split gates extends across the QPC connecting the two edges of the sample. Equilibration between the bulk and split gates edge channels introduces backscattering.

the QPC circulating in between the two edge of the sample. Equilibration between them and the bulk edge channel passing at the edge of the sample underneath the split gates transports electrons to the opposite side of the sample introducing backscattering as show in Fig. 3.6c.

Summary

In the course of this chapter, we have introduced the quantum point contact as an electronic device capable of controlling the transmission of quantum Hall edge channels through a constriction. We have derived the expressions for the different resistances in a six-terminal device equipped with a QPC. The diagonal resistance is particularly important since it directly probes the number of transmitted edge channels.

We have pointed out that a QPC in graphene at zero magnetic field does not exhibit conductance quantisation due to Klein tunnelling allowing electrons to pass directly through a hole doped region. In the quantum Hall regime, however, we have seen that it is possible to realise configurations of edge channels in the bulk and underneath the split gates to control the number of transmitted edge channels through the QPC.

Nevertheless, the situation is more complex due to the phenomenon of equilibration between edge channels. Equilibration which is due to inelastic scattering between the charge carriers introduces both short-circuits and backscattering. In order to fully understand the transport properties of a QPC in graphene, we will have a closer look at the consequences of equilibration between edge channels especially at the interface between electrons and holes in the following chapter.

CHAPTER 4

EQUILIBRATION IN A GRAPHENE PN-JUNCTION IN THE QUANTUM HALL REGIME

In the previous chapter, we have discussed that the transport properties of a QPC in graphene in the quantum Hall regime are determined by the equilibration between edge channels. In this chapter, we have a closer look at equilibration at a pn-interface and discuss its consequences on transport properties.

We begin by investigating the propagation of edge channels along the pn-interface defined by the bending of the Landau levels. Afterwards, we turn to the pnp-junction and we apply the Landauer-Büttiker formalism on the three regimes of equilibration, each of which is characterised by a different edge channel configuration. Afterwards, we compare theoretical predictions with experimental observations in a pnp-junction with degenerated edge channels and when the spin and valley degeneracies are lifted. We conclude this chapter by discussing in more detail the QPC in graphene including the equilibration between edge channels.

1 Edge channel equilibration at the pn-interface

When the current is not equally spread among edge channels, inelastic scattering leads to a redistribution of current to have an equal fraction in each of the edge channels. This process of equilibration defines transport properties across a pn-interface. In the following, we have a closer look at the evolution of Landau levels across a pn-interface to understand the propagation of edge channels in its vicinity.

1.1 Evolution of the Landau levels across the pn-interface

The charge carrier density in graphene can be locally adjusted by adding a local electrostatic gate separated from the graphene by a thin insulating layer. The region of the flake underneath this top-gate is doped differently than the bulk as presented in the example in Fig. 4.1. When, for instance, a positive voltage is applied on the backgate while the top-gate is at a negative potential, holes are accumulated below the top-gate while the bulk outside of the top-gate region is electron-doped, thus forming a pn-interface.

The different doping in the two adjacent regions cause the Fermi level to be in the conduction band on one side and in the valence band in the other, as shown in Fig. 4.2a. The Landau levels in each region are filled differently inducing a bending of the Landau levels at the pn-interface (see Fig. 4.2b).

The Fermi level of the electron-doped left side is situated between the $N = 2$ and $N = 6$ Landau level. The filling factor on the left side is, therefore, $\nu_1 = 2$ and, hence, one degenerated edge channel circulates in this region as presented in Fig. 4.2c. On the right side of Fig. 4.2b, the Fermi level lies below the $N = -6$ Landau level, leading to a filling factor of $\nu_2 = -6$. Therefore, two degenerated hole edge channels circulate in the right region (see Fig. 4.2c).

At the interface of the electron- and hole-doped regions, the Fermi level crosses the electron-like $N = 2$ as well as the hole-like $N = -2$ and $N = -6$ Landau levels giving rise to the propagating edge channels along the interface. The group velocity within the edge channel is directly proportional to the slope of the confining potential which leads to the bending of the Landau levels of the form[1]

$$v_g = \frac{1}{|e|B}\frac{\partial V_y}{\partial y}$$

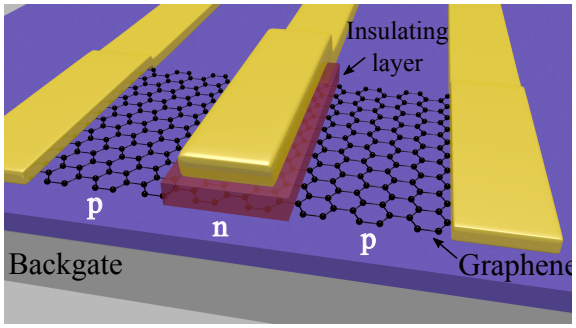

Figure 4.1: Schematic drawing of a pnp-junction in graphene. The top-gate above the centre of the graphene flake is decoupled from it by an insulating layer.

1 We introduced the group velocity in equation (1.9) in the first chapter.

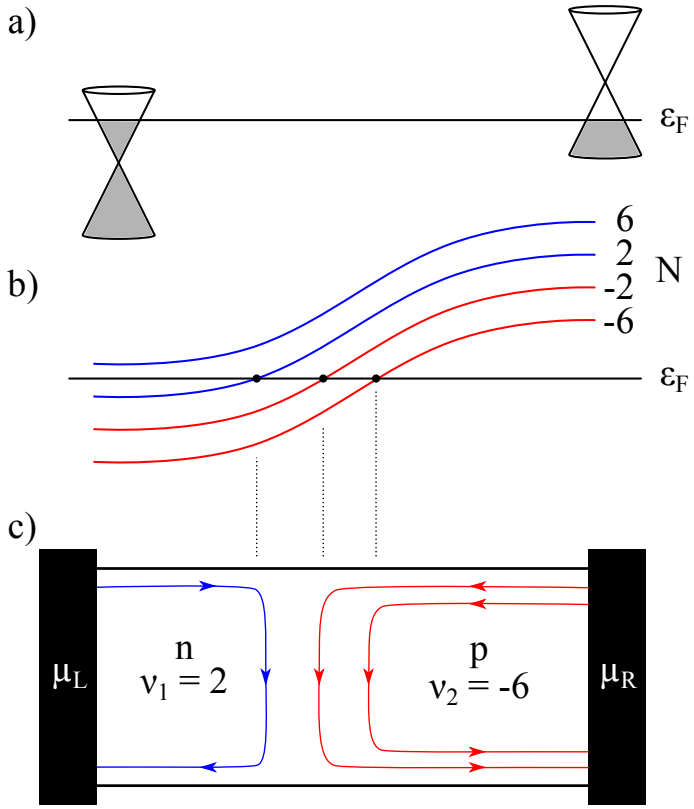

Figure 4.2: a) The Fermi level lies in the electron-doped region within the conduction band while it is situated in the valence band in the hole-doped region. b) Due to the changing potential across the pn-interface, the Landau levels bend. The Fermi level crosses the Landau levels at $N = 2$ as well as $N = -2$ and $N = -6$ where edge channels emerge. c) The electron edge channels circulate on the left side while the hole edge channels propagate on the right side. Along the pn-interface, the oppositely charged carriers move in the same direction.

Therefore, the electron- and hole-like edge channels propagate in the same direction along the pn-interface.

1.2 Equilibration and inelastic scattering

The influence of inelastic scattering at the pn-interface on mode mixing and the resulting resistance has been discussed by J. Li et al [87] and W. Long et al [88] as well as J.-C. Chen et al [89] in six-terminal devices. They emphasise that the observation of fractional plateaus are only possible due to inelastic scattering between the edge channels and its consequential equilibration between them. In the absence of scattering, the device becomes insulating with high resistance since the current cannot flow between the source and the drain. By adding inelastic scattering, the resistance decreases rapidly since electron- and hole-like edge channels start to mix in vicinity of the pn-boundary. When the strength of inelastic scattering is further increased, at some point, the edge channels are fully mixed resulting in the observed plateau features in the resistance.

One way to introduce inelastic scattering is by adding disorder which is, for instance, due to vacancies, impurities and potential fluctuations. J.C. Chen et al point out in their theoretical simulations that conductance plateaus originate from inelastic scattering as an interplay of disorder and dephasing processes. The latter destroying the particle's phase

but not its momentum, is induced, for instance, by electron-phonon and electron-electron interactions [90].

2 Equilibration of degenerated quantum Hall edge channels in a pnp-junction

In 2007, the first measurement of a pn-junction in the quantum Hall regime was conducted on graphene on SiO_2 by the group of C.M. Marcus [91]. The theoretical understanding of their results was developed in a companion paper by D.A. Abanin and L.S. Levitov [92].

The more complex structure of a pnp-junction is realised by placing a top-gate above the central part of the graphene as shown in Fig. 4.1. In 2009, measurements of a pnp-junction in graphene on SiO_2 were performed in the two-terminal configuration by the group of P. Kim [93] and in multiterminal devices by D.-K. Ki and H.-J. Lee [94]. S.-G. Nam et al. were able to develop a fabrication procedure of embedding the local gate which decouples the central region from the influence of the backgate [95].

Only recently in 2014, the group of Goldhaber-Gordon was successful in measuring a pnp-junction in high mobility graphene on hexagonal boron nitride. They discovered that when the four-fold degeneracy is lifted, equilibration between edge channels is selective depending on the spin polarisation of each edge channel [96].

In the following, first, we derive the various resistances of a pnp-junction in a six-terminal configuration based on Landauer-Büttiker formalism. Afterwards, we compare the theoretical predictions with the experimental results of D.-K. Ki and H.-J. Lee [94]. In this section, we assume that the degeneracies of spin and valley are not lifted which leads to non-polarised, degenerated edge states. In the next section, we discuss the consequences of the lifting of the degeneracies and the resulting polarised edge states on transport properties in a pnp-junction.

2.1 Theoretical framework of a pnp-junction

In a pnp-junction, we denote the outer two regions of the same filling factor by ν_1 and the central region of a different filling factor by ν_2. In the following, we derive the different resistances in a multiterminal measurement of a pnp-junction in the form of a Hall bar (see Fig. 4.4a).

In the previous chapter, we derived various resistances (R_H, R_L, R_D) for a six-terminal

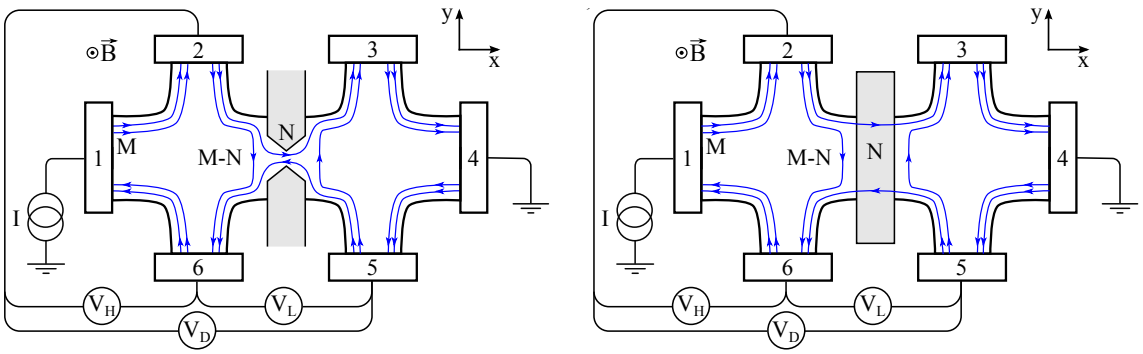

Figure 4.3: Schematic of a Hall bar equipped with a QPC to compare with the pnp-junction.

Hall bar equipped with a QPC (see Fig. 4.3a) of the form

$$\begin{aligned} R_H &= \frac{h}{e^2}\frac{1}{M} \\ R_L &= \frac{h}{e^2}\frac{M-N}{M\cdot N} \\ R_D &= \frac{h}{e^2}\frac{1}{N} \end{aligned} \tag{4.1}$$

in which out of M edge channels, N edge channels are transmitted.

Let us have a look at the same Hall bar configuration, replacing the QPC with a top-gate which covers the full width of the device as shown in Fig. 4.3b. In an analogue to the QPC, out of M edge channels, N edge channels are transmitted, passing underneath the junction along the edge of the sample. $M-N$ edge channels are backscattered. If we derive the various resistances (R_H, R_L, R_D) within this configuration of a pnp-junction with Landauer-Büttiker formalism, we will obtain the same relations (4.1).

In the next step, we need to adapt (4.1) in order to include equilibration between edge channels of the bulk and those underneath the split gates. The parameter N no longer corresponds directly to the filling factor ν_2 in the central region. In order to find an accurate relation between the number of transmitted channels and the two filling factors ν_1 and ν_2, we need to distinguish three regimes depending on the sign and value of both filling factors.

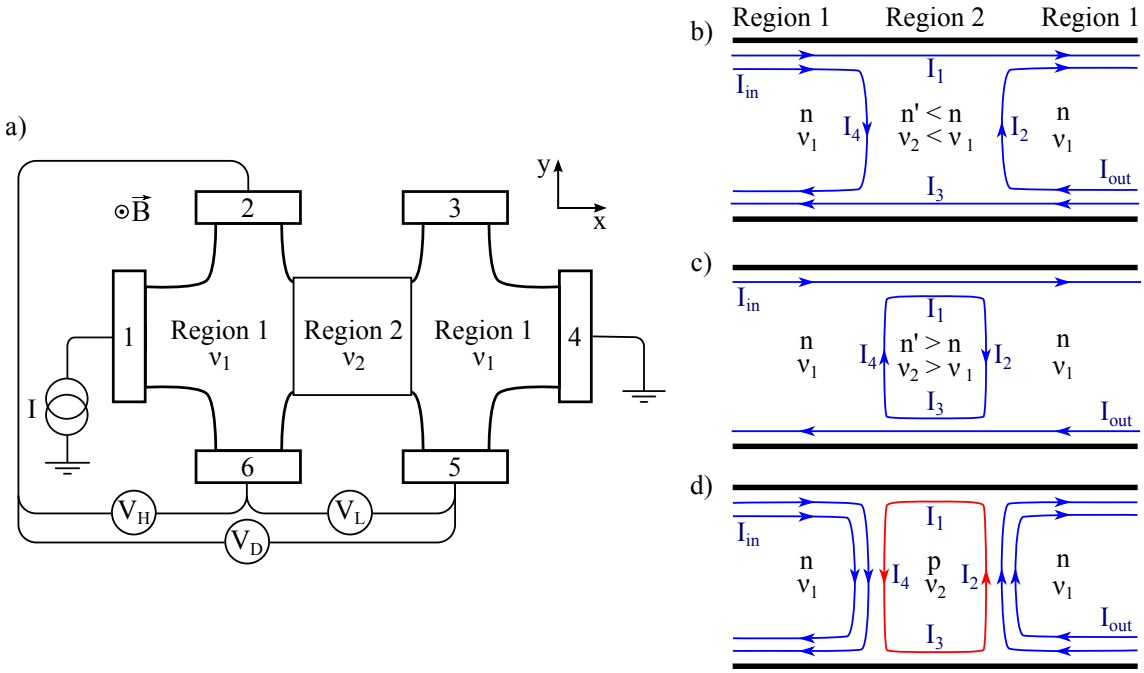

Figure 4.4: Schematic of a pnp-junction in the three possible regimes. a) Schematic drawing of a Hall bar with three regions of which the outer two are described by the filling factor ν_1 and the central region is characterised by the filling factor ν_2. b) Edge-state transmission regime: $\nu_1 \cdot \nu_2 > 0$ and $|\nu_1| \geq |\nu_2|$. c) Partial equilibration regime: $\nu_1 \cdot \nu_2 > 0$ and $|\nu_1| < |\nu_2|$. d) Full equilibration regime: $\nu_1 \cdot \nu_2 < 0$.

Edge-state transmission regime The charge carriers in this regime have the same polarity ($nn'n$ or $pp'p$) and the filling factor in the central region is lower than that of the outer regions ($\nu_1 > \nu_2$) (see Fig. 4.4b). Since the total number of edge channels is higher than those in the central region, only the edge channels of the filling factors which they have in common are transmitted. The additional edge channels in the outer regions are backscattered. The number of transmitted channels N corresponds, therefore, to the filling factor in the central region ($N = |\nu_2|$).

$$\begin{aligned} R_H &= \frac{h}{e^2}\frac{1}{|\nu_1|} \\ R_L &= \frac{h}{e^2}\frac{|\nu_1| - |\nu_2|}{|\nu_1| \cdot |\nu_2|} \\ R_D &= \frac{h}{e^2}\frac{1}{|\nu_2|} \end{aligned} \tag{4.2}$$

The edge-state transmission regime is, hence, in close analogy to the QPC.

Partial equilibration regime The charge carriers have still the same polarity ($nn'n$ or $pp'p$) but the filling factor in the central region is higher than that of the outer regions ($|\nu_1| < |\nu_2|$) (see Fig. 4.4c). The edge channels of the common filling factors propagate from the source to the drain. The additional edge channel circulates in the central region and, due to equilibration, mixes with the counterpropagating outer edge channels introducing backscattering.

The number of transmitted edge channels is defined by the edge channels of common filling factors and adjusted by the contribution of equilibration. It is derived by calculating the outgoing current $I_{out} = \frac{e^2}{h}(\mu_L - \mu_R) N$. We assume that the current emerges only from the left side. By using current conservation (see Fig. 4.4b), we find the following relations:

$$I_1 = I_{in} + I_4 \qquad I_2 = I_3$$
$$I_2 = \frac{|\nu_2| - |\nu_1|}{|\nu_2|} I_1 \qquad I_4 = \frac{|\nu_2| - |\nu_1|}{|\nu_2|} I_3$$

Therefore, I_{out} is obtained by

$$I_{out} = I_1 - I_2 = \frac{|\nu_1|}{|\nu_2|} I_1$$

Since the incoming current is given by $I_{in} = \frac{e^2}{h}(\mu_L - \mu_R)|\nu_1|$, we derive I_{out} by considering the relation

$$\frac{I_{out}}{I_{in}} = \frac{\frac{|\nu_1|}{|\nu_2|}}{\frac{2|\nu_1|}{|\nu_2|} - \left(\frac{|\nu_1|}{|\nu_2|}\right)^2} = \frac{|\nu_2|}{2|\nu_2| - |\nu_1|}$$

The outgoing current is, hence,

$$I_{out} = \frac{e^2}{h}\left(\mu_L - \mu_R\right) \underbrace{\frac{|\nu_1| \cdot |\nu_2|}{2|\nu_2| - |\nu_1|}}_{=N} \tag{4.3}$$

Including the expression of N (4.3) into the general relation of the resistances (4.1), we obtain

$$\boxed{\begin{aligned} R_H &= \frac{h}{e^2}\frac{1}{|\nu_1|} \\ R_L &= \frac{h}{e^2}\frac{|\nu_2| - |\nu_1|}{|\nu_1| \cdot |\nu_2|} \\ R_D &= \frac{h}{e^2}\frac{2|\nu_2| - |\nu_1|}{|\nu_1| \cdot |\nu_2|} \end{aligned}} \tag{4.4}$$

The partial equilibration regime only exists in the configuration of a $nn'n$ or $pp'p$-junction and not in the nn' or pp'-junction in which the additional edge channels cannot circulate and partially equilibrate with each other.

Full equilibration regime In the last regime, charge carriers have opposite polarity (*npn* or *pnp*) (see Fig. 4.4d). At each pn-interface, the electron- and hole-like edge channels propagate in the same direction, equilibrating with each other.

We use the same approach of current conservation as in the partial equilibration regime to calculate the number of transmitted edge channels. We obtain the relations:

$$\begin{aligned} I_1 &= I_{in} + I_4 & I_2 &= I_3 \\ I_2 &= \frac{|\nu_1| + |\nu_2|}{|\nu_2|} I_1 & I_4 &= \frac{|\nu_1| + |\nu_2|}{|\nu_2|} I_3 \\ I_{out} &= -\frac{|\nu_1|}{|\nu_2|} I_1 & I_{in} &= \left(1 - \left(1 + \frac{|\nu_1|}{|\nu_2|}\right)^2\right) I_1 \end{aligned}$$

Therefore, the ratio of incoming and outgoing current becomes:

$$\frac{I_{out}}{I_{in}} = \frac{-\frac{|\nu_1|}{|\nu_2|}}{\left(1 - \left(1 + \frac{|\nu_1|}{|\nu_2|}\right)^2\right)} = \frac{|\nu_2|}{2|\nu_2| + |\nu_1|}$$

The outgoing current takes the form:

$$I_{out} = \frac{e^2}{h}\left(\mu_L - \mu_R\right) \underbrace{\frac{|\nu_1| \cdot |\nu_2|}{2|\nu_2| + |\nu_1|}}_{=N} \tag{4.5}$$

We use the expression of N (4.5) to insert it into the general relation of the resistances

(4.1) and obtain

$$\begin{aligned} R_H &= \frac{h}{e^2}\frac{1}{|\nu_1|} \\ R_L &= \frac{h}{e^2}\frac{|\nu_1|+|\nu_2|}{|\nu_1|\cdot|\nu_2|} \\ R_D &= \frac{h}{e^2}\frac{2|\nu_2|+|\nu_1|}{|\nu_1|\cdot|\nu_2|} \end{aligned} \tag{4.6}$$

The transverse resistance R_H remains unchanged in all three regimes depending only on the total number of edge channels. At this point we mention that the expressions of the resistances (4.2), (4.4) and (4.6) are taken at a fixed direction of magnetic field. If its direction is inverted, R_H and R_L remain unchanged but R_D needs to be calculated with the current and voltage probes switched (for more details see [94]). Table 4.1 summarises the relations for the three regimes including R_D for both directions of the magnetic field.

2.2 Experimental results on the pnp-junction on SiO_2

Measurements of a pnp-junction in graphene on SiO_2 have been performed in two-terminal configuration by the group of P. Kim [93] and in multiterminal devices by D.-K. Ki and H.-J. Lee [94].

In the following, we discuss briefly some of the results on multiterminal devices [94] focusing on the longitudinal resistance as a primary example. A device of graphene exfoliated on SiO_2 was decoupled from the local top-gate by an insulating layer of PMMA. Its schematic configuration and scanning electron microscope (SEM) image are presented in Fig. 4.5a and b, respectively. The dashed line in the SEM image represent the border of the graphene flake.

Fig. 4.5c shows the colour map of the longitudinal resistance as a function of the backgate and top-gate voltage. The longitudinal resistance exhibits plateaus at fractional values of $\frac{p}{q}\frac{h}{e^2}$ which depend on the three equilibration regimes which we derived above. The precise values of quantisation become clear in the linecuts at a fixed backgate voltage of $V_{BG} = 50.5\,\mathrm{V}$ (Fig. 4.5d) and of $V_{BG} = 22\,\mathrm{V}$ (Fig. 4.5e). The red and the blue lines were

Table 4.1: Summary of the three regimes of a pnp-junction in a multiterminal configuration.

Regime	Filling factors	R_L	$R_D(B)$	$R_D(-B)$	R_H
Edge-state transmission	$\nu_1\cdot\nu_2 > 0$ $\lvert\nu_1\rvert \geq \lvert\nu_2\rvert$	$\frac{h}{e^2}\frac{\lvert\nu_1\rvert-\lvert\nu_2\rvert}{\lvert\nu_1\rvert\cdot\lvert\nu_2\rvert}$	$\frac{h}{e^2}\frac{1}{\lvert\nu_2\rvert}$	$-\frac{h}{e^2}\frac{2\lvert\nu_2\rvert-\lvert\nu_1\rvert}{\lvert\nu_1\rvert\cdot\lvert\nu_2\rvert}$	$\frac{h}{e^2}\frac{1}{\lvert\nu_1\rvert}$
Partial equilibration	$\nu_1\cdot\nu_2 > 0$ $\lvert\nu_1\rvert < \lvert\nu_2\rvert$	$\frac{h}{e^2}\frac{\lvert\nu_2\rvert-\lvert\nu_1\rvert}{\lvert\nu_1\rvert\cdot\lvert\nu_2\rvert}$	$\frac{h}{e^2}\frac{2\lvert\nu_2\rvert-\lvert\nu_1\rvert}{\lvert\nu_1\rvert\cdot\lvert\nu_2\rvert}$	$-\frac{h}{e^2}\frac{1}{\lvert\nu_2\rvert}$	$\frac{h}{e^2}\frac{1}{\lvert\nu_1\rvert}$
Full equilibration	$\nu_1\cdot\nu_2 < 0$	$\frac{h}{e^2}\frac{\lvert\nu_1\rvert+\lvert\nu_2\rvert}{\lvert\nu_1\rvert\cdot\lvert\nu_2\rvert}$	$\frac{h}{e^2}\frac{2\lvert\nu_2\rvert+\lvert\nu_1\rvert}{\lvert\nu_1\rvert\cdot\lvert\nu_2\rvert}$	$\frac{h}{e^2}\frac{1}{\lvert\nu_2\rvert}$	$\frac{h}{e^2}\frac{1}{\lvert\nu_1\rvert}$

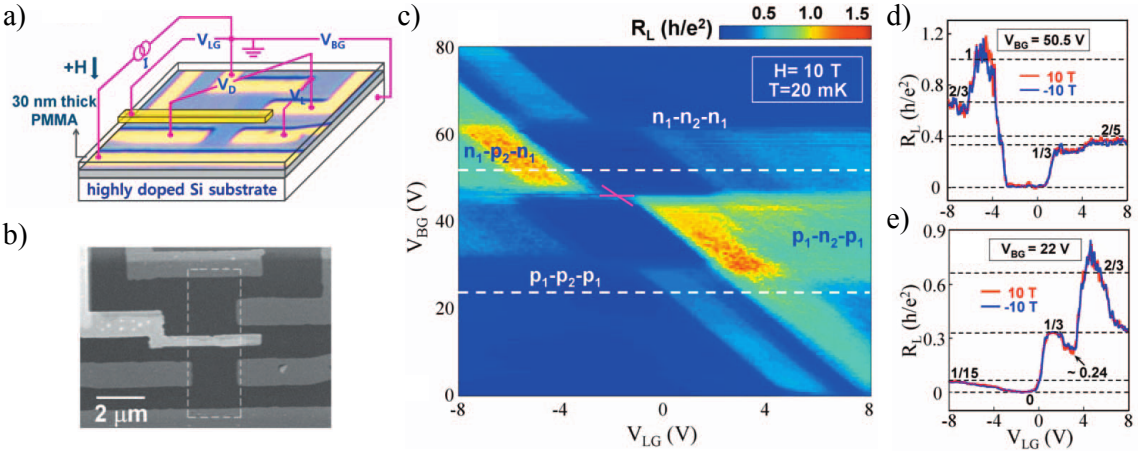

Figure 4.5: Experimental results of a pnp-junction of graphene on SiO_2. a) Schematic drawing of the graphene device equipped with a local top-gate. b) SEM image of the graphene device. The dashed line defines the borders of the graphene flake. c) R_L is plotted as a function of V_{BG} and V_{LG}. d) Linecut extracted from c) at a fixed $V_{BG} = 50.5\,\mathrm{V}$ for a magnetic field of 10 T (red curve) and $-10\,\mathrm{T}$ (blue curve). The curves exhibit fractional plateaus which correspond well to the theoretical values (dashed lines). e) Linecut extracted from c) at a fixed $V_{BG} = 22\,\mathrm{V}$ analogue to d). Fig. taken from [94].

measured at magnetic field of 10 T and $-10\,\mathrm{T}$, respectively. We see that the two curves completely overlap indicating that a change in direction of the magnetic field does not influence R_L. Both curves exhibit plateaus at fractional values of R_L which correspond well to the theoretically expected values of R_L within the three regimes (dashed lines in Fig. 4.5d and e).

For instance, in Fig. 4.5e, R_L exhibits a plateau of $\frac{1}{3}\frac{h}{e^2}$ at $V_{LG} \simeq 2\,\mathrm{V}$ where the filling factor in the bulk is $\nu_1 = -6$ and the filling factor in the central region is $\nu_2 = -2$. Since $|\nu_1| \geq |\nu_2|$ and $\nu_1 \cdot \nu_2 > 0$, we need to use (4.2) of the edge-state transmission regime and we obtain $R_L = \frac{1}{3}\frac{h}{e^2}$ which corresponds to the observed plateau.

We pick a second example, a plateau-like feature at $R_L = \frac{2}{3}\frac{h}{e^2}$ at $V_{LG} \simeq -8\,\mathrm{V}$ in Fig. 4.5d. This plateau appears when $\nu_1 = 2$ and $\nu_2 = -6$ which is located in the full equilibration regime. Applying (4.6), we obtain $R_L = \frac{2}{3}\frac{h}{e^2}$ in agreement with the experimental result.

3 Spin selective equilibration of quantum Hall edge channels

When the degeneracies of spin and valley are completely lifted, edge channels are spin- and/or valley polarised. F. Amet in the group of D. Goldhaber-Gordon discovered that equilibration between edge channels seems to depend on their spin and/or valley polarisation [96]. For instance, edge channels of differing spin polarisation do not equilibrate with each other but edge channels of different valley polarisation do.

In the following we have a closer look at their results. They measured pnp-junctions in high-mobility graphene devices located on hexagonal boron-nitride (hBN) and equipped with a suspended local top-gate (see Fig. 4.7a).

Order of the lifting of the degeneracies In their devices, the degeneracies of spin and valley are fully lifted, resulting in plateaus in the conductance at every multiple of $\frac{e^2}{h}$. By setting the filling factor in the bulk at a constant value of, for instance, $\nu_B = -6$, the

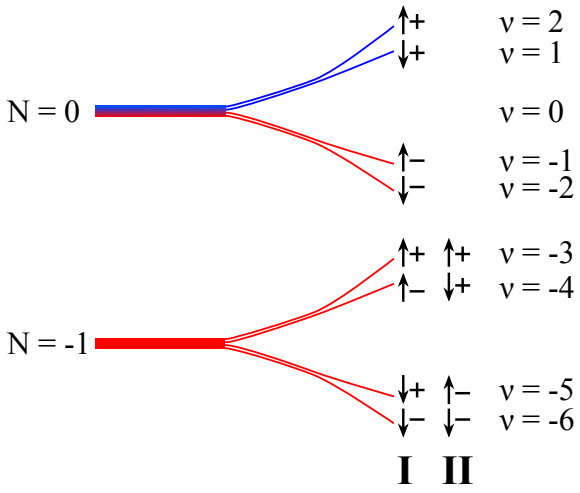

Figure 4.6: The order of the splitting of the $N = 0$ and $N = -1$ Landau level due to the lifting of the spin and valley degeneracies defines the polarisation of the edge channels. In the schema, $\uparrow, \downarrow$ indicate the polarisation of the spin and $+, -$ describe the valley polarisation.

number of transmitted edge channels is varied by changing the voltage of the top-gate V_{TG} and thereby the filling factor ν_T underneath it. The two-terminal conductance decreases in steps of $\frac{e^2}{h}$ with decreasing ν_T due to the increasing constriction for edge channels to pass (see Fig. 4.7b).

In the previous chapter, we discussed various theoretical approaches to describe the lifting of the four-fold degeneracies of spin and valley resulting in the splitting of the Landau levels into spin- and valley polarised states. Whether the spin or the valley degeneracy gets lifted first depends especially on the interplay and strength of the Coulomb interaction, the Zeeman coupling and valley anisotropies. Amet et al observed an insulating behaviour in the $\nu = 0$ state indicating that the valley degeneracy is lifted first (see Fig. 4.6). For the $N = -1$ (analogue to $N = 1$) Landau level, they point out that two scenarios (I, II) of the polarisation of states are possible depending on the order of the lifting of the degeneracies. Scenario I assumes that the spin degeneracy lifts first whereas II exhibits first the lifting of the valley degeneracy.

Spin selective equilibration in $N = 0$ Landau level We see in the schema 4.6 that the two states $\nu = -1$ and $\nu = -2$, both belonging to the $N = 0$ Landau level, have the same valley polarisation but are oppositely polarised in their spins. Amet et al observed that these two states do not equilibrate with each other due to the opposite spin polarisation. This phenomenon becomes visible in Fig. 4.7c in which the two-terminal conductance g is measured as a function of ν_T at fixed $\nu_B = -1$. We see in this curve that g stays constant at $\frac{e^2}{h}$ over the range $\nu_T = -1$ and -2. If we consider the two-terminal conductance of a pnp-junction in the partial equilibration regime

$$g = \frac{e^2}{h} \frac{\nu_T \nu_B}{2\nu_T - \nu_B} \tag{4.7}$$

we would expect $g = \frac{e^2}{h}$ for $\nu_T = -1$ and $g = \frac{2}{3}$ for $\nu_T = -2$ at constant $\nu_B = -1$. Since the conductance stays at $\frac{e^2}{h}$ when the edge channel of $\nu_T = -2$ is added, we can assume

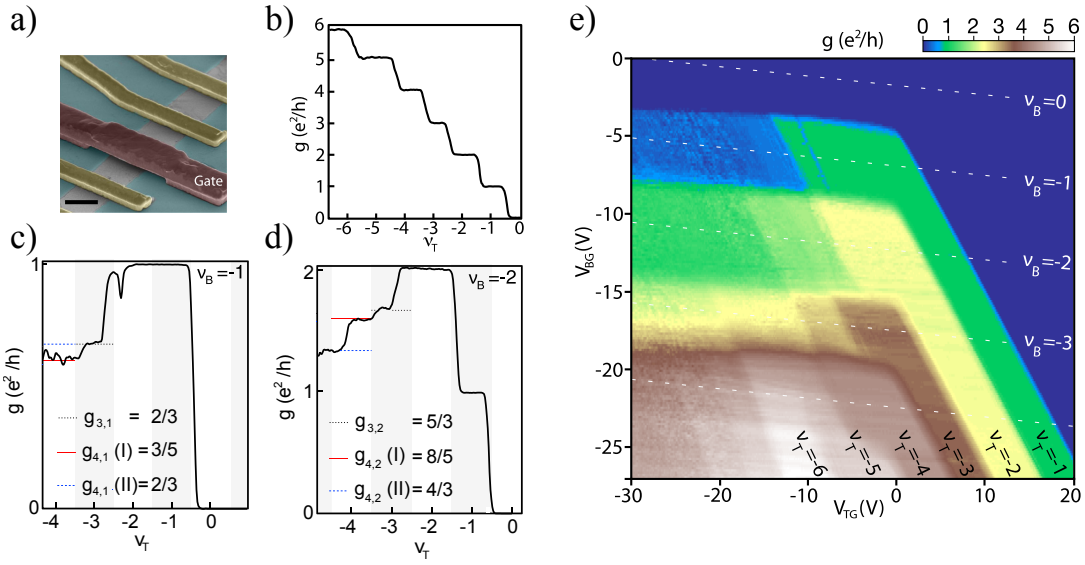

Figure 4.7: Experimental results on a high-mobility pnp-junction in graphene. a) False-coloured image taken with an scanning electron microscope. The suspended top-gate (red) is deposited above a graphene flake (gray) which itself is located on hBN (blue). b) At fixed filling factor in the bulk of $\nu_B = -6$, the filling factor ν_T beneath the top-gate is decreased. The conductance g decreases step-like with decreasing ν_T since the number of transmitted edge channels is constricted. c) The conductance as a function of ν_T at constant $\nu_B = -1$. The states $\nu_B = -1$ and $\nu_T = -2$ do not equilibrate with each other due to their opposite spins leaving the conductance unchanged. The state $\nu_T = -3$ mixes with $\nu_B = -1$ inducing a change in conductance. d) The conductance as a function of ν_T at fixed $\nu_B = -2$. The given values of g result from (4.8) corresponding to the observed plateaus. e) The two-terminal conductance as a function of the top-gate voltage V_{TG} and the backgate voltage V_{BG}. Fig. taken from [96].

that this additional edge channel below the top-gate does not equilibrate with the edge channel $\nu_B = -1$.

In contrast, when changing the top-gate to the $\nu = -3$ state of the first Landau level we see that the conductance decreases and exhibits a plateau at $\frac{2}{3}\frac{e^2}{h}$ instead of $g = \frac{3}{5}\frac{e^2}{h}$ which is expected from (3.5). The $\nu_T = -3$ and the $\nu_B = -1$ states which have the same spin polarisation equilibrate with each other.

Both states have, however, different valley polarisations which leads to intervalley mixing. Thus, the valley polarisation is not conserved which may be due to the disordered plasma-etched edges of their sample.

Amet et al propose an adaptation for the two-terminal conductance (4.7) in the partial equilibration regime which takes into account the spin polarisation of each state:

$$g_{spin} = \sum_{i=\downarrow,\uparrow} \frac{\nu_{T,i} \cdot \nu_{B,i}}{2\nu_{T,i} - \nu_{B,i}} \tag{4.8}$$

The sum accounts for the two spin polarisations $\nu_{T,\uparrow}$ and $\nu_{T,\downarrow}$ (as well as $\nu_{B,\uparrow}$ and $\nu_{B,\downarrow}$) in each combination (ν_T,ν_B). For instance, an equilibration between the states of $\nu_B = -1$ and $\nu_T = -3$ is calculated for each spin configuration:

- $\nu_{T,\uparrow} = -2$ and $\nu_{B,\uparrow} = -1 \rightarrow g_{spin,\uparrow} = \frac{2}{3}\frac{e^2}{h}$
- $\nu_{T,\downarrow} = -1$ and $\nu_{B,\downarrow} = 0 \quad \rightarrow g_{spin,\downarrow} = 0$

The total conductance of $g_{spin} = \frac{2}{3}\frac{e^2}{h}$ confirms the observed plateau in Fig. 4.7c. Tab. 4.2 compares the results of the conductance obtained from (4.7) and from (4.8) with their experimental results of the $N = 0$ Landau level which confirms their model that states equilibrate only if they have the same spin polarisation independent of their valley polarisation.

Spin selective equilibration in $N > 0$ Landau level Let us have a look at the conductance when we include higher Landau levels. As mentioned above, two scenarios (I, II) are possible depending on whether the spin or the valley degeneracy is lifted first, resulting in two solutions for eq. (4.8) for the conductance. For instance, considering $\nu_T = -4$ at fixed $\nu_B = -1$, the two solutions of (4.8) are for I: $g_{spin} = \frac{3}{5}\frac{e^2}{h}$ and for II: $g_{spin} = \frac{2}{3}\frac{e^2}{h}$. In Fig. 4.7c, a conductance plateau of $\frac{3}{5}\frac{e^2}{h}$ at $\nu_T = -4$ is visible which is in agreement with scenario I. Fig. 4.7d presents another example of a conductance curve at constant $\nu_B = -2$. At $\nu_T = -4$, the conductance is expected to exhibit plateaus at I: $g_{spin} = \frac{8}{5}\frac{e^2}{h}$ or at II: $g_{spin} = \frac{4}{3}\frac{e^2}{h}$ which both are observed in Fig. 4.7d indicating that both scenarios are possible.

Absence of equilibration in the bipolar regime Fig. 4.7e presents the complete conductance map of (ν_B,ν_T) measured at 1 K and 14 T. On the right side of the map, hole edge channels circulate in the bulk while electron edge channels are localised underneath the top-gate. The transport properties in this configuration are characterised by the full equilibration regime. However, we do not observe any change in colour on the right side of the map in Fig. 4.7e indicating that there is no equilibration between electron- and hole-like edge channels. Amet et al suggest that the absence of equilibration is due to the narrow insulating strip at $\nu = 0$ separating the electron and hole like edge channels.

Table 4.2: Conductance plateaus in the partial equilibration regime comparing the conductance obtained from (4.7) with (4.8) which takes the spin polarisation of each state into account. The results of both equations are compared with the experimental results of [96].

ν_B	ν_T	$g\left(\frac{e^2}{h}\right)$ eq. (4.7)	$g_{spin}\left(\frac{e^2}{h}\right)$ eq. (4.8)	$g_{exp}\left(\frac{e^2}{h}\right)$
1	1	1	1	1.00 ± 0.01
	2	$\frac{2}{3}$	1	0.98 ± 0.04
	3	$\frac{3}{5}$	$\frac{2}{3}$	0.660 ± 0.005
	4	$\frac{4}{7}$	I: $\frac{3}{5}$ II: $\frac{2}{3}$	0.60 ± 0.03
2	2	2	2	2.01 ± 0.01
	3	$\frac{3}{2}$	$\frac{5}{3}$	1.68 ± 0.01
	4	$\frac{4}{3}$	I: $\frac{8}{5}$ II: $\frac{4}{3}$	1.590 ± 0.005

The gap at $\nu = 0$ was measured to have a size of 200 K at 15 T [51] which is, in fact, one order of magnitude smaller than the cyclotron gap of 1500 K at 15 T between the $N = 0$ and $N = 1$ Landau level. However, even though the cyclotron gap is much larger, Amet et al observed equilibration between the $N = 0$ and $N = 1$ Landau level.

Highly insulating behaviour at $\nu = 0$ The groups of Geim and Novoselov [97] as well as the groups of Jarillo-Herrero and Ashoori [85] observed systematically a highly insulating behaviour at the charge neutrality point in graphene on hBN due to a band gap of an estimated size of 360 K at zero magnetic field [97]. This behaviour seems to depend on the relative rotation angle between the graphene and the BN lattices and the resulting moiré pattern.

On the other hand, in our devices of encapsulated high mobility graphene, we observe equilibration between electron and hole states. Our results are in agreement with the groups of Geim and Novoselov [97] who observe systematically a resistivity peak at the charge neutrality point of the order of several kΩ suggesting a much smaller gap at the neutrality point.

4 Equilibration in a Quantum point contact

At this point, we come back to the quantum point contact in graphene which we have already introduced in chapter 3 (sect. 3.3). The group of C.M. Marcus realised the first QPC in graphene on SiO_2 [98]. In their work, the graphene is connected to six contacts as presented in Fig. 4.8 allowing to determine the longitudinal resistance R_L between the contacts D1 and S1 on which we will focus our discussion.

4.1 Selective transmission through the QPC

The measurement of R_L as a function of the top-gate and backgate voltages is shown in Fig. 4.9a. We see various regions of R_L of zero resistance and fractions of $\frac{h}{e^2}$. The diagram of the theoretical calculations is presented in Fig. 4.9b for comparison with the measured data of Fig. 4.9a.

The areas of dark blue represent zero longitudinal resistance, where the bulk edge channels pass the constriction without being able to equilibrate with edge channels of the split gates. In Fig. 4.10a(i) to c(i), we present some configurations which result in zero resistance. In the configuration a(i) of $\nu_{bulk} = 2$ and $\nu_{gate} = 6$, one bulk edge channel

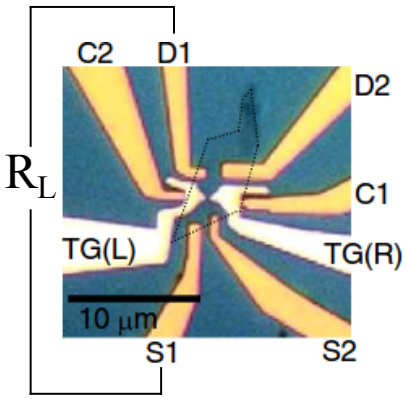

Figure 4.8: Optical image of the graphene QPC device on SiO_2 in which the graphene is indicated by a dotted line. TG represents the QPC which is decoupled by an insulating layer of Al_2O_3 from the graphene. The six contact leads to the graphene allow to measure multiple resistances simultaneously as the longitudinal resistance R_L. Fig. taken from [98].

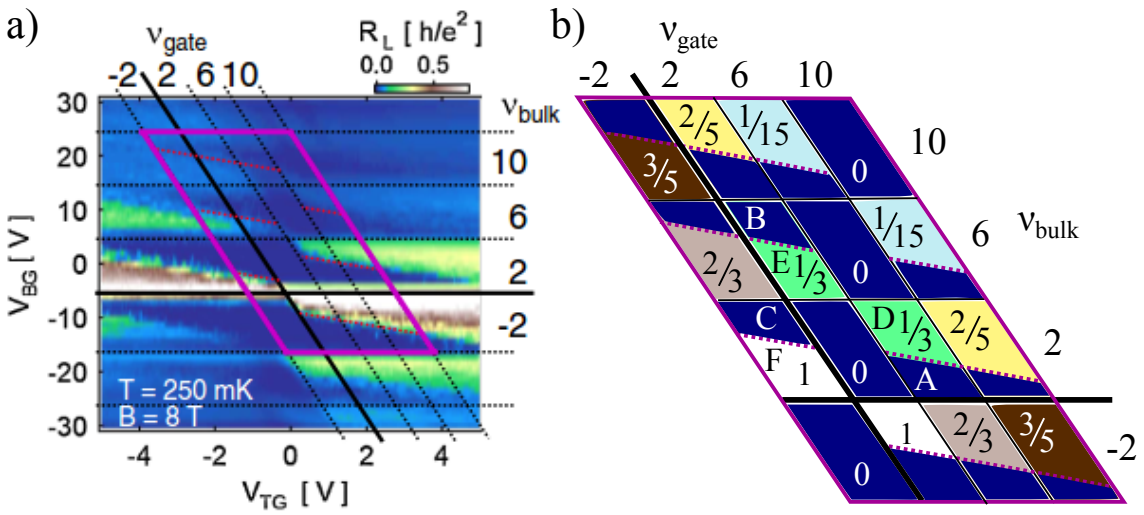

Figure 4.9: Experimental results on a QPC in graphene on SiO_2. a) Longitudinal resistance R_L as a function of the top-gate voltage V_{TG} and the backgate voltage V_{BG}. The magenta parallelogram emphasises specific filling factors in the bulk ν_{bulk} and below the top-gate ν_{gate} to directly compare them with the theoretical predictions in b). Fig. taken from [98]. b) Theoretical values of R_L in units of $\frac{e^2}{h}$ for various pairs of (ν_{bulk},ν_{gate}). Each small parallelogram is subdivided along the red dotted line at which the QPC changes from open to closed.

passes underneath the split gates and one additional edge channel is localised underneath the split gates. In the case b(i) of $\nu_{bulk} = 6$ and $\nu_{gate} = 2$, one bulk edge channel passes along the edge of the device underneath the split gates. The second bulk edge channel does not have any equivalent beneath the split gates, so it has to pass through the QPC. In the third configuration c(i) of $\nu_{bulk} = 2$ and $\nu_{gate} = -2$ the bulk edge channel is forced to pass through the QPC while hole edge channels are localised underneath the split gates.

The configurations b(i) and c(i) embody the effect of the QPC in which the edge channels are forced to pass through the QPC and, therefore, the number of transmitted edge channels are selected by changing the split gate voltage.

4.2 Equilibration between edge channels

We see in both the experimental results of Fig. 4.9a and in the theoretical diagram of Fig. 4.9b that when ν_{bulk} and ν_{gate} are not identical, the dark blue area within each parallelogram is separated by a red dashed line from a non-zero area of fractional value. In fact, in the dark-blue area of zero resistance, the QPC is open while it becomes pinched off passing the red dashed lines to the fractions.

Case of $\nu_{bulk} = 2$ and $\nu_{gate} = 6$ Let us come back to the configuration a(i) in Fig. 4.10. By slightly increasing the backgate or the split gate voltage, we observe that even though the number of edge channels remains unchanged, the QPC shifts from open to pinch-off mode of non-zero resistance. The reason is that the $\nu_{gate} = 6$ edge channel extends across the QPC and, therefore, circulates between the edges of the sample as shown in Fig. 4.10a(ii). The $\nu_{gate} = 6$ state equilibrates with the $\nu_{bulk} = 2$ state which introduces backscattering. The resulting longitudinal resistance increases to the fractional value of $\frac{1}{3}\frac{h}{e^2}$ (partial equilibration regime (4.4)).

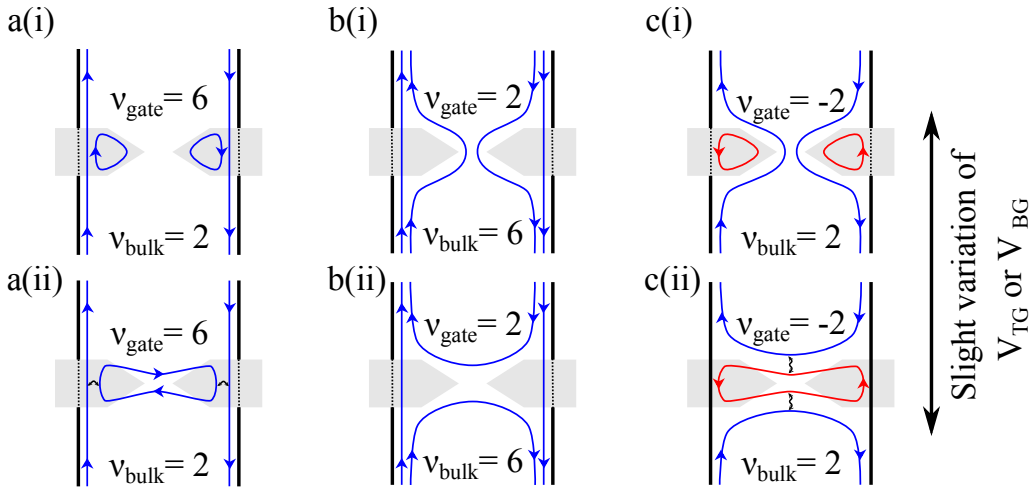

Figure 4.10: Schematics of configurations in Fig. 4.9b. a(i): $\nu_{bulk} = 2$ and $\nu_{gate} = 6$: One bulk edge channel passes underneath the split gates and one edge channel is localised beneath the split gates $\rightarrow R_L = 0$. b(i): $\nu_{bulk} = 6$ and $\nu_{gate} = 2$: One bulk edge channel passes underneath the split gates and the second one is transmitted through the QPC $\rightarrow R_L = 0$. c(i): $\nu_{bulk} = 2$ and $\nu_{gate} = -2$: Due to localised hole-like edge channels underneath the split gates, the bulk edge channel is transmitted through the QPC $\rightarrow R_L = 0$. a(i) to c(i): Increase of V_{BG} or V_{TG} to pass the dotted line in Fig. 4.9b: a(ii): The $\nu_{gate} = 6$ edge channel circulates between the split gates introducing backscattering and, hence, $R_L > 0$. b(ii): Backscattering of the $\nu_{bulk} = 6$ edge channel leading to $R_L > 0$. c(ii): The hole-like edge channel circulates across the split gates leading to the backscattering of the bulk edge channel resulting in $R_L > 0$. Fig. adapted from [98].

Case of $\nu_{bulk} = 6$ and $\nu_{gate} = 2$ In configuration b(i) in Fig. 4.10, when $\nu_{bulk} > \nu_{gate}$, the additional edge channel in the bulk is forced to pass through the QPC. A slight decrease of either V_{BG} or V_{TG} causes a decrease of the charge carrier density in the regions both beneath the split gates and inside the QPC until the $\nu_{bulk} = 6$ edge channel cannot pass the QPC and is backscattered as in the configuration b(ii) in Fig. 4.9. The resistance increases to a value of $\frac{1}{3}\frac{h}{e^2}$ (edge-state transmission regime (4.2)).

Case of $\nu_{bulk} = 2$ and $\nu_{gate} = -2$ In configuration c(i) in Fig. 4.10, the bulk edge channel passes through the QPC since hole edge channels are localised underneath the split gates. A slight increase in V_{BG} or V_{TG} while keeping the the filling factors constant, prompts the hole state to extend across the QPC causing the bulk edge channel to be backscattered. Equilibration between the states of $\nu_{bulk} = 2$ and $\nu_{gate} = -2$ leads to a current transfer across the QPC as shown in configuration c(ii) in Fig. 4.10. This configuration results in a resistance of $\frac{h}{e^2}$ (full equilibration regime (4.6)).

Similarity of a QPC to a pnp-junction Considering the different combinations of ν_{bulk} and ν_{gate}, the observed fractional values of resistance can be explained by applying the above derived equations of the three regimes, summarised in table 4.1. Therefore, a QPC in graphene exhibits similar behaviour to a pnp-junction. However, there are some features specific to a QPC in graphene which we discuss in the following.

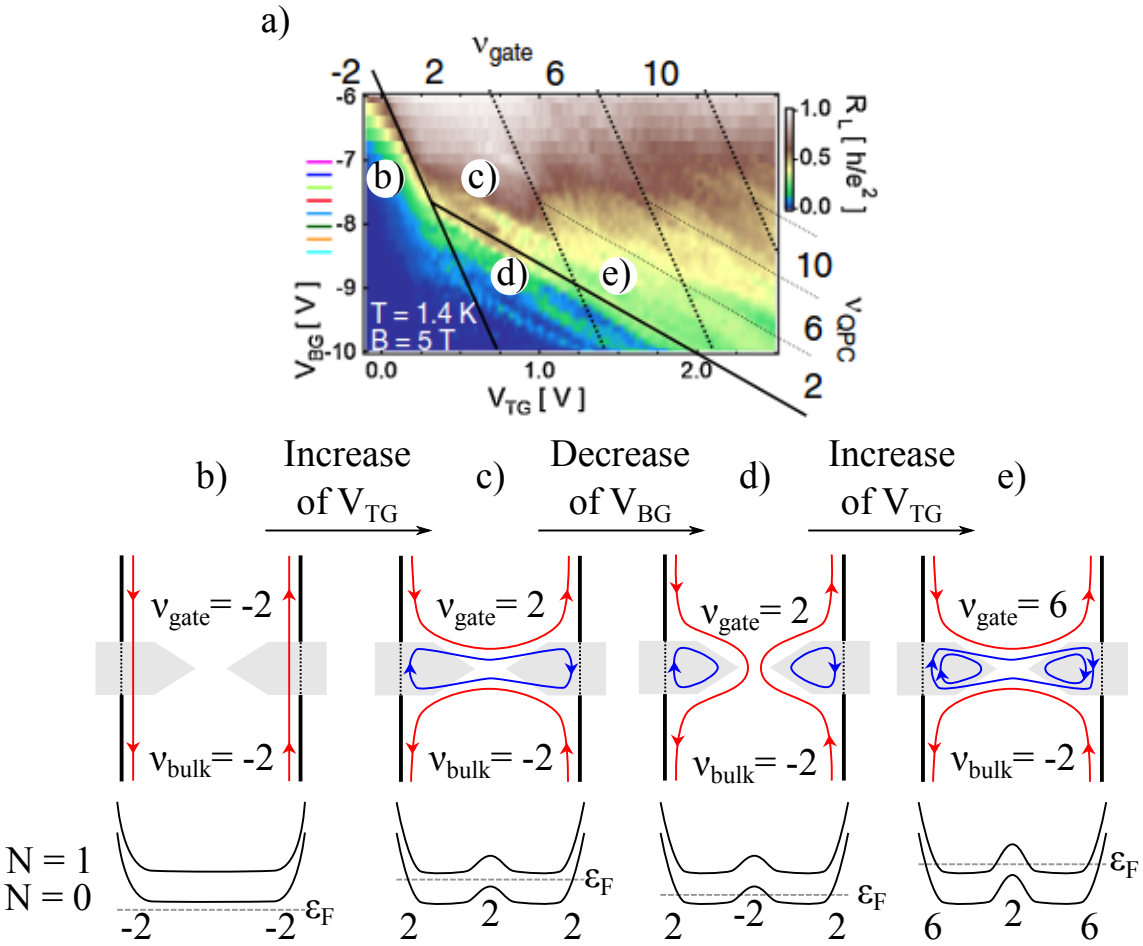

Figure 4.11: a) Zoom of Fig. 4.9a at $\nu_{bulk} = -2$. Two slopes become visible due to ν_{gate} and ν_{QPC}. Fig. taken from [98]. b) $\nu_{bulk} = -2$ and $\nu_{gate} = -2$: The bulk edge channel passes underneath the split gates. Due to the same charge carrier density in the whole graphene, the Landau levels across the QPC is flat, with the Fermi level below the $N = 0$ Landau level. c) $\nu_{bulk} = -2$ and $\nu_{gate} = 2$: The bulk edge channel is backscattered due to the circulating electron-like edge channel of the split gates. The Landau levels across the QPC are bent up at the border of the sample and inside the QPC. The Fermi level lies in between the $N = 0$ and $N = 1$ Landau levels. d) A slight rise of V_{BG} lowers the Fermi level which crosses the $N = 0$ Landau level inside the QPC. The electron-like edge channel is localised underneath the split gates while the bulk edge channel passes through the QPC resulting in $R_L = 0$. e) $\nu_{bulk} = -2$ and $\nu_{gate} = 6$: The Fermi level crosses the $N = 0$ level at the border of the sample while it intersects the $N = 1$ Landau level at the border and inside the QPC. Therefore, one edge channel is localised underneath the split gates and the second one circulates between the two edges of the sample. They equilibrate with the backscattered bulk edge channel. b) to e) adapted from [98]

4.3 Signature of a third filling factor within the QPC

At this point, we have a closer look at what happens inside the QPC during the transition from opened to pinched-off mode. Zooming in closer on the structures of equal ν_{bulk} and ν_{gate} of Fig. 4.9a which is presented in Fig. 4.11a, we recognise two different slopes, one associated with the already familiar ν_{gate} and the other one introducing a third filling factor ν_{QPC}. Since the charge carrier density in the region between the split gates inside the QPC is influenced by both the split gates and the backgate, the third filling factor ν_{QPC} has a value in between ν_{bulk} and ν_{gate}.

In the following, we discuss the origin of these two slopes and the differing filling factors of ν_{gate} and ν_{QPC} taking the Landau level profile across the QPC into account. We assume that ν_{bulk} is fixed at -2. When ν_{gate} is equally at -2, the hole-like bulk edge channel passes underneath the split gates and the longitudinal resistance is zero as presented in Fig. 4.11b.

$\nu_{gate} = 2$ extended across the QPC When ν_{gate} is increased to 2, the electron-like edge channel circulates in between the two edges of the sample. The bulk edge channel can no longer pass the constriction and is backscattered as presented in Fig. 4.11c. The resistance increases to $\frac{h}{e^2}$ (full equilibration regime).

The corresponding Landau level profile across the QPC exhibits a maximum in the middle of the QPC whose height depends on the difference between ν_{bulk} and ν_{gate}. The $N = 0$ Landau level is completely filled across the split gates and the QPC while the $N = 1$ Landau level remains empty with the Fermi energy in between the two levels (see Fig. 4.11c).

$\nu_{gate} = 2$ localised underneath the split gates In Fig. 4.11d, a slight decrease of V_{BG} keeping the same number of edge channels propagating in the bulk, changes the Fermi level. The bulk edge channel passes through the QPC since ν_{QPC} becomes -2 when the Fermi level crosses the $N = 0$ Landau level in the middle of the QPC. The electron-like edge channels are constricted to circulate underneath the split gates. The longitudinal resistance R_L drops to zero in this configuration indicated by the dark blue region in Fig. 4.11a.

The transition from c) to d) in Fig. 4.11 depends only on the charge carrier density and, hence, ν_{QPC} inside the QPC since the number of edge channels in the bulk and underneath the split gates remain unchanged. Therefore, the slope from c) to d) in Fig. 4.11 corresponds to ν_{QPC}.

$\nu_{gate} = 6$ localised underneath the split gates A slight change of V_{TG} modifies both the Fermi level and increases the maximum of the Landau level inside the QPC since the difference between the bulk and the split gate filling factors becomes larger. In the configuration of Fig. 4.11f, ν_{gate} is increased to 6. The $N = 0$ Landau level is completely filled across the QPC being crossed by the Fermi level only at the border of the sample. Therefore, the $\nu_{gate} = 2$ edge channel circulates between the split gates. The Fermi level crosses the $N = 1$ Landau level at the border of the sample as well as in the QPC. Therefore, the $\nu_{gate} = 6$ edge channel is localised in the area underneath the split

gates. The longitudinal resistance increases to $\frac{2}{3}\frac{h}{e^2}$ (full equilibration regime) due to the equilibration between the hole-like edge channels in the bulk and the electron-like edge channels underneath the split gates and inside the QPC.

Summary

In the course of this chapter, we introduced the crucial process of equilibration which arises from inelastic scattering between electrons. Depending on the value and sign of the filling factor in the bulk and the one underneath the top-gate, the transport properties in a pnp-junction are classified into three regimes of transmission and equilibration, respectively. For each regime, we derived the basic relations for the resistances as a function of the filling factors in the bulk and underneath the top-gate in a six-terminal configuration.

In disordered graphene, when the degeneracies are not lifted, equilibration occurs between all edge channels. As soon as the degeneracy is lifted, equilibration is limited to states of identical spins.

In the last part, we discussed the QPC in graphene among other things its similarities to a pnp-junction in terms of equilibration but also the crucial difference due to the presence of a third filling factor.

By this chapter, we have discussed the last essential ingredient of the transmission and equilibration of quantum Hall edge channels for this work. At this point, we are prepared to present our results on the QPC in high mobility graphene devices which we will discuss in chapter 7. Before doing so, we take a brief detour to describe the fabrication of our encapsulated graphene devices in the next chapter.

CHAPTER 5

FABRICATION OF GRAPHENE HETEROSTRUCTURES

Carrier mobility in graphene is highly dependent on the underlying substrate and the amount of residue on its surface coming from the fabrication process. In this chapter, we describe the techniques to fabricate high mobility graphene devices lying on an atomically flat and clean substrate, namely hexagonal boron nitride (hBN). We begin with the dry transfer technique used to place graphene on hBN. Afterwards, we turn to the van-der Waals transfer technique which allows the encapsulation of graphene in between two flakes of hBN. The graphene is then contacted only at its edge forming one-dimensional contacts. In the course of this chapter, we emphasise various processes used to clean the graphene and, especially, to obtain a good coupling between the graphene and the contacts.

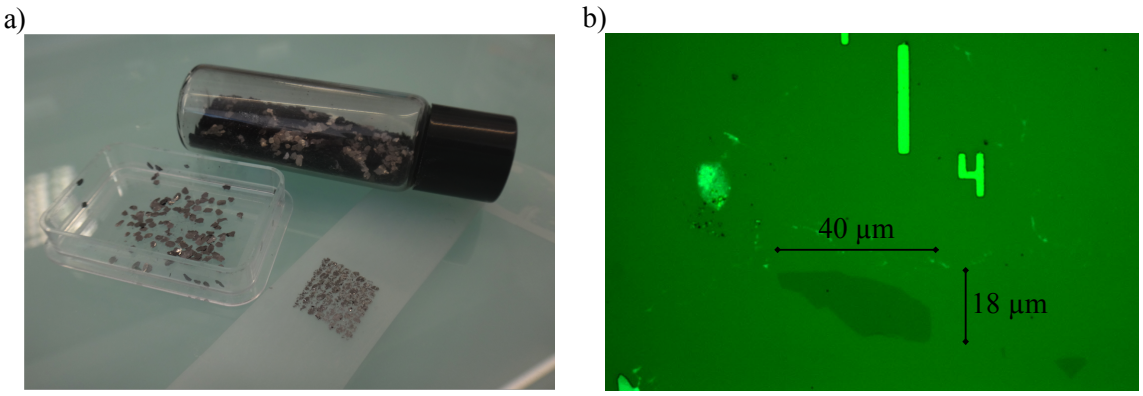

Figure 5.1: a) The tape is repeatedly peeled off that the graphite is cleaved to gradually thinner and thinner layers. It is important that the graphite is homogeneously spread on the tape. b) Large flake of monolayer graphene exfoliated onto SiO_2 and observed with an optical microscope using a green filter for ease the search.

1 Fabrication of graphene on SiO_2

K.S. Novoselov and A.K. Geim were the first one to isolate a single layer of graphene by mechanical exfoliation [1]. Scotch tape was used to gradually cleave a crystal of graphite into thinner and thinner layers.

We have also used the technique of exfoliation to produce monolayers of graphene for our devices. Our method is as follow: We position a flat flake of graphite onto the adhesive side of a half-transparent Scotch magic tape. The piece of tape is then folded and peeled apart several times until the graphite is homogeneously spread on the tape as presented in Fig. 5.1. The tape is placed onto a clean substrate. We do not apply any direct pressure onto the surface but rather stroke it lightly with a flat edge of, for instance, a pen for 2 min. The tape is, then, peeled off at a small angle.

With this technique of light pressure, we minimise the amount of glue on the substrate and obtain large, pristine flakes of graphene up to 30 µm to 40 µm.

In order to fabricate graphene devices, we use highly doped (p++) silicon with a 285 nm thick layer of silicon dioxide (SiO_2) as a substrate which is mostly used for the exfoliation of graphene. One main advantage of this substrate is that a monolayer of graphene is well visible with an optical microscope [99]. However, the roughness of the SiO_2 surface together with randomly distributed charge impurities in the SiO_2 substrates and at the interface of SiO_2-graphene limit the mobility of the graphene.

2 Fabrication of graphene on hBN

Graphene placed on a flake of hexagonal boron nitride (hBN) has proven to have a much higher mobility due to the absence of charge traps in the hBN. In the following, we present the fabrication of graphene on hBN which is based on the dry transfer technique first developed in the group of P. Kim [48].

Exfolation on PMMA

Graphene is exfoliated onto a film of PMMA which itself is placed onto a film of PVA (polyvinyl alcohol) (see Fig. 5.2a). PMMA (poly(methyl methacrylate)) is a polymer

which we usually use as a positive resist for electron-beam lithography. The advantage of using PMMA underneath the graphene is that it can be conveniently removed from the graphene after the transfer with acetone. PVA is a polymer which dissolves in water. By dunking the substrate of PVA/PMMA/graphene into water (see Fig. 5.2b), the PVA dissolves separating the PMMA/graphene from the substrate and leaving it floating on the surface of the water (see Fig. 5.2c). The key is to avoid contact between the graphene and the water.

The floating film of PMMA is caught with a glass slide with a hole in the middle. The PMMA needs to be placed on the glass slide in a way that the graphene is approximately centred above the hole, which poses the biggest challenge of this transfer technique. When the glass slide is turned upside down, the PMMA sticks well to the glass around the hole but above the hole, the PMMA forms a dip. The graphene has to be located at the lowest point of the dip, in order to transfer it without any wrinkles and folding of the graphene.

Transfer

The hBN is exfoliated onto a Si++/SiO_2-substrate. Our hBN crystals are fabricated by K. Watanabe and T. Taniguchi who produce highly pure hBN [100].

Only completely clean and flat flakes (confirmed by atomic force microscopy (AFM) measurements) are used as the underlying substrate of the graphene to ensure surface quality. The substrate with the selected BN flake is placed on a small hotplate.

The glass slide with the film of PMMA and graphene is assembled to a micro-manipulator above the substrate with the BN flake (see Fig. 5.2d). The graphene flake needs to be perfectly aligned to the BN flake before the two flakes are brought into contact.

The hotplate is heat to about 120 °C causing the PMMA film to soften and to wet the surface of the Si++/SiO_2-substrate. By staying at this temperature for at least 15 min the PMMA film becomes so fluid that it remains on the Si++/SiO_2-substrate when the glass slide is lifted up. The graphene transferred onto the BN is still covered by the PMMA which is easily removed by acetone.

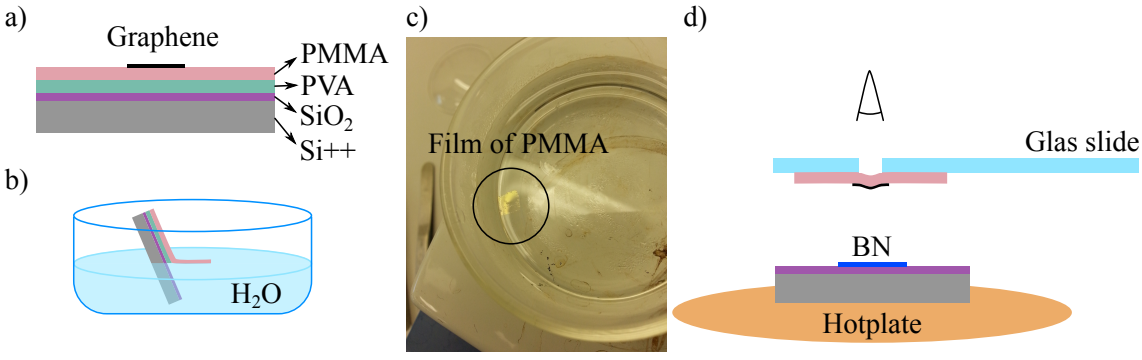

Figure 5.2: Steps of transferring graphene onto hBN. a) PVA and PMMA is spincoated onto a Si++/SiO_2-substrate onto which graphene is exfoliated. b) The PVA dissolves in water separating the film of PMMA/graphene from the substrate. c) The film of PMMA/graphene floats on the surface of the water. d) The PMMA is stuck onto a glass slide such that the graphene is centred above the hole in the slide. The hBN exfoliated onto another Si++/SiO_2-substrate is placed on a small hotplate underneath the glass slide together with the PMMA/graphene. The graphene flake needs to be well aligned to the hBN before bringing them into contact.

Raman spectroscopy

Raman spectroscopy offers a powerful tool to determine the number of graphene layers and to characterise the level of disorder within a graphene flake. Monochromatic light of a laser is focussed onto the graphene. The photons excite atoms, molecules or even sublattices into a different vibrational or rotational state. As a result, inelastically scattered photons of a different frequency than the initial light are emitted and measured by a detector.

The frequency and amount of the measured inelastically scattered photons are specific for the vibrational and rotational modes of each material. We do not go into detail about the complex scattering processes which lead to the individual signatures in the Raman spectrum and only mention the expected frequency shifts.

We performed Raman spectroscopy measurements on the graphene on hBN with a green laser of 532 nm. The resulting Raman shift (frequency shift) is presented in Fig. 5.3 exhibiting three pronounced peaks. A single crystal of hexagonal boron nitride possesses a characteristic peak at about $1367\,\mathrm{cm}^{-1}$ [101, 102] which is well visible in the Raman spectrum of Fig. 5.3.

The two additional peaks G and $2D$ are distinctive for graphene at about $1580\,\mathrm{cm}^{-1}$ and $2700\,\mathrm{cm}^{-1}$, respectively [103]. The shape of the $2D$ peak changes with the number of layers. The single peak with a full width at half maximum of $22\,\mathrm{cm}^{-1}$ confirms the flake to be a monolayer. In bilayer graphene, the $2D$ peak becomes wider ($>40\,\mathrm{cm}^{-1}$) since it is composed of two nearby peaks. Furthermore, the absence of the D at $1350\,\mathrm{cm}^{-1}$ is a good indication that disorder is low at this position within the graphene.

Cleaning the graphene

After the transfer of graphene onto hBN, the graphene is covered by a film of PMMA. The lift-off of the PMMA in acetone leaves residue of resist on the graphene (see Fig. 5.4a).

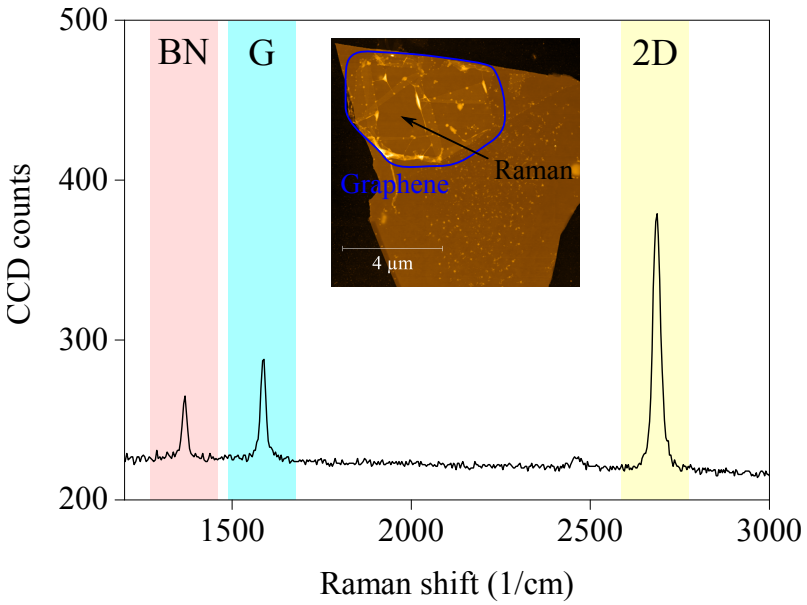

Figure 5.3: Raman spectroscopy of graphene on hBN. The hBN flake leads to a peak at about $1367\,\mathrm{cm}^{-1}$. The two peaks G and $2D$ at about $1580\,\mathrm{cm}^{-1}$ and $2700\,\mathrm{cm}^{-1}$, respectively, are characteristic for graphene.

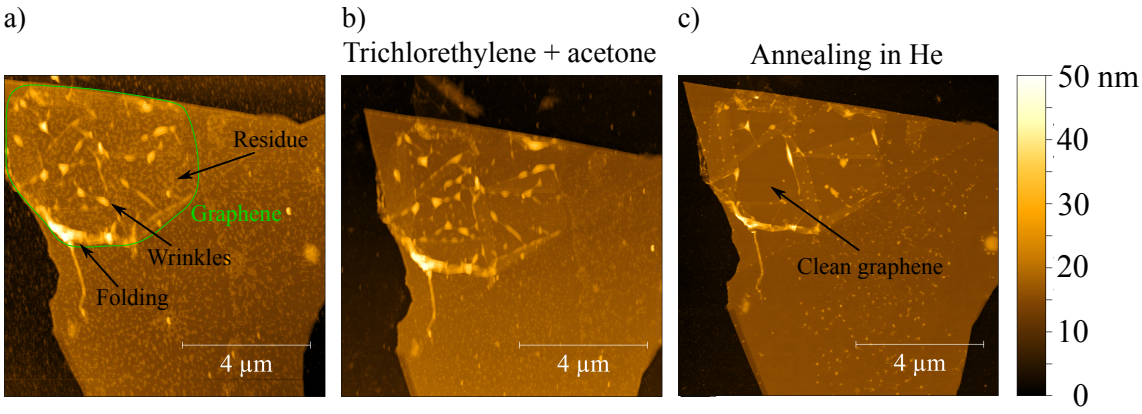

Figure 5.4: Cleaning of graphene on hBN. a) After the lift-off, a lot of residue of resist remains on the surface of the graphene. b) Cleaning with trichlorethylene and acetone (1:1) for 10 min does not remove most of the residue. c) Annealing in He at 350 °C for 30 min removes efficiently the residue of resist.

Within our investigation of different solvents, we found that none cleans the graphene efficiently and reliably. The cleaning, for instance, with trichlorethylene and acetone (1:1) for 10 min removes some residue but the graphene remains fairly dirty (see Fig. 5.4b).

A more efficient method to clean the graphene of residue is to anneal it in high temperature to evaporate and burn the residue of resist. The group of P. Kim, for instance, anneal their graphene devices in an atmosphere of flowing H_2Ar gas at 340 °C for 3.5 h [48].

We annealed the graphene in an atmosphere of Helium[1] at 350 °C for 30 min which appears to be a promising method to remove residue from the surface of graphene (see Fig. 5.4c).

After placing the metal contact by means of electron-beam lithography and metal deposition (an example of a device is presented in Fig. 5.5), a second annealing is required to remove the residue from the preceding treatments. This annealing, however, destroyed the contact to the graphene. At that time, we did not have any oven available

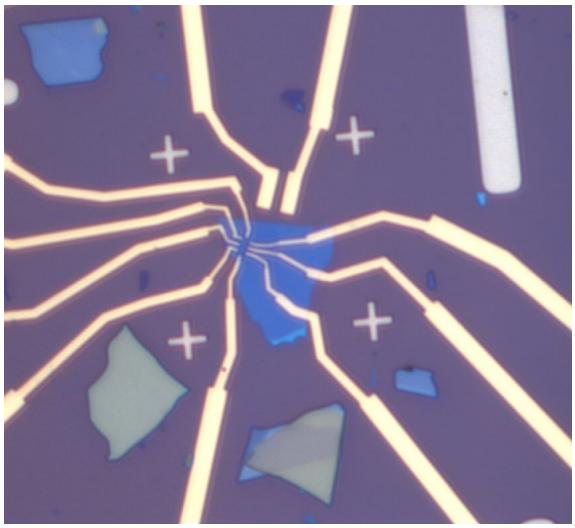

Figure 5.5: Device of a Hall bar of graphene on hBN.

1 Helium gas was the only possibility in our facilities at that time.

to anneal the graphene devices in a different atmosphere or even in vacuum. Therefore, we temporarily stopped the fabrication of graphene on hBN and turned to hBN/graphene/hBN heterostructures.

3 Fabrication of BN-Graphene-BN stacks

In order to fabricate high mobility, ballistic graphene devices, one essential component is, as discussed before, the underlying substrate. However, the level of impurities due to the fabrication process also has an important impact on the quality of the graphene as we have seen in fabricating graphene devices on hBN. The group of P. Kim has developed a transfer technique of encapsulating graphene between two flakes of hBN in a way that the graphene is never exposed to resist or any other chemical treatment [104]. This technique is based on the principle that the van-der-Waals force is stronger between the graphene and the hBN than the adhesion to the SiO_2 substrate. In the following, we present the fabrication technique which we have implemented in our lab.

3.1 Exfoliation and identification

The graphene as well as the hBN are exfoliated on separate SiO_2-substrates with the scotch tape technique. Both materials are optically searched to identity suitable flakes. The hBN flakes up to a thickness of about 50 nm which appear in blue in the optical microscope can be used for the heterostructure devices. The transfer technique works well with thicker flakes but the thicker the hBN flake is, the higher the deposited metal for the contacts has to be and the less efficient becomes the backgate and possible topgates.

A selected number of promising flakes of both graphene and hBN are then scanned by AFM to determine their flatness and cleanliness (examples in Fig. 5.6). Only atomically flat hBN flakes without any clear crystallographic imperfections and steps are usable for the transfer. The larger of the two selected hBN flakes is used as the bottom hBN. Most important is that both hBN flakes are larger than the graphene flake so that the graphene becomes fully protected. If, for instance, the top hBN is smaller than the graphene flake, the part of the graphene which is not covered by the hBN, will either stay behind on the substrate or get folded forming multilayer graphene.

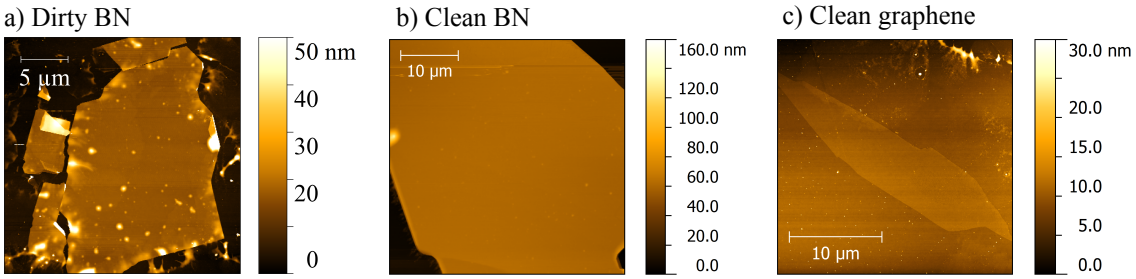

Figure 5.6: AFM images of flakes of hBN and graphene to determine their cleanliness and flatness of each flake. a) Dirty hBN flake b) Clean hBN flake c) Clean graphene flake

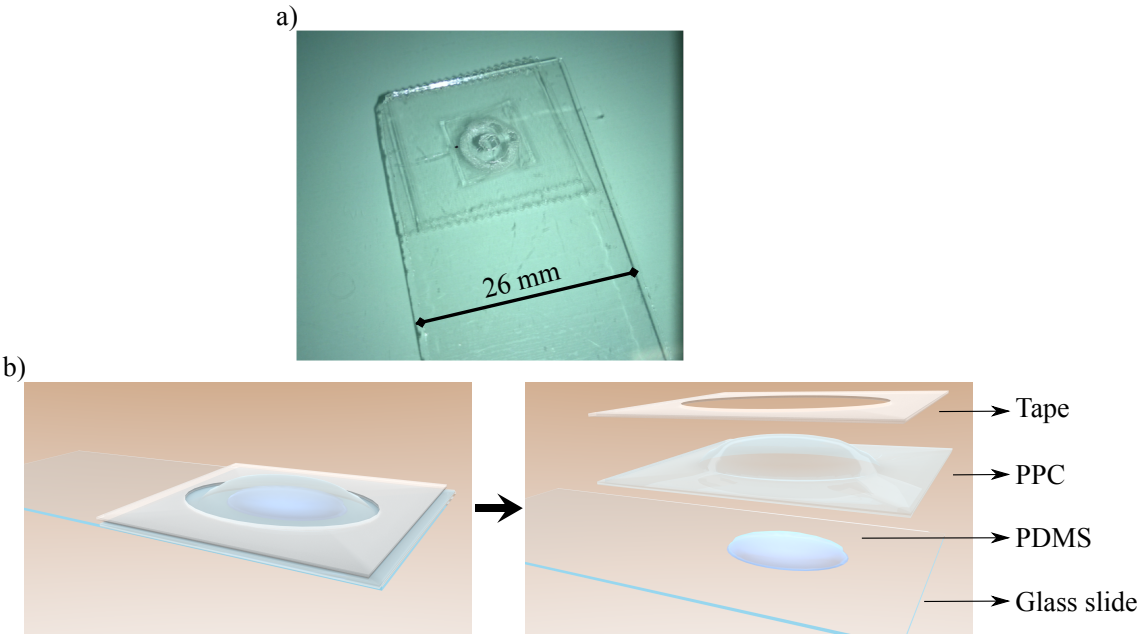

Figure 5.7: a) Photo of a stamp on a glass slide. b) Composition of the stamp used for the transfer: On a glass slide, a square of transparent PDMS of the shape of a dome is placed. On top of it, a film of PPC is stuck by a transparent tape with a hole to the glass slide.

3.2 Transfer and stack-building

3.2.1 Stamp

The stamp for the pick-up transfer is prepared on a glass slide presented in Fig. 5.7. A small square of about 1 mm^3 of transparent PDMS (polydimethylsiloxane) is glued on one side of the glass slide with a transparent tape and shaped in the form of a dome. A film of PPC (polypropylene carbonate), a transparent polymer, is stuck with a transparent tape on top of the dome shaped PDMS. It is crucial that the tape has a hole in the centre of the PPC above the PDMS that the PPC can touch the surface of the substrate.

3.2.2 Transfer set-up

The first set-up which we assembled to fabricate encapsulated graphene is presented in Fig. 5.8. The glass slide is mounted on a long cantilever which is itself screwed onto a micro manipulator allowing to adjust its position within a precision of less than 1 µm. The substrate is glued with water glue onto a small home-made hotplate whose temperature can be adjusted by 1 °C and has a maximum temperature of 130 °C.

The hotplate with the substrate are placed under an optical microscope. A magnification of 10x to 50x is used during the transfer. By adjusting the height of the cantilever and the optical table, both the PPC and the substrate are brought into focus which is most useful to align flake to one another.

One disadvantage of this set-up was that it is highly sensitive to vibrations. Touching the table or a person walking by may shake the set-up so strong that the stack is ruined.

In the course of this thesis, we have designed a new set-up with Didier Dufeu and Laetitia Marty (Institute Néel) which is completely dedicated and, therefore, well adapted to the transfer of flakes and fabrication of stacks. Fig. 5.9 presents our new set-up which includes

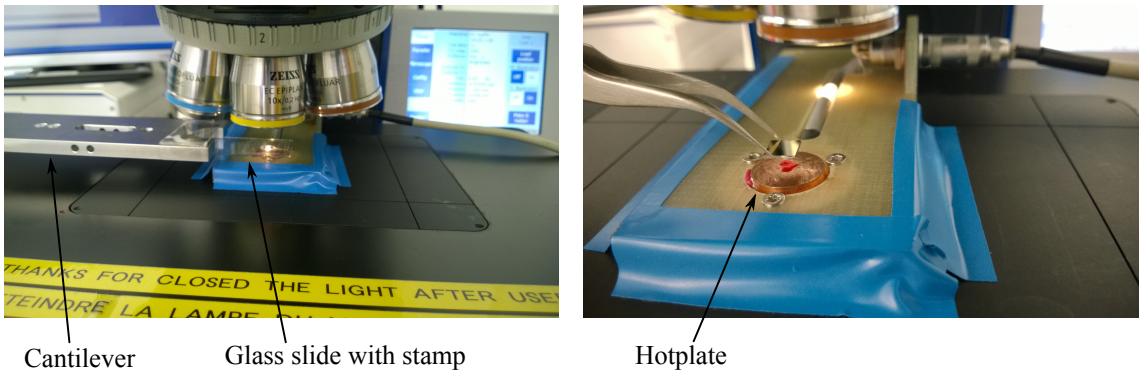

Figure 5.8: First set-up for the fabrication of stacks. The glass slide of the stamp is fixed on a long cantilever which itself is mounted on a micromanipulator. The substrate is glued onto a small hotplate.

the microscope, micromanipulator and the sample holder.

The table where the new set-up is placed is insensitive to vibrations in the room which improves the stability of the set-up during the transfer. The glass slide is directly fixed on the micromanipulator avoiding any cantilever which introduces additional vibrations. The sample is placed on a piezoelectric XYZ stage allowing nanometer scale positioning.

Another essential improvement is that the focus of the microscope is adjusted by changing its height. Therefore, changing the focus from the glass slide to the substrate, only the height of the microscope is modified and both the glass slide and the substrate do not need to be touched.

The custom designed sample holder of a diameter of 2” is capable of heating up to 180 °C in steps of 0.1 °C and to cool down with a flow of nitrogen gaz. The sample is stuck to the holder with a vacuum pump allowing to avoid pollution of the substrate with glue.

3.2.3 Pick-up of the first hBN flake

The substrate with the selected first hBN flake which will serve as the top flake is glued onto the small hot plate since its temperature needs to be steadily adjusted during the transfer.

The prepared stamp is inverted and fixed onto the long cantilever The domed shape of the stamp cause the PPC to touch the surface of the substrate only in a small area. The touching point is positioned to be directly next to the selected hBN flake (Fig. 5.10a). The PPC is sticky at about 40 °C. By bringing the PPC in contact with the substrate and heating up the substrate and with that indirectly the PPC, it starts to flow with increasing temperature and wet the surface (Fig. 5.10b). Once the hBN flake is completely covered by the PPC, we turn down the heater to 40 °C and, once it is cooled down, move the stamp and the sample apart. The hBN flake remains stuck to the PPC and is, therefore, picked up with the stamp (Fig. 5.10c).

3.2.4 Pick-up of the graphene flake

In the next step, the graphene flake will be picked up (Fig. 5.10d). The substrate with the graphene flake is placed on the small heater below the stamp on which still the first hBN flake sticks (Fig. 5.10e). The graphene needs to be well aligned to the hBN before they are brought in contact by again heating up the substrate and, hence, the PPC. Once the

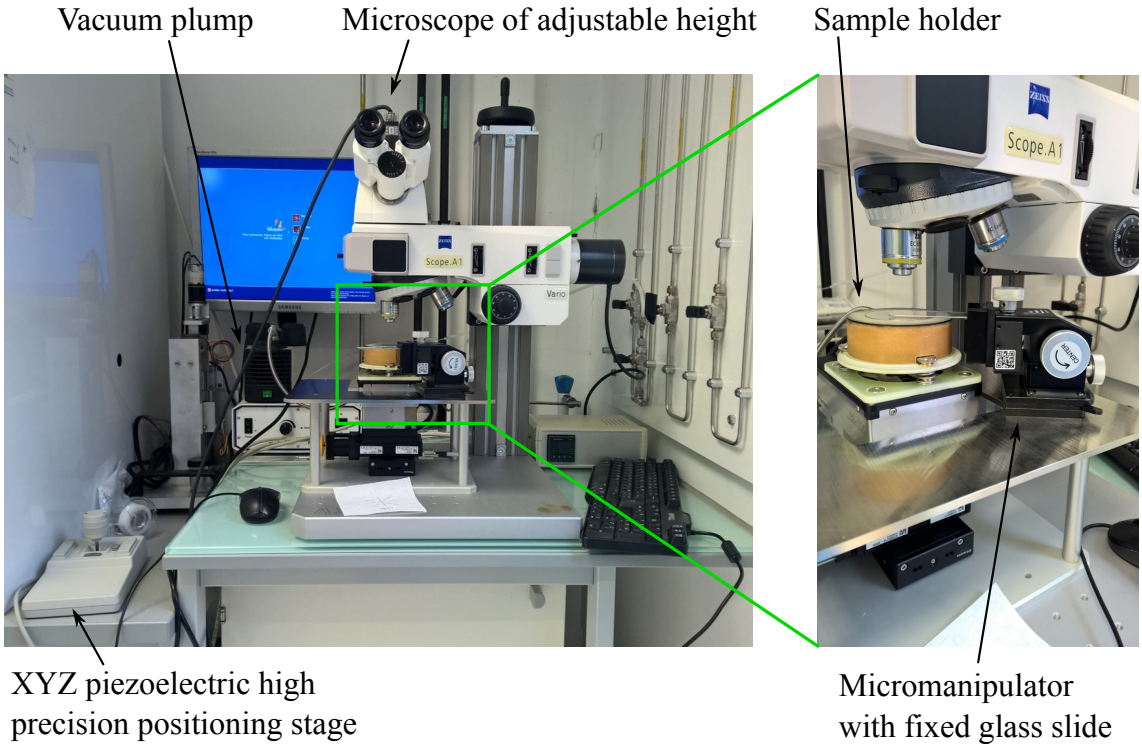

Figure 5.9: New set-up dedicated to the fabrication of heterostructures.

flow of the PPC covers the hBN and graphene, the substrate is cooled down and separated from the stamp. Due to van-der-Waals forces, the graphene sticks to the hBN rather than to the SiO_2 substrate (Fig. 5.10f).

3.2.5 Lowering onto the second hBN flake

At this point, we have already picked-up the top hBN and the graphene flake which stick to the stamp. In the last step, this structure is put down onto the second hBN which serves as the bottom flake. The substrate of the second hBN flake is placed on the heater below the stamp (Fig. 5.10g). This time, the PPC is not only heated up until the flakes are wetted but that the wetting edge of the PPC extends far away from the BN-graphene-BN heterostructure. When the substrate is lowered, two possible scenarios of releasing the stack of BN-graphene-BN. First, the soft PPC tears apart at the edge of the contact area where it has become thin which leaves behind a film of PPC on the stack. Second, the PPC peels of completely leaving behind the BN-graphene-BN heterostructure (Fig. 5.10i). The complete BN-graphene-BN stack is presented in Fig. 5.10j.

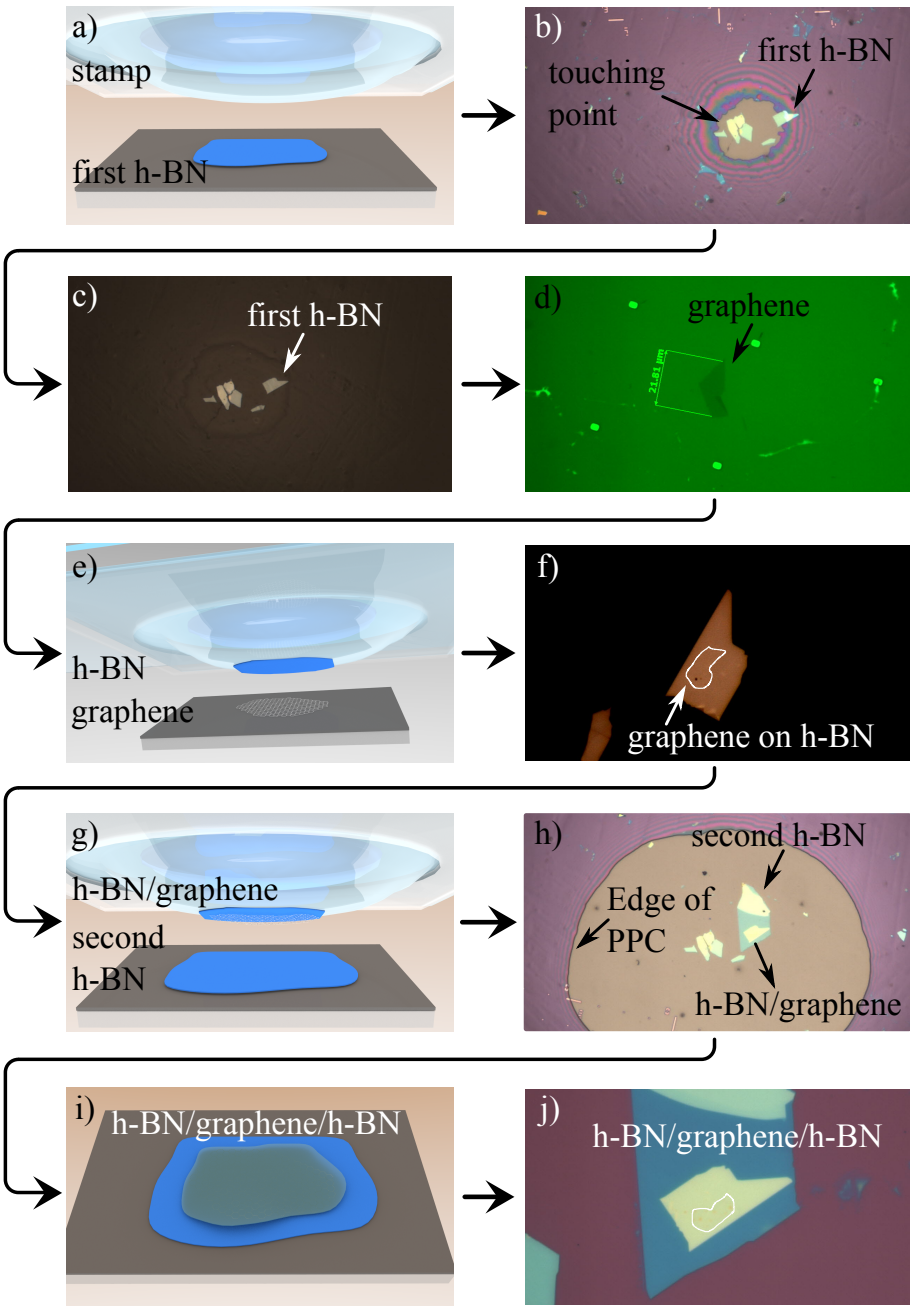

Figure 5.10: Fabrication steps of BN-graphene-BN heterostructure. a) First hBN flake is placed below the stamp. b) The PPC touching the substrate starts to flow by heating. c) Separating the stamp from the substrate, the hBN flake sticks to the PPC (image through the stamp). d) Graphene flake. e) The substrate of the graphene flake is placed below the stamp. f) Due to van-der-Waals force, the graphene sticks rather to the hBN than to the SiO_2 substrate (white line = graphene). g) The substrate of the second hBN is placed below the stamp. h) After bringing the hBN-graphene into contact to the second hBN, the PPC is heated up that the edge of the touching point is far away from the heterostructure. i) BN-graphene-BN heterostructure. j) The BN-graphene-BN stack will become the device of the high-mobility quantum point contact.

4 One-dimensional contacts

The challenge of contacting encapsulated graphene between the two hBN flakes was likewise achieved by the group of P. Kim [104]. We discuss briefly the process of exposing the graphene edge and depositing contacts.

4.1 Alignment with a field of markers

The exfoliation of hBN and graphene leads to randomly distributed flakes on the substrate. In order to perform an electron-beam lithography and place contacts on a flake, its position needs to be precisely defined. Therefore, we have developed a markerfield to determine the position of each flake on the substrate.

An overview of the markerfield is presented in Fig. 5.11a. The field of markers is determined by a number coding reflecting each horizontal and vertical position within the full substrate. A grid of $x - y$ coordinates is separated by 200 µm and subdivided by additional dots spaced by 50 µm. This markerfied allows precise alignment of optical images for further lithography steps (see Fig. 5.11b).

In the first step of performing an electron-beam lithography, in order to prepare a design, photos of the stack are aligned to the underlying markers (see Fig. 5.11c). Therefore, the exact position and dimensions of the stack are implemented into the design. To recover its position during the electron-beam lithography, the large circles, the horizontal and vertical lines and the small dots are used for the automatic and manual alignment of the electron beam and the stage with our substrate to the design.

4.2 Etching

In order to access the graphene's edge, the hBN is plasma etched revealing a one-dimensional graphene edge. Therefore, the stack needs to be protected at the positions where it should not be attacked. We spin coat an 80 nm layer of HSQ resist (hydrogen silesquioxane) which, once exposed by standard electron beam lithography and developed with MF26, turns into a silica-like material and can only be removed by HF (hydrofluoric acid). To avoid this acid for the lift-off, we spin coat a layer of thin PMMA (polymethylmethacrylat) below

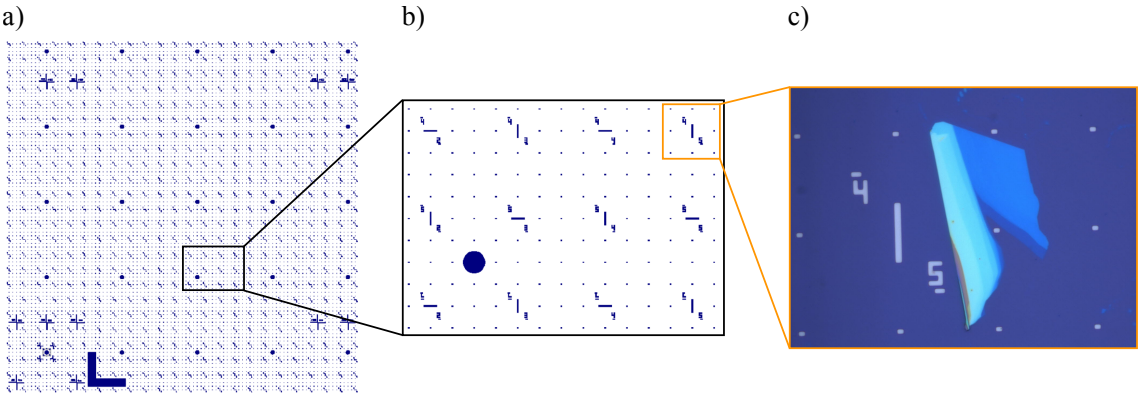

Figure 5.11: a) A field of markers allows to define the precise location and dimension of a stack within the substrate which is essential for electron-beam lithography. b) Each pair of numbers represents the number of the column and line within the field of markers. The small dots are relevant for an even more precise location. c) The location and dimension of the stack is defined within the field of markers.

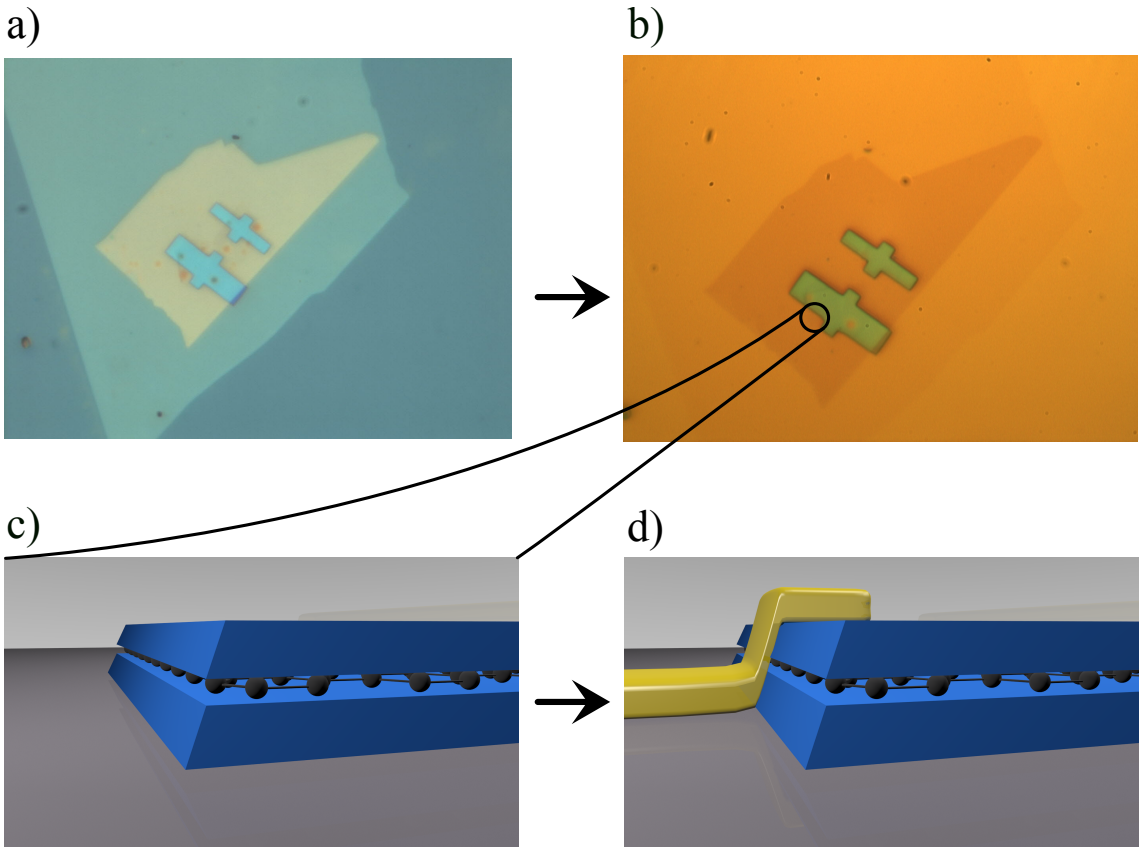

Figure 5.12: Images of the etching and contacting a BN-graphene-BN stack. a) A mask of the bilayer PMMA/HSQ protects the BN-graphene-BN stack from being plasma etched. b) The plasma etches the stack outside of the mask which is, then, lifted off in acetone. c) A small angle arises at the border of the stack which ensures a better contact between the graphene and the metal. d) After a second e-beam lithography, the metal side contact are deposited.

the HSQ. The bilayer of PMMA/HSQ can then be easily lifted-off with acetone.

As a negative resist, the HSQ stays during the development where it is exposed (Fig. 5.12a). Afterwards, the stack is etched with a rate of about $25\,\mathrm{nm\,min^{-1}}$ in a plasma mixture of O_2 and CHF_3. After the lift-off in acetone, the stack with fully accessible graphene edges is ready for e-beam lithography to deposit the metal contacts (Fig. 5.12b).

The group of P. Kim determined that during the plasma etching, a small angle arises at the etched borders of the hBN (Fig. 5.12c). This small angle is crucial to achieve an electric coupling between the metal contacts and the graphene. There are two ways to generate an angle during the etching. First, if the atmosphere of the plasma etch contains polymerised ingredients such as CF_x, they are deposited on the edges of the HSQ resist. Therefore, during the course of etching the stack, the HSQ mask grows, reducing the exposed hBN surface and, hence, introducing an angle into the etched stack. The O_2 plasma removes the polymer of CF_x leaving behind the required angle at the border of the stack. Second, the plasma etches the mask laterally which then becomes increasingly smaller during the etching process resulting in an angled border of the stack. Which of these two procedures apply to our form of plasma etching remains unclear.

4.3 High dose electron-beam lithography

After etching the stack, a second electron-beam lithography is performed for depositing the contacts to the graphene. We have observed that the resist PMMA 4 % used for electron-beam lithography, leaves a lot of residue behind on the graphene. Even after a lift-off in acetone, traces of PMMA remain on the graphene as we see on the graphene on SiO_2 in Fig. 5.13a).

An electron-beam lithography on PMMA with the usual dose of 250 µC cm^{-2} and the suitable development in a mixture of MIBK (methyl isobutyl ketone) and IPA (2-Propanol) leaves a lot of residue of resist in the tranches in which the contacts are placed (see Fig. 5.13b). Especially on graphene, the amount of residue is not negligible which would add a barrier between the graphene and the contacts. In order to get rid of the residue of resist, we employed the following strategy: We heavily overdosed the PMMA to maximise the cracking of the polymers of the exposed PMMA. Therefore, we use a three times higher dose than standard. Due to the larger proximity effect with higher dose, a weaker development is required. Therefore, we develop our devices in a mixture of IPA and deionised (DI) water (3:1) for 1.5 min at 4 °C. We observe that the graphene is much cleaner which leads to a better transmission to the contacts (see Fig. 5.13c).

After the development, the metal side contacts are deposited (Fig. 5.12d). The thickness of the deposited metal has to be higher than the full height of the stack to ensure a good coupling to the graphene. It is worth emphasising that the graphene is contacted only at its edge to the metal resulting in 1-dimensional contacts.

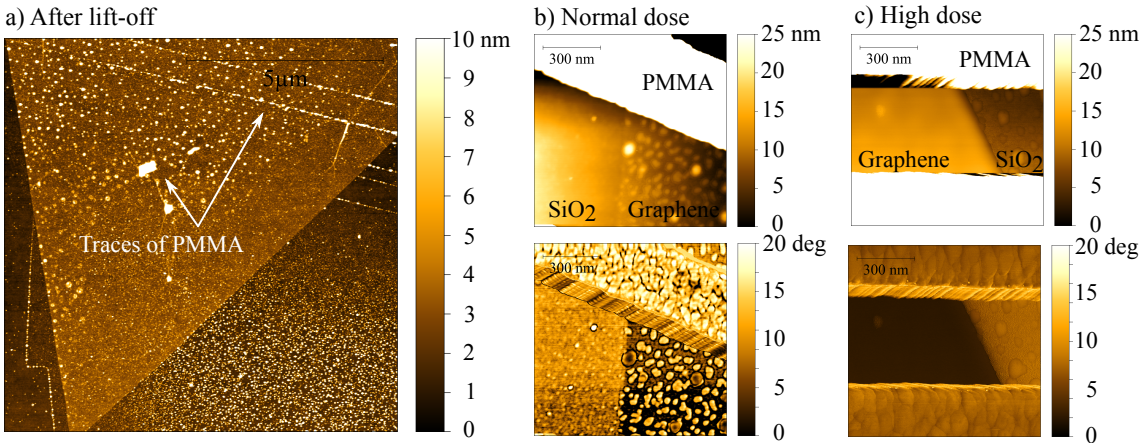

Figure 5.13: a) Even after a lift-off in acetone, residue of PMMA is left on the surface of graphene. b) An electron-beam lithography on PMMA 4 % with the usual dose of 250 µC cm^{-2} and the development in MIBK/IPA leaves a lot of residue behind on the graphene (AFM images: upper image is the topography and lower image is the phase). c) An electron-beam lithography with a three times higher dose and a development in IPA/DI water leads to a much cleaner surface of the graphene (AFM images: upper image is the topography and lower image is the phase).

5 QPC Devices

The main focus of this thesis is on devices of encapsulated graphene equipped with quantum point contacts which we present in the following.

We further process the BN-graphene-BN stack presented in Fig. 5.10j whose top hBN flake has a height of 32 nm and the bottom one of 17 nm. After a first e-beam lithography, the stack is etched in O_2 and CHF_3 plasma for 2 min. After a second e-beam lithography, six metal side contacts of Cr (10 nm), Au (95 nm) and Pt (5 nm) in the form of a Hall bar are deposited in an e-beam evaporator.

Another important advantage of the top hBN flake is that a BN flake provides an excellent insulating layer between the graphene and the topgate. The topgate in the form of a quantum point contact (QPC) is directly deposited on the top hBN in the same step as the metal contacts.

In total, we have fabricated three devices of encapsulated graphene equipped with QPC. We will present the transport properties of these high quality devices in the next chapter.

Summary

In this chapter, we described the transfer technique used to place graphene on hBN. In this process, the graphene is directly in contact with resist making it dirty. We have tested many procedures to clean the graphene afterwards and found the annealing at 350 °C the most efficient.

In the second part of this chapter, we described the van-der Waals dry transfer technique used to fabricate clean encapsulated graphene heterostructures. The graphene is then coupled to 1D side contacts which are deposited after a high dose electron-beam lithography and cold development to avoid residue of resist in between the graphene and the metal contact.

In the last part, we introduced our devices of encapsulated graphene of the form of a Hall bar equipped with a QPC whose transport properties in zero and low magnetic fields as well as in the QH regime, we will study in the next chapter. In the seventh chapter, we will investigate the influence of the QPC on the propagating quantum Hall edge channels.

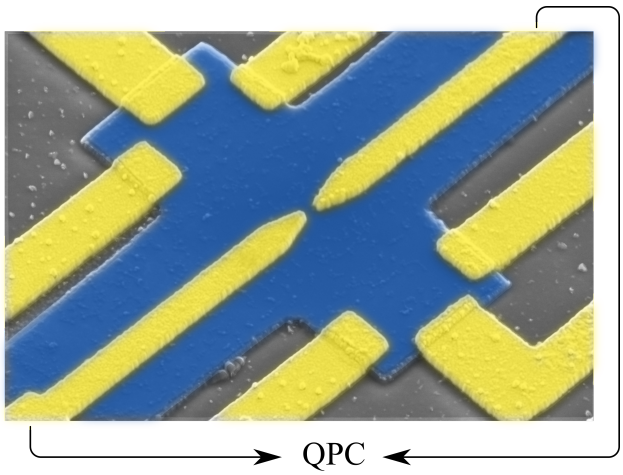

Figure 5.14: False-coloured SEM image of the encapsulated graphene device equipped with a quantum point contact. The top hBN flake is coloured in blue and the contacts are draw in yellow.

CHAPTER 6

BALLISTIC TRANSPORT AND QUANTUM HALL EFFECT IN HIGH-MOBILITY GRAPHENE DEVICES

The fascinating physics of the relativistic quantum Hall effect in graphene depends highly on the quality of the device. This "quality" is quantified in the mobility or mean free path which characterises the amount of scattering centres of, for instance, impurities and lattice vibrations. The mean free path l_e describes the distance between elastic scattering centres that cause a change of the initial electron momentum. If l_e is much larger than the length of the sample L, the electron motion is ballistic otherwise it is diffusive.

In the course of this chapter, we explore the transport properties in the ballistic regime. We focus on characterising device A09 which is a hBN-graphene-hBN heterostructure patterned in a Hall bar, equipped with split gates forming a quantum point contact (QPC). A 3D sketch of the device is presented in Fig. 6.1.

We analyse the transport properties of the graphene device **without regarding the QPC**: The split gates are kept floating. The properties of the QPC will be considered in detail in the next chapter. The high quality of the graphene encapsulated between two flakes of hBN is apparent in the high mobility of about $250\,000\,\mathrm{cm\,V^{-2}\,s^{-1}}$ and mean free path of about 1.8 µm which corresponds to the distance between neighbouring contacts. We detect signatures of ballistic transport such as focusing and zero four-terminal resistance at zero and low magnetic fields which we describe in the following. In addition, we discuss the full symmetry breaking of the quantum Hall states and present in detail the observed fractional plateaus.

We will compare the transport properties of A09 with a graphene Hall bar device on SiO_2 (A07).

1 Introduction to the experimental set-up

Measurements were conducted either in a liquid helium bath at 4.2 K or in a dilution ^{3}He-^{4}He cryostat with a base temperature of 0.05 K. The refrigerator is equipped with a superconducting coil generating a magnetic field of up to 15.5 T. Both current and voltage have been measured by standard lock-in techniques with a current bias of 1 nA to 10 nA or a voltage bias of 2 µV to 30 µV at about 17 Hz.

We measured resistances in three different configurations. The numbers on the six contacts in Fig. 6.1 help to specify the measurement configuration. The index of $R_{ij,kl}$ signifies that the current flows from the contacts j to i while the voltage is measured between the contacts k and l.

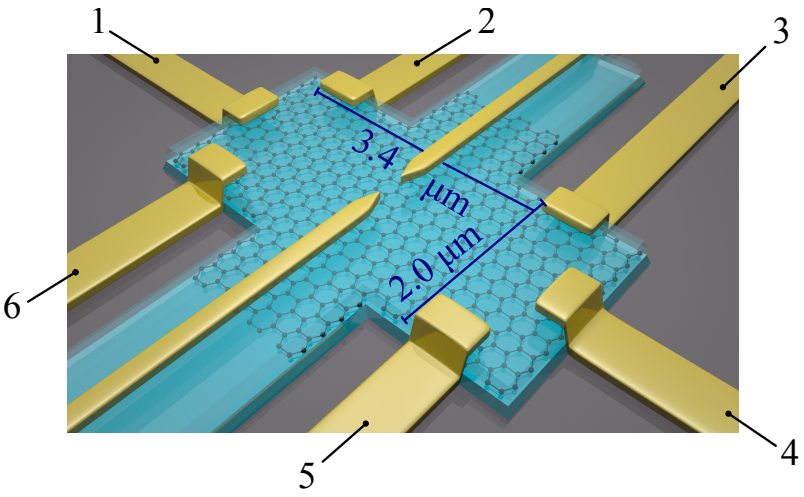

Figure 6.1: 3D model of our QPC device A09 of BN-graphene-BN heterostructure. The numbers index the six contacts to specify each resistance presented within this chapter.

2 Transport properties of high-mobility graphene

2.1 Substrate induced disorder

The transport properties of a graphene flake depend highly on the underlying substrate. The field effect curve of the sheet resistance $R_{xx} = R_{14,23}$ versus backgate voltage V_{bg} for the encapsulated graphene device A09 and, for comparison, a graphene device on SiO_2 is presented in Fig. 6.2.

R_{xx} is measured in four-probe configuration to eliminate the contact resistances. Both curves of encapsulated graphene and graphene on SiO_2 are shifted with respect to the charge neutrality point V_{bg}^{CNP} in order to centre the Dirac peak at zero voltage. We notice that the resistance peak of the encapsulated graphene is much steeper and narrower than the one of the SiO_2 device which indicates its much higher mobility.

The sharpness of the maximum of the resistance peak quantifies the potential fluctuations of the electrons within the graphene. Its quantity provides an order of magnitude of the residual charge carrier inhomogeneities n^* which can be obtained from a logarithmic plot of the longitudinal conductance G_{xx} versus the charge carrier density n (Fig. 6.2b). In the plot of $\log(G_{xx})$ versus $\log(n)$, n^* represents the crossing point between the constant value of $\log(G_{xx})$ at low carrier density and the linear fit of $\log(G_{xx})$ at high carrier density where we observe a linear relation of $\log(G_{xx})$ to $\log(n)$.

We realise that we cannot precisely fit the constant value of $\log(G_{xx})$ at low carrier density since the resolution of data points is not sufficient around the Dirac peak. Additionally, for both linear fits of $\log(G_{xx})$ at low and high carrier density, the resistance peak needs to be symmetric around the charge neutrality point and its maximum to be well defined. For the sample A09, we observe that the resistance peak is slightly asymmetric making

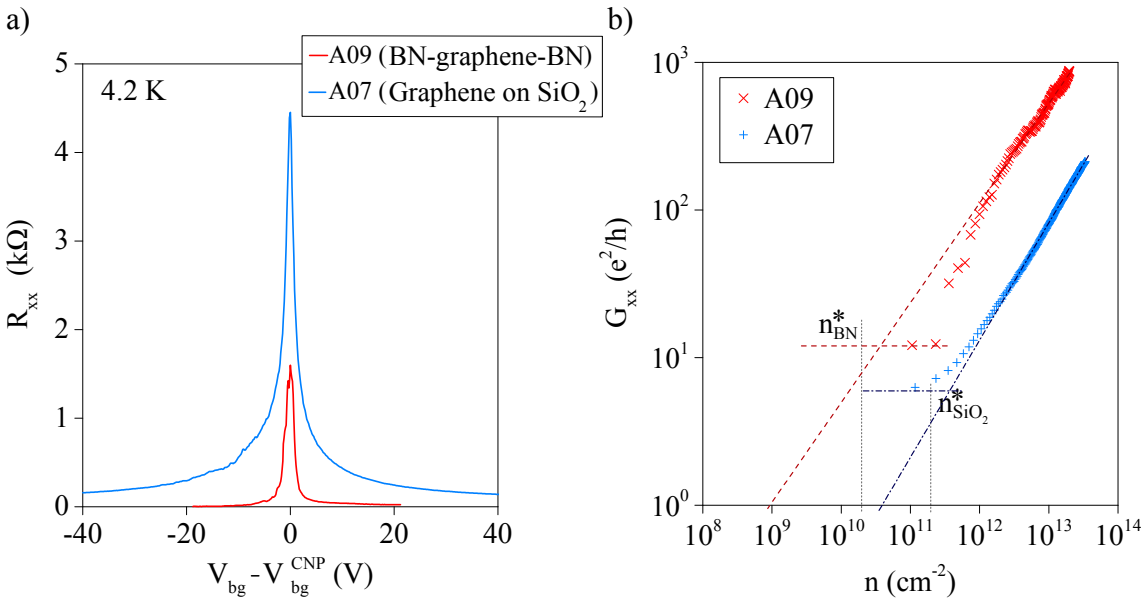

Figure 6.2: a) Electric field effect curve of device A09 (encapsulated graphene) (red) and, for comparison, of device A07 (graphene on SiO_2) (blue) at zero magnetic fields and at 4.2 K. The Dirac peak of A09 is narrower with a steeper slop than for the A07. b) Log-log plot of the longitudinal conductance G_{xx} as a function of the charge carrier density n for both devices A09 and A07.

it difficult to determine the shift V_{bg}^{CNP} precisely. A small change in the value of V_{bg}^{CNP} would modify the slope at high density and, therefore, result in a different value of n^*.

Hence, we need to take the obtained values of n^* for both samples with caution and assume them to be an estimation to compare their different orders of magnitude. We obtained for the sample A09 of encapsulated graphene a value of $n^*_{BN} \simeq 4 \times 10^{10}\,\mathrm{cm}^{-2}$ which is in comparison to $n^*_{SiO_2} \simeq 4 \times 10^{11}\,\mathrm{cm}^{-2}$ of graphene on SiO_2 one order of magnitude smaller. This estimation reflects the lower disorder density of encapsulated graphene.

2.2 Zero four-terminal resistance state

If we take a closer look at the hole-side of the field effect curve of A09 in Fig. 6.2, we observe a surprising feature: The longitudinal resistance drops to zero as shown in Fig. 6.3. This zero resistance is systematic in all measured field effect curves. Let us in the following understand the origin of this zero resistance.

We have seen in the first chapter (sect. 1.1.3.1) that zero resistance in a four-terminal configuration can be a manifestation of ballistic transport, when the electrochemical potential stays constant between the current leads. The potential drops only at the contacts taking the value of the potential of the corresponding reservoirs μ_L or μ_R. In microscopic devices, the side contacts used to measure the voltage drop are invasive, introducing scattering centres which cause a drop of the chemical potential at these contacts (upper example in Fig. 6.3b). By reducing the transparency of the side contacts to the graphene, the influence of the contacts on the potential within the conductor becomes smaller. If, for instance, contact transparency is low, the influence of the side contacts

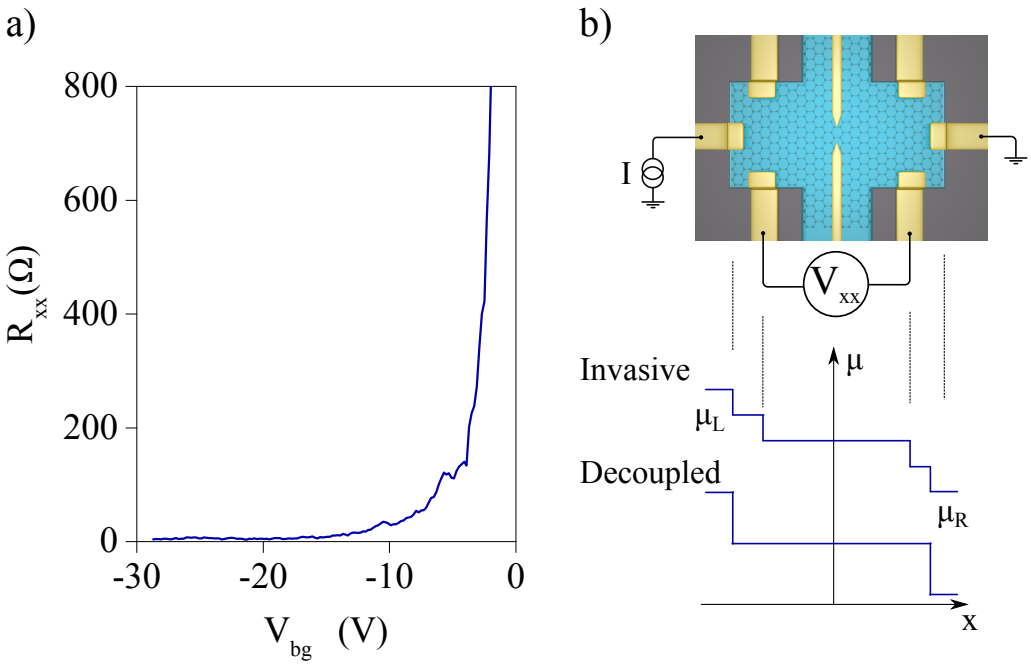

Figure 6.3: a) Zero four terminal resistance in the hole-doped regime of the field effect curve of the longitudinal resistance as a function of the backgate. b) The strength of the transparency between the voltage probes and the conductor influences the electrochemical potential within the conductor. In one case, invasive contacts cause a drop of the potential at them. In the other, decoupled side contacts do not change the potential leading to a zero resistance state.

becomes negligible (lower example in Fig. 6.3b). The potential stays constant along the conductor leading to a zero four-terminal resistance.

We will see in the next section that the side contacts of the encapsulated graphene device are not well coupled to the graphene on the hole-side for which reason, the potential drop is minimal at them. Interestingly, all of our contacts show identical low transmission on the hole side. Therefore, our interpretation of the observed zero resistance state on the hole side is that of a ballistic conductor with weakly coupled voltage probes. A zero-resistance state has already been observed by the group of R. de Picciotto in a ballistic quantum wire [105].

2.3 Asymmetrical contact resistance

In contrast to the four-terminal configuration, which only measures the resistance of the bulk graphene, the two-terminal configuration also includes the contact resistance of the graphene-metal interface. Fig. 6.4a presents the 2-terminal resistance as a function of the backgate voltage in which an asymmetry between the electron- and hole-side is apparent. The contact resistance can be estimated by comparing the sheet resistance of the 4-terminal configuration with the two-terminal resistance. In Fig. 6.4b we present the contact resistance normalised by the width of the contact. We see that the contact resistance on the hole-side is more than twice that of the electron-side.

This observed electron-hole asymmetry may be caused by the charge transfer from the metallic contact to the graphene due to a mismatch of the work functions between the two [106]. Therefore, the charge carrier density is modified in vicinity of the metal contacts where the graphene is doped differently than in the bulk. Depending on the deposited metal, a *pn*-junction and accordingly a *pp′*-junction[1] can emerge. This induced potential

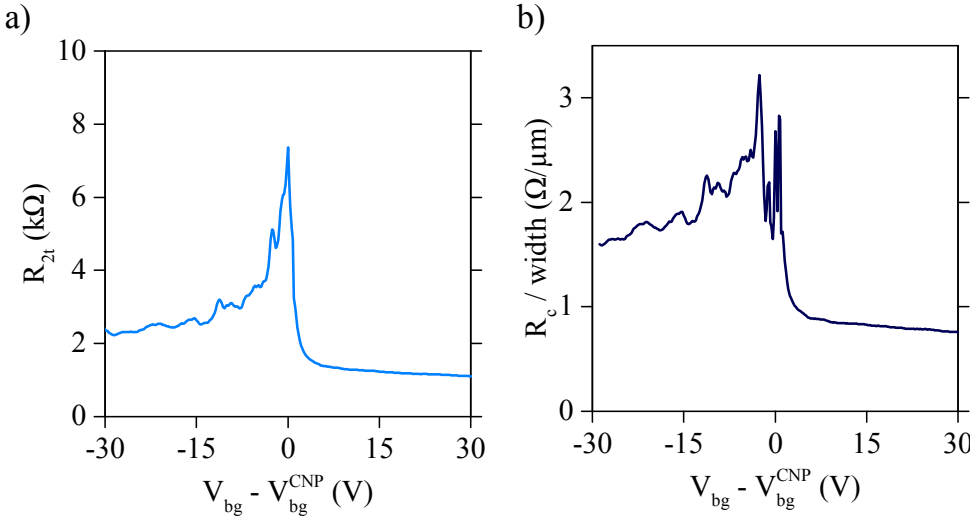

Figure 6.4: a) The 2-terminal resistance as a function of the backgate voltage features an asymmetry between electron and holes. b) The contact resistance as a function of the backgate is estimated by subtracting the 4-terminal sheet resistance from the 2-terminal resistance. The electron-hole asymmetry is apparent in R_c which is at least twice as high on the hole-side than on the electron-side.

1 or *nn′*-junction, whichever polarity is present in the graphene bulk

step yields an additional resistance. The height of the potential step depends on the strength of the doping and the length over which the carrier density is influenced [106, 107].

2.4 Transport characteristics

Hall measurements in low magnetic fields allow us to extract the mobility μ, the mean free path l_e and the charge carrier density n_b where the b stands for the bulk. This notation allows to distinguish from other local density, for instance, beneath the split gates which will be involved later on with the QPC. In the following, we make use of the standard analysis which is essential later to determine precisely the filling factors in the quantum Hall regime.

The transverse resistance $R_{xy} = R_{14,26}$ where the current flows from the contacts 1 to 4 while the voltage is measured between the contacts 2 and 6, is plotted as a function of the backgate voltage at various magnetic fields in Fig. 6.5a. The sign of R_{xy} depends on the polarity of the charge carriers. In the inset of Fig. 6.5a, we already observe quantum Hall plateaus at 0.6 T.

The linear behaviour of the Hall effect in B is evident in Fig. 6.5b and allows us to extract the carrier density and to calculate the capacitance of the backgate.

We derive n_b and obtain its backgate dependence presented in Fig. 6.6a. The expected linear behaviour is visible on the electron-side while the transmission of the contacts is lower on the hole-side as we have seen in the previous section, resulting in deviations of the linear dependence of n_b to V_{bg}.

The slope of the n_b-V_{bg}-curve of Fig. 6.6a is directly proportional to the geometrical capacitance formed between the graphene and the backgate:

$$C_{bg} = \frac{en_b}{V_{bg} - V_{bg}^{CNP}}$$

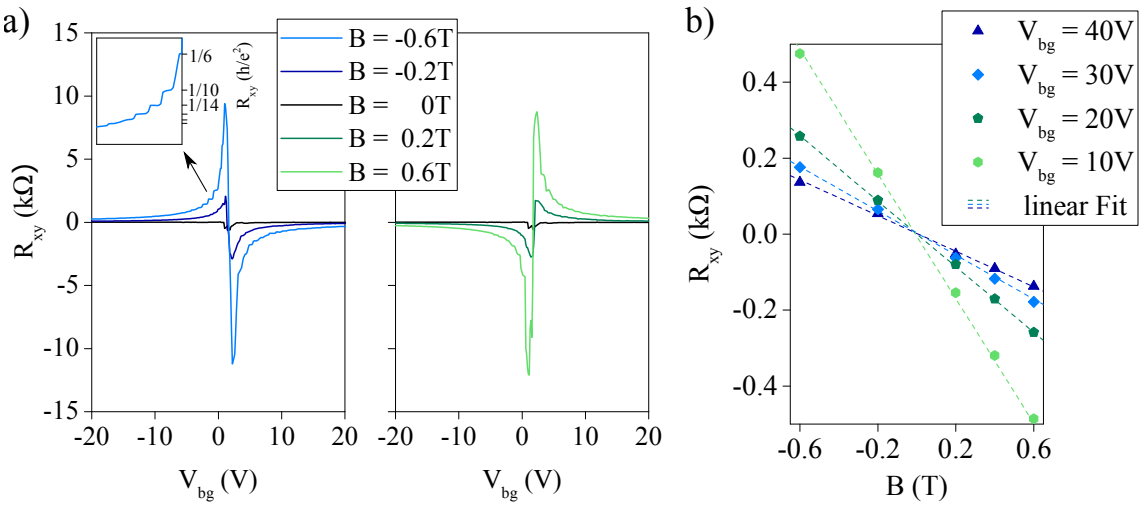

Figure 6.5: a) The transverse resistance R_{xy} plotted as a function of the backgate V_{bg} increases with increasing magnetic fields B measured at 0.05 K. Inset: Zoom on the curve at 0.6 T to emphasis the already visible quantum Hall plateaus. b) R_{xy} increases linearly with B. Its slope is inversely proportional to the charge carrier density which decreases approaching the CNP leading to an increase of the slope.

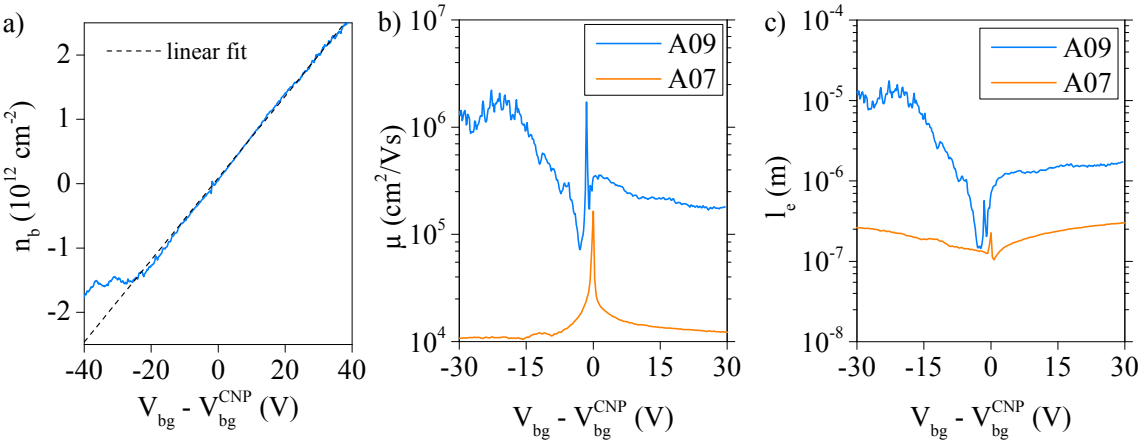

Figure 6.6: Transport characteristics of A09. a) Charge carrier density as a function of the backgate V_{bg}. The curve on the electron-side is fitted with a linear slope which is proportional to the capacitance C_{bg}. b) Mobility μ calculated from (6.1) as a function of V_{bg}. The mobility of A09 is one order of magnitude higher than in the A07 device (graphene on SiO_2) c) Mean free path l_e obtained from (6.2) as a function of V_{bg}. The mean free path in A09 is almost one order of magnitude higher than in A07.

allowing us to estimate the capacitance of the bottom BN flake. We obtain for the total geometrical capacitance a value of 11.1 nF cm^{-2} which includes the capacitance of both the bottom BN flake of 17 nm and the 285 nm thick SiO_2. The geometrical capacitance $C_{bg} = \frac{\varepsilon_0 \varepsilon_r}{d}$ of SiO_2 with a relative permittivity $\varepsilon_r^{SiO_2} = 3.9$ is $C^{SiO_2} = 12.1\,\mathrm{nF\,cm^{-2}}$. From the serial connection of two capacitors, we can directly calculate the geometrical capacitance of the BN of $C^{BN} = 130\,\mathrm{nF\,cm^{-2}}$ which results in a relative permittivity $\varepsilon_r^{BN} = 2.5$. This value is in the range of $\varepsilon_r^{BN} = 2$ to 4 which has been reported for hexagonal BN flakes in [108].

From the carrier density and the longitudinal resistance we can directly derive the mobility μ by

$$\mu = \frac{1}{e n_b R_{xx}|_{B=0T}} \tag{6.1}$$

which includes the longitudinal sheet resistance R_{xx}. The mobility as a function of the backgate of the encapsulated graphene device and, for comparison, of the graphene device on SiO_2 is presented in Fig. 6.6b. On the electron-side, the mobility is approximately constant at the value of about 250 000 cm^2 V^{-1} s^{-1}. The mobility of the device of graphene on SiO_2 is 14 000 cm^2 V^{-1} s^{-1} which is comparable to similar devices on SiO_2 in literature [1, 3, 109] and one order of magnitude smaller than the one of encapsulated graphene.

Another important parameter to characterise a device and to classify it into the ballistic or diffusive limit is the mean free path l_e which reads:

$$l_e = v_F \cdot \tau = \frac{\hbar \mu k_F}{e}$$

With $k_F = \sqrt{\pi n_b}$ and $\frac{1}{R_{xx}} = \mu n_b e$, we can extract l_e from

$$l_e = \frac{h\sigma_L}{2e^2\sqrt{\pi n_b}} \tag{6.2}$$

The mean free path calculated with (6.2) is plotted in Fig. 6.6c as a function of the backgate voltage. A mean free path of about 1.8 µm at $V_{bg} = 15\,\mathrm{V}$ corresponds to the distance between neighbouring contacts on each side of the Hall bar (see Fig. 6.1) which demonstrates that the device is in the ballistic limit and, therefore, the mobility calculated previously is not the intrinsic mobility as it is limited by the sample edges.

3 Signature of ballistic transport

3.1 Negative non-local resistance

A signature for ballistic transport in our sample is observed in the non-local resistance $R_B = R_{24,16}$ for which the current is applied between the contacts 2 and 4 while the voltage is measured between the contacts 1 and 6 (Fig. 6.7b). The non-local resistance is in literature also occasionally referred to as the bend resistance. This resistance as a function of the backgate voltage is presented in Fig. 6.7a for zero (black curve) and increasing (blue and orange curves) magnetic fields. At zero magnetic fields, R_B is negative away from the CNP. A portion of the electrons travels ballistically directly from the current source (contact 2) to the voltage measurement (contact 1) causing the measured resistance to be negative. With increasing magnetic fields R_B increases, which results from the bending of the electrons' trajectories due to the Lorentz force which prevents them from travelling to

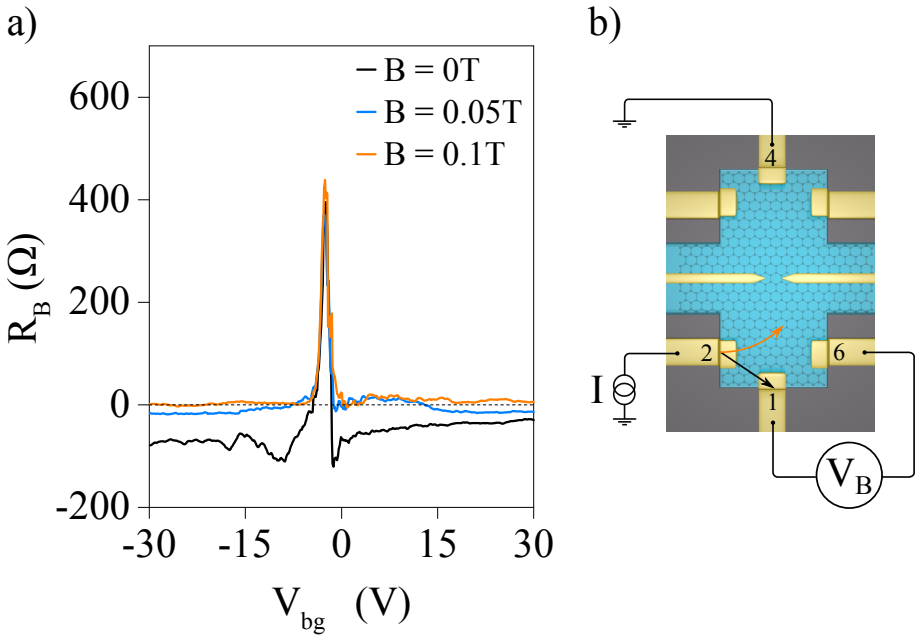

Figure 6.7: Evidence for ballistic transport in the bend resistance. a) The bend resistance $R_B = R_{24,16}$ as a function of the backgate V_{bg} becomes negative beyond the Dirac point at zero magnetic fields. b) With increasing magnetic fields, the electronic trajectory is curved preventing electrons from arriving at the contacts 1 and 6.

the voltage probe (contact 1).

The negative non-local resistance as well as its decrease with magnetic fields as a manifestation of ballistic transport was already theoretically predicted [110, 111] and detected in GaAs-AlGaAs [112, 113] in the late 1980s. It has also been recently observed in high mobility graphene in the group of A.K. Geim [114].

3.2 Focusing of charge carriers

Let us proceed one step further to draw a full picture of the non-local resistance to study the effect of electron focusing. The trajectory of electrons is bent in the presence of a magnetic field due to the Lorentz force in a cyclotron motion of radius r_c. The magnetic field acts as a lens focusing the electron flow at a distance $2r_c$. Upon changing B, r_c varies and, therefore, changes the focal point of the electrons. An essential requirement of studying electron focusing is ballistic transport of the charge carriers. To obtain a focal point at a distance L, a magnetic field of:

$$B_f^{(p)} = \left(\frac{2\hbar k_F}{eL}\right) p = \left(\frac{2\hbar\sqrt{\pi n_b}}{eL}\right) p \tag{6.3}$$

is required. The focal point of the electrons' trajectory can be tuned to be centred on the voltage probe of contact 1 or 6 (Fig. 6.8a). The parameter $p-1$ gives the number of reflections at the graphene edge. For instance, $p=1$ conforms to a direct path between the current source and the voltage probe.

We have performed electron focusing measurements on our Hall bar of encapsulated graphene (Fig. 6.8a). The non-local resistance R_B exhibits interesting features with

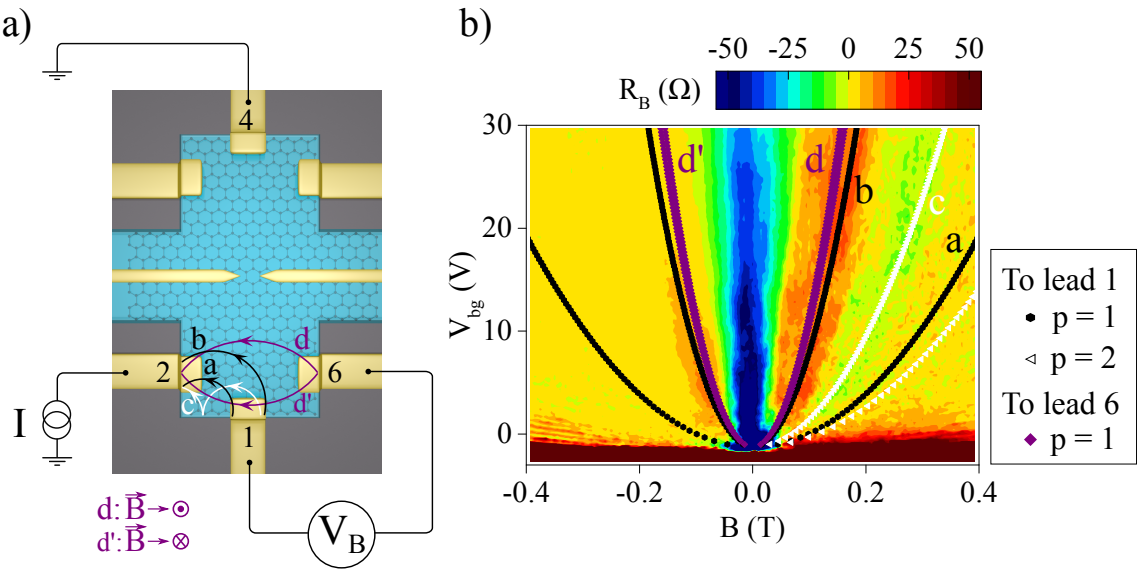

Figure 6.8: Experimental results on electron focusing. a) The current and the voltage probes are given in the Hall bar configuration. The orbital lines indicate the electrons' trajectories with different magnetic fields and, hence, differing cyclotron radius which correspond to curves in Fig. (b). b) The non-local resistance given by the ratio of the voltage probes 1 and 6 and the incoming current I, is plotted as a function of the magnetic field B and the backgate voltage V_{bg}. The curves in various colours are calculated using (6.3) for the different distances between the current and the two voltage probes for zero and multiple reflections.

increasing magnetic fields. R_B, which is given by the measured voltage between the contacts 1 and 6 divided by the incoming current I, is plotted as a function of the backgate voltage and the magnetic field in Fig. 6.8b. A large resistance peak at $V_{bg} = V_{bg}^{CNP} \simeq -2\,\mathrm{V}$ which is B-independent is the charge neutrality point (in red). Upon varying B and V_{bg}, we observe features of positive and negative resistance which are symmetric with respect to $B = 0\,\mathrm{T}$ and $V_{bg} = V_{bg}^{CNP}$. These features exhibit, according to (6.3), a square root dependence of the charge carrier density. The understanding of this series of B and V_{bg} dispersive lines can be illustrated by drawing the classical trajectories of the electron. In Fig. 6.8b, we see that the dotted lines obtained from (6.3) added to the colour map, follow reasonably well the data. For instance, the first resistive peak corresponds to the trajectories with the lowest radius between the current source of contact 2 to the voltage lead 6 (dotted lines d).

When the electron flow is focused on the voltage lead 1, we observe as expected a negative resistance peak. A direct focussing on the voltage probe 1 is located in the region of the colour map between the black dotted lines a, and b, in which a represents the largest distance at the outer corners of the incoming current (contact 2) to the voltage probe 1 and b is the closest distance between the inner corners of these contacts.

The electron beam may bounce once or several times at the edge of the graphene flake before arriving at a voltage probe. The dotted lines in white (region c) illustrate the predicted trajectories of (6.3) for multiple reflections. The two dotted lines in white indicate the trajectory of the largest and the smallest possible radius within one reflections ($p = 2$). Due to the large size of the contacts (∼700 nm), we see that the regions of increased number of reflections overlap making the observation of distinct separate lines impossible.

The group of P. Jarillo-Herrero have studied the phenomenon of transverse magnetic

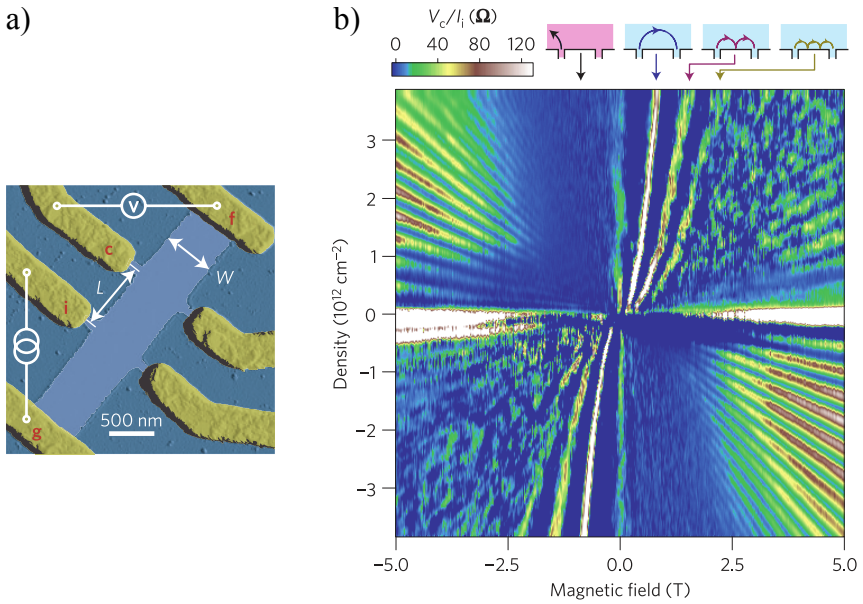

Figure 6.9: Results on electron focusing by Jarillo-Herrero's group. a) AFM image of their graphene device presents the configuration to measure focusing effects. b) Lines of zero and multiple reflections are visible in the map of resistance versus backgate and magnetic field. Fig. taken from [115].

focusing in graphene in the configuration of a Hall bar presented in Fig. 6.9 [115]. The features in resistance as a function of the backgate voltage and the magnetic field are well distinguishable due to the smaller width of their contacts which are ∼100 nm (Fig. 6.9).

At negative magnetic fields, the electrons' trajectory is bent in the opposite direction. In P. Jarillo-Herrero's configuration of a Hall bar, the injector and the collector are located next to each other and not at an angle. Therefore, at negative magnetic fields, the electrons move away from the collector, resulting in the absence of a focussing peak. In our data, we see clearly a focussing peak at negative magnetic fields (region d' in Fig. 6.8b). As indicated schematically in d and d' in Fig. 6.8a, even if the electrons' trajectory is bent in the opposite direction, it is still possible for electrons to be focussed on a voltage probe resulting in a non-zero signal.

Let us mention another interesting feature in Fig. 6.8b. We observe small stripes in the electron-doped region at $V_{bg} \simeq 1\,\mathrm{V}$ from a magnetic field of $-0.3\,\mathrm{T}$. These small stripes are oscillations in resistance which are, in fact, already an onset of Shubnikov-de Haas oscillations.

The vertical stripe of negative resistance at zero magnetic fields above the CNP (blue regions in Fig. 6.8b) is a manifestation of ballistic transport which we have discussed in the previous section 3.1 of the non-local resistance.

At this point, we draw some conclusions about our results on the magnetic focusing in comparison to the results of P. Jarillo-Herrero's group. The observation of focussing peaks in both sets of data point out ballistic transport in both devices which is the crucial requirement for focusing experiments. The observed focussing peaks of P. Jarillo-Herrero are narrow and well separated due to the small width of their contacts (∼100 nm) in comparison to their distance (∼500 nm). In our configuration, the width of the contacts of our device is large in relation to their distance. For instance, the distance between the contacts 2 (current source) and 1 (voltage probe) is minimally 680 nm and maximally 1820 nm which is of the same order than the size of the contacts of ∼700 nm. Therefore, the focussing peaks are large and not well separated.

3.3 Last Hall plateau

The transverse resistance R_{xy} can also exhibit features arising from the focusing of charge carriers. Fig. 6.10 presents R_{xy} as a function of the magnetic field for different backgate voltages. We observe that R_{xy} deviates from its linear behaviour at a critical magnetic field of around $B = 0.1\,\mathrm{T}$ where it has a peak-like feature indicated by the red arrow in Fig. 6.10. This feature of enhanced R_{xy} disperses with decreasing backgate voltage.

This critical value of B corresponds to a cyclotron radius of the distance to the voltage probes. Therefore, this peak-like feature arises when electrons are focused directly on the voltage probe 3 as shown in Fig. 6.10b. Applying (6.3) for the distance between the current contact 2 and the voltage probe 3, we obtain $B_f^{(0)} \simeq 0.1\,\mathrm{T}$ at $V_{bg} = 30\,\mathrm{V}$ confirming the nature of electron focusing as the origin of this peak-like feature.

The peak-like feature becomes smaller with decreasing backgate voltage until it disappears completely at the CNP which is due to the decreasing charge carrier density n_b approaching zero at the CNP.

The so-called "last Hall plateau" has already been studied both theoretically [110, 116] and experimentally in GaAs-AlGaAs [117–120]. It has already been observed in ballistic

graphene devices in the group of A.K. Geim [114].

4 High-mobility graphene in the quantum Hall regime

4.1 Broken symmetry states

In this section, we address the properties of our ballistic device in the quantum Hall regime. Measurements were conducted at dilution temperature of 0.05 K and at a magnetic field up to 15.5 T. The transverse conductance G_{xy} is defined as

$$G_{xy} = \frac{R_{xy}}{\sqrt{R_{xy}^2 + \left(\frac{W}{L} R_{xx}\right)^2}}$$

where W is the width and L is the length of the device (see device configuration in Fig. 6.1). Fig. 6.11 presents the transverse conductance and the longitudinal resistances as a function of the filling factor at 14 T. The applied backgate voltage is directly converted into the filling factor by:

$$\nu_b = \frac{\phi_0 n_b}{B} = \frac{\phi_0 C_{bg} \left(V_{bg} - V_{bg}^{CNP}\right)}{eB}$$

which takes into account the charge carrier density n_b and the capacitance C_{bg} which we obtained previously in the Hall measurements.

G_{xy} exhibits plateaus at all integers of the filling factor $\nu = n$, indicating that the degeneracy of spin and valley becomes lifted (Fig. 6.11). At the location of the plateaus in G_{xy}, the longitudinal resistance R_{xx} drops to zero.

We observe a plateau-like feature in G_{xy} at $\nu = 0$ while R_{xx} exhibits a peak up to

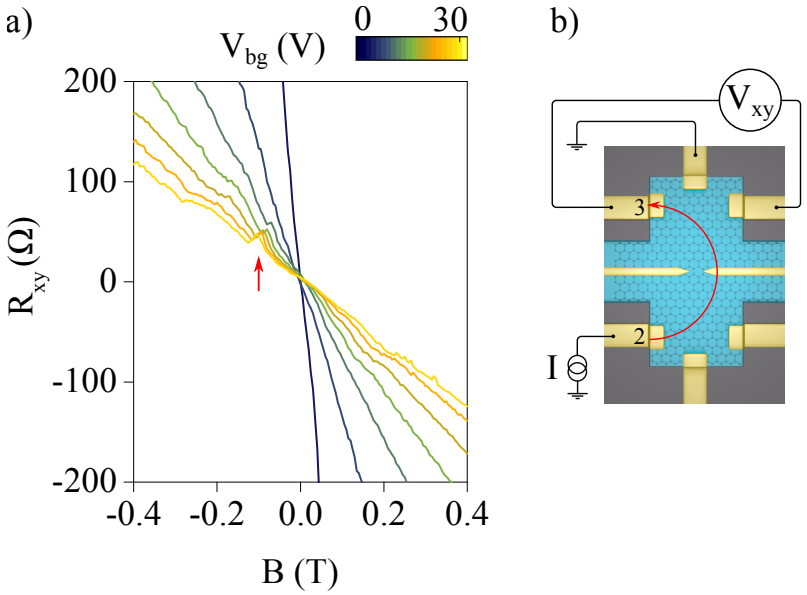

Figure 6.10: a) Evidence for ballistic transport in the transverse resistance R_{xy} plotted as a function of the magnetic field for various values of V_{bg} features deviations from the expected linear behaviour due to a direct focusing of the electrons on contact 3 (b).

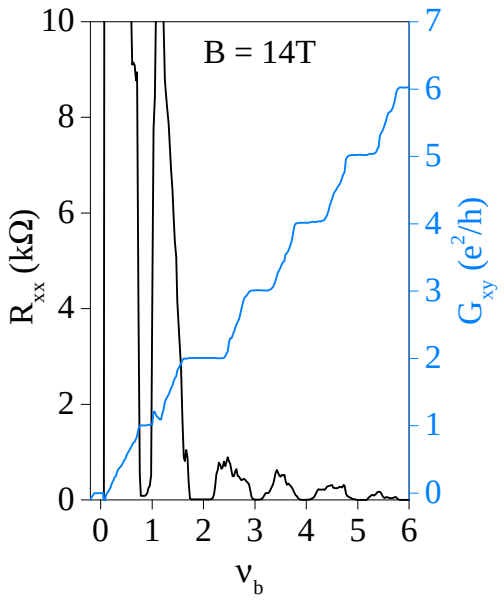

Figure 6.11: The transverse conductance G_{xy} (blue) and the longitudinal resistance R_{xx} (black) is plotted as a function of the filling factor ν_b measured at 0.05 K and at 14 T for the sample A09. The lifting of the degeneracies of spin and valley leads to plateaus in G_{xy} and minima in R_{xx} at all integer filling factors.

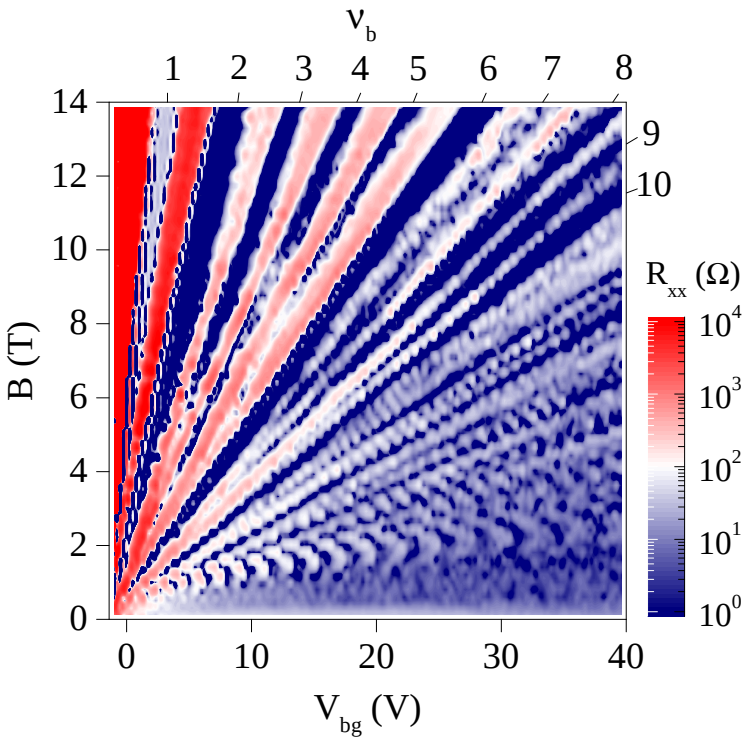

Figure 6.12: Fan-diagram of R_{xx} as a function of B and V_{bg} presents the evolution of quantum Hall states. The $\nu_b = 2$ state is observed from 0.5 T and the degeneracy of the $N = 0$ Landau level gets lifted from 3 T.

0.1 MΩ. This plateau results from the lifting of the degeneracy of the $N = 0$ Landau level. The insulating state arises at $\nu = 0$ indicating that the valley degeneracy is lifted first which leads to a gapped edge excitation.

Fig. 6.12 presents the full evolution of R_{xx} as a function of the magnetic field and the backgate voltage in the form of a so-called Landau fan diagram. The blue stripes of $R_{xx} = 0$ occur at every integer of the filling factor representing the quantum Hall states. We observe the usual sequence of $\nu_b = \frac{4e^2}{h}\left(N + \frac{1}{2}\right)$ and, additionally, all of the symmetry breaking states at integer filling factors. The symmetry of the $N = 0$ Landau level and of the half-filling $\nu_b = 4,8,12\ldots$ are broken at a magnetic field of 3 T. The quarter-filled $\nu_b = 3,5\ldots$ states are resolved above $B = 5$ T.

Let us compare our results of the lifting of the degeneracies with the theoretical predictions of the phase diagram of quantum Hall ferromagnetism in Fig. 2.7 by K. Nomura and A.H. MacDonald [56] which we presented in chapter 2. With a mobility of 250 000 $\mathrm{cm^2\,V^{-1}\,s^{-1}}$, the phase diagram predicts the lifting of $\nu = 1$ at 3 T, of $\nu = 4$ at 10 T and of $\nu = 3$ and $\nu = 5$ at 11 T. The predicted appearance of the $\nu = 1$ state at 3 T corresponds well to our observation. For the states $\nu = 3$ to 5, the phase diagram predicts a two times higher magnetic field than we observe.

At this stage, we cannot draw any conclusions about the spin or valley polarisation of the quantum Hall states. In order to determine the polarisation of states, measurements in tilted high magnetic fields are required as has been performed by the group of P. Kim [51]. We did not have the technical equipment to set an angular rotation of the magnet nor to apply magnetic fields as high as 30 T. In the next chapter, when we include the QPC into our discussion to study equilibration between edge channels, we will obtain information about the polarisation of states.

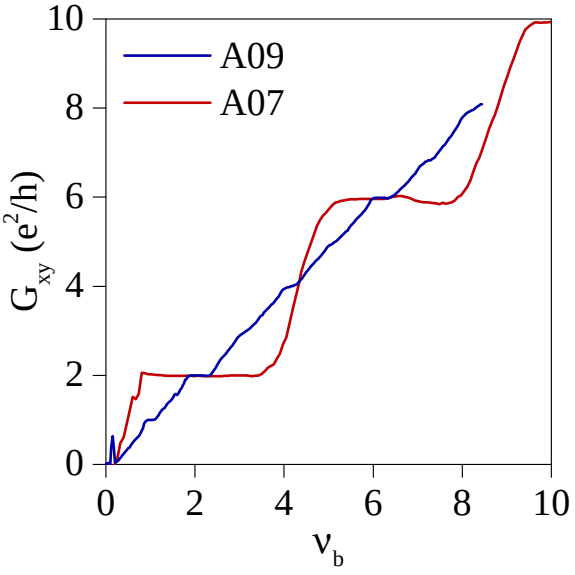

Figure 6.13: The transverse conductance is plotted as a function of the filling factor for the disordered device on SiO_2 (A07) and for the high-mobility device encapsulated between BN (A09) to compare the width of the quantum Hall plateaus. Both measurements were taken at a temperature of 4.2 K and a magnetic field of 14 T. The width of the plateaus of A09 are much narrower than the plateaus of A07 due to the reduced disorder in A09.

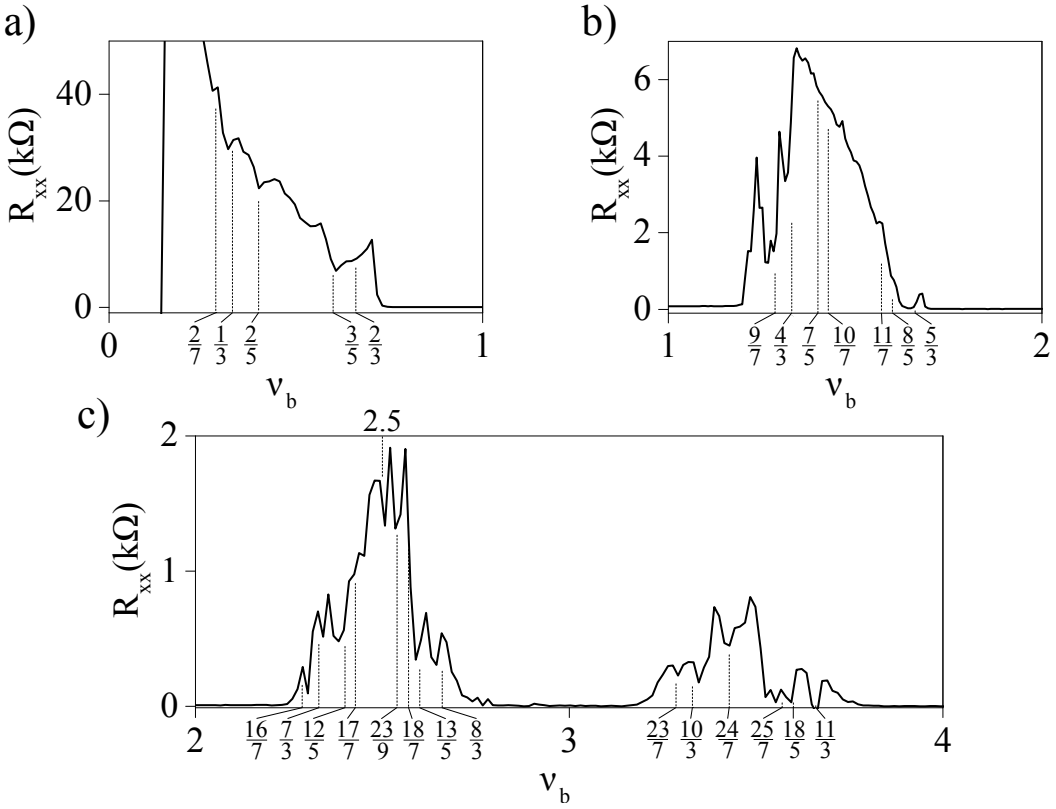

Figure 6.14: Fractional quantum Hall effect in high-mobility graphene. The longitudinal resistance R_{xx} and the transverse conductance G_{xy} are plotted as a function of the filling factor ν_b in the range of a) $\nu_b = 0$ to 1, b) $\nu_b = 1$ to 2 and c) $\nu_b = 2$ to 4 at 14 T and at 0.05 K. The observed fractional states are summarised in table 6.1.

4.1.1 Effects of disorder

We compare the size of the quantum Hall plateaus of the encapsulated graphene device A09 with those of disordered graphene device A07 on SiO_2. Fig. 6.13 presents the transverse conductance as a function of the filling factor measured at a temperature of 4.2 K and a magnetic field of 14 T. We observe that the plateaus of A09 are much smaller than of A07. In fact, the plateaus of A09 are almost not visible due to their small size and the curve nearly reassembles the classical ohmic Hall effect.

We have seen in the first chapter (sect. 1.1.2.4) that some degree of disorder is actually essential for the observation of quantum Hall plateaus of finite width. The small size of the plateaus of A09 suggests that the device has a low level of disorder and is "too clean" to observe large quantum Hall plateaus as is the case for the graphene device A07 on SiO_2.

4.2 Fractional quantum Hall effect

In the sample A09, we observe signatures of the fractional quantum Hall effect (FQHE). A set of our results are presented in Fig. 6.14 in which the longitudinal resistance measured at 14 T and at 0.05 K is plotted as a function of the bulk filling factor. The minima in R_{xx} are more pronounced than the plateaus in R_{xy} for which reason we focus on R_{xx} in our discussion. The dashed lines correspond to the theoretical value of the filling factor of each fraction. The deviation of the experimental value to the theory is maximally 5 % in ν_b.

4.2.1 Composite fermion series

The fractional states are expected to follow the composite fermions series of

$$\nu_b = \frac{p}{2kp \pm 1} \tag{6.4}$$

for p and k being integer. A composite fermion consists of an electron with $2k$ magnetic flux quanta attached to it. Within this theoretical framework, the fractional quantum Hall effect of highly interacting electrons is regarded as the integer quantum Hall effect of non-interacting composite fermions. An introduction of composite fermions has been given in the first chapter (sect. 1.2.2) and specific to graphene in the second chapter (sect. 2.4.2).

Table 6.1 lists all of the fractions expected from (6.4) for $p = 1$ to 4 and $k = 1$ to 4. Minima in R_{xx} which are visible in our data in Fig. 6.14 are highlighted by a blue background. The less pronounced but still visible minima in R_{xx} are coloured in grey. We notice that all of the observed fractions fit well the composite fermions series (6.4) for $p = 1$ to 4 and $k = 1$ and sometimes even $k = 2$. The fractions follow, with one exception, in ascending order of this series: If a fraction of $k = 1$ is not observed then the fractions of $k = 2$ are also absent. The same applies for the p parameter.

Table 6.1: Our results on fractional quantum Hall states in comparison to the composite fermion series.

$\nu_b = \frac{p}{2kp+1}$	$p=1$		$p=2$		$p=3$		$p=4$	
	$k=1$	$k=2$	$k=1$	$k=2$	$k=1$	$k=2$	$k=1$	$k=2$
$\nu_b = 0$	$\frac{1}{3}$	$\frac{1}{5}$	$\frac{2}{5}$	$\frac{2}{9}$	$\frac{3}{7}$	$\frac{3}{13}$	$\frac{4}{9}$	$\frac{4}{17}$
$\nu_b = 1$	$\frac{4}{3}$	$\frac{6}{5}$	$\frac{7}{5}$	$\frac{11}{9}$	$\frac{10}{7}$	$\frac{16}{13}$	$\frac{13}{9}$	$\frac{21}{17}$
$\nu_b = 2$	$\frac{7}{3}$	$\frac{11}{5}$	$\frac{12}{5}$	$\frac{20}{9}$	$\frac{17}{7}$	$\frac{29}{13}$	$\frac{22}{9}$	$\frac{38}{17}$
$\nu_b = 3$	$\frac{10}{3}$	$\frac{16}{5}$	$\frac{17}{5}$	$\frac{29}{9}$	$\frac{24}{7}$	$\frac{42}{13}$	$\frac{31}{9}$	$\frac{55}{17}$

$\nu_b = \frac{p}{2kp-1}$	$p=1$		$p=2$		$p=3$		$p=4$	
	$k=1$	$k=2$	$k=1$	$k=2$	$k=1$	$k=2$	$k=1$	$k=2$
$\nu_b = 0$	1	$\frac{1}{3}$	$\frac{2}{3}$	$\frac{2}{7}$	$\frac{3}{5}$	$\frac{3}{11}$	$\frac{4}{7}$	$\frac{4}{15}$
$\nu_b = 1$	2	$\frac{4}{3}$	$\frac{5}{3}$	$\frac{9}{7}$	$\frac{8}{5}$	$\frac{14}{11}$	$\frac{11}{7}$	$\frac{19}{15}$
$\nu_b = 2$	3	$\frac{7}{3}$	$\frac{8}{3}$	$\frac{16}{7}$	$\frac{13}{5}$	$\frac{25}{11}$	$\frac{18}{7}$	$\frac{34}{15}$
$\nu_b = 3$	4	$\frac{10}{3}$	$\frac{11}{3}$	$\frac{23}{7}$	$\frac{18}{5}$	$\frac{36}{11}$	$\frac{25}{7}$	$\frac{49}{15}$

The observed fractional states correspond mostly to the results in Goldhaber-Gordon's group [6] which we discussed in the second chapter (sect. 2.4.2). However, contrary to their results, we do not observe the fractions $\frac{22}{9}$ and $\frac{17}{5}$. In their case, the measured minima in R_{xx} are more pronounced at the same magnetic fields but they did not measure the fractional states of the form $\frac{s}{7}$ with $s = 2$, 9, 10, 11, 16 and 23.

The less pronounced minima in R_{xx} in our case can either be due to small inhomogeneities due to the split gates or non-ideal contacts. The former influences the charge carrier density due to doping from the split gates. Since fractional states occur only in a narrow window of the charge carrier density, a slight fluctuation may easily mask the fractional quantum Hall states. The latter leads to nn′-junctions in vicinity to the metal contacts as we have seen in 2.3.

4.2.2 Symmetry of the degeneracy lifting

Let us have a closer look at the significance of the observed fractions and their correlation to the lifting of the degeneracies of spin and valley. Depending on the strength of the Zeeman and the valley splitting in comparison to the Coulomb interaction, there are three possible scenarios for the lifting of the four-fold degeneracies [5, 41]:

1. The Coulomb interaction dominates over the Zeeman effect and valley splitting resulting in non-polarised, mixed states. The approximate SU(4) symmetry remains intact for which reason the FQHE states are also completely mixed and non-polarised. In this case, the only relation between fractional states is the particle-hole symmetry of $\nu \leftrightarrow -\nu$ relating, for instance $\frac{1}{3}$ to the hole state $-\frac{1}{3}$.
2. If either the Zeeman efffect or valley splitting become sufficiently strong, one degeneracy is fully lifted resulting in either spin- or valley polarised states. A SU(2) symmetry of either spin or valley is still present. Therefore, the FQHE states are also mixed either in spin or in valley polarisation. The remaining SU(2) symmetry requires a relation between the fractional states of $\nu \leftrightarrow 2 - \nu$ which relates, for instance, the states $\frac{1}{3} \leftrightarrow \frac{5}{3}$ as well as $\frac{2}{3} \leftrightarrow \frac{4}{3}$.
3. Both, the Zeeman energy and the valley splitting are sufficiently strong that the degeneracies are fully lifted and the resulting states are spin and valley polarised which corresponds to the ideal case presented in previous chapters as in Fig. 2.11. The SU(4) symmetry is fully broken. Hence, the FQHE states cannot mix spin and valley polarisations. In this case, the fractional states are related by $\nu \leftrightarrow 1 - \nu$ which relates, for instance, the states $\frac{1}{3} \leftrightarrow \frac{2}{3}$ as well as $\frac{4}{3} \leftrightarrow \frac{5}{3}$.

The presence or absence of fractions at the correlated states $\frac{1}{3}$, $\frac{2}{3}$ $\frac{4}{3}$ and $\frac{5}{3}$ provides an indication of the nature of the lifting of the degeneracies and the underlying and still existent symmetry. The observation of the four states $\frac{1}{3}$, $\frac{2}{3}$ $\frac{4}{3}$ and $\frac{5}{3}$ in our data is in agreement with all three scenarios. The presence of the $\frac{5}{3}$ state suggests that the individual states have at least one broken SU(2) symmetry and are spin- or valley polarised.

4.2.3 Even denominator fractions

Interestingly, in 6 out of 14 data sets measured at 14 T and at 15.5 T, we observe a minimum in R_{xx} at $\nu_b = 2.5 = \frac{5}{2}$ shown in Fig. 6.15. The position of the minimum in R_{xx} has less than 5 % deviation in ν_b to $\frac{5}{2}$.

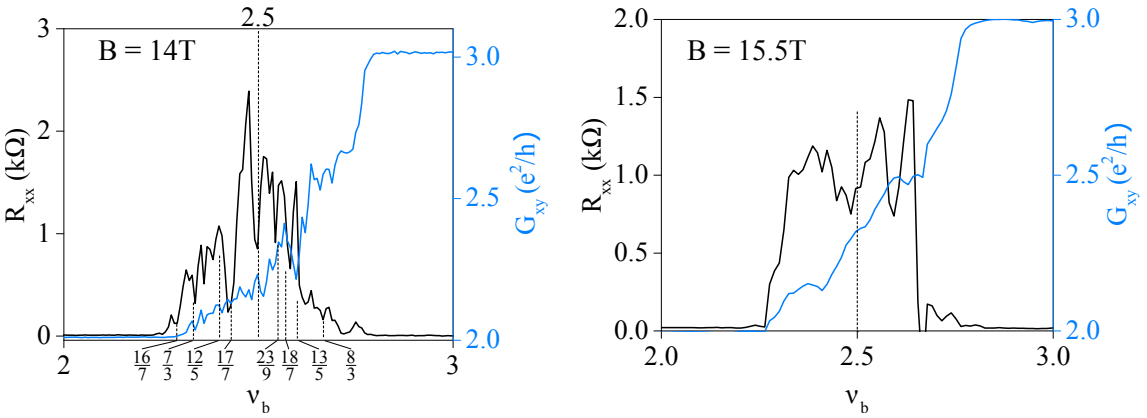

Figure 6.15: Even denominator fractional quantum Hall state of $\nu_b = \frac{5}{2}$ measured at a) 14 T and b) 15.5 T.

In contrast to the other fractional states which we discusses above of the composite fermion series, the $\frac{5}{2}$ state is theoretically a compressible state. As we discussed in the first chapter (sect. 2.3), in the theory of composite fermions, the $\frac{5}{2}$ state as an analogy to the $\frac{1}{2}$ state has been observed to have neither a minimum in R_{xx} nor a plateau in R_{xy}. Another theoretical approach of the $\frac{5}{2}$ state is that it cannot be obtained by the picture of a single composite fermion (6.4) but is rather due to a BCS-like pairing of composite fermions. This state has already been observed by W. Pan et al [33] in GaAs/AlGaAs but it has never been reported in graphene.

Even though we observe a fractional state at $\nu_b = \frac{5}{2}$ in various data sets at different magnetic fields, these results need to be verified in a high-mobility Hall bar without the influence of any split gates. Due to local doping of the split gates the filling factor underneath them may be slightly different than that of the bulk, resulting in a nn′-junction. We cannot exclude a non trivial equilibration process between nearby fractional states which may lead to the observation of a minimum at $\nu_b = \frac{5}{2}$ as the origin for our observation. This fraction needs to be systematically studied to be clarified.

Summary

In the course of this chapter, we presented the magnetotransport properties of our high mobility encapsulated graphene devices. We observe signatures of ballistic transport as a negative non-local resistance as well as magnetic electron focusing.

In the quantum Hall regime, we observe conductance plateaus at integer filling factors indicating the full lifting of the degeneracies of spin and valley. Furthermore, we observe several fractional quantum Hall states which are in agreement with the sequence of composite fermions. Especially, the fractional states of $\frac{1}{3}$, $\frac{2}{3}$, $\frac{4}{3}$ and $\frac{5}{3}$ confirm that at least one SU(2) symmetry is broken.

After having fully characterised the transport properties in our devices, we will include the quantum point contact and study the selective transmission and equilibration of edge channels in the quantum Hall regime in the following chapter.

CHAPTER 7

QUANTUM POINT CONTACT IN THE INTEGER QUANTUM HALL REGIME IN HIGH-MOBILITY GRAPHENE

In this chapter we turn to the main result of this PhD thesis: the quantum point contact (QPC) in graphene. First, we look at the QPC at zero magnetic field from which we determine the capacitive coupling of the split gates to the graphene which is crucial for identifying the filling factor underneath the split gates in the quantum Hall regime.

Afterwards, we present our results on the QPC in the quantum Hall regime. We illustrate the selective transmission of integer quantum Hall edge channels through the QPC. The breaking of the spin and valley symmetry reveals specific features of equilibration between quantum Hall edge channels. We observe that equilibration depends on the spin and, in the case of electron-hole edge channels is additionally limited to the $N = 0$ Landau level.

We complete this chapter with the measurements in low magnetic fields of degenerate quantum Hall states.

1 Device configurations

In this chapter, we discuss our results on the graphene device equipped with a QPC whose configuration is presented in Fig. 7.1. A bias current I_{bias} or voltage V_{bias} is applied on one side of the Hall bar while the current is measured on the other side. We detected both the longitudinal voltage V_L and the diagonal voltage V_D by standard lock-in techniques allowing to calculate the corresponding resistances.

While the backgate voltage V_{bg} changes the charge carrier density in the whole graphene flake, the voltage on the split gates of the QPC, V_{sg} modifies the carrier density only in the graphene underneath it. Therefore, two areas with different doping are established: n_b in the bulk and n_g beneath the split gates.

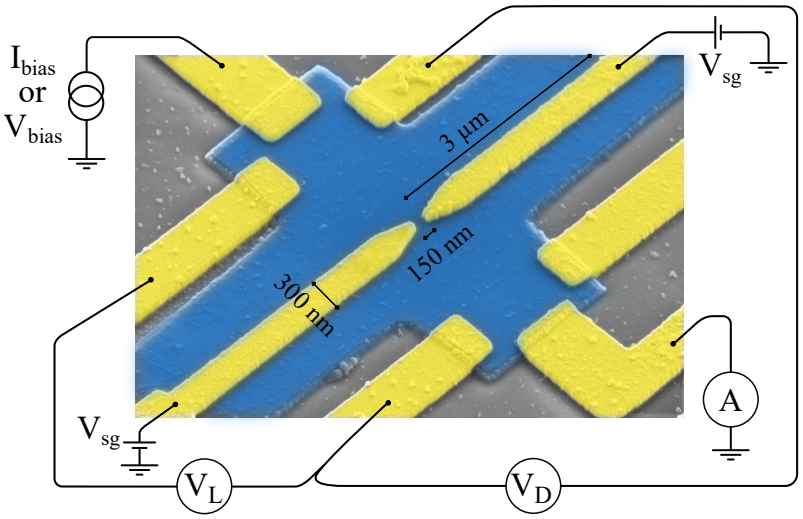

Figure 7.1: SEM image of our QPC device in graphene to illustrate the configurations: A voltage V_{sg} is applied on the split gates. A bias current or voltage is applied on one side and the current is measured on the other side. The longitudinal and diagonal voltages are measured.

2 QPC at zero magnetic field

We start the discussion with our results on the QPC at zero magnetic field. Fig. 7.2a presents the longitudinal resistance R_L as a function of the backgate voltage V_{bg} and the split gate voltage V_{sg}. We identify two lines of high resistance, one runs horizontally and the second one diagonally. The horizontal red line at $V_{bg} = -1\,\mathrm{V}$ marks the charge neutrality point (CNP) in the bulk, while the diagonal line represents charge neutrality beneath the split gates. These two lines divide the map into four quadrants of different doping configuration depending on the polarity of the charge carriers (np'n, nn'n, pp'p and pn'p).

The curves of Fig. 7.2b and c are extracted from the map of Fig. 7.2a at a fixed voltage of b) $V_{bg} = 15\,\mathrm{V}$ and c) $V_{sg} = 3\,\mathrm{V}$, respectively. In Fig. 7.2b, we observe an asymmetric peak in the $R_L(V_{sg})$ curve with its maximum at $V_{sg} = -2\,\mathrm{V}$, indicating the CNP underneath the split gates. To the left side of the peak, the graphene is partially electron- and partially hole-doped (np'n) and on the right side, the graphene is electron doped (nn'n). The $R_L(V_{bg})$ curve of Fig 7.2c exhibits a resistance peak up to $3\,\mathrm{k\Omega}$ corresponding to charge neutrality in the bulk. On the left side of the peak, the graphene is electron- and hole-doped[1] while on the right side, the graphene is only electron-doped.

The height of the resistance peak of the CNP underneath the split gates is lower than

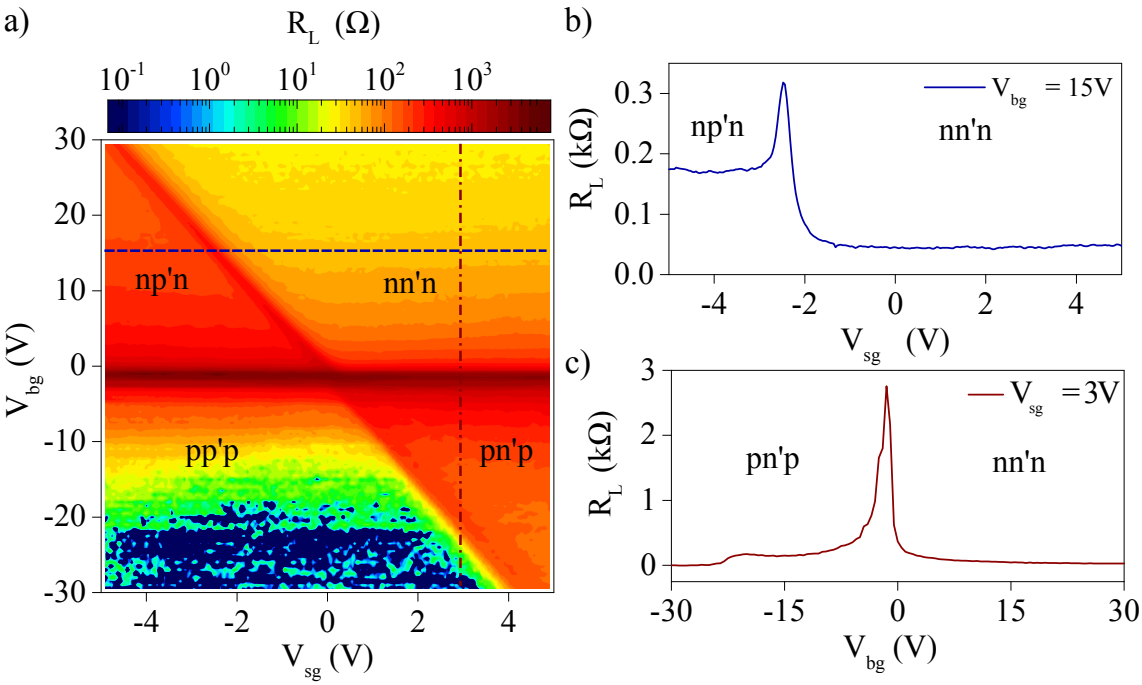

Figure 7.2: a) The longitudinal resistance R_L is plotted as a function of the backgate voltage V_{bg} and the split gate voltage V_{sg}. The horizontal line of high resistance represents the CNP in the bulk, while charge neutrality underneath the split gates is maintained at the diagonal line. b) $R_L(V_{sg})$ at fixed $V_{bg} = 15\,\mathrm{V}$ exhibits a peak around $V_{sg} = -2\,\mathrm{V}$ signifying the CNP underneath the split gates. c) $R_L(V_{bg})$ at fixed $V_{sg} = 3\,\mathrm{V}$ possesses a large resistance peak at $V_{bg} = 0\,\mathrm{V}$ which is the CNP in the bulk.

1 Note also the presence of a small pp'p region at the very left of the graph

the one in the bulk. The smaller peak height corresponds directly to the smaller physical area of the graphene covered by the split gates of $1.8\,\mu m^2$ in comparison to the bulk of $17.5\,\mu m^2$. Indeed, the peak height in Fig. 7.2b is about 8.6 times smaller than the one in Fig. 7.2c which conforms with the ratio of the physical area underneath the split gates to the total area of the graphene.

2.1 Capacitive coupling of the split gates

With the charge carrier density in the bulk and the geometrical capacitance C_{bg} between the backgate and the device (see sect. 6.2.4), we determine the geometrical capacitance of the split gates which is essential for identifying the filling factor in the quantum Hall regime. The slope of the diagonal line in Fig. 7.2a is directly proportional to the ratio of capacitance couplings of the split gates to the backgate $\frac{C_{sg}}{C_{bg}}$. With $C_{bg} = 11.1\,\mathrm{nF\,cm^{-2}}$ which we derived in chapter 6 (sect. 6.2.4), we obtain $C_{sg} = 78\,\mathrm{nF\,cm^{-2}}$.

The relative permittivity of BN can be directly calculated by $C_{sg} = \frac{\varepsilon_0 \varepsilon_r}{d_{BN}}$ which includes the thickness d_{BN} of the top BN flake of 36 nm resulting in $\varepsilon_r^{BN} = 3.2$. This value is consistent with the measurement of hexagonal BN films, in which a dielectric constant of 2 to 4 was obtained [108].

2.2 Discussion of the QPC at zero field

Let us draw our attention to the left region of hole doping both in the bulk and underneath the split gates (pp'p). In the previous chapter (sect. 6.2.2), we have shown that the resistance of the field effect curve becomes zero on the hole-doped side. In fact, in Fig. 7.2a we observe that a large part of resistance in the hole-doped region is zero which is, as argued before, a signature for ballistic transport.

The curve of $R_L(V_{sg})$ in Fig. 7.2b is asymmetric with respect to the charge neutrality point underneath the split gates. The resistance in the bipolar quadrants of np'n and pn'p is higher than the one in the unipolar quadrants of nn'n and pp'p. The effect of Klein tunnelling is that in the bipolar regime the region underneath the local gate rather filters out electrons of a large incident angle. The backscattering of a proportion of the electrons leads to an increase in resistance in this regime which gives an explanation of the asymmetry in $R_L(V_{sg})$.

The resistance map versus backgate and split gate voltages in Fig. 7.2a has a strong resemblance to the resistance map of a pnp-junction in graphene measured by the group of D. Goldhaber-Gordon [121]. At zero magnetic field, our QPC in graphene shows, indeed, the same physical properties as a pnp-junction. The small area of about $150\,\mathrm{nm}\times 300\,\mathrm{nm}$ of the constriction of the QPC which is uncovered by the split gates may slightly change the total resistance but does not change the shape of $R_L(V_{bg},V_{sg})$.

From our results at zero magnetic field, we can draw the following conclusions. We do not observe any quantisation due to the QPC in contrast to measurements in GaAs discussed in chapter 3 (sect. 3.3). In fact, due to Klein tunnelling at a pn-interface, electrons cannot be confined by the split gates to pass only through the constriction of the QPC. Therefore, quantisation in the conductance is not expected in graphene at zero magnetic field, which we confirm in our data.

3 Selective transmission of integer quantum Hall edge channels

3.1 Conductance controlled by the filling factor in the QPC

We begin to discuss the effect of the split gates in the quantum Hall regime by focussing on a conductance map versus the backgate and split gate voltages taken at a magnetic field of 7 T. Since we have seen in the previous chapter that the spin and valley degeneracies are fully lifted at $B > 5\,\mathrm{T}$ (see Fig. 6.12), quantum Hall states appear at every integer filling factor.

We present in Fig. 7.3 the diagonal conductance $G_D = \frac{1}{R_D}$ as a function of V_{bg} and V_{sg}. On the left side of this figure for $V_{sg} < 0$, we observe diagonally running strips with quantised values of conductance. For instance, the yellow strip is quantised at $G_D = \frac{2e^2}{h}$ and the red one at $G_D = \frac{3e^2}{h}$. On this side, electron edge channels propagate in the bulk while hole edge channels are localised underneath the split gates. Here, we expect the effect of the QPC that the bulk edge channels are forced to pass through the constriction of the QPC because of the presence of the hole edge channels underneath the split gates.

On the right side for $V_{sg} > 0$, we observe horizontal parallel strips of quantised conductance. In order to go further in the analysis and understanding of these features, we need to determine precisely the filling factors involved.

3.1.1 Calculation of the filling factor underneath the split gates

The filling factor ν_g underneath the split gates,

$$\nu_g = \frac{n_g \phi_0}{B}$$

is given by the capacitive coupling between the device and the split gates and its ratio to the geometrical capacitance of the backgate, which we obtained at zero magnetic field in the previous section. The ratio $\frac{C_{sg}}{C_{bg}} = 7.03$ dictates the slope within the $V_{sg} - V_{bg}$-plane. This slope is identical to the second Dirac peak running diagonally in Fig. 7.2a. To find the position of each integer filling factor, we derive the relation between ν_g and V_{sg}. Taking the linear dependence of the charge carrier density to the gate voltage into account, we get

$$\nu_g = \frac{C_{sg}}{e}\left(V_{sg} - V_{sg}^{CNP}\right)\frac{\phi_0}{B} \tag{7.1}$$

in which V_{sg}^{CNP} reflects charge neutrality underneath the split gates. Inverting (7.1) to $V_{sg}(\nu_g)$, we obtain the split gate voltage for each filling factor underneath the split gates at $V_{bg} - V_{bg}^{CNP} = 0$. Together with the slope $\frac{C_{sg}}{C_{bg}}$, we can compute the lines of integer ν_g in the (V_{sg},V_{bg}) plane. These lines are added to Fig. 7.3.

This determination of ν_g leads us to the first important observation: Inspecting Fig. 7.3, we see that the position and slope of ν_g do not correspond to the observed diagonal strips at negative V_{sg}. This leads us to conclude that there is a third filling factor, denoted as ν_{QPC} responsible for these diagonal strips.

3.1.2 The third filling factor ν_{QPC} responsible for diagonal strips

The third filling factor is actually related to the charge carrier density within the constriction of the QPC. We, therefore, note it ν_{QPC}. Since the graphene inside the QPC is influenced

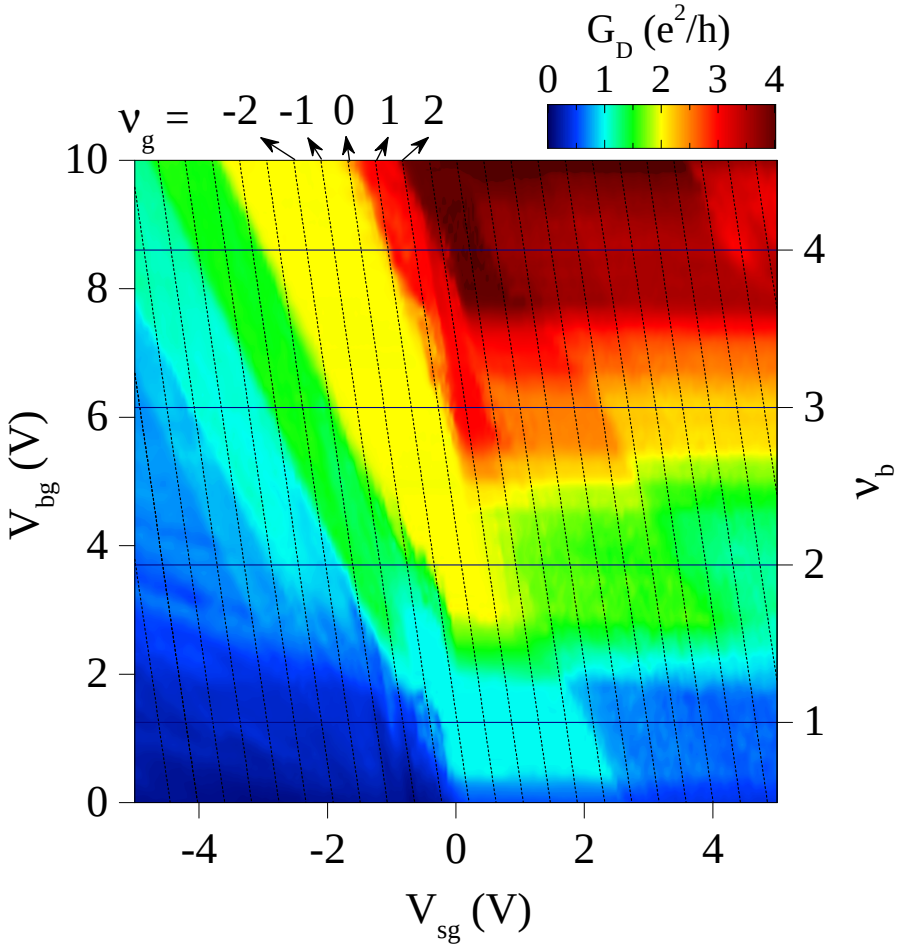

Figure 7.3: Conductance map $G_D = \frac{1}{R_D}$ as a function of backgate and split gates voltages, V_{bg} and V_{sg}, respectively at 7 T and at 0.05 K. The two main structures of horizontal strips on the right side ($V_{sg} > 0$) and diagonal strips on the left side ($V_{sg} < 0$) as well as many small patterns are an implication of the interplay of three filling factors ν_b, ν_g and ν_{QPC}.

by the backgate and split gate voltages, the carrier density in the QPC has to be in between the carrier density of the bulk and underneath the split gates. Therefore, we have

$$\begin{cases} \nu_g < \nu_{QPC} < \nu_b & \text{for } \nu_g < \nu_b \\ \nu_g > \nu_{QPC} > \nu_b & \text{for } \nu_g > \nu_b \end{cases}$$

Fig. 7.4 presents a schematic drawing of the location of the three filling factors and shows the distribution of the charge carrier density of the first case $\nu_g < \nu_{QPC} < \nu_b$. In this example, the bulk is set to be electron-doped while the graphene underneath the split gates is hole-doped. The charge carrier density inside the QPC is in between n_g and n_b and in our example this region is electron-doped.

We observe in Fig. 7.3 that the diagonal strips start at around $V_{sg} = 0$ and remain constant up to higher filling factors in the bulk. For instance, the yellow strip of the plateau at $G_D = \frac{2e^2}{h}$ remains constant even when the edge channels $\nu_b = 3$ and 4 are added in the bulk. This means that only two edge channels are transmitted and the third and fourth

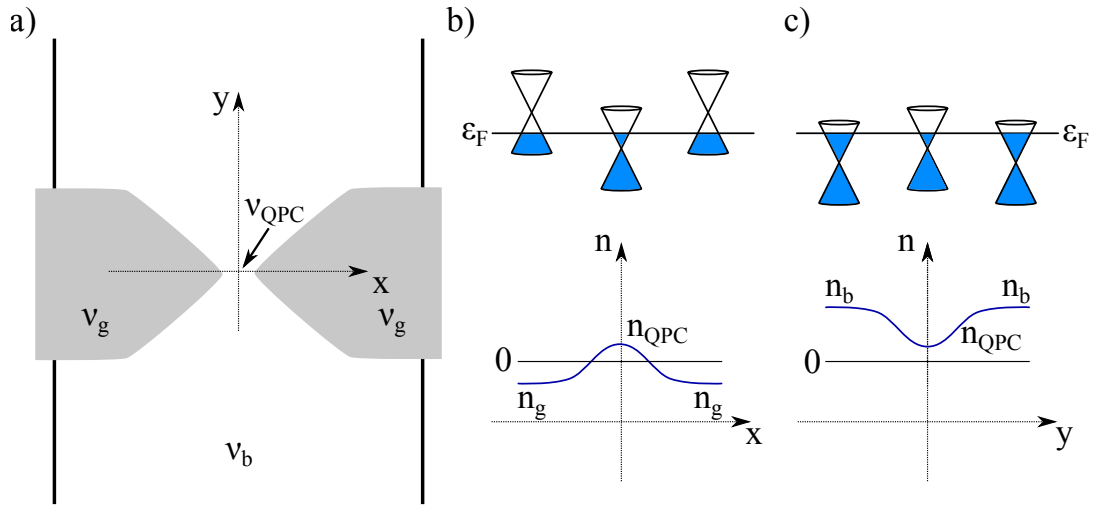

Figure 7.4: Schema of the distribution of the charge carrier density in a QPC in graphene for $\nu_g < \nu_{QPC} < \nu_b$. a) We determine three filling factors in a QPC in graphene: ν_b, ν_g and ν_{QPC}. b) Along the split gates and across the QPC, the graphene is hole-doped underneath the split gates while it is electron-doped inside the QPC. c) Inside the bulk and across the QPC, the graphene in the bulk and inside the QPC is both electron-doped.

ones are backscattered at the QPC.

This is consistent with the hypothesis that the slope of the strips at negative V_{sg} are determined by ν_{QPC}. Thus ν_{QPC} can be interpreted as the number of transmitted edge channels. We will see that this assumption is consistent with our data which we present in the course of this chapter.

To simplify the identification of the exact filling factors, we convert the conductance map of Fig. 7.3 to be as a function of ν_b and ν_g by means of a suitable rotation. The resulting graph is presented in Fig. 7.5. When $\nu_b = \nu_g$, which is indicated by the black dots in Fig. 7.5, the charge carrier density is homogeneous in the entire graphene flake. ν_{QPC} can then be determined since $\nu_{QPC} = \nu_b = \nu_g$ at these points. At these positions, we can add lines to index ν_{QPC} in Fig. 7.5. These lines have the same slope as the diagonal strips.

3.2 Results on the transmission of edge channels

After having determined the three filling factors ν_b, ν_g and ν_{QPC} in our QPC device, we discuss in the following the observed plateaus in more details. Fig. 7.6a presents the diagonal conductance as a function of negative split gate voltage for $\nu_b = 1$ to 4 extracted from the conductance map in Fig. 7.3. We observe different conductance plateaus at integer multiples of $\frac{e^2}{h}$ which correspond to the diagonal strips discussed before. Let us discuss several configurations of edge channels in the bulk and underneath the split gates indexed by the letters A to C in Fig. 7.5 and 7.6. We focus on the curve of $\nu_b = 4$ but the other curves follow accordingly.

At point A in Fig. 7.6a, the conductance is $\frac{4e^2}{h}$. At this point, the three filling factors are identical $\nu_b = \nu_g = \nu_{QPC} = 4$ since $V_{sg} = 0$, so four edge channels are present in the QPC. The drawing of 7.6A shows the corresponding configuration of four edge channels passing underneath the split gates.

At point B in Fig. 7.6a, the split gate voltage is lowered and we observe a lower

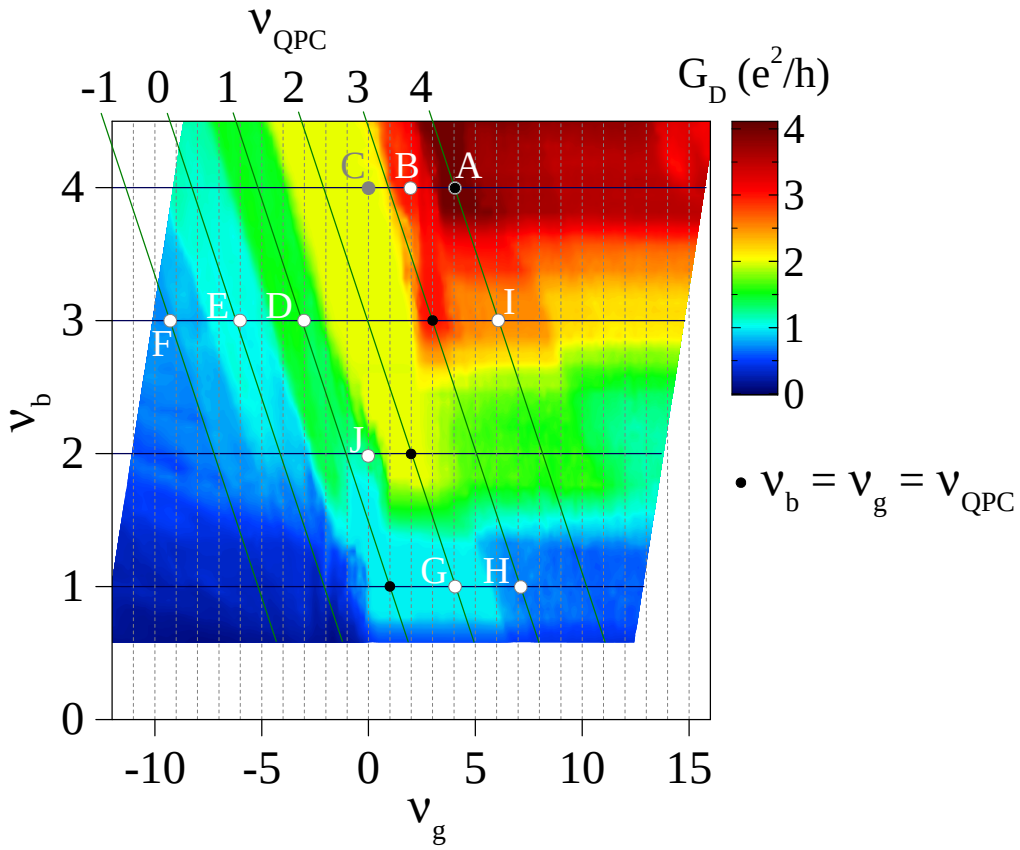

Figure 7.5: Conductance map $G_D = \frac{1}{R_D}$ as a function of the bulk and split gates filling factors, ν_b and ν_g, respectively at 7 T and at 0.05 K. At the positions of the black dots, $\nu_b = \nu_g = \nu_{QPC}$ and the charge carriers are homogeneously spread in the entire graphene flake. The white and grey dots and letters represent configurations which are discussed in this chapter.

conductance of $\frac{3e^2}{h}$. Its corresponding edge channel configuration is presented in the drawing 7.6B. At this point, $\nu_g = 2$ and therefore, the $\nu_b = 3$ edge channel can no longer propagate underneath the split gates and is forced to pass through the QPC. The inner edge channel of $\nu_b = 4$ is backscattered.

At point C in Fig. 7.6a, the split gate voltage is further decreased, which leads to a further decrease of the conductance to $\frac{2e^2}{h}$. The corresponding configuration of edge channels is presented in the drawing 7.6C. Since $\nu_g = 0$, none of the bulk edge channels pass underneath the split gates. The two outer edge channels pass through the QPC which leads to the observed conductance of $\frac{2e^2}{h}$ in Fig. 7.6a. The two inner edge channels of $\nu_b = 3$ and 4 are backscattered and do not contribute to the current transport.

Ideal QPC without equilibration

We observe that a change in the split gate voltage allows to select the number of edge channels which are transmitted through the QPC and those which are backscattered as expected for a QPC in the quantum Hall regime. By converting $G_D(V_{sg})$ to $G_D(\nu_{QPC})$ in Fig. 7.6b, we can directly examine the dependence of G_D on ν_{QPC}.

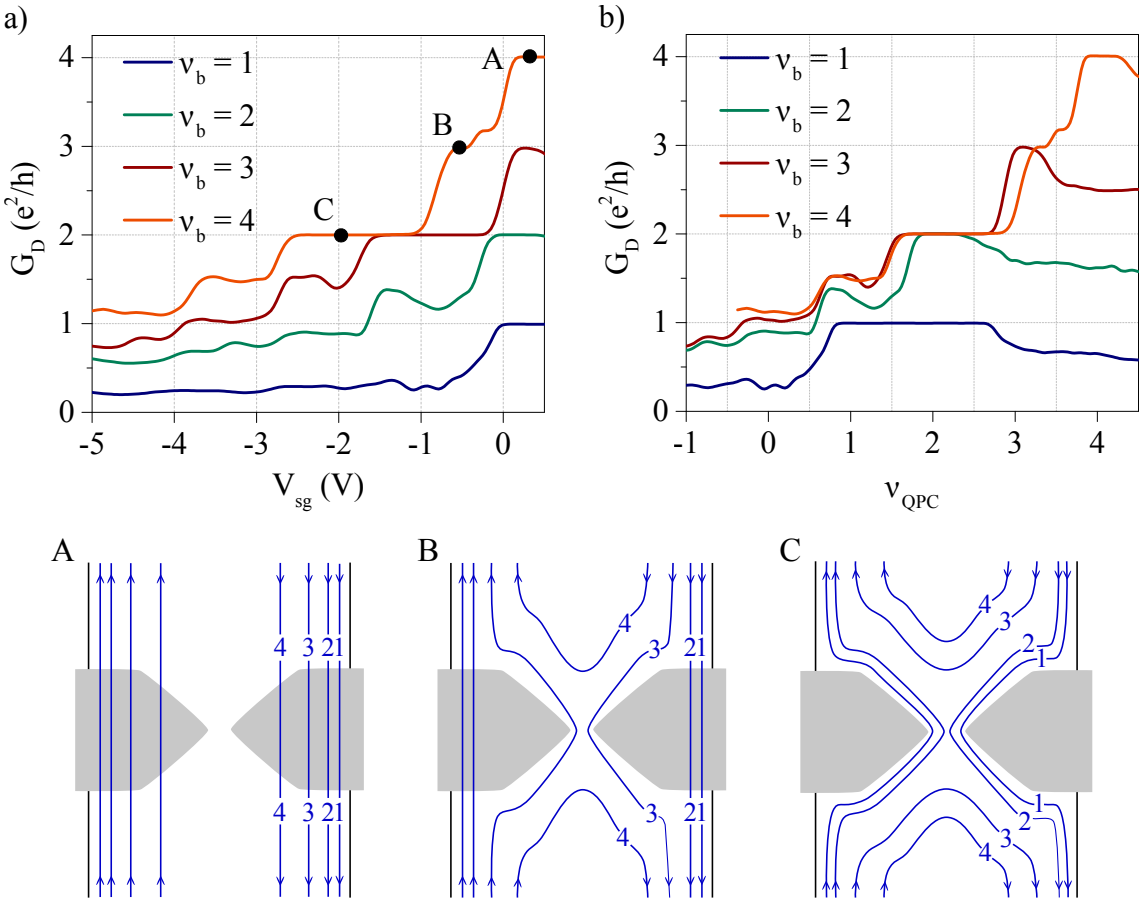

Figure 7.6: Selective transmission of integer quantum Hall states is observed in the diagonal conductance as a function of a) V_{sg} and b) ν_{QPC} for $\nu_b = 1$ to 4. The curves were extracted from the conductance map at 7 T of Fig. 7.3. Schematics of three configurations of edge channel transmission: **A**: The four bulk edge channels pass directly underneath the split gates resulting in $G_D = \frac{4e^2}{h}$. **B**: When $\nu_g = 2$, the $\nu_b = 3$ edge channel is forced to pass through the QPC while the inner edge channel is backscattered resulting in $G_D = \frac{3e^2}{h}$. **C**: The two inner edge channels are forced to pass through the QPC while the two outer edge channels are backscattered resulting in $G_D = \frac{2e^2}{h}$. The positions of the configurations A to C are labelled in the map of Fig. 7.5.

At integer values of ν_{QPC} when $\nu_b \geq \nu_{QPC}$, we observe a direct proportionality of G_D to ν_{QPC}: for instance at $\nu_{QPC} = 4$, $G_D = \frac{4e^2}{h}$ and at $\nu_{QPC} = 2$, $G_D = \frac{2e^2}{h}$. As presented in chapter 4 (sect. 4.2), the theoretical diagonal conductance of an ideal QPC is proportional to the number of transmitted edge channels which here corresponds to ν_{QPC}. Therefore, the diagonal conductance takes the form:

$$G_D = \frac{e^2}{h}\nu_{QPC} \tag{7.2}$$

Eq. (7.2) explains well the observed conductance plateaus at integer multiples of $\frac{e^2}{h}$ for $\nu_b > 2$ due to selective transmission through the QPC.

Nevertheless, within the $N = 0$ Landau level ($\nu_{QPC} = 0$, 1), in Fig. 7.6b, we observe plateaus which cannot be explained by the eq. (7.2) and need further analysis.

4 Spin selective equilibration between electron and hole states

In each curve with $\nu \geq 2$ in Fig. 7.6b, we observe a plateau at $G_D = \frac{3e^2}{2h}$ at $\nu_{QPC} = 1$ where we would expect $G_D = \frac{e^2}{h}$ from eq. (7.2). At $\nu_{QPC} = 0$, according to (7.2), we expect zero conductance, whereas we observe also here an anomalous plateau at $G_D = \frac{e^2}{h}$. These two conductance plateaus of

$$\begin{cases} G_D = \frac{3e^2}{2h} & \text{at } \nu_{QPC} = 1 \\ G_D = \frac{e^2}{h} & \text{at } \nu_{QPC} = 0 \end{cases}$$

cannot be explained by the standard transmission of edge channels in a QPC given by eq. (7.2).

In the following, we show that taking into account equilibration between electron and hole edge channels enables a full understanding of these anomalous plateaus.

4.1 Full equilibration expanded to three filling factors

The formula for a pnp-junction of only two filling factors as we presented in chapter 4 (sect. 4.2), does not reflect the actual configuration of a QPC. We need to derive a new formula which includes the third filling factor ν_{QPC} and the specific QPC configuration.

We thus derive the diagonal conductance for the QPC geometry including ν_b, ν_g and ν_{QPC}, and consider equilibration between edge channels in the bulk and edge channels of opposite polarity localised underneath the split gates. For instance, electron-doped edge channels exist in the bulk while hole-doped edge channels circulate below the split gates.

We distinguish two configurations. First, electron edge channels from the bulk pass through the QPC ($\nu_{QPC} \geq 0$) and second, the hole edge channels from underneath the split gates extend across the QPC ($\nu_{QPC} < 0$). Our calculations are based on the current conservation law which we already used in chapter 4 (sect. 4.2).

4.1.1 Configuration $\nu_{QPC} \geq 0$

We consider the configuration in which some electron edge channels from the bulk are transmitted through the QPC while hole states are localised underneath the split gates. Fig. 7.7 illustrates the schematic of propagation of the bulk and split gates edge channels in the device and the corresponding electric circuit with the contributing currents. The incoming current I_{in} splits into two branches in the vicinity of the QPC. One part of the current is transmitted through the constriction and the rest is backscattered. While the electron-doped edge channels from the bulk propagate alongside the hole-doped edge channels underneath the split gates, they may mix and equilibrate (grey areas in Fig. 7.7). There are, therefore, two possible sections for equilibration for each split gate - one on each side of the junction. In the following, we assume that the equilibration is complete when the current splits from I_2 into I_3 and I_5.

To derive the conductance, we consider the distributions of the current in the different regions of the device as indicated in Fig. 7.7. In Fig. 7.7b, we consider each section as a wire of conductance given by the number of co-propagating edge channels times $\frac{e^2}{h}$. We

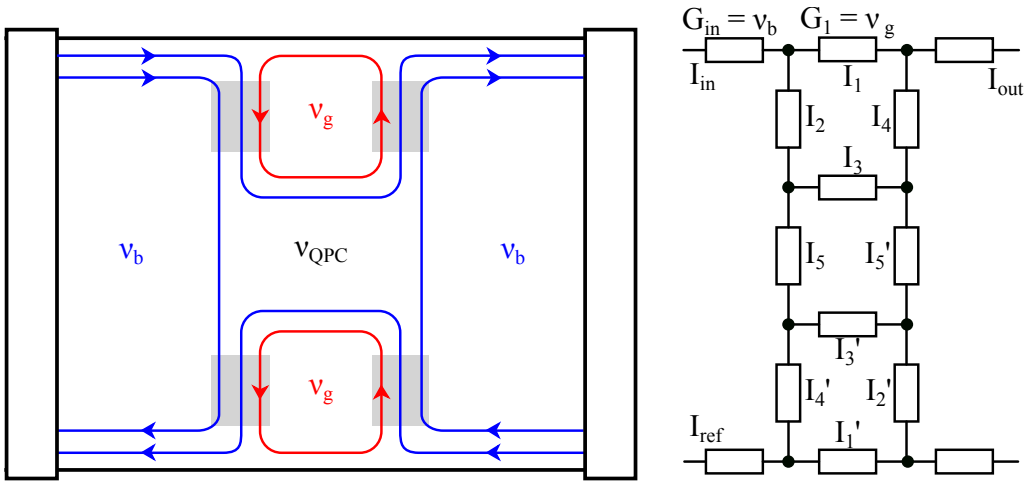

Figure 7.7: Schematic drawing of the edge channels in the QPC and the electric circuit for calculating the outgoing current I_{out} in dependence of the three filling factors. The grey areas indicate the regions of equilibration of edge channels.

can, thus, write:

$$I_1 = rI_4 \tag{7.3}$$
$$I_1' = rI_4' \tag{7.4}$$
$$I_3 = r'I_2 \tag{7.5}$$
$$I_3' = r'I_2' \tag{7.6}$$

with

$$r = \frac{|\nu_g|}{|\nu_b| + |\nu_g|} \tag{7.7}$$
$$r' = \frac{|\nu_{QPC}| + |\nu_g|}{|\nu_b| + |\nu_g|} \tag{7.8}$$

The conservation of currents at the eight nodes give the eight relations:

$$I_2 = I_1 + I_{in} = I_3 + I_5 \tag{7.9}$$
$$I_4 = I_1 + I_{out} = I_3 + I_5' \tag{7.10}$$
$$I_2' = I_1' = I_3' + I_5' \tag{7.11}$$
$$I_4' = I_1' + I_{ref} = I_3' + I_5 \tag{7.12}$$

in which we assume that no current is injected from the right lead. Including the eqs. (7.3)

to (7.6) into the eqs. (7.9) to (7.12), we obtain:

$$I_2 = rI_4 + I_{in} = \frac{1}{1-r'} I_5 \tag{7.13}$$

$$I_4 = \frac{1}{1-r} I_{out} = r' I_2 + I_5' \tag{7.14}$$

$$I_2' = rI_4' = \frac{1}{1-r'} I_5' \tag{7.15}$$

$$I_4' = \frac{1}{1-r} I_{ref} = r' I_2' + I_5 \tag{7.16}$$

In order to derive the conductance, we need to determine I_{out} as a function of I_{in}. By using eqs. (7.13) to (7.16), we obtain:

$$I_{out} = \frac{r - 2rr' + r'}{1 + r - 2rr'} I_{in}$$

or including the filling factors eqs. (7.7) and (7.8):

$$I_{out} = \frac{2|\nu_b|\ |\nu_g| - |\nu_{QPC}|\ |\nu_g| + |\nu_b|\ |\nu_{QPC}|}{3|\nu_b|\ |\nu_g| + |\nu_b|^2 - 2|\nu_{QPC}|\ |\nu_g|} I_{in}$$

The incoming current I_{in} depends merely on the number of incoming edge channels which corresponds to ν_b and on the potential difference $\mu_1 - \mu_2$ of the form $I_{in} = \frac{e^2}{h}|\nu_b|\,(\mu_1 - \mu_2)$. Including the expression for I_{in} into I_{out}, we obtain:

$$I_{out} = \frac{e^2}{h}|\nu_b| \frac{2|\nu_b|\ |\nu_g| - |\nu_{QPC}|\ |\nu_g| + |\nu_b|\ |\nu_{QPC}|}{3|\nu_b|\ |\nu_g| + |\nu_b|^2 - 2|\nu_{QPC}|\ |\nu_g|} (\mu_1 - \mu_2)$$

With $G_D = \frac{I_{out}}{\mu_1 - \mu_2}$, we obtain the diagonal conductance

$$\boxed{G_D = \frac{e^2}{h}|\nu_b| \frac{2|\nu_b|\ |\nu_g| - |\nu_{QPC}|\ |\nu_g| + |\nu_b|\ |\nu_{QPC}|}{3|\nu_b|\ |\nu_g| + |\nu_b|^2 - 2|\nu_{QPC}|\ |\nu_g|}} \tag{7.17}$$

which depends solely on the three filling factors ν_b, ν_g and ν_{QPC}.

4.1.2 Configuration $\nu_{QPC} < 0$

In the second configuration, the hole states from underneath the split gates extend into the QPC leading to $\nu_{QPC} < 0$. The hole states propagate across the QPC between the opposite edges of the sample leading to a similar configuration than a pnp-junction. One crucial difference is that both hole states propagating across the QPC and those localised underneath the split gates can equilibrate with the electron edge channels of the bulk. The latter are backscattered at the pn-interface and without equilibration between electron and hole states, the current transport would be fully pinched-off. Equilibration, thus, enables current flow across the device.

In the following, we derive the diagonal conductance of the configuration presented in Fig. 7.8. The electron edge channels of the incoming current I_{in} pass alongside the hole

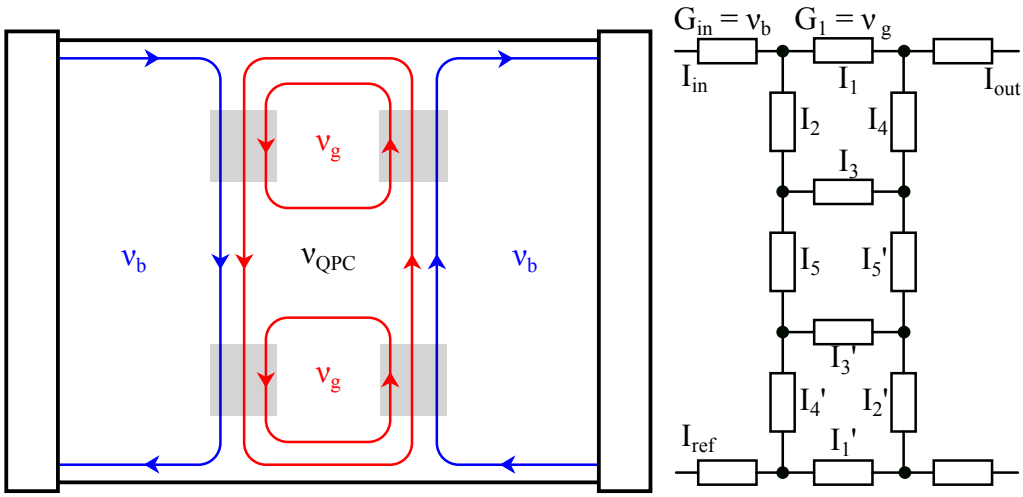

Figure 7.8: Schematic drawing of the edge channels in the QPC and the electric circuit for calculating the outgoing current I_{out} in dependence of the three filling factors in a configuration similar to a pnp-junction. The grey areas indicate the regions of equilibration of edge channels.

states of the split gates at the pn-interface where they equilibrate in the areas indicated in grey in Fig. 7.8. In analogy to the previous section, we write

$$I_1 = rI_4$$
$$I_1' = rI_4'$$
$$I_3 = r''I_2$$
$$I_3' = r''I_2'$$

with

$$r = \frac{|\nu_g|}{|\nu_b| + |\nu_g|}$$
$$r'' = \frac{|\nu_g| - |\nu_{QPC}|}{|\nu_b| + |\nu_g|}$$

Following the same approach as in the previous section, we obtain the diagonal conductance of the form

$$G_D = \frac{e^2}{h}|\nu_b|\frac{2|\nu_b|\ |\nu_g| + |\nu_{QPC}|\ |\nu_g| - |\nu_b|\ |\nu_{QPC}|}{3|\nu_b|\ |\nu_g| + |\nu_b|^2 + 2|\nu_{QPC}|\ |\nu_g|} \tag{7.18}$$

Equations (7.17) and (7.18) are identical apart from three sign changes given by the sign change of ν_{QPC} and can be summarised into one equation

$$\boxed{G_{D,np'n} = \frac{e^2}{h}|\nu_b|\frac{2|\nu_b|\ |\nu_g| - \nu_{QPC}\ |\nu_g| + |\nu_b|\ \nu_{QPC}}{3|\nu_b|\ |\nu_g| + |\nu_b|^2 - 2\nu_{QPC}\ |\nu_g|}} \tag{7.19}$$

At this point, we can proceed to compare our experimental results to the theoretical expectations of (7.19).

4.2 Experimental results in comparison to the theory

From our conductance map in 7.5, we can infer two important points for the understanding of the anomalous plateaus at $\nu_{QPC} = 0$ and 1 and the role of equilibration between electron and hole edge channels:

1. The width of the diagonal bands are much larger than the extension of each integer filling factor of ν_g of the gate. Therefore, adding additional edge channels underneath the split gates does not change the conductance.
2. The anomalous plateaus of the diagonal strips at $\nu_{QPC} = 0$ and $\nu_{QPC} = 1$ arise at $\nu_b = 2$ and stay constant for higher ν_b. Therefore, only when the $\nu_b = 2$ edge channel is backreflected, these anomalous plateaus appear and are unaffected by the increase of ν_b, that is, to the addition of more backscattered bulk edge channels.

We can, therefore, assume that equilibration does not occur equally between all the different states suggesting a selective equilibration. The measurement of a high mobility pnp-junction in graphene by the group of Goldhaber-Gordon revealed that quantum Hall states equilibrate only if their spins are identical [96]. We follow their findings and assume also that equilibration takes only place between states of the same spin.

From our observations, we can even go a step further: Since the plateaus at $\nu_{QPC} = 0$ and $\nu_{QPC} = 1$ remain constant even when ν_b is increased and more bulk edge channels are backscattered, we can assume that **equilibration is limited to the $N = 0$ Landau level**.

Fig. 7.9 presents the diagonal conductance as a function of ν_{QPC} for $\nu_b = 3$ and 4 which are extracted from the conductance map in Fig. 7.3. Let us first focus on our data before comparing them with the theoretical prediction of (7.19).

In both experimental curves, we observe clearly the plateaus of $G_D = \frac{3}{2}\frac{e^2}{h}$ at $\nu_{QPC} = 1$ and of $G_D = \frac{e^2}{h}$ at $\nu_{QPC} = 0$.

Case of $\nu_{QPC} = 1$ Fig. 7.9D presents the corresponding edge channel configuration of the $G_D = \frac{3}{2}\frac{e^2}{h}$ plateau at $\nu_{QPC} = 1$. One bulk edge channel is transmitted while the second and the third edge channels are backscattered. Assuming equilibration between states of the same spin and limited to the $N = 0$ Landau level ($\nu_b = -2\downarrow, -1\uparrow, 1\downarrow, 2\uparrow$), the backscattered $\nu_b = 2$ state can only equilibrate with the first hole state $\nu_g = -1$ (see Landau level diagram in Fig. 7.10).

In order to include spin selection, we extend eq. (7.19) by summing over the two spin configurations restricted to the $N = 0$ Landau level leading to

$$G_{D,np'n} = \frac{e^2}{h} \sum_{i=\downarrow,\uparrow} |\nu_{b,i}| \left. \frac{2|\nu_{b,i}|\ |\nu_{g,i}| - \nu_{QPC,i}\ |\nu_{g,i}| + |\nu_{b,i}|\ \nu_{QPC,i}}{3|\nu_{b,i}|\ |\nu_{g,i}| + |\nu_{b,i}|^2 - 2\nu_{QPC,i}\ |\nu_{g,i}|} \right|_{|\nu_{b,i}|,|\nu_{g,i}|,|\nu_{QPC,i}|\leq 2} \tag{7.20}$$

In (7.20), note that $\nu_{b,i}$, $\nu_{g,i}$ and $\nu_{QPC,i}$ count the number of edge channels of identical spins which equilibrate.

To apply (7.20) to configuration 7.9D, we sum up two terms, one for spin-down and one for spin-up. The first term of spin-down describes the transmission of the $\nu_{b,\downarrow} = 1$

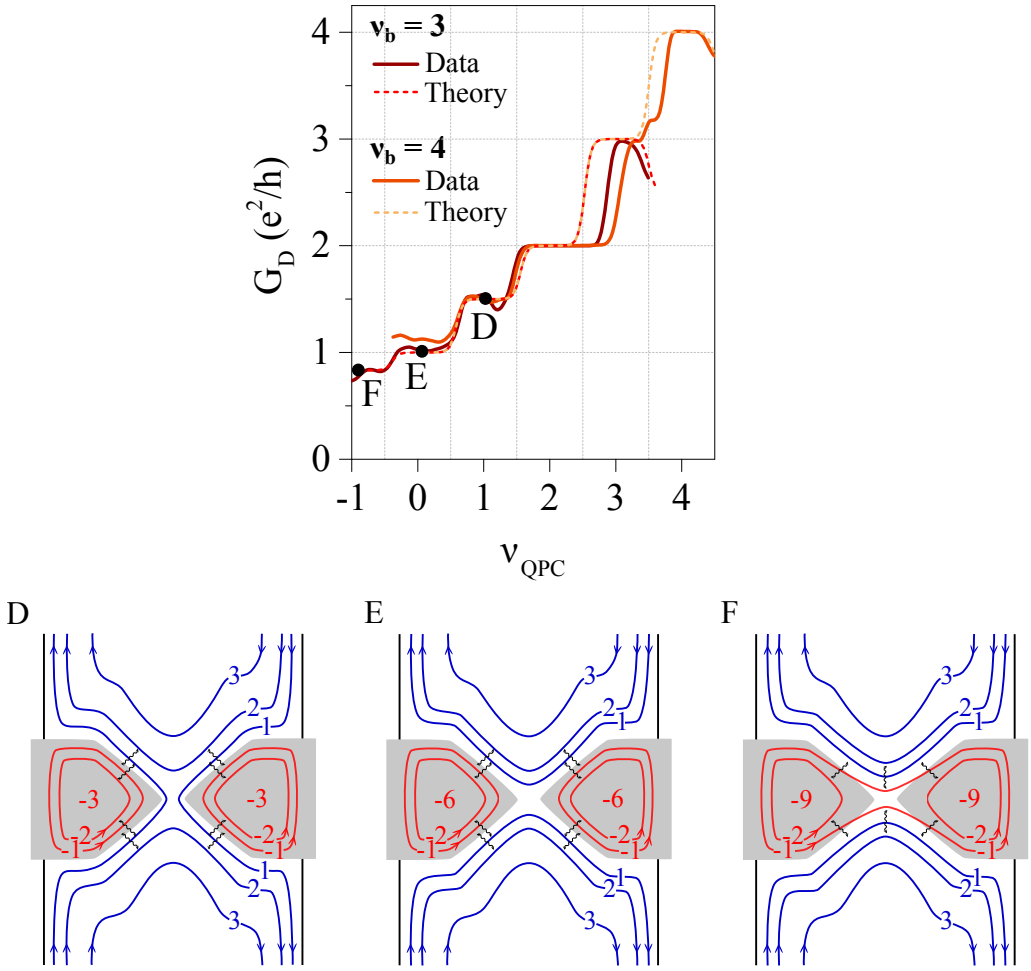

Figure 7.9: Results on the diagonal conductance in comparison to the theory (7.20) extracted from the conductance map of Fig. 7.3 at $\nu_b = 3$ and 4. The theoretical curves include that equilibration only occurs within the $N = 0$ Landau level and is limited to states of identical spin. Schematics of edge channel configurations for $\nu_b = 3$ and $\nu_g \leq -4$. **D**: $\nu_{QPC} = 1$, the state $\nu_b = 2$ equilibrates with the state $\nu_g = -1$. Together with the transmitted $\nu_b = 1$ state, the conductance is quantised at $\frac{3}{2}\frac{e^2}{h}$. **E**: $\nu_{QPC} = 0$, all three bulk edge channels are backscattered. The current is transferred across the QPC via equilibration between the states $\nu_b = 1$ and $\nu_g = -2$ as well as $\nu_b = 2$ and $\nu_g = -1$. **F**: $\nu_{QPC} = -1$, equilibration between the states $\nu_b = 1$ and $\nu_g = -2$ as well as $\nu_b = 2$ and $\nu_g = -1$ leads to current transport across the QPC. The positions of the configurations D to F are labelled in the map of Fig. 7.5.

state through the QPC. The second term of spin-up can be deduced from the Landau level energy diagram in Fig. 7.10. The sublevel $\nu_b = 2$ and $\nu_g = -1$ have the same spin and will, thus, equilibrate. Therefore, one bulk state equilibrates with one localised state underneath the split gates. Applying (7.20) for $\nu_{b,\uparrow} = 1$ and $\nu_{g,\uparrow} = 1$, we obtain $G_D = \frac{1}{2}\frac{e^2}{h}$. Adding $\frac{e^2}{h}$ from the transmitted edge channel leads to a total conductance of $G_D = \frac{3}{2}\frac{e^2}{h}$.

Case of $\nu_{QPC} = 0$ Fig. 7.9E presents the configuration of edge channels of the plateau at $\nu_{QPC} = 0$. All three bulk edge channels are backscattered and current is transferred only via equilibration between the states $\nu_b = 1$ and $\nu_g = -2$, and between the states $\nu_b = 2$ and $\nu_g = -1$, which have identical spins and are in the $N = 0$ Landau level (see

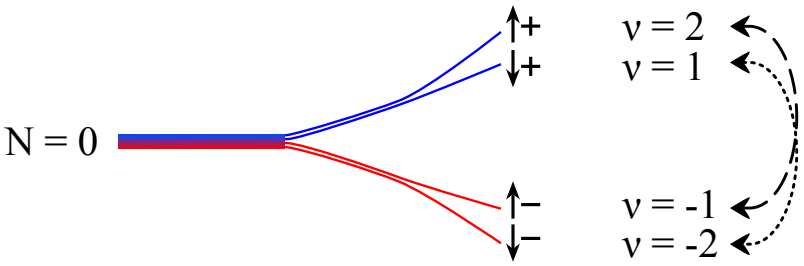

Figure 7.10: The lifting of first the valley and then the spin degeneracy leads to a splitting of the $N = 0$ Landau level into two electron and two hole states. These states are spin and valley polarised. We observe equilibration only within the $N = 0$ Landau level between sublevel of identical spin: $\nu = -2 \leftrightsquigarrow \nu = 1$ and $\nu = -1 \leftrightsquigarrow \nu = 2$.

Landau level diagram of Fig. 7.10). Applying eq. (7.20), we again distinguish the two spin configurations and count only the number of involved states which leads to:

- $\nu_{b,\downarrow} = 1$, $\nu_{g,\downarrow} = -1$ and $\nu_{QPC,\downarrow} = 0 \rightarrow G_{D,np'n,\downarrow} = \frac{1}{2}\frac{e^2}{h}$
- $\nu_{b,\uparrow} = 1$, $\nu_{g,\uparrow} = -1$ and $\nu_{QPC,\uparrow} = 0 \rightarrow G_{D,np'n,\uparrow} = \frac{1}{2}\frac{e^2}{h}$

The total conductance of $\frac{e^2}{h}$ complies with the observed plateau at $\nu_{QPC} = 0$.

Let us determine the conductance in a different configuration of $\nu_{QPC} < 0$.

Case of $\nu_{QPC} = -1$ Fig. 7.9F presents the configuration of edge channels for $\nu_{QPC} = -1$. All three bulk edge channels are backscattered. The first hole edge channel extends across the QPC connecting both sides of the split gates. Similar to the case of $\nu_{QPC} = 0$, current is only transported across the QPC via equilibration. We suppose that equilibration occurs between the states $\nu_b = 1$ and $\nu_g = -2$ and between the states $\nu_b = 2$ and $\nu_{QPC} = -1$ due to their identical spins (see Landau level diagram in Fig. 7.10). We apply (7.20) for the two spin configurations taking only into account the involved states:

- $\nu_{b,\downarrow} = 1$, $\nu_{g,\downarrow} = 0$ and $\nu_{QPC,\downarrow} = -1 \rightarrow G_{D,np'n,\downarrow} = \frac{1}{2}\frac{e^2}{h}$
- $\nu_{b,\uparrow} = 1$, $\nu_{g,\uparrow} = -1$ and $\nu_{QPC,\uparrow} = -1 \rightarrow G_{D,np'n,\uparrow} = \frac{1}{3}\frac{e^2}{h}$

The total conductance is $G_D = \frac{5}{6}\frac{e^2}{h} \simeq 0.83\frac{e^2}{h}$ which complies with the observed plateau of $G_D \simeq 0.85\frac{e^2}{h}$ at $\nu_{QPC} = -1$.

Our three examples of $\nu_{QPC} = 1$, 0 and -1 present an excellent agreement of eq. (7.20) to our data. Applying (7.20) on the full range of ν_{QPC} for $V_{sg} < 0$, we obtain the theoretical curves (dotted lines) in Fig. 7.9. We observe that the theoretical conductance is in good agreement with our data.

5 Spin selective equilibration of electronic states

In this section, we turn to the right side of the conductance map for $V_{sg} > 0$ in Fig. 7.3. The charge carrier density is now larger underneath the split gates than in the bulk. Therefore, the filling factor underneath the split gates is also higher than the one in the bulk ($\nu_g > \nu_b$) as illustrated in Fig. 7.11. In the following we consider the equilibration between electron edge channels originating from the bulk and those localised underneath the split gates.

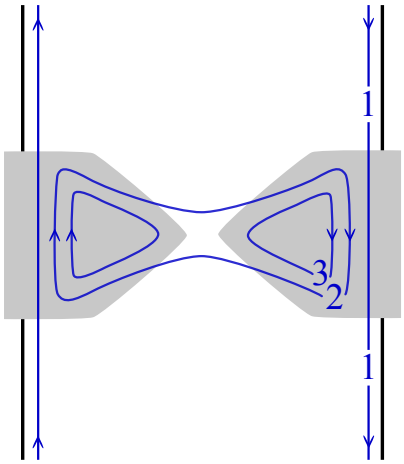

Figure 7.11: Schematic of edge channel configuration in the unipolar regime for $V_{sg} > 0$: Electron edge channels from the bulk pass underneath the split gates. The remaining edge channels $(\nu_g - \nu_b)$ are either localised underneath the split gates or extend across the QPC connecting both sides of the sample.

5.1 Configuration of equilibration

Since $\nu_b < \nu_g$, the electron bulk edge channels pass underneath the split gates as shown in Fig. 7.11 for the case $\nu_b = 1$, $\nu_g = 3$ and $\nu_{QPC} = 1$. The additional electron edge channels $(\nu_g - \nu_b)$ are either localised underneath the split gates ($\nu_g = 3$ in Fig. 7.11) or extend across the QPC ($\nu_g = 2$ in Fig. 7.11). The latter combines with its counterpart inside the QPC and connects the two edges of the sample leading to equilibration.

The equilibration between the bulk edge channel $\nu_b = 1$ in Fig. 7.11 with the split gate edge channel $\nu_g = 2$ would introduce backscattering and, thus, decrease the conductance. In contrast, equilibration between the states $\nu_b = 1$ and $\nu_g = 3$ does not introduce backscattering as it does not connect the left and right edges. Therefore, equilibration only has an impact on the conductance if the edge channels underneath the split gates extend across the QPC connecting the counter-propagating bulk edge channels and introducing backscattering.

The important filling factor which we need to consider is, thus, ν_{QPC}. It includes the number of bulk edge channels passing underneath the split gates plus the number of edge channels circulating across the QPC. In the following discussion, we focus, therefore, on the two filling factors ν_b and ν_{QPC}.

5.2 Comparison of experimental results to the theory

Fig. 7.12 presents the diagonal conductance as a function of ν_{QPC} for $\nu_b = 1$ to 4 extracted from the conductance map in Fig. 7.3. We observe several plateaus in each of the curve whose origin we discuss in the following.

Case of $\nu_b = 1$ The $\nu_b = 1$ curve has a large plateau of $G_D = \frac{e^2}{h}$ at $\nu_b = \nu_{QPC} = 1$ where the one bulk edge channel passes underneath the split gates. The conductance remains quantised at $\frac{e^2}{h}$ even for $\nu_{QPC} = 2$ when the second edge channel circulates across the QPC as shown in the drawing 7.12G. The fact that the conductance does not decrease indicates that no equilibration occurs between the states $\nu_b = 1$ and $\nu_{QPC} = 2$ which can be explained as they do not have the same spin (see Landau level diagram in Fig. 7.13).

We observe that the conductance of the $\nu_b = 1$ curve decreases to $0.7\frac{e^2}{h}$ at $\nu_{QPC} = 3$ suggesting that the $\nu_b = 1$ state equilibrates with the $\nu_{QPC} = 3$ state whose spins are

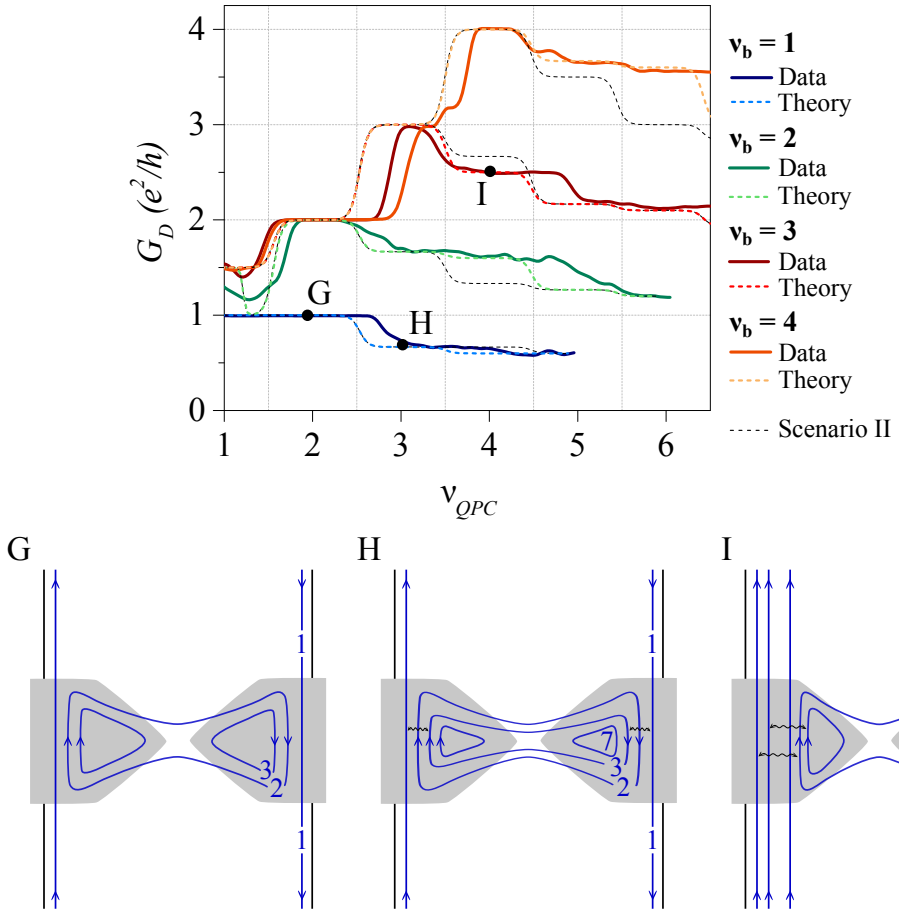

Figure 7.12: Results on the diagonal conductance extracted from the conductance map for $V_{sg} > 0$ of Fig. 7.3 at various bulk filling factors. The theoretical curves are calculated from (7.21) which includes that equilibration only occurs between states of identical spins. All coloured theoretical curves are based on scenario I which are in agreement to the data (see Landau level diagram in Fig. 7.13). The black dashed curves represent the solution of scenario II. Schematics of edge channel configurations: G and H: $\nu_b = 1$. **G**: $\nu_{QPC} = 2$, the bulk edge channel passes underneath the split gates while a second edge channel circulates across the QPC. The states $\nu_b = 1$ and $\nu_{QPC} = 2$ do not equilibrate due to their differing spins. **H**: $\nu_{QPC} = 3$, the third edge channel in the QPC equilibrates with the $\nu_b = 1$ state introducing backscattering. **I**: $\nu_b = 3$ and $\nu_{QPC} = 4$. The $\nu_b = 1$ state equilibrates with the $\nu_{QPC} = 4$ state leading to backscattering. The positions of the configurations G to I are labelled in the map of Fig. 7.5.

identical as shown in the configuration 7.12H. The backscattering causes the conductance to decrease.

In chapter 4 (sect. 4.3), we presented the results in high mobility graphene pnp-junction of the group of Goldhaber-Gordon [96]. They extended the partial equilibration regime in a pnp-junction (see sect. 4.2) to the case of spin selective equilibration. We adapt their conductance equation (4.8) to our Hall bar configuration equipped with a QPC:

$$G_{D,nn'n} = \frac{e^2}{h} \sum_{i=\downarrow,\uparrow} \frac{|\nu_{b,i}|\ |\nu_{QPC,i}|}{2|\nu_{QPC,i}| - |\nu_{b,i}|} \tag{7.21}$$

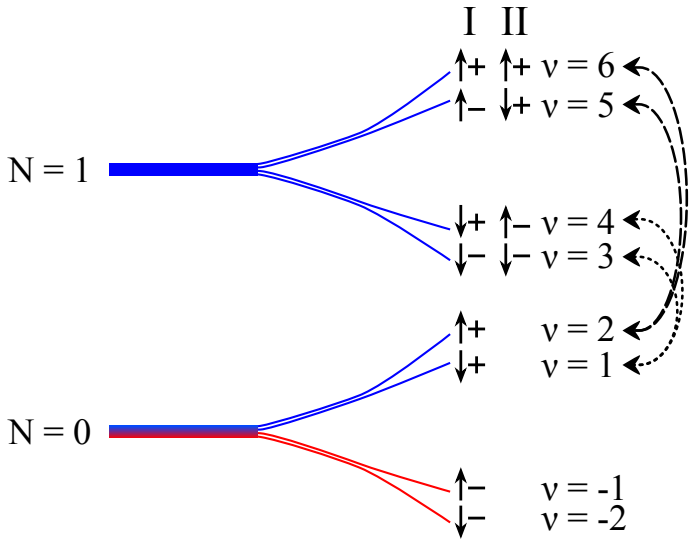

Figure 7.13: Diagram of the $N = 0$ and $N = 1$ Landau level. The two scenarios (I, II) indicate the two orders of the splitting of the degeneracies of the $N = 1$ Landau level. Equilibration occurs between the sublevels of identical spins indicated by the dashed and dotted arrows.

We come back to the $\nu_b = 1$ curve in Fig. 7.12 and use (7.21) to calculate the conductance for the equilibration between the states $\nu_b = 1$ and $\nu_{QPC} = 3$ by considering only the number of involved states for each spin configuration: For spin-up, we have $\nu_{b,\uparrow} = 1$ and $\nu_{QPC,\uparrow} = 2$ which contains the transmitted edge channel plus the edge channel across the QPC. For the spin-down, only one edge channel circulates across the QPC. For both configurations, we obtain:

- $\nu_{b,\uparrow} = 1$ and $\nu_{QPC,\uparrow} = 2 \quad \rightarrow G_{D,nn'n,\uparrow} = \frac{2}{3}\frac{e^2}{h}$
- $\nu_{b,\downarrow} = 0$ and $\nu_{QPC,\downarrow} = 1 \quad \rightarrow G_{D,nn'n,\downarrow} = 0$

The total conductance of $\frac{2}{3}\frac{e^2}{h}$ corresponds well to the observed plateau at $\nu_{QPC} = 3$.

To illustrate how the equilibration process provides information on the polarisation of the successive levels, let us discuss the case for $\nu_b = 3$.

Case of $\nu_b = 3$ The $\nu_b = 3$ curve exhibits a plateau at $G_D = \frac{3e^2}{h}$ when $\nu_b = \nu_{QPC} = 3$. Setting $\nu_{QPC} = 4$, the fourth edge channel will circulate across the QPC as shown in the configuration 7.12I. Here, we observe a decrease in the conductance to $2.49\frac{e^2}{h}$ which we explain by the equilibration between the states $\nu_b = 1$ and $\nu_{QPC} = 4$ due to their identical spins (see Landau level energy diagram in Fig. 7.13).

Spin selective equilibration depends on the order of the splitting of the degeneracies of spin and valley in the $N \geq 1$ Landau levels which we introduced in chapter 4 (sect. 4.3). The group of Goldhaber-Gordon suggests two possible scenarios of the order of the splitting of the first and higher Landau levels if either the spin or the valley symmetry is broken first. Scenario I assumes the spin degeneracy to lift first while scenario II suggests that the valley degeneracy is first lifted. In the Landau level diagram of Fig. 4.6, the two scenarios are indexed with I and II, each with its respective spin and valley configuration.

Using (7.21) for scenario I, we obtain a conductance of $G_{D,nn'n} = \frac{5}{2}\frac{e^2}{h}$. Scenario II leads to a conductance of $G_{D,nn'n} = \frac{8}{3}\frac{e^2}{h}$. We see that scenario I corresponds well to the data[2].

Table 7.1 summarises the measured diagonal conductance in comparison to the theoretical conductance obtained from eq. (7.21) for the scenarios I and II. We observe a clear similarity of our data towards scenario I.

Another clear way to compare our data with the theoretical conductance of (7.21) for the scenarios I and II is by adding the theoretical curves in Fig. 7.12. The coloured dashed curves are based on scenario I while the black dashed curves take scenario II into account (see Landau level diagram of Fig. 7.13). As seen in table 7.1, the theoretical curves of scenario I correspond well to our data.

In the unipolar regime, we determine that equilibration only occurs between states of identical spins analogue to the bipolar regime discussed in the previous section. However, in the unipolar regime, we do not observe any restriction to a single Landau level but equilibration extends from the $N = 0$ to the $N = 1$ Landau level.

Table 7.1: Results of the QPC in graphene in the unipolar regime for $V_{sg} > 0$ in comparison to eq. (7.21) for scenario I and II (see Landau level diagram in Fig. 7.13).

ν_b	ν_{QPC}	G_D measured $\left(\frac{e^2}{h}\right)$	$G_{D,nn'n}$ (I) $\left(\frac{e^2}{h}\right)$	$G_{D,nn'n}$ (II) $\left(\frac{e^2}{h}\right)$
1	2	0.99	1	1
	3	0.70	$\frac{2}{3} \simeq 0.67$	$\frac{2}{3} \simeq 0.67$
	4	0.65	$\frac{3}{5} = 0.60$	$\frac{2}{3} \simeq 0.67$
2	3	1.70	$\frac{5}{3} \simeq 1.67$	$\frac{5}{3} \simeq 1.67$
	4	1.62	$\frac{8}{5} = 1.60$	$\frac{4}{3} \simeq 1.33$
	5	1.45	$\frac{19}{15} \simeq 1.27$	$\frac{19}{15} \simeq 1.27$
3	4	2.49	$\frac{5}{2} = 2.50$	$\frac{8}{3} \simeq 2.67$
	5	2.20	$\frac{13}{6} \simeq 2.17$	$\frac{13}{6} \simeq 2.17$
	6	2.12	$\frac{21}{10} = 2.10$	$\frac{21}{10} = 2.10$
4	5	3.65	$\frac{11}{3} \simeq 3.67$	$\frac{7}{2} = 3.50$
	6	3.56	$\frac{18}{5} = 3.60$	3

2 Even though, the state $\nu_g = 5$ equilibrates with the state $\nu_b = 2$, the latter is localised underneath the split gates and, therefore, has no impact on the conductance.

6 Pinch-off of the QPC in the $N = 0$ Landau level

6.1 Pinch-off for $\nu_b = 2$

Let us discuss another interesting feature in the conductance maps of Fig. 7.3 and 7.5: We observe a triangular shaped feature at around $V_{sg} = 0\,\mathrm{V}$ ($\nu_g = 0$) and $V_{bg} = 3\,\mathrm{V}$. This feature becomes more pronounced in a theoretical conductance map in Fig. 7.16b which we will present in the next section.

This feature represents a region of "pinch-off" where bulk edge channels are no longer transmitted through the QPC and get backscattered. Fig. 7.14 presents the edge channel configuration in the centre of this triangle in which one bulk edge channel is transmitted and one backscattered. Since the second bulk edge channel transforms from being transmitted through the QPC to being backscattered, the right slope of the triangle is defined by ν_{QPC}.

When the $\nu_g = -1$ hole state is added underneath the split gates, the equilibration between the $\nu_b = 2$ electron state and the $\nu_g = -1$ hole state transfers current across the constriction, and the $\nu_b = 2$ edge channel is no longer fully pinched-off. The equilibration is induced by the adding of the $\nu_g = -1$ hole state, for which reason, the left slope of the triangle is defined by ν_g.

6.2 Full pinch-off of the QPC for $\nu_b = 1$

The data illustrated in the conductance map of Fig. 7.3 and its line-cuts in Fig. 7.6 were measured in current bias configuration. A voltage source together with a high shunt resistor R_{shunt} of $100\,\mathrm{M\Omega}$ constitutes a current source in which the current is fixed across the device if $R_{shunt} \gg R_{device}$. The voltage across the device is determined by the resistance of the device.

A resistance of the device of the order of $\frac{e^2}{h} = 25\,812\,\Omega$ at, for instance, $\nu_b = 1$ and $V_{sg} = 0\,\mathrm{V}$ to $5\,\mathrm{V}$ is much lower than R_{shunt}. In this configuration, with a current bias of $10\,\mathrm{nA}$ the voltage across the device is $26\,\mu\mathrm{V}$. This excitation translated into temperature scale is about $0.26\,\mathrm{K}$ which is above the base temperature of $0.05\,\mathrm{K}$ of our cryostat and, therefore, can lead to electron overheating.

When the QPC is fully closed, for instance, at $\nu_b = 1$ and $V_{sg} \simeq -2\,\mathrm{V}$ in Fig. 7.3, insulating behaviour with a large resistance is expected. In this region, in current bias

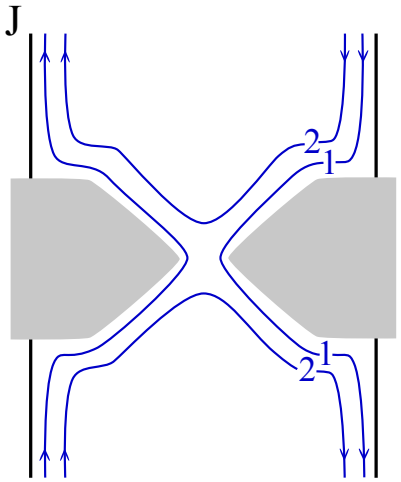

Figure 7.14: J: Pinch-off of the second bulk edge channel. The position of the configuration J is labelled in the map of Fig. 7.5.

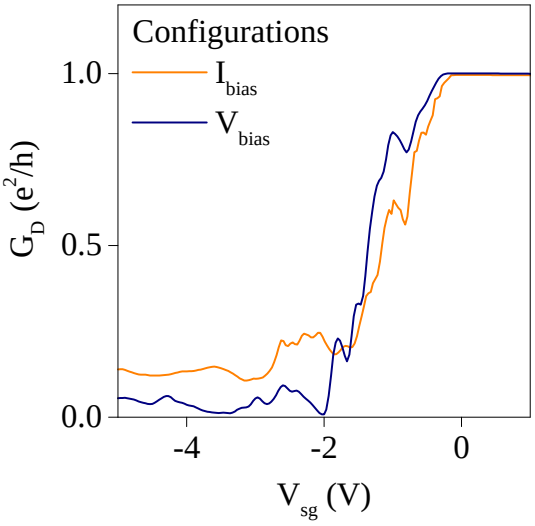

Figure 7.15: Comparison of current and voltage bias in the full pinch-off regime of high resistance ($V_{sg} < -2\,\mathrm{V}$). The blue curve of voltage bias drops almost completely to zero when the QPC is closed.

configuration, the voltage across the device increases to 1 mV which corresponds to a high excitation of 10 K and could overcome the gap between Landau levels in the QPC.

In this region of full pinch-off, the resistance of the device could be the order of R_{shunt} and the voltage excitation is much higher than the temperature of our measurement set-up. We thus switched to a voltage bias configuration while keeping the measurement of the diagonal voltage to get rid of the contact resistances. Here, the voltage across the device is fixed to, for instance, 15 µV used to measure the blue curve of $\nu_b = 1$ in Fig. 7.15.

The blue curve of $\nu_b = 1$ in Fig. 7.15 exhibits a plateau at $G_D = \frac{e^2}{h}$ at around $V_{sg} = 0$ before it drops almost completely to zero at $V_{sg} = -2.0\,\mathrm{V}$. In this measurement of voltage bias, the nearly full pinch-off of the QPC is well visible in contrast to the orange curve of $\nu_b = 1$ measured in current bias.

7 Conclusion on the QPC in high field

7.1 Summary of the different regimes

In the previous sections we discussed in detail the conductance map presented in Fig. 7.16a measured at 7 T. The map can be divided into three regions (I, II and III) based on the presence or absence of equilibration and the participating equilibrating edge channels.

Region I For $V_{sg} < 0$ in region I, we observed that the conductance is determined by the equilibration which occurs only between quantum Hall states of identical spins and within the $N = 0$ Landau level. In this region, the diagonal conductance is determined by eq. (7.20) which depends on the three filling factors ν_b, ν_g and ν_{QPC}.

Region II For $V_{sg} < 0$ in region II, the graphene underneath the split gates is depleted forcing bulk edge channels to pass through the constriction of the QPC. In the absence of equilibration, the conductance is directly proportional to the number of transmitted edge channels, that is, to the filling factor in the QPC given by eq. (7.2). This is the region of ideal QPC operation with selective transmission of quantum Hall edge channels.

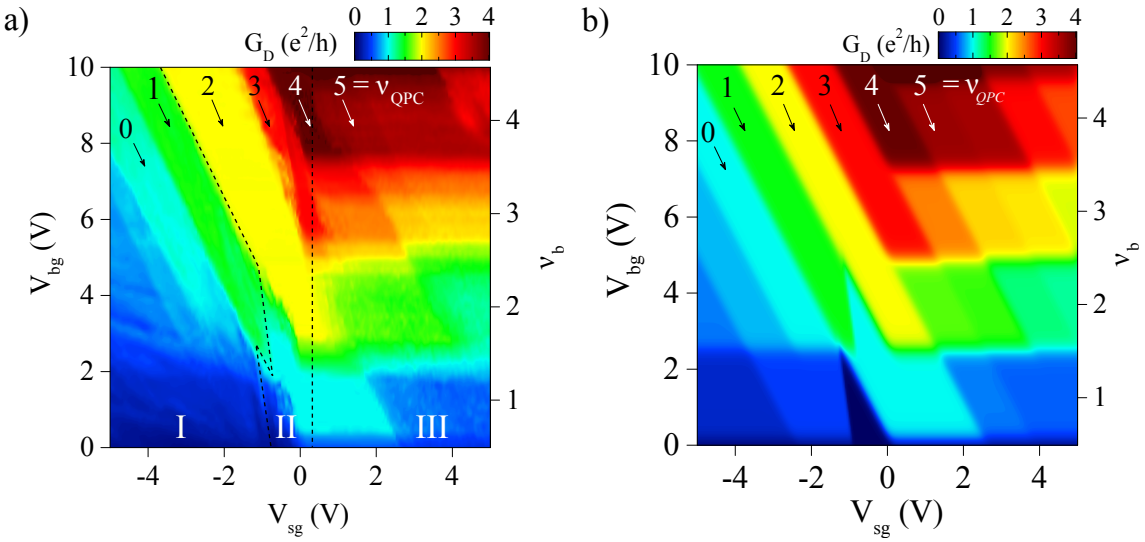

Figure 7.16: A comparison between a) the experimental measurement at 7 T and b) the theoretical prediction of (7.20) and (7.21) are in excellent agreement. The dashed line in a) divides the map into three regions (I, II, III) based on the absence or presence of equilibration and the participating edge channels.

Region III This region corresponds to $V_{sg} > 0$: The charge carrier density underneath the split gates is higher than in the bulk and, hence, $\nu_g > \nu_b$. We observed that equilibration occurs between the electronic states of bulk and split gates of identical spins which is in good agreement with eq. (7.21) and the results of a high mobility graphene pnp-junction of the group of Goldhaber-Gordon, including the type of scenario for the degeneracy lifting [96].

Based on equations (7.20) and (7.21) of spin selective equilibration, we calculated the conductance in the full range of backgate and split gate voltages resulting in the theoretical conductance map presented in Fig. 7.16b. The theoretical model exhibits diagonal strips ($V_{sg} < 0$) and horizontal strips ($V_{sg} > 0$) of quantised conductance which comparing with our results in Fig. 7.16a, is in excellent agreement with our measured data.

7.2 Equilibration limited by the Landau level

We determined that equilibration in the bipolar regime of $V_{sg} < 0$ is limited to the $N = 0$ Landau level. The cyclotron gap between the $N = 0$ and $N = 1$ Landau level of the order 1500 K is one order of magnitude larger than the gap between electron and hole states, being about 200 K at 15 T [51] which may explain why we do not observe any equilibration between electron and hole states outside of the $N = 0$ Landau level.

However, in the unipolar regime of $V_{sg} > 0$, equilibration is not restricted to the $N = 0$ Landau level but occurs also with higher Landau levels. In this regime, we observe the same spin selective equilibration than the group of Goldhaber-Gordon [96]. Equilibration occurs underneath the split gates near the edge of the graphene. The crystallographic edge induces disorder which causes inelastic scattering leading to equilibration between edge channels of different Landau levels.

In the bipolar regime equilibration takes places along the pn-interface which is far away from the edge of the graphene and therefore, due to the absence of disorder inelastic

scattering between edge channels of different Landau levels, is suppressed. However, we still observe equilibration between electron and hole states in the $N = 0$ Landau level. At the pn-interface, the in-plane electric field of the split gates causes the Landau levels to collapse which according to [122] leads to a smaller gap at $\nu = 0$.

7.3 Absence of conservation of the valley polarisation

We do not observe any selective equilibration due to the valley index indicating that the valley polarisation is not conserved in the process of equilibration.

In the unipolar regime, the vicinity to the crystallographic edge of the graphene may induce intervalley scattering causing states of different valley polarisation to equilibrate. The group of Goldhaber-Gordon argued that the plasma etched edges of the graphene are disordered and induce, therefore, strong intervalley scattering [96]. In our case, the graphene edges are not etched close to the region of equilibration but intervalley scattering is still enhanced at the crystallographic edge of the graphene.

However, in the bipolar regime, equilibration occurs along the pn-interface far away from the graphene edge. Since our QPC device shows clear signatures of ballistic transport (see chapter 6 in sect. 6.3), we assume that the amount of disorder is minor and, hence does not explain the equilibration of states of different valleys.

The valley polarisation has so far never been experimentally determined. So far we assumed that breaking of the valley symmetry leads to two valley singlet states, one polarised in K and the other one in K'. However, it could also be that the breaking leads rather to two mixed states of K and K'. In this case, a distinction between the polarisation of K and K' is not possible. Many aspects of the nature of the lifting of the degeneracy of the valley are still open and under debate.

8 Equilibration of degenerate quantum Hall states

In the last part of this chapter, we adapt the theoretical approach of equilibration of edge channels of (7.19) and (7.21) to the degenerate quantum Hall states in low magnetic fields. At 1.5 T, the spin and valley symmetry is not broken, and we observe the usual series of plateaus at the filling factor $\nu_b = 4\left(N + \frac{1}{2}\right)$.

Fig. 7.17 presents the diagonal conductance measured at 1.5 T as a function of the filling factor in the QPC for $\nu_b = 2$, 10 and 18. In the following, we focus on the red curve of $\nu_b = 10$ in our discussion.

Equilibration in the bipolar regime At point A, we observe a conductance of about $2.66\frac{e^2}{h}$. The corresponding configuration 7.18A shows that two degenerate bulk edge channels are transmitted and the rest of them are backscattered. In this configuration, if no equilibration occurs between the electron and hole states, the conductance is expected to be $\frac{2e^2}{h}$ according to (7.2). Since the observed conductance is higher, equilibration occurs between the backscattered bulk edge channels and the localised hole states leading to an additional current flow across the QPC.

At point B in Fig. 7.17, the conductance increases to $6\frac{e^2}{h}$ as expected at $\nu_{QPC} = 6$. Thus, we do not observe any equilibration at this point. As the $\nu_b = 10$ degenerate edge channel is backscattered as shown in the configuration Fig. 7.18B, we conclude that it

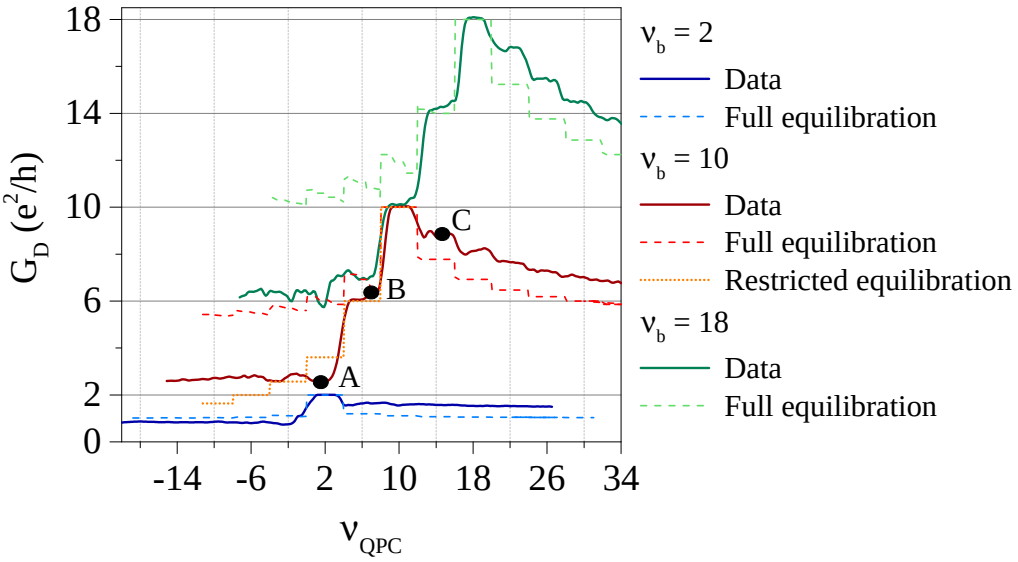

Figure 7.17: The experimental results on G_D versus ν_{QPC}) (solid lines) measured at 1.5 T and at 0.05 K are compared with theoretical predictions (dashed lines) of (7.19) and (7.21) in the equilibration of degenerate quantum Hall states. We observe that when equilibration is restricted to the $N = 0$ and $N = 1$ Landau levels, the resulting orange curve of restricted equilibration is close to our data.

does not equilibrate with localised states.

For $\nu_{QPC} < 10$ (including the points A and B), the theoretical dashed curves marked as "full equilibration" in Fig. 7.17 are calculated from eq. (7.17) without any spin selection. We observe that these theoretical curves predict a higher conductance than we have measured. The lower measured conductance suggests that less equilibration occurs than theoretically assumed. If the backscattered bulk edge channels equilibrate less efficiently with the hole states of the split gates, less current is transported across the hole doped region and the QPC which leads to a lower conductance.

One way to reduce the equilibration is to restrict the number of mixing states. In the orange dotted curve in Fig. 7.17, as we have seen that $\nu_b = 10$ does not equilibrate with hole states, we assume equilibration only between the bulk states $\nu_b = 2$ and 6 with the hole states $\nu_g = -2$ and -6 of the split gates. We observe that the height of the theoretical curve fits already better to the data. We therefore conclude that equilibration seems to be restricted to the $N = 0$ and $N = 1$ Landau levels.

Equilibration in the unipolar regime When $\nu_{QPC} > 10$, the charge carrier density is higher underneath the split gates than in the bulk and, hence, $\nu_g > \nu_b$. At point C, the conductance is about $8.8\frac{e^2}{h}$. In this region, all bulk edge channels pass beneath the split gates and the additional $(\nu_g - \nu_b)$ split gate states either remain localised underneath them or extend across the QPC connecting both sides of the sample as presented in Fig. 7.18C. Equilibration between the electron states of the bulk and split gates introduces backscattering of the bulk edge channels and hence reduces the conductance.

The theoretical curve for $\nu_{QPC} > 10$ is calculated from (7.21) without spin selection. We

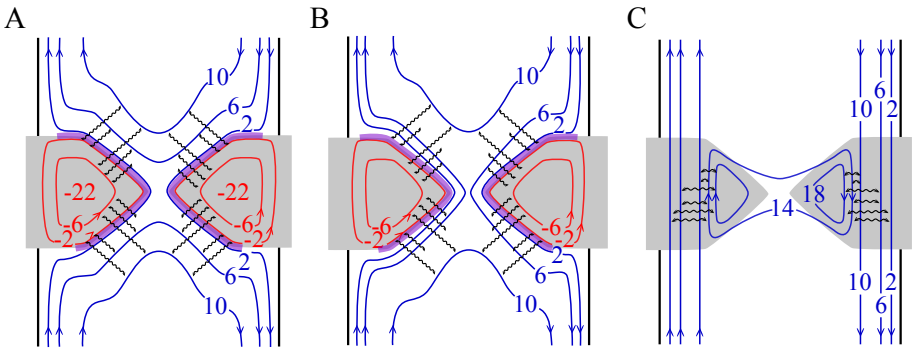

Figure 7.18: Schematics of edge channel configurations of $\nu_b = 10$ of Fig. 7.17. A: The backscattered bulk edge channels equilibrate with the hole states of the split gates and in the QPC leading to a current transport across the QPC. The states of 2 and -2 belong to the same Landau level which causes them to be completely mixed at the pn-interface. B: The electron edge channels of the bulk are partially transmitted and partially backscattered. The latter equilibrates with the hole states underneath the split gates. C: The additional edge channels of the split gates circulate across the QPC connecting both sides of the sample. Their equilibration with the bulk edge channels introduces backscattering.

observe that the theoretical curve is lower than the data which means that equilibration is less efficient than expected in theory.

We observe that the theoretical curves of "full equilibration" in Fig. 7.17 give a conductance that is much higher for $\nu_{QPC} < 10$ and much lower for $\nu_{QPC} > 10$ than our experimental data. In both cases, equilibration is less efficient than expected from theoretical models of (7.17) and (7.21).

In the previous sections, we presented the equilibration of spin polarised quantum Hall states in high magnetic fields where the presence of equilibration enables a complete understanding of the data. Here, equilibration between electron and hole states is restricted to the $N = 0$ Landau level. Our observations at low magnetic field that equilibration in the bipolar regime is restricted to the $N = 0$ and $N = 1$ Landau levels is consistent with the high field regime. At 1.5 T, the cyclotron gap between $N = 0$ and $N = 1$ Landau levels is reduced to half of its size to 490 K in comparison to 1060 K at 7 T which may explain why the $N = 1$ Landau level is additionally included in equilibration.

Summary

In the course of this chapter, we studied the influence of the QPC on the transport properties of high mobility graphene. In the first part, we derived the capacitive coupling of the split gates to the graphene from zero magnetic field measurements which is crucial for determining the local filling factor underneath the split gates in the quantum Hall regime.

In the main part of this chapter, we studied the selective transmission and equilibration of quantum Hall edge channels in the QPC in the case of full lifting of the degeneracies. By changing the voltage on the split gates, we were able to selectively transmit integer quantum Hall edge channels. In the bipolar regime, we observe that equilibration between electron and hole states is limited to states of identical spin polarisation within the $N = 0$ Landau level. We adapted, therefore, the calculation of the full equilibration regime in a pnp-junction in graphene to the case of a QPC including the three filling factors (ν_b, ν_g,

ν_{QPC}).

In the bipolar regime, equilibration between electron edge channels occurs between states of identical spin polarisation but with no restriction of Landau level.

In the last part, we applied the calculations to the equilibration of degenerate edge channels in low magnetic field. We observe that in this regime the equilibration is slightly more efficient than at high field and partially involves equilibration between $N = 0$ and $N = 1$ Landau levels in the bipolar regime (but not to the $N = 2$ Landau level). This is consistent with the equilibration restricted to the $N = 0$ Landau level at high field when the cyclotron gap is increased.

The selective transmission of edge channels allows us to bring edge channels in close proximity to one another in order to study their inter-edge tunnelling. In this way, it is possible to probe the nature of the edge channels especially in the fractional quantum Hall regime. In the next chapter, we will study the tunnelling between fractional edge channels to investigate their nature as a one-dimensional Luttinger liquid.

CHAPTER 8

SELECTIVE TRANSMISSION AND TUNNELLING OF FRACTIONAL EDGE CHANNELS

A quantum point contact in the quantum Hall regime offers an ideal system to study the tunnelling of charge carriers between counter-propagating integer and fractional edge channels. In the case of the fractional quantum Hall effect, edge channels are comprised of highly correlated, one-dimensional fermions which are described by the theory of Tomonaga-Luttinger. In this chapter, we first present our results on the fractional quantum Hall effect in the QPC in graphene and demonstrate that the transmission of fractional edge channels can also be controlled by the QPC. We then turn to the tunnelling of fractional edge channels and present briefly the theory of the so-called Luttinger liquid and the theoretical prediction for the tunnelling of electrons and quasi-particles in a QPC in the fractional quantum Hall regime. Afterwards, we review some experimental results of quasi-particle tunnelling of fractional states in a QPC in GaAs-AlGaAs heterostructures.

In the last part of this chapter, we present our results on the tunnelling between fractional quantum Hall edge channels in our QPC device in graphene. We focus on the fractional state of $\nu = \frac{7}{3}$ which provides an analogue of the Laughlin $\frac{1}{3}$ state, to explore the tunnelling characteristics as a function of temperature.

1 Selective transmission of fractional quantum Hall edge channels

At a magnetic field of 14 T, we observe fractional quantum Hall states of the series of composite fermions which we presented in chapter 6 (sect. 6.4.2). In chapter 7 (sect. 7.3), we demonstrated that the QPC can control the transmission probability of the integer quantum Hall edge channels in region II. The diagonal conductance is then directly proportional to the number of transmitted edge channels and, hence, to ν_{QPC}. We now examine the effect of the QPC on fractional quantum Hall states.

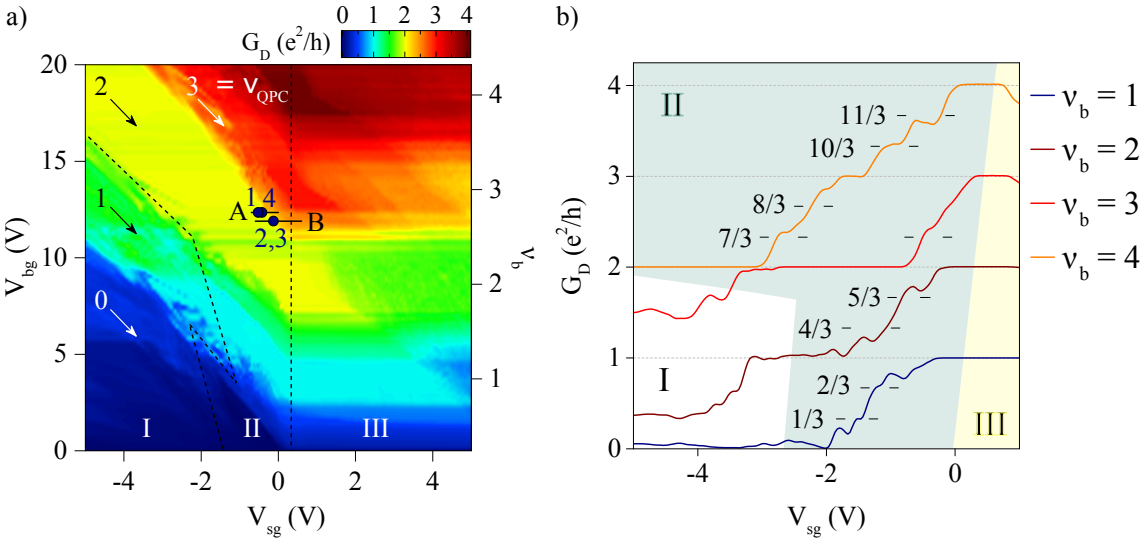

Figure 8.1: a) Diagonal conductance is plotted as a function of backgate and split gate voltages at 14 T and 0.05 K. The dotted lines show the outline of the three regions of transmission and equilibration. The lines A and B show the position of the IV measurements in Fig. 8.10 and the numbered dots mark the positions of the tunnelling conductance peaks which we will discuss in this chapter. b) Curves of diagonal conductance as a function of the split gate voltage extracted from a) at $\nu_b = 1$ to 4 present the selective transmission of fractional quantum Hall edge channels in region II.

Fig. 8.1a presents a conductance map as a function of backgate and split gate voltages measured at a magnetic field of 14 T and a temperature of 0.05 K. With its diagonal strips for $V_{sg} < 0$ and parallel strips for $V_{sg} > 0$, the map resembles the conductance map at 7 T (see Fig. 7.3) which we analysed and obtained a full understanding of in chapter 7. As for the 7 T data of Fig. 7.3, we divide the conductance map in Fig. 8.1a into three regions (I, II and III): transmission of edge channels, equilibration in the unipolar regime and equilibration in the bipolar regime.

Fig. 8.1b presents the diagonal conductance as a function of the split gate voltage extracted from Fig. 8.1a for $\nu_b = 1$ to 4. First, we observe conductance plateaus at integer multiples of $\frac{e^2}{h}$ in analogy to the results at 7 T in Fig. 7.6b. In between these integer plateaus, we also observe plateaus of fractional states. To determine if these fractional plateaus are, indeed, transmitted through the constriction of the QPC, we divide the curves of Fig. 8.1b into the three regions (I, II and III). The following fractional plateaus are observed in region II:

- $\nu_b = 4$: $\frac{7}{3}$, $\frac{8}{3}$, $\frac{10}{3}$ and $\frac{11}{3}$
- $\nu_b = 3$: $\frac{7}{3}$
- $\nu_b = 2$: $\frac{4}{3}$ and $\frac{5}{3}$
- $\nu_b = 1$: $\frac{1}{3}$ and $\frac{2}{3}$

In this region of ideal QPC operation, the fractional edge channels are transmitted through the constriction of the QPC and the QPC can control the transmission probability of these fractional edge channels. These data thus provide the first demonstration of a QPC effect on fractional quantum Hall edge channels in graphene.

2 Theory on the tunnelling of fractional edge channels

2.1 One-dimensional Luttinger liquid

We have seen in the first chapter (sect. 1.2) that the fractional quantum Hall effect cannot be explained in terms of a non-interacting Fermi liquid of electrons. X.G. Wen demonstrated, instead, that the edge excitations can be described by the theory of the Luttinger liquid [123–125] which defines one-dimensional interacting fermions [126]. The specific feature of the quantum Hall regime is that the chiral nature of the charge carrier transport separates the usual right and left movers of the Luttinger liquid onto the two opposite edges of the sample. Edge channel excitations in the fractional quantum Hall effect are, thus, referred to as a chiral Luttinger liquid [127].

In 1996, F.P. Milliken and C.P. Umbach presented the first indication that fractional quantum Hall edge channels can be described by Luttinger liquid theory [128]. However, given the very small number of tunnelling experiments performed in the fractional quantum Hall regime since then, there are still many open questions about the structure of fractional edge channels. For instance, Laughlin states of the series $\nu = \frac{1}{m}$ are expected to follow the chiral Luttinger liquid theory for tunnelling, but basic theoretical parameters such as the fractional charge of the quasi-particles could not be convincingly determined by transport

measurements[1]. The picture becomes even more complicated for fractional states of the hierarchical series in which multiple modes propagate in opposite directions on the same edge [123, 131].

One way to directly explore this rich physics is to use a QPC to performing tunnelling experiments. This enables to bring edge channels which originate from opposite sides of the sample close together. We can then control tunnelling between chiral Luttinger liquids which acts as a single scattering centre for the left and right movers. In the following, we discuss the physics of tunnelling between fractional edge channels.

2.2 Tunnelling of edge channels

The tunnelling between quantum Hall edge channels is determined by two limits of weak backscattering and weak tunnelling. In a QPC geometry, these two limits correspond to the nearly open QPC (full transmission) and to the nearly closed QPC (full reflection), respectively.

For the case of a nearly closed QPC, the weak tunnelling limit corresponds to a small tunnelling current between the almost fully backscattered edge channels (sketched in Fig. 8.2a). The weak backscattering limit which is pictured in Fig. 8.2b describes the case where a small tunnelling current enables charge transfer from one edge channel to the other, leading to weak backscattering.

The major difference between these two limits is the following: Weak tunnelling leads to tunnelling of electrons through vacuum whereas weak backscattering involves quasi-particle tunnelling through the quantum Hall fluid from one edge to the other.

In the following we present the specific temperature dependence of the tunnelling conductance for the two limits and their relations with the filling factor of the fractional quantum Hall states. The discussion is based on [127].

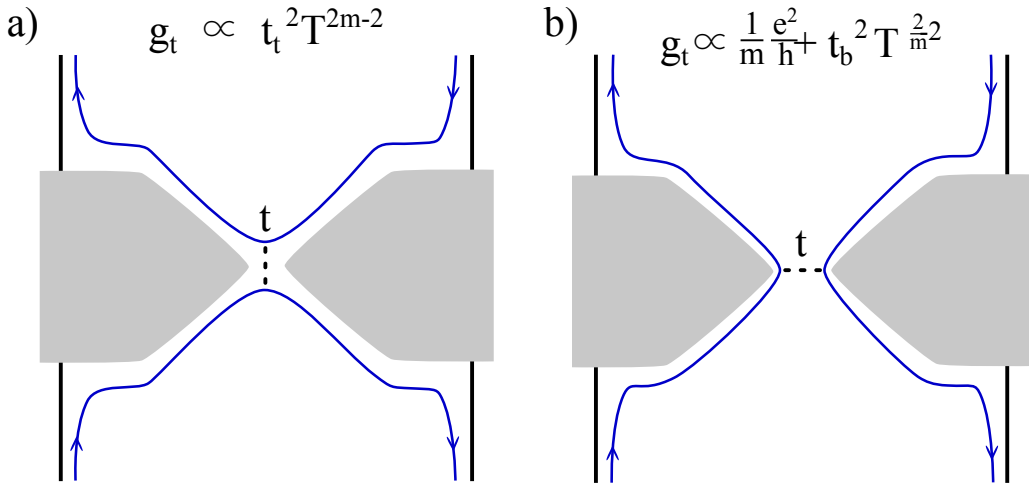

Figure 8.2: The two limits of tunnelling in a QPC are a) weak tunnelling of electrons (nearly closed QPC) and b) weak backscattering of quasi-particles (nearly open QPC).

1 The determination of the fractional charge in the fractional quantum Hall regime has been firmly done otherwise by shot noise experiments [129, 130].

2.2.1 Weak tunnelling limit

We consider here the limit of a nearly closed QPC where a small tunnelling coupling still enables charge transfer between the two backscattered edge channels. Such a process involves tunnelling of electrons through vacuum of the nearly depleted constriction.

The temperature dependence of the tunnelling conductance is completely different for the integer and fractional quantum Hall regime. In the case of the integer quantum Hall effect, the Fermi-liquid is composed of non-interacting electrons which allows the application of the Landauer-Büttiker formalism introduced in the first chapter (sect. 1.3). The conductance possesses ohmic behaviour and is proportional to the tunnelling probability $T_r = |t_t|^2$ in agreement with (1.10). In this regime, the conductance is independent of the temperature and remains constant for $T \to 0$ as shown by F.P. Milliken et al in Fig. 8.3a for $\nu = 1$.

In the fractional quantum Hall regime, the fractional edge channel is a 1D Luttinger liquid of highly correlated electrons. One of the key properties of such a 1D Luttinger liquid is the non-constant density of states which vanishes at the Fermi level as a power law. Theory also predicts a non-ohmic tunnelling conductance of the form [132]

$$g_T \propto {t_t}^2 \, |V|^{2m-2}$$

for the fractional state $\nu = \frac{1}{m}$. The temperature dependence of the conductance derived from Fermi's golden rule gives

$$\boxed{g_T \propto {t_t}^2 \, T^{2m-2}} \tag{8.1}$$

As a result, the conductance of the $\nu = \frac{1}{3}$ vanishes for $T \to 0$ with a power law of $g_T \propto T^4$.

The difference in behaviour of the conductance upon cooling of the tunnelling within

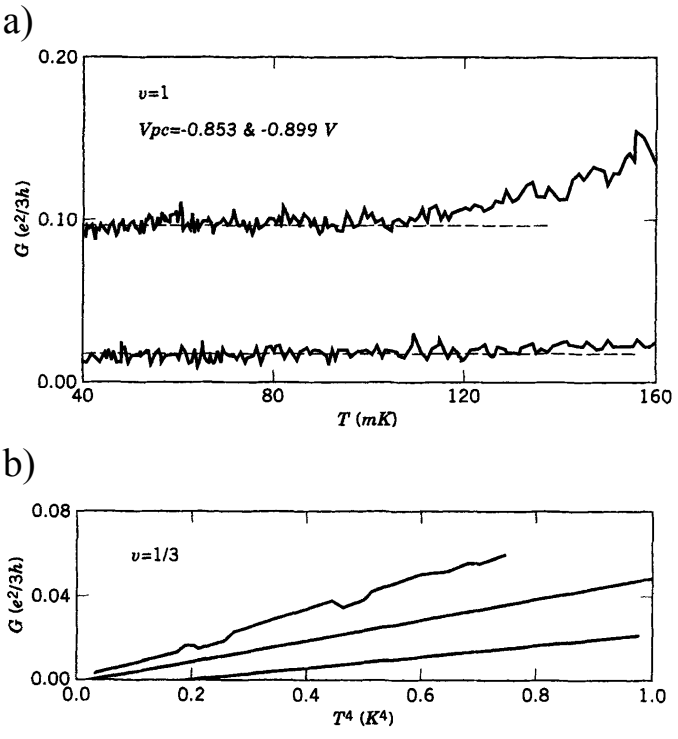

Figure 8.3: Temperature dependence in the weak tunnelling limit of the a) integer QH effect at $\nu = 1$ and b) fractional QH effect at $\nu = \frac{1}{3}$. While the integer state stays constant with decreasing temperature, the fractional state has a clear temperature dependence of T^4 for $\nu = \frac{1}{3}$. Fig. taken from [127, 128]

integer and fractional quantum Hall edge channels was demonstrated by F.P. Milliken and C.P. Umbach [128]. The conductance of an integer state stays constant with decreasing temperature (see Fig. 8.3a). The $\frac{1}{3}$ fractional state shows a temperature dependence of the conductance of $g_T \propto T^4$ in the low-temperature regime presented in Fig. 8.3b. The good agreement of the temperature dependence of the conductance of the $\frac{1}{3}$ state to the theoretical prediction of (8.1) was one of the first indication of the Luttinger liquid behaviour in the fractional quantum Hall regime [128].

2.2.2 Weak backscattering limit

In the second limit, the QPC is almost completely open. The configuration of weak backscattering is presented in Fig. 8.2b. The transmitted edge channels are brought in close proximity by the QPC so that tunnelling occurs between the left and right edge channels. The charges which tunnel through the quantum Hall liquid are Laughlin quasi-particles carrying a fractional charge $e^* = \frac{e}{m}$.

The tunnelling between the transmitted edge channels introduces backscattering which lowers the conductance. The weak backscattering limit treated perturbatively for an ideal Luttinger liquid gives a backscattered current of [133]

$$I_{back} \propto {t_b}^2 \ |V|^{\frac{2}{m}-2}$$

which includes the tunnelling probability ${t_b}^2$. The resulting temperature dependence of the conductance reads [127]

$$\boxed{g_T - \frac{1}{m}\frac{e^2}{h} \propto {t_b}^2 \ T^{\frac{2}{m}-2}} \tag{8.2}$$

In the fractional quantum hall regime, for $m > 1$, we see that the conductance diverges at low temperature. Therefore, the rate of quasi-particle tunnelling increases at low temperature in contrast to electron tunnelling. Consequently, on lowering the temperature for a fixed QPC constriction, the divergence of the tunnelling conductance tends to a limit of fully pinched off QPC. Such behaviour is quite striking as the QPC saddle point potential stays unchanged.

2.2.3 Nonlinear regime in the weak backscattering limit

X.-G. Wen studied the non-linear regime of the differential tunnelling conductance g_T and derived an expression for g_T as a function of temperature and bias voltage [134, 135]:

$$g_T(T,I_{dc}) = AT^{(2g-2)}F\left(g,\frac{e^*I_{dc}R_{xy}}{k_BT}\right) \tag{8.3}$$

with

$$F(g,x) = B\left(g+i\frac{x}{2\pi},g-i\frac{x}{2\pi}\right)\left[\pi\cosh\left(\frac{x}{2}\right) - 2\sinh\left(\frac{x}{2}\right)\mathrm{Im}\left[\Psi\left(g+i\frac{x}{2\pi}\right)\right]\right]$$

which includes the Euler beta function $B(x,y)$ and the digamma function $\Psi(x)$ as well as the fractional charge e^*. The Coulomb interaction parameter g is given by $g = \frac{{e^*}^2}{\nu e^2}$ [136]. For the Laughlin fractional states of $\nu = \frac{1}{m}$, the two latter parameters read $e^* = \frac{e}{m}$ and

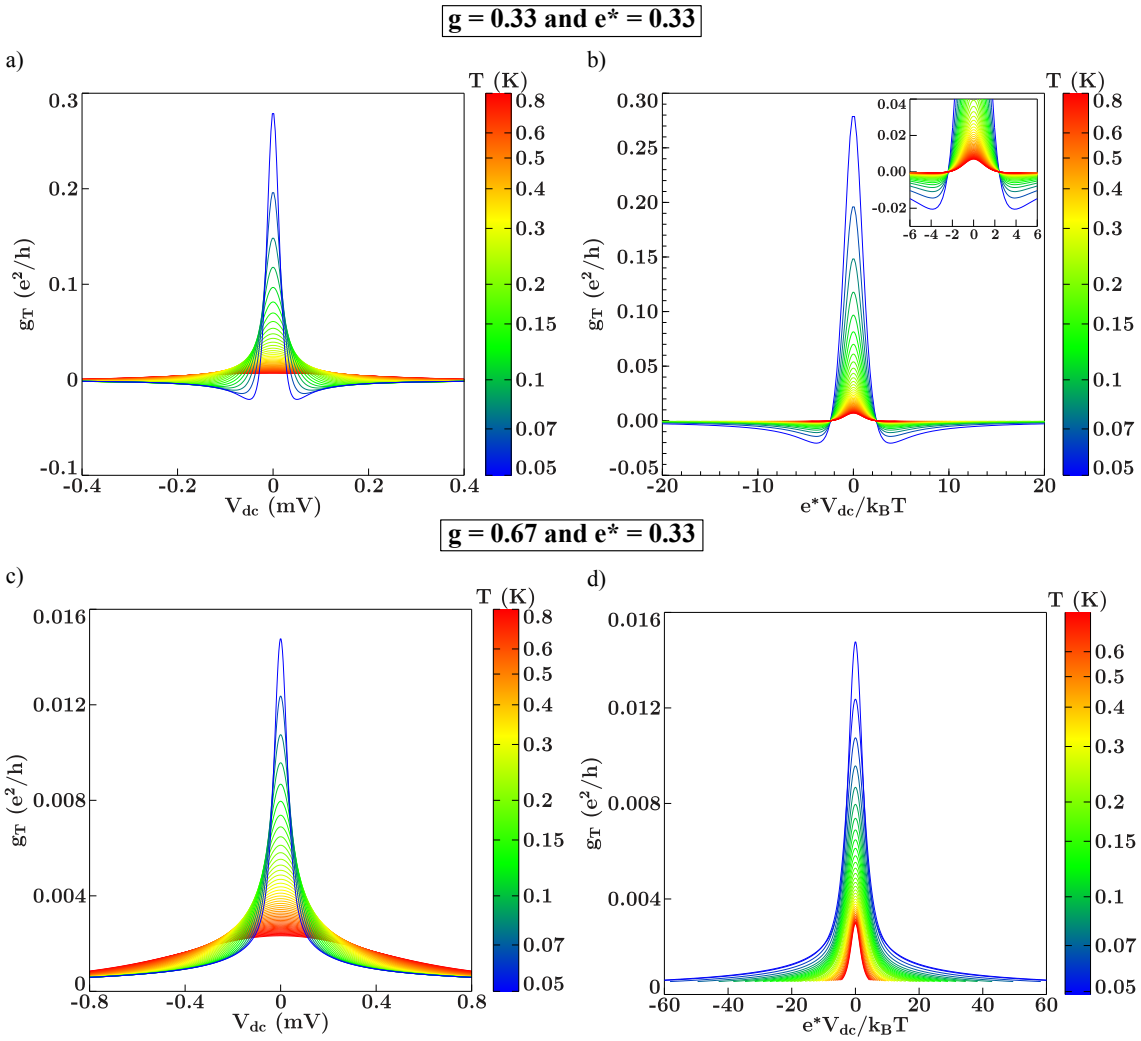

Figure 8.4: a) Theoretical curve of the differential tunnelling conductance of (8.3) for $g = \frac{1}{3}$ and $e^* = \frac{1}{3}$. The peak and the two side-dips decrease with increasing temperature. b) For g_T versus $\frac{eV_{dc}}{k_BT}$, the undershoots are at the same position of the x-axis (see zoom in inset), and hence the energy scale for all curves is the same. c) Theoretical curve of g_T of (8.3) for $g = \frac{2}{3}$ and $e^* = \frac{1}{3}$. The two undershoots on each side of the peak vanish for $g > 0.5$. d) The curves of g_T versus $\frac{eV_{dc}}{k_BT}$ for $g = \frac{2}{3}$ and $e^* = \frac{1}{3}$ at various temperatures do neither cross each other nor have undershoots on each side of the central peak.

$g = \frac{1}{m} = \nu$.

Fig. 8.4 presents the theoretical curves calculated from eq. (8.3) for the two cases of $g = \frac{1}{3}$ and $g = \frac{2}{3}$ keeping $e^* = \frac{e}{3}$.

Case of $g = \frac{1}{3}$ and $e^* = \frac{e}{3}$ The theoretical curves of g_T for various temperatures are presented in Fig. 8.4a for $g = \frac{1}{3}$ and $e^* = \frac{e}{3}$. The value of these two parameters are expected for the $\nu = \frac{1}{3}$ Laughlin state. We observe a zero-bias peak whose height decreases as a power law of $g_T \propto T^{-\frac{4}{3}}$ with increasing temperature (coefficient $T^{(2g-2)}$ in (8.3)). At high temperatures ($> 0.5\,\mathrm{K}$), this peak disappears and the Ohmic IV behaviour of a constant conductance is nearly recovered.

We observe undershoots on each side of the zero-bias peak. The conductance of these

undershoots become less negative with increasing temperature. Above $|V_{dc}| \gtrsim 0.3\,\mathrm{V}$, all curves saturate at zero tunnelling conductance.

In Fig. 8.4b, the theoretical curves of g_T are directly retraced as a function of $\frac{eV_{dc}}{k_B T}$. We see that the undershoots on each side of the peak are at the same energy scale of $\frac{e^* V_{dc}}{k_B T} \simeq 3.8$.

Case of $g = \frac{2}{3}$ and $e^* = \frac{e}{3}$ Fig. 8.4c presents curves of the theoretical tunnelling conductance as a function of the bias voltage for $g = \frac{2}{3}$ while keeping the same $e^* = \frac{1}{3}$. The undershoots on each side of the zero-bias peak are absent.

Keeping the parameters of $g = \frac{2}{3}$ and $e^* = \frac{1}{3}$, Fig. 8.4d presents g_T as a function of $\frac{eV_{dc}}{k_B T}$. In contrast to Fig. 8.4b in which $g < 0.5$, the curves of different temperatures do not cross at a single point due to the absence of undershoots on each side of the peak.

From eq. (8.3) and the theoretical curves of Fig. 8.4, we can estimate the influence of the two parameters g and e^* by the form of the zero-bias peak. The parameter e^* influences the width of the peak and, therefore, the energy scale: The smaller e^*, the wider the peak. The parameter g changes the width and the height of the peak but, most importantly defines the presence and size of the undershoots on each side of the peak. For $g > 0.5$, these undershoots vanish.

Consequently, this theory should in principle allow the extraction of the fractional charge by fitting the IV characteristics and verifying the relation between the filling factor and the interaction parameter g in the temperature dependence of the zero-bias peak.

2.2.4 Transition between the limits

So far we have seen that the tunnelling conductance transits from weak backscattering to weak tunnelling, hence, from a nearly open QPC to an almost closed QPC with decreasing temperature.

Therefore, since weak tunnelling dominates the low temperature regime, the tunnelling conductance is predicted to vanish as $g_T \propto T^{2m-2}$ for $T \to 0$, and the system becomes insulating.

At high temperature, weak backscattering is predicted to dominate, and, therefore, the conductance is given by $g_T \propto \frac{1}{m}\frac{e^2}{h} - {t_b}^2\, T^{\frac{2}{m}-2}$. The transition between the two limits is

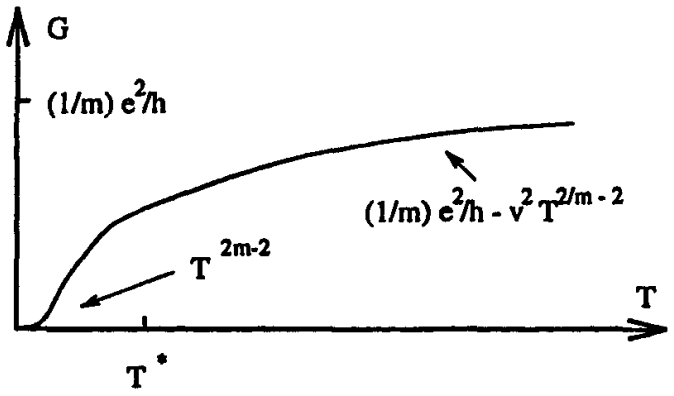

Figure 8.5: Full temperature dependence of the tunnelling conductance. In low T, the weak tunnelling limit dominates while at high T, the weak backscattering limit controls the conductance. Fig. taken from [127]

predicted to be at

$$T^* \propto {t_b}^{\frac{m}{m-1}}$$

Fig. 8.5 presents the whole temperature dependence of the conductance including the weak tunnelling limit dominating at low temperature and the weak backscattering limit controlling the high temperature regime.

2.2.5 Resonant tunnelling

When localised states induced by local disorder are present at the same energy as the incident edge channel in the vicinity of the QPC, resonant tunnelling through the localised states can occur. Fig. 8.6 presents sketches of resonant tunnelling through a localised state in both limits of weak tunnelling and weak backscattering.

In the integer quantum Hall case, the tunnelling conductance would exhibit a peak at zero-bias voltage which has a Lorentzian shape with a temperature independent width at low temperature [127]. This shape holds for both the weak tunnelling and the weak backscattering limit.

In the fractional quantum Hall regime, the conductance peak of resonant tunnelling differs in height and width for weak tunnelling and weak backscattering.

Weak tunnelling limit The tunnelling conductance across a localised state is predicted to have a temperature dependence of [127]

$$G_{res} \propto {t_t}^2 \; T^{m-2}$$

Therefore, the peak height of resonant tunnelling decreases more slowly than in the direct tunnelling between fractional states. For instance, for $\nu = \frac{1}{3}$, the peak height scales as $G_{res} \propto T$ in resonant tunnelling and as $g_T \propto T^4$ in direct tunnelling.

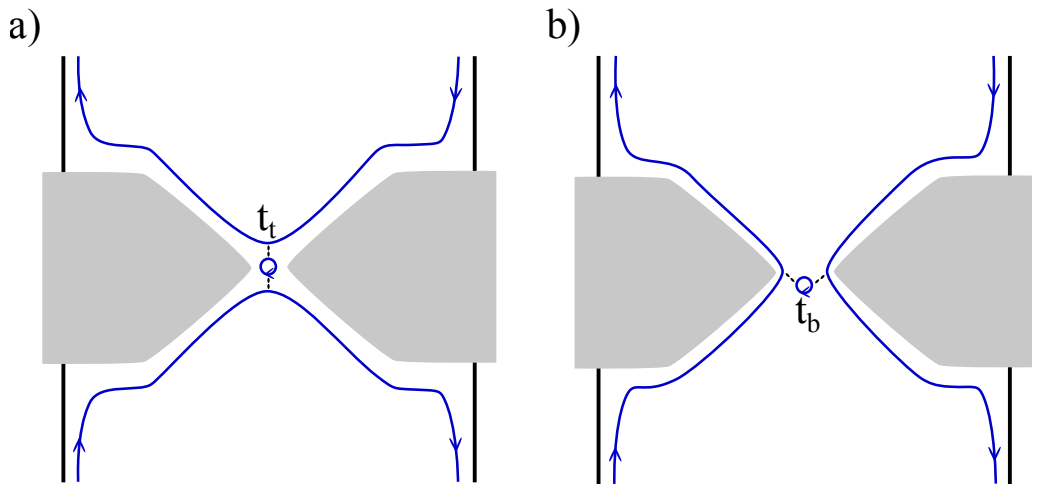

Figure 8.6: Resonant tunnelling across a localised state in the two limits of a) weak tunnelling of electrons and b) weak backscattering of quasi-particles.

Weak backscattering limit Resonances in the weak backscattering limit are usually concealed by direct inter-edge tunnelling. Only at $T = 0$, resonance becomes dominant since inter-edge tunnelling is suppressed. At $T = 0$, the transmission is predicted to be perfect resulting in a tunnelling conductance across localised states of $G_{res} = \nu\frac{e^2}{h}$ and the resonant peak is supposed to be infinitely sharp [137].

3 Tunnelling in conventional 2DEG systems

The measurement of the temperature dependence of the tunnelling conductance across the QPC allows access to the fractional charge e^* of the quasi-particle and the Coulomb interaction parameter g.

In 2003, S. Roddaro et al studied the nonlinear IV characteristics of inter-edge tunnelling of the fractional state $\nu = \frac{1}{3}$ and its evolution with temperature in a QPC in GaAs/AlGaAs heterostructures [136]. Fig. 8.7a presents the differential tunnelling conductance for T =0.03 K to 0.9 K. The zero-bias peak observed from $T > 0.4$ K decreases with increasing temperature and depends on the bias voltage V_T in contrast to Ohmic behaviour of integer quantum Hall states. These characteristics are predicted for inter-edge tunnelling of fractional edge channels in the weak backscattering limit.

Fig. 8.7b presents the theoretically expected tunnelling conductance for the $\nu = \frac{1}{3}$ state to compare with the experimental curves at the same temperatures in Fig. 8.7c. The overall evolution of the maxima and the width of the measured curves is qualitatively in agreement with the theory. However, an exact fit turns out to be an impossible task.

In 2007 [138] and 2008 [134], the groups of C.M. Marcus and K.W. West studied the temperature dependence of the tunnelling conductance of the state $\nu = \frac{5}{2}$ in GaAs. Only recently in 2014, the groups of K. Ensslin and W. Wegschneider investigated the quasi-particle tunnelling of the fractional states $\nu = \frac{5}{2}$ as well as $\nu = \frac{7}{3}$ and $\nu = \frac{8}{3}$ [139]. In all of these tunnelling experiments the fit of the theoretical tunnelling conductance (8.3) to the experimental curves remains challenging and does not reveal precise values of the fractional charge.

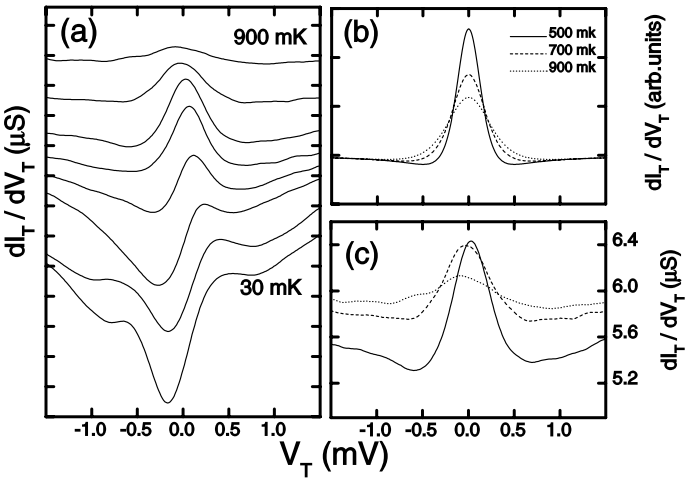

Figure 8.7: Results on the tunnelling of the $\frac{1}{3}$ fractional state. a) Differential tunnelling conductance is plotted as a function of the bias voltage for various temperatures. b) Theoretical tunnelling conductance to compare with the c) experimental curves at the same temperatures. Fig. taken from [136]

4 Tunnelling of the $\nu = 7/3$ fractional state in graphene

After having demonstrated at the beginning of this chapter that the transmission of fractional edge channels is controlled by the QPC, we present our results on tunnelling in the fractional quantum Hall regime in our QPC device in graphene focussing on the fractional state of $\nu = \frac{7}{3}$.

4.1 Device configuration

For the measurements of the diagonal and transverse resistances as a function of a dc-bias voltage, we used the configuration of the device presented in Fig. 8.8. An ac-voltage of 5 µV to 20 µV superimposed to a dc-voltage is applied on one side of the Hall bar. The measurement of the current on the other side of the Hall bar and of the transverse and diagonal voltages enable to determine the diagonal and transverse resistances without the contribution of any contact resistance.

In order to obtain the actual voltage drop across the device without the contact resistances, we derive the bias voltage by $V_{dc} = I_{dc}R_D$ with the measured dc-current I_{dc} and the diagonal resistance R_D across the QPC.

4.2 Theoretical prediction for the tunnelling of $\nu = 7/3$

In chapter 2 (sect. 2.4), we introduced the theoretical filling factor $\nu_f = \nu - 2$ which we need to take into consideration when we compare fractional states in graphene with those in conventional 2DEG systems. The $\nu = \frac{7}{3}$ fractional state in graphene corresponds, therefore, to the theoretical state of $\nu_f = \frac{1}{3}$ which is a Laughlin state with a single fractional edge channel.

Let us consider the expected temperature dependence for the tunnelling conductance of this Laughlin fractional state $\nu_f = \frac{1}{3}$. Eq. (8.1) and (8.2) lead to:

$$\begin{cases} g_T \propto T^4 & \text{for weak tunnelling of electrons} \\ g_T - \frac{1}{3}\frac{e^2}{h} \propto T^{-\frac{4}{3}} & \text{for weak backscattering of quasi-particles} \end{cases}$$

Let us briefly discuss which properties are expected in the zero-bias diagonal resistance in each limit of tunnelling. Fig. 8.9 presents a drawing of the transition of the diagonal

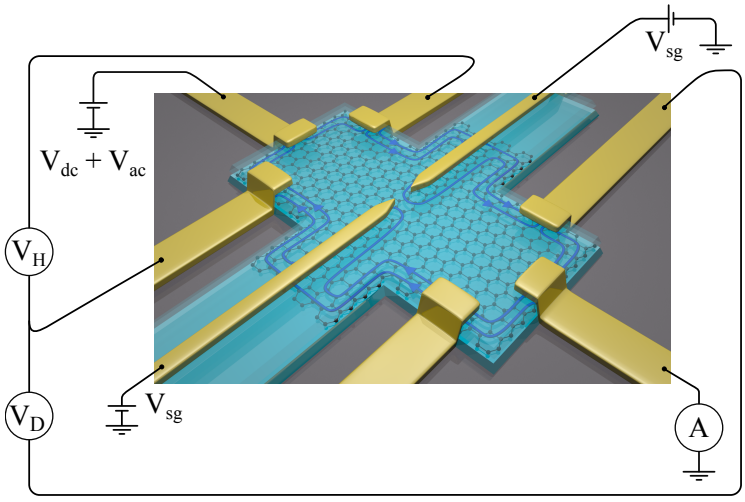

Figure 8.8: Device configuration to measure the tunnelling properties in our QPC device. An ac-voltage added to a dc-bias voltage is applied to one side of the Hall bar while the current as well as the diagonal and transverse voltages are measured.

resistance from the $\nu = \frac{7}{3}$ fractional state to the $\nu = 2$ integer state with decreasing temperature. At high T, R_D has a value of $\frac{3}{7}\frac{e^2}{h}$. With decreasing temperature, the resistance starts to increase due to tunnelling between the counter-propagating fractional edge channels entering the weak backscattering limit (blue circle in Fig. 8.9).

The tunnelling probability increases further with decreasing temperature such that at some point the $\frac{7}{3}$ edge channel is backscattered. Tunnelling occurs then between the backscattered $\frac{7}{3}$ edge channels which is settled in the weak tunnelling limit (orange circle in Fig. 8.9). By further decreasing T, the resistance reaches the integer plateau of $\nu = 2$.

The tunnelling conductance between the left and right edge channels which are brought in close proximity in the QPC, is experimentally obtained by measuring R_D and R_H to calculate [134]

$$g_t \simeq \frac{R_D - R_H}{R_H^2} \tag{8.4}$$

Eq. (8.4) is only valid if the bulk is at the filling factor of the fractional state whose tunnelling is studied.

4.3 Experimental signature of tunnelling of fractional states

In order to perform tunnelling experiment in the $\frac{7}{3}$ fractional state in graphene, we set the backgate voltage to a) $V_{bg} = 12.35\,\mathrm{V}$ ($\nu_b = 3$) and b) $V_{bg} = 11.90\,\mathrm{V}$ ($\nu_b = \frac{8}{3}$) (positions A and B in Fig. 8.1a) and continuously close the QPC by decreasing the split gate voltage. Fig. 8.10 presents the diagonal resistance normalised by its high dc-bias value as a function of the dc-bias voltage and the split gate voltage. The diagonal conductance at zero-bias voltage is superimposed for each resistance map in Fig. 8.10 (black curves).

In Fig. 8.10a, the backgate voltage is fixed at a bulk filling factor of $\nu_b = 3$. We observe several peaks and dips in the normalised resistance in the region of zero bias voltage. These peaks and dips are even more evident in the zero-bias conductance curve. This curve decreases with decreasing V_{sg} reaching $\frac{2e^2}{h}$ at $V_{sg} = -0.64\,\mathrm{V}$.

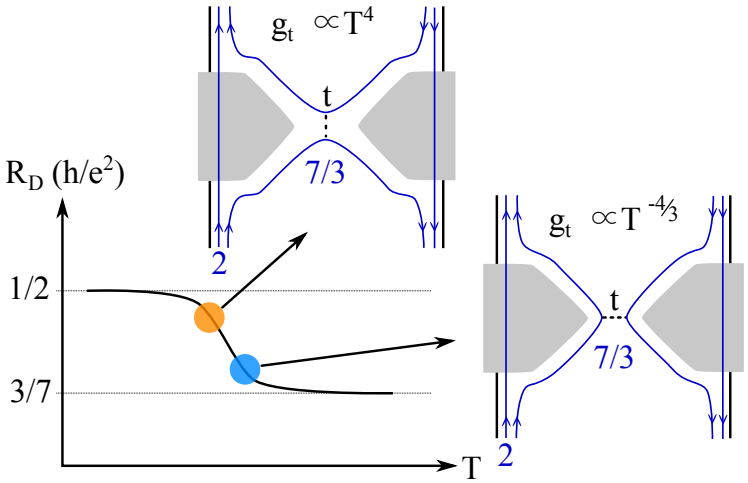

Figure 8.9: Drawing of the transition from the fractional state $\frac{7}{3}$ to the integer state 2 with decreasing temperature. During the transition the fractional state passing from weak backscattering (blue circle) to weak tunnelling (orange circle) with decreasing temperature.

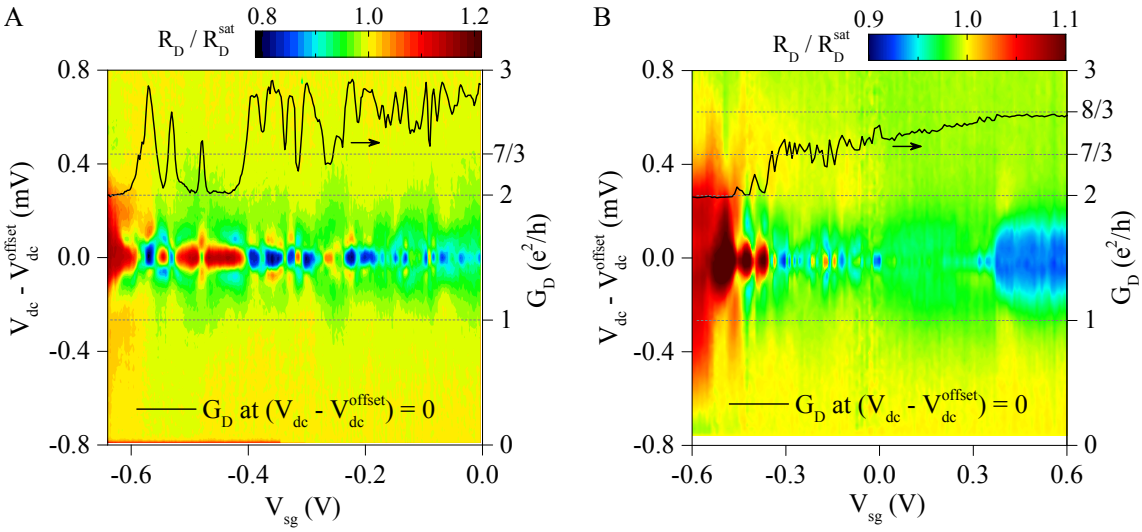

Figure 8.10: The normalised diagonal resistance measured at 14 T and at 0.05 K is plotted as a function of the split gate and bias voltages at fixed backgate voltage of a) $V_{bg} = 12.35\,\mathrm{V}$ ($\nu_b = 3$) and b) $V_{bg} = 11.90\,\mathrm{V}$ ($\nu_b = \frac{8}{3}$). Their position is marked in the conductance map in Fig. 8.1a. The zero-bias conductance curve in black is added to emphasise the peaks and dips at zero-bias voltage.

By decreasing the split gate voltage, the number of transmitted integer and fractional edge channels decreases: At high V_{sg} the $\nu = 3$ integer edge channel is transmitted. The decrease of V_{sg} leads to the backscattering of first the $\nu = 3$ edge channel, then the $\nu = \frac{8}{3}$ and $\nu = \frac{7}{3}$ edge channels resulting in the observed decrease of G_D. For $V_{sg} < -0.6\,\mathrm{V}$, the $\nu = 2$ edge channel is transmitted leading to $G_D = \frac{2e^2}{h}$.

Just before the transmitted fractional and integer edge channels are backscattered, tunnelling directly between the edge channels or via a localised state occurs which manifests itself as a series of peaks (resonances).

In Fig. 8.10b, the bulk filling factor is fixed at $\nu_b = \frac{8}{3}$. In the zero-bias conductance curve, we observe a plateau at $\frac{8e^2}{3h}$ at high split gate voltage without any peaks upon closing the QPC. In contrast, the plateau at $\frac{7e^2}{3h}$ at $V_{sg} \simeq -0.2\,\mathrm{V}$ is marked by many conductance peaks and dips indicating tunnelling. The nature of the two fractional states of $\frac{7}{3}$ and $\frac{8}{3}$ is completely different. While the $\frac{7}{3}$ state is a Laughlin state with one fractional edge channel, the $\frac{8}{3}$ state which corresponds to $\nu_f = \frac{2}{3}$ is predicted to be constituted of two fractional edge channels one neutral and one charged [140], leading to a more complex tunnelling scenario.

At $V_{sg} \simeq -0.35\,\mathrm{V}$, the height and width of the peaks become larger than for higher split gate voltage. This may mark the transition from the weak backscattering limit of quasi-particles to the weak tunnelling limit of electrons.

Non-linear IV-characteristics of the tunnelling between fractional states

In order to get a clear idea of the difference in shape of the zero-bias resistance peaks of integer and fractional quantum Hall states, Fig. 8.11 presents resistance peaks versus dc-bias voltage.

The blue curve in Fig. 8.11a is measured at $V_{bg} = 4.31\,\mathrm{V}$ and at $V_{sg} = 2.88\,\mathrm{V}$. The peak exhibits a wide zero-bias maximum of $\frac{h}{e^2}$. This curve is settled at the integer plateau of

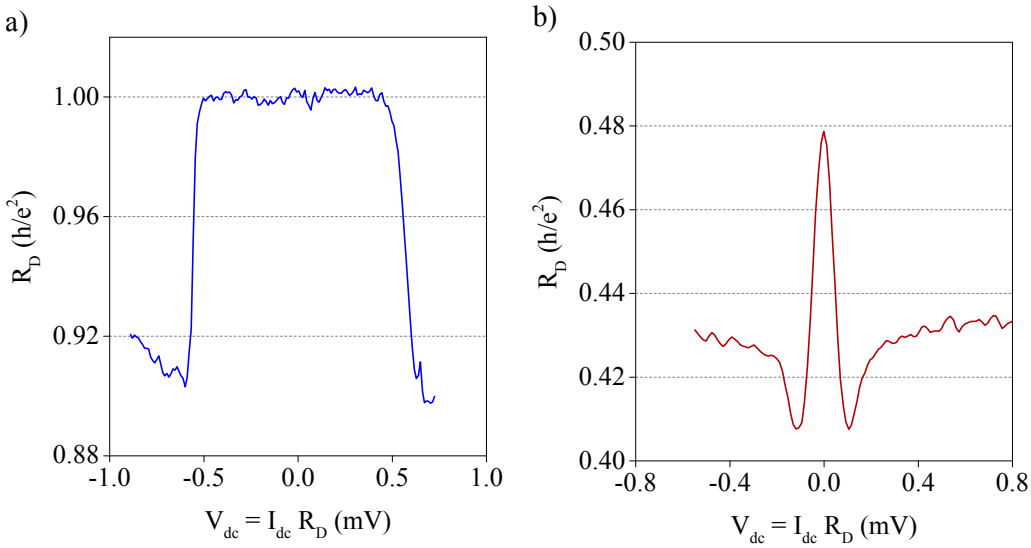

Figure 8.11: Diagonal resistance measured at 0.05 K is plotted as a function of the dc-bias voltage to present the tunnelling of a) integer and b) fractional quantum Hall states. a) The blue curve represents the zero-bias peak of the integer state of $\nu = 1$ while b) the red curve has a clear resemblance to the theoretical curves of (8.3) of tunnelling between fractional states.

$\nu = 1$.

The red curve in Fig. 8.11b is measured at $V_{bg} = 12.35\,\mathrm{V}$ and at $V_{sg} = 0.51\,\mathrm{V}$. It possesses a much narrower zero-bias peak with a maximum of $0.48\frac{h}{e^2}$ and dips on each side of the peak. We observe that its shape differs distinctly from the resistance peak at the integer state. Its shape has a strong resemblance to the theoretical curve in the weak backscattering limit of eq. (8.3) for $g < 0.5$ presented in Fig. 8.4a. This confirms that tunnelling between fractional quantum Hall states behaving as chiral Luttinger liquid does occur in our QPC.

4.4 Temperature dependence of the non-linear tunnelling conductance

4.4.1 Shape of the zero-bias conductance peak

Diagonal resistance We discuss a zero-bias peak in the diagonal resistance which is measured as a function of the dc-bias voltage at a fixed bulk filling factor of $\nu_b = \frac{8}{3}$ and at $V_{sg} = -0.52\,\mathrm{V}$ which corresponds to $\nu_{QPC} = \frac{7}{3}$ (point C in Fig. 8.1a). The diagonal conductance is plotted as a function of the dc-bias voltage for various temperatures in Fig. 8.12a.

From the shape and peak height, we can already deduce some properties of the tunnelling process. We observe that the zero-bias peak and the dips on each side decrease with increasing temperature. At the lowest temperature of 0.05 K, the peak height is almost at $\frac{h}{2e^2}$. This may suggest that the $\nu = \frac{7}{3}$ fractional state transits to the $\nu = 2$ integer state with decreasing temperature in the weak tunnelling limit (orange circle in Fig. 8.9).

The saturated value R_D^{sat} of R_D at high dc-bias voltage is about $0.428\frac{h}{e^2}$ which is in agreement with the theoretical value of $\left(\frac{7}{3}\frac{e^2}{h}\right)^{-1} = 0.429\frac{h}{e^2}$ confirming that the $\frac{7}{3}$ fractional state passes through the QPC. The two undershoots on each side of the resistance peak are theoretically expected and observed for a Coulomb interaction parameter $g < 0.5$ [139, 141] (see Fig. 8.4 for comparison).

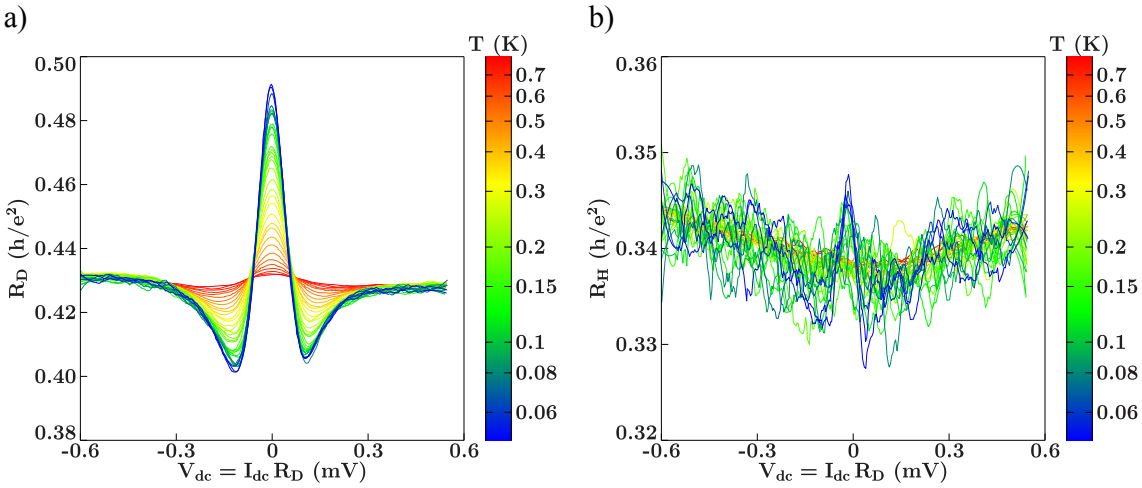

Figure 8.12: a) Diagonal resistance as a function of dc-bias voltage presents a zero-bias peak and dips on each side which all decrease with increasing temperature. It represents the tunnelling between fractional edge channels. Its position is at the point 1 in the conductance map in Fig. 8.1a. b) The transverse resistance is almost constant in dc-bias voltage and independent of temperature.

Transverse resistance Fig. 8.12b presents the transverse resistance R_H (see device configuration in Fig. 8.8) as a function of the dc-bias voltage for the same temperatures as in Fig. 8.12a. We observe that apart from fluctuations due to noise, R_H is relatively constant along the dc-bias range at a value of about $0.34\frac{h}{e^2}$ and does not change with temperature. Since R_H depends only on the bulk filling factor without the influence of the QPC, we expect R_H to be $\frac{3}{8}\frac{h}{e^2} \simeq 0.38\frac{h}{e^2}$, and we found $\sim 0.34\frac{h}{e^2}$.

Tunnelling conductance Since $R_H \neq \frac{3}{7}$, the bulk is not at a filling factor of $\frac{7}{3}$ and, hence (8.4) cannot be directly applied but needs to be adapted to calculate the tunnelling

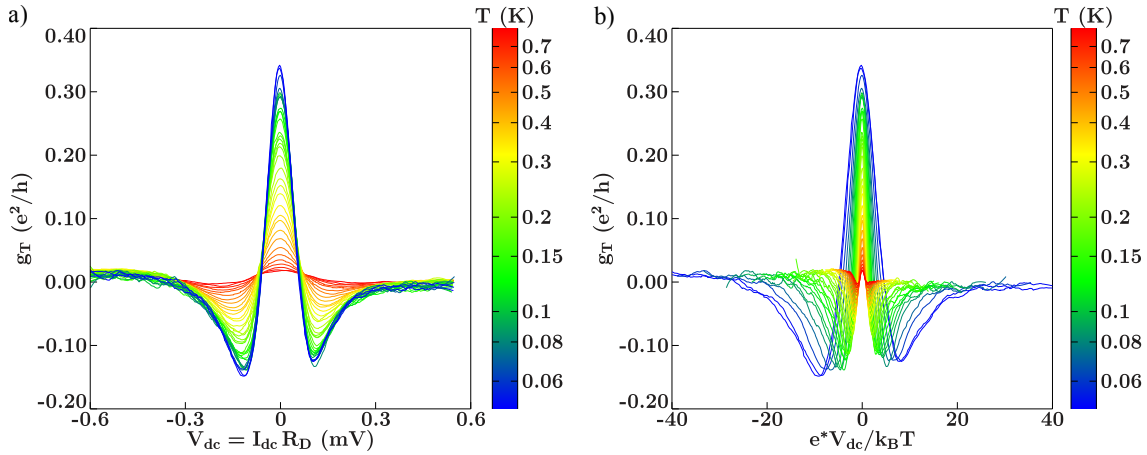

Figure 8.13: a) The tunnelling conductance of the fractional state $\nu = \frac{7}{3}$ is calculated by using (8.5) and plotted as a function of the dc-bias voltage for various temperatures. b) The tunnelling conductance is plotted as a function of $\frac{e^* V_{dc}}{k_B T}$. The change of the position of the undershoots is due to a change in the energy scale with increasing temperature. Its position is at the point 1 in the conductance map in Fig. 8.1a.

conductance. We replace R_H by a resistance $R_{trans} = \frac{1}{\nu}\frac{h}{e^2}$ with $\nu = \frac{7}{3}$ which is based on the edge channels transmitted through the QPC leaving out those edge channels which are backscattered. Therefore, the tunnelling conductance is given by

$$g_T \simeq \frac{R_D - \frac{3}{7}\frac{h}{e^2}}{\left(\frac{3}{7}\frac{h}{e^2}\right)^2} \tag{8.5}$$

Fig. 8.13 presents g_T as a function of the dc-bias voltage. We observe the similar shape of the curve to R_D in Fig. 8.12a.

Before studying its temperature dependence in more detail, we look at these curves as a function of $\frac{eV_{dc}}{k_B T}$ in Fig. 8.13b. We assume the theoretically expected fractional charge of $e^* = \frac{e}{3}$ for the $\nu_f = \frac{1}{3}$ Laughlin state. We observe a drastic change in the position of the undershoots and the width of the peak with increasing temperature. If this zero-bias peak in the tunnelling conductance was due to weak backscattering, the energy scale should not change as we observed in the theoretical curves in Fig. 8.4.

4.4.2 Temperature dependence of the zero-bias conductance peak

Fig. 8.14 presents in logarithmic scale the temperature dependence of the zero-bias peak height of g_T. We observe two different slopes whose linear fits give $T^{-0.28\pm0.03}$ at low temperatures and $T^{-2.25\pm0.05}$ at higher temperatures. None of the above discussed temperature dependences in the weak backscattering and weak tunnelling regime or resonant tunnelling explain these two slopes.

In the low temperature regime, the small slope of $T^{-0.28\pm0.03}$ indicates that the relative height of the resistance peak seems to saturate. The $\frac{7}{3}$ fractional state crosses over to the integer state of $\nu = 2$ with decreasing temperature. In this scenario, the resistance is expected to saturate to a value of $\frac{1}{2}\frac{e^2}{h}$ which is close to the observed saturation value of $0.35\frac{e^2}{h}$.

The offset is the crucial parameter for the analysis of the slope in a logarithmic plot.

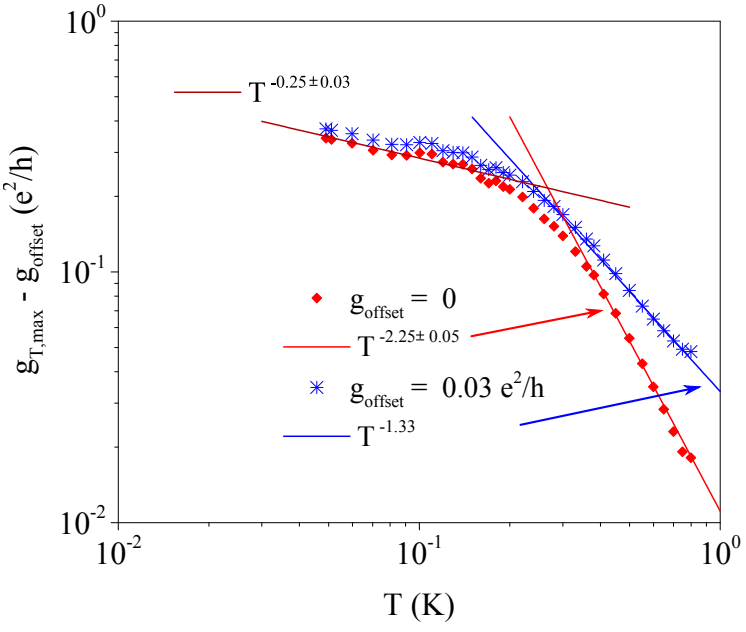

Figure 8.14: The temperature dependence of the height of the zero-bias peak in g_T extracted from 8.13a exhibits a slope of $T^{-2.25\pm0.05}$ at high T and saturates at low T (in red). A slight change in the offset of $0.03\frac{e^2}{h}$ in $g_{T,max}$ leads to the expected temperature dependence of $T^{-1.33}$ (in blue).

Even a small offset significantly changes the slope of the data points. When we add a slight offset of $0.03\frac{e^2}{h}$, we obtain a slope of $T^{-1.33}$ at high temperatures which is in agreement with the theoretically expected value for the weak backscattering limit of the $\nu_f = \frac{1}{3}$ fractional state.

4.4.3 Temperature dependence of the isolated Laughlin state $\nu = 1/3$

The fractional state of $\frac{7}{3}$ is supposed to be composed of the integer state of $\nu = 2$ and the Laughlin fractional state of $\frac{1}{3}$. In order to isolate the contribution of the $\nu = \frac{1}{3}$ fractional state of the conductance, we subtract the contribution of the $\nu = 2$ state from the total conductance:

$$R_D^{\nu=\frac{1}{3}} = \frac{1}{\frac{1}{R_D} - \frac{1}{R_D^{\nu=2}}} = \frac{R_D}{1 - 2\frac{R_D}{Rq}}$$

with $R_D^{\nu=2} = \frac{1}{2}\frac{h}{e^2} = \frac{1}{2}Rq$. The tunnelling conductance is, hence,

$$g_T^{\nu=1/3} = \frac{R_D^{\nu=\frac{1}{3}} - R_{trans}}{R_{trans}^2} \tag{8.6}$$

with $R_{trans} = 3\frac{h}{e^2}$ for the $\nu = \frac{1}{3}$ fractional state transmitted through the QPC.

Fig. 8.15a presents $g_T^{\nu=1/3}$ as a function of the bias voltage. We observe a huge zero-bias peak up to $3\frac{e^2}{h}$ at the lowest temperature. With increasing temperature the peak decreases rapidly.

For weak backscattering, a tunnelling conductance of $g_T \ll 1$ is expected. The high peak of $g_T > 1$ in Fig. 8.15a indicates a transition to weak tunnelling between the backscattered $\frac{1}{3}$ fractional edge channels at low temperature.

The temperature dependence of the peak height is plotted in logarithmic scale in Fig. 8.15b. We observe a slope of $T^{-2.14\pm0.05}$ which does not correspond to any theoretical

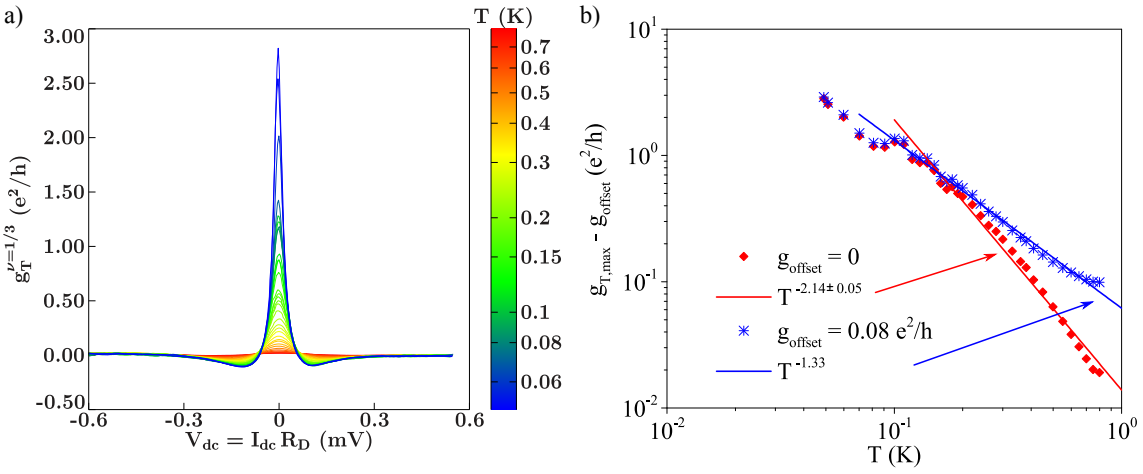

Figure 8.15: a) The tunnelling conductance $g_T^{\nu=1/3}$ exhibits a large zero-bias peak at low temperatures which decreases fast with increasing T indicating a transition to weak tunnelling. b) The peak height extracted from a) exhibits a slope of $T^{-2.14\pm0.05}$ (in red). By slightly changing the offset of $0.08\frac{e^2}{h}$, a slope of $T^{-1.33}$ is obtained (in blue).

expectation. We notice that this temperature dependence of the isolated $\nu = \frac{1}{3}$ state is close to the exponent $T^{-2.25\pm0.05}$ which we obtained considering the total tunnelling conductance of the $\nu = \frac{7}{3}$ state (see Fig. 8.14).

By subtracting a small offset of $0.08\frac{e^2}{h}$, we obtain a slope of $T^{-1.33}$ at high temperatures which is theoretically expected for the weak backscattering of the $\nu = \frac{1}{3}$ fractional state.

4.5 Overview of different zero-bias conductance peaks

4.5.1 Shape of three other conductance peaks

Let us have a look at Fig. 8.16 of three other sets of tunnelling conductance curves taken at other gate positions. The first row of plots shows the tunnelling conductance g_T calculated from eq. (8.5) as a function of V_{dc}. We observe that the zero-bias peak and the deep undershoots on each side decrease rapidly with temperature. We notice that the peak height of the three curves goes maximally until $0.3\frac{e^2}{h}$ which is much lower than the first conductance peak in Fig. 8.13. Importantly, these three peaks appear narrower than the first peak in Fig. 8.13. The differing shape and peak height suggest a different origin of this peak when comparing to the first peak discussed.

4.5.2 Energy scale of the conductance peaks

The dependence of g_T in energy scale $\frac{e^*V_{dc}}{k_BT}$ is plotted in the second row of Fig. 8.16. We assume again the theoretically expected fractional charge of $e^* = \frac{e}{3}$ for the $\nu_f = \frac{1}{3}$ Laughlin state. We observe that the undershoots on each side of the zero-bias peak are at the same energy scale than the theoretical curve of weak backscattering in Fig. 8.4b in which we set $g = \frac{1}{3}$ and $e^* = \frac{e}{3}$ (see inset of Fig. 8.4b).

Table 8.1 summarises our results on the energy scale $\frac{e^*V_{dc}}{k_BT}$. Peak number 1 corresponds to the first conductance peak which we presented in sect. 8.4.4 and the peaks 2 to 4 are discussed above. The position of the side-dips is theoretically expected at $\frac{e^*V_{dc}}{k_BT} \simeq 3.8$. We see that peak 1 has twice the energy scale which is expected from weak backscattering. The other three peaks are with values ranging from 3.3 to 4.4 in agreement to the energy scale of the theoretical g_T of eq. (8.3) in the weak backscattering limit.

We are not able to fit the theoretical tunnelling conductance of (8.3) to our data due to the deep undershoots. However, since the sets of the peaks 2 to 4 are in agreement to the theoretical energy scale $\frac{e^*V_{dc}}{k_BT} \simeq 3.8$, we can obtain an estimation for the fractional charge of $e^* \simeq 0.33e$.

However, in contrast to the theoretical curves, we observe a decrease in energy of the undershoots with increasing temperature.

4.5.3 Temperature dependence of three additional conductance peaks

The third row of Fig. 8.16 presents in logarithmic scale the temperature dependence of the three zero-bias peak heights of g_T extracted from the plots in the first row. The temperature dependence of the three peaks are $T^{-1.48\pm0.08}$ (peak 2), $T^{-2.14\pm0.11}$ (peak 3) and $T^{-2.13\pm0.17}$ (peak 4). The temperature dependence of peak 2 is in agreement with the theoretical exponent of $T^{-1.33}$ of weak backscattering without adjusting the offset. For the two other slopes, a small offset in the range of 0.045 to $0.06\frac{e^2}{h}$ enables to obtain the theoretically expected dependence of $T^{-1.33}$.

The last row of Fig. 8.16 presents in logarithmic scale the temperature dependence

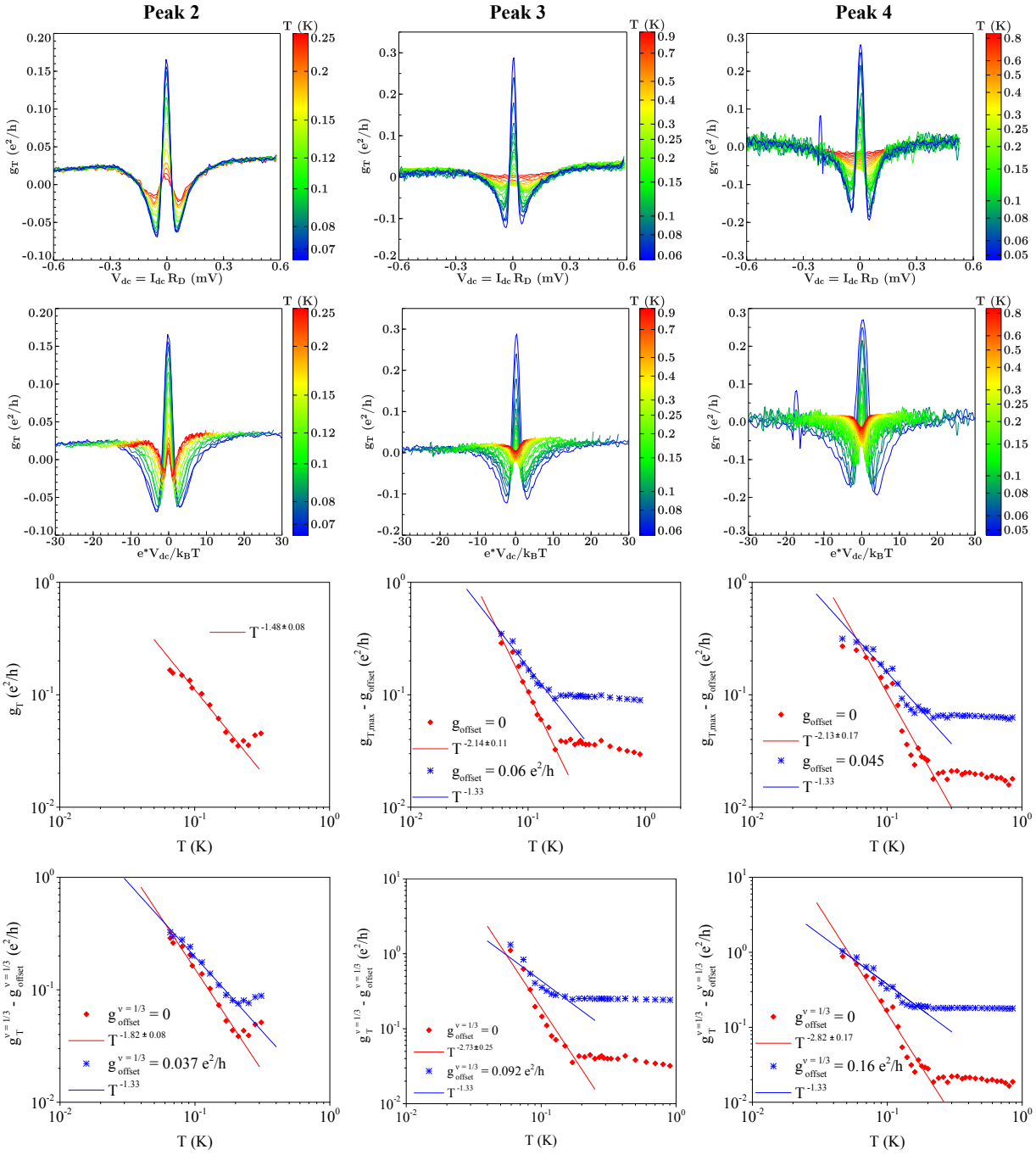

Figure 8.16: Row 1: Three zero-bias conductance peaks are plotted as a function of V_{dc}. Row 2: g_T versus $\frac{e^* V_{dc}}{k_B T}$ for $e^* = \frac{e}{3}$ shows that the three plots have the same energy scale. Row 3: Temperature dependence of the peak height in g_T (in red). A small change of the offset leads to the theoretically expected temperature dependence $T^{-1.33}$ (in blue). Row 4: Temperature dependence of $g_T^{\nu=1/3}$ calculated from (8.6). The positions of these three peaks are marked as 2, 3 and 4 in the conductance map at 14 T in Fig. 8.1a.

of the isolated $\frac{1}{3}$ state of $g_T^{\nu=1/3}$ calculated from (8.6). Within this representation, the temperature dependences are $T^{-1.82\pm0.08}$ (peak 2), $T^{-2.73\pm0.25}$ (peak 3) and $T^{-2.82\pm0.17}$ (peak 4). A slight adjustment of the offset of 0.037 to $0.16\frac{e^2}{h}$ changes the slope to be in agreement to the theoretical expectation of $T^{-1.33}$.

The exponents of all temperature dependences and the added offsets are summarised in table 8.1.

4.6 Discussion on the temperature dependence

The four tunnelling conductance peaks which we measured can be divided into two categories depending on the size and shape of the conductance peak as well as its energy scale.

Conductance peak in transition to $\nu = 2$ at low T The first peak in the tunnelling conductance (see Fig. 8.13a) has about twice the energy scale in $\frac{e^*V_{dc}}{k_BT}$ than theoretically expected for weak backscattering for $g = \frac{1}{3}$ and $e^* = \frac{e}{3}$. From its IV characteristics and the temperature dependence, we made the following observations: At the base temperature, the relative peak height seems to saturate to $\frac{h}{2e^2}$ of the integer state $\nu = 2$ (orange circle in Fig. 8.9). When we subtract the contribution of the integer state $\nu = 2$, the tunnelling conductance of $\nu = \frac{1}{3}$ exhibits a large zero-bias peak which may be due to a transition to weak tunnelling at low temperature.

At high temperature, the temperature dependence of the tunnelling conductance does not correspond to the theoretical expected values of $g_T \propto T^{-4/3}$ of weak backscattering nor $g_T \propto T^4$ of weak tunnelling at low T. However, a slight offset of $0.03\frac{e^2}{h}$ changes the temperature dependence to the expected $g_T \propto T^{-1.33}$.

Adjustment of the offset The approach of adding a small offset has been done by the groups of K. Ensslin and W. Wegschneider [139]. For their analysis of the $\frac{5}{2}$ fractional

Table 8.1: Energy scale and temperature dependence of several zero-bias tunnelling conductance peaks. From the theoretical tunnelling conductance of eq. (8.3), the energy scale of $\frac{e^*V_{dc}}{k_BT}$ is calculated for $g = \frac{1}{3}$ and $e^* = \frac{e}{3}$.

Peak	Energy scale of $\frac{e^*V_{dc}}{k_BT}$ of the peak at 0.05 K	T dependence of g_T	Offset to obtain $T^{-1.33}$ $\left(\frac{e^2}{h}\right)$	T dependence of $g_T^{\nu=1/3}$	Offset to obtain $T^{-1.33}$ $\left(\frac{e^2}{h}\right)$
Theory	3.8	−1.33	–	–	–
1	8.7 ± 0.2	−2.25 ± 0.05	0.030	−2.14 ± 0.05	0.080
2	3.5 ± 0.1	−1.48 ± 0.08	–	−1.82 ± 0.08	0.037
3	3.3 ± 0.1	−2.14 ± 0.11	0.060	−2.73 ± 0.25	0.092
4	4.4 ± 0.1	−2.13 ± 0.17	0.045	−2.82 ± 0.17	0.160

state, they explicitly subtracted without any justification an offset of $0.1\frac{e^2}{h}$. Therefore, their results on the temperature dependence should be interpreted with caution.

In our analysis of the four zero-bias conductance peaks, we added an offset $< 0.1\frac{e^2}{h}$ to obtain an exponent which is close to the theoretically expected temperature dependence of $T^{-1.33}$. It is clear that any exponent can be obtained in logarithmic scale by adjusting adequately an offset of the data.

Conductance peak with the expected exponent The three other tunnelling conductance peaks are of the same energy scale than theoretically expected for weak backscattering in eq. (8.3) for a fractional charge of $e^* = \frac{e}{3}$ and an interaction parameter of $g = \nu = \frac{1}{3}$. Peak 2 exhibits a temperature dependence of $T^{-1.48\pm0.08}$ (see Fig. 8.16) which is close to the theoretical dependence of $T^{-\frac{4}{3}}$ of weak backscattering. This result is obtained without adding any offset to the data.

Resonant tunnelling In IV measurements presented in Fig. 8.10, we observe a series of zero-bias resonant peaks which are due to multiple tunnelling processes. An ideal QPC in which tunnelling occurs only at a single point, is rarely observed experimentally. These series of resonances show that our QPC has an imperfect shape in which tunnelling can occur at different locations of the QPC. These multiple tunnelling processes could explain the differently shaped peaks in the tunnelling conductance with their varying temperature dependences when the split gate voltage is slightly changed.

We observe a change in energy of the undershoots on each side of the zero-bias peak of the tunnelling conductance in all of our measured sets of curves. This decrease of the energy scale $\frac{e^*V_{dc}}{k_BT}$ with increasing temperature could be explained by resonant tunnelling between localised states and the non-constant density of states of the Luttinger liquid which increases as a power law with energy. Therefore, we could classify the four measured tunnelling conductance peaks to originate from resonant tunnelling with localised states.

Summary

A QPC offers a perfect system to study the nature of fractional edge channels by investigating the tunnelling between counter-propagating edge channels. In this chapter, we first demonstrated that the QPC can also control the transmission of fractional quantum Hall edge channels.

We presented a theoretical framework of tunnelling between fractional edge channels. We briefly reviewed the theoretically expected temperature dependence of the tunnelling conductance in the weak tunnelling and weak backscattering limit. Afterwards, we discussed experimental results on the tunnelling between fractional edge channels in GaAs/AlGaAs heterostructures.

In the second part of this chapter, we presented our results on the tunnelling of the $\frac{7}{3}$ fractional state in our QPC device in graphene. We discussed the different shapes of the zero-bias resistance peak of integer and fractional quantum Hall states and confirmed that we measured tunnelling of the $\nu = \frac{7}{3}$ fractional state.

We studied the shape, the energy scale and the temperature dependence of four zero-bias peaks in the tunnelling conductance. We determined that three out of the four peaks are close to the theoretical energy scale of weak backscattering. From the energy scale, we

obtained an estimation of the fractional charge of $e^* = \frac{e}{3}$. In one conductance peak, we measured the expected temperature dependence of weak backscattering. The deviation of the obtained temperature dependences to the theoretical predictions can be due to multiple tunnelling of many resonant states.

CONCLUSION AND PERSPECTIVES

In this thesis, we have achieved the fabrication of state-of-the-art encapsulated graphene and have successfully realised a QPC in high mobility graphene devices.

High mobility graphene devices

In order to fabricate clean, high mobility and ballistic graphene devices, we implemented a transfer technique of encapsulating graphene between two flakes of hBN in our facilities. This technique is based on the principle that the van-der Waals adhesion force is stronger between the graphene and the hBN than to the SiO_2 substrate. We have designed and assembled two set-ups which allow us to pick-up a flake of graphene with a flake of hBN and to put them down onto a second hBN flake. The encapsulated graphene is never exposed to resist or any other chemical treatment and, therefore, remains clean.

After plasma etching the hBN, the graphene is accessed only at its edge by one-dimensional metal contacts. In order to minimise the residue of resist which remains after an electron beam lithography and development in the trenches for the metal contacts, we heavily overdose the PMMA and employ a cold development.

QPC in high mobility graphene

We equipped the encapsulated, high mobility graphene of the form of a Hall bar with a QPC. The high quality of our device is apparent in the high mobility of about $250\,000\,\mathrm{cm^2\,V^{-1}\,s^{-1}}$ and a mean free path of about 1.8 µm which corresponds to the distance between neighbouring contacts. Additionally, we detect signatures of ballistic transport as a negative non-local resistance, a zero-resistance state in the field-effect curve as well as electron focusing. In the quantum Hall regime, we observed conductance plateaus at integer filling factors from a magnetic field of 5 T when the degeneracies of spin and valley lift. The fractional quantum Hall states which we observed are in agreement with the sequence of composite fermions.

We show that the QPC affects the quantum Hall edge channels in graphene. It enables to manipulate both integer and fractional quantum Hall edge channels and control their transmission probability through the constriction.

The transport properties of a QPC in graphene are strongly influenced by the process of equilibration between the quantum Hall edge channels. We determined that a selective equilibration between electron and hole edge channels occurs only between states of identical spins and sublevels of the $N = 0$ Landau level. We observed a similar spin selective equilibration in the unipolar regime but no restriction to any Landau level which may be caused by its proximity to the graphene edge. Taking this selective and restrictive

equilibration in the unipolar and bipolar regime into account, we obtained an excellent agreement between the theoretical model and our data.

The selective transmission of fractional edge channels allows a close proximity of the counter-propagating left and right edge channels in the QPC so that tunnelling occurs in-between them. The observed zero-bias peaks in the tunnelling conductance has a strong resemblance to theoretical predictions confirming that we measured the tunnelling of the $\nu = \frac{7}{3}$ fractional state in graphene.

Three out of the four tunnelling conductance peaks are in agreement to the theoretical energy scale of weak backscattering. From the energy scale, we were able to obtain an estimation of the fractional charge of $e^* = \frac{e}{3}$ for the $\nu = \frac{7}{3}$ state. We even measured the expected temperature dependence of weak backscattering in one tunnelling conductance peak. Our analysis provides a strong indication that the measured zero-bias tunnelling conductance peaks arise from resonant tunnelling between fractional edge channels across localised states. The tunnelling of quasi-particle in a QPC offers a way to study the rich physics of Luttinger liquids but obtaining precise experimental evidence remains a challenge.

Our results provide the basis for various further studies of transport properties in high mobility encapsulated graphene. The next natural step to continue on the studies of quantum Hall edge channels in a QPC is to perform shot noise measurements to determine the fractional charge. A step further of electron quantum optics devices is an interferometer in the quantum Hall regime in high mobility graphene.

We have already fabricated an interferometer in encapsulated graphene presented in the figure below. However, due to a small misalignment during the electron-beam lithography of the contacts and gate electrodes, the graphene had a short-circuit to one of the split gates. We are in the process of fabricating another interferometer in encapsulated graphene.

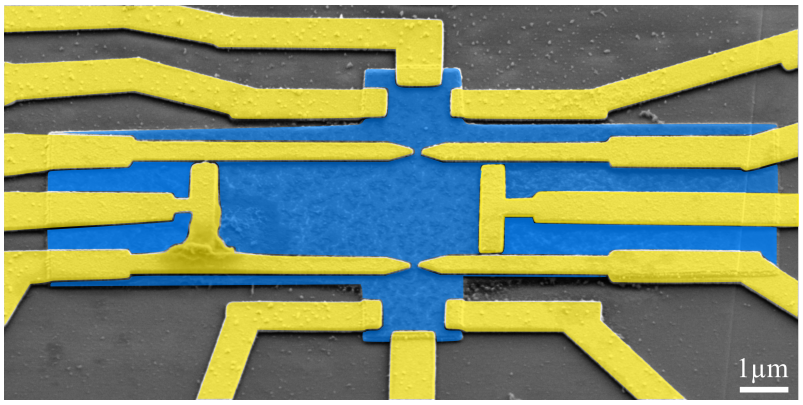

Device of an Fabry-Perot interferometer in encapsulated graphene. Yellow: contacts and gate electrodes. Blue: top BN flake

BIBLIOGRAPHY

[1] K. Novoselov, A. Geim, S. Morozov, D. Jiang, M. Katsnelson, I. Grigorieva, S. Dubonos, and A. Firsov: 'Two-dimensional gas of massless Dirac fermions in graphene'. *Nature* (Nov. 2005), vol. 438(7065): pp. 197–200 (cit. on pp. 1, 5, 27, 30, 32, 33, 80, 99).

[2] K. v. Klitzing, G. Dorda, and M. Pepper: 'New Method for High-Accuracy Determination of the Fine-Structure Constant Based on Quantized Hall Resistance'. *Phys Rev Lett* (6 Aug. 1980), vol. 45: pp. 494–497 (cit. on pp. 1, 5, 14, 15).

[3] Y. Zhang, Y. Tan, H. Stormer, and P. Kim: 'Experimental observation of the quantum Hall effect and Berry's phase in graphene'. English. *Nature* (Nov. 2005), vol. 438(7065): pp. 201–204 (cit. on pp. 1, 5, 32, 33, 99).

[4] K. S. Novoselov, Z. Jiang, Y. Zhang, S. V. Morozov, H. L. Stormer, U. Zeitler, J. C. Maan, G. S. Boebinger, P. Kim, and A. K. Geim: 'Room-Temperature Quantum Hall Effect in Graphene'. *Science* (2007), vol. 315(5817): p. 1379 (cit. on pp. 1, 5, 36).

[5] C. R. Dean, A. F. Young, P. Cadden-Zimansky, L. Wang, H. Ren, K. Watanabe, T. Taniguchi, P. Kim, J. Hone, and K. L. Shepard: 'Multicomponent fractional quantum Hall effect in graphene'. *Nature Phys* (Sept. 2011), vol. 7(9): pp. 693–696 (cit. on pp. 1, 5, 34, 40, 42–44, 109).

[6] F. Amet, A. J. Bestwick, J. R. Williams, L. Balicas, K. Watanabe, T. Taniguchi, and D. Goldhaber-Gordon: 'Composite fermions and broken symmetries in graphene'. *Nat Commun* (Jan. 2015), vol. 6 (cit. on pp. 1, 5, 43, 47, 48, 109).

[7] D. A. Wharam, T. J. Thornton, R. Newbury, M. Pepper, H. Ahmed, J. E. F. Frost, D. G. Hasko, D. C. Peacock, D. A. Ritchie, and G. A. C. Jones: 'One-dimensional transport and the quantisation of the ballistic resistance'. *Journal of Physics C: Solid State Physics* (1988), vol. 21(8): p. L209 (cit. on pp. 1, 5, 17, 51).

[8] D. C. Tsui, H. L. Stormer, and A. C. Gossard: 'Two-Dimensional Magnetotransport in the Extreme Quantum Limit'. *Phys Rev Lett* (22 May 1982), vol. 48: pp. 1559–1562 (cit. on pp. 10, 22, 23).

[9] T. Ihn: *Semiconductor Nanostructures: Quantum States and Electronic Transport*. Oxford University Press, 2009 (cit. on pp. 10, 11, 19, 23).

[10] S. Datta: *Electronic Transport in Mesoscopic Systems*. Cambridge Books Online. Cambridge University Press, 1995 (cit. on p. 10).

[11] D. K. Ferry, S. M. Goodnick, and J. Bird: *Transport in nanostructures*. 2nd ed. Cambridge University Press, 2009 (cit. on pp. 10, 23).

[12] Y. M. Galperin: *Quantum Transport*. Lecture notes for the Singapore session "Ultracold Gases and Quantum Information" of Les Houches Summer School. 2009 (cit. on pp. 10, 23).

[13] B. I. Halperin: 'Quantized Hall conductance, current-carrying edge states, and the existence of extended states in a two-dimensional disordered potential'. *Phys Rev B* (4 Feb. 1982), vol. 25: pp. 2185–2190 (cit. on p. 15).

[14] B. J. van Wees, H. van Houten, C. W. J. Beenakker, J. G. Williamson, L. P. Kouwenhoven, D. van der Marel, and C. T. Foxon: 'Quantized conductance of point contacts in a two-dimensional electron gas'. *Phys Rev Lett* (9 Feb. 1988), vol. 60: pp. 848–850 (cit. on pp. 17, 51, 52).

[15] R. Landauer: 'Spatial variation of currents and fields due to localised scatterers in metallic conduction'. *IBM Journal of research and development* (1957), vol. 1(3): pp. 223–231 (cit. on p. 17).

[16] M. Büttiker: 'Symmetry of electrical conduction'. *IBM Journal of research and development* (May 1988), vol. 32(3): pp. 317–334 (cit. on p. 19).

[17] M. Büttiker: 'Absence of backscattering in the quantum Hall effect in multiprobe conductors'. *Phys Rev B* (14 Nov. 1988), vol. 38: pp. 9375–9389 (cit. on p. 19).

[18] D. B. Chklovskii, B. I. Shklovskii, and L. I. Glazman: 'Electrostatics of edge channels'. *Phys Rev B* (7 Aug. 1992), vol. 46: pp. 4026–4034 (cit. on p. 21).

[19] H. L. Stormer, A. Chang, D. C. Tsui, J. C. M. Hwang, A. C. Gossard, and W. Wiegmann: 'Fractional Quantization of the Hall Effect'. *Phys Rev Lett* (24 June 1983), vol. 50: pp. 1953–1956 (cit. on pp. 22, 23).

[20] R. B. Laughlin: 'Anomalous Quantum Hall Effect: An Incompressible Quantum Fluid with Fractionally Charged Excitations'. *Phys Rev Lett* (18 May 1983), vol. 50: pp. 1395–1398 (cit. on p. 22).

[21] J. K. Jain: 'Composite-fermion approach for the fractional quantum Hall effect'. *Phys Rev Lett* (2 July 1989), vol. 63: pp. 199–202 (cit. on pp. 22, 24).

[22] J. K. Jain: 'Theory of the fractional quantum Hall effect'. *Phys Rev B* (11 Apr. 1990), vol. 41: pp. 7653–7665 (cit. on pp. 22, 24).

[23] R. Willett, J. P. Eisenstein, H. L. Störmer, D. C. Tsui, A. C. Gossard, and J. H. English: 'Observation of an even-denominator quantum number in the fractional quantum Hall effect'. *Phys Rev Lett* (15 Oct. 1987), vol. 59: pp. 1776–1779 (cit. on pp. 22, 25).

[24] G. Moore and N. Read: 'Nonabelions in the fractional quantum hall effect'. *Nuclear Physics B* (1991), vol. 360(2–3): pp. 362–396 (cit. on pp. 23, 25).

[25] M. Greiter, X.-G. Wen, and F. Wilczek: 'Paired Hall state at half filling'. *Phys Rev Lett* (24 June 1991), vol. 66: pp. 3205–3208 (cit. on pp. 23, 25).

[26] W. Pan, H. L. Stormer, D. C. Tsui, L. N. Pfeiffer, K. W. Baldwin, and K. W. West: 'Fractional Quantum Hall Effect of Composite Fermions'. *Phys Rev Lett* (1 Jan. 2003), vol. 90: p. 016801 (cit. on pp. 23, 24, 43).

[27] F. D. M. Haldane: 'Fractional Quantization of the Hall Effect: A Hierarchy of Incompressible Quantum Fluid States'. *Phys Rev Lett* (7 Aug. 1983), vol. 51: pp. 605–608 (cit. on p. 23).

[28] B. I. Halperin: 'Statistics of Quasiparticles and the Hierarchy of Fractional Quantized Hall States'. *Phys Rev Lett* (18 Apr. 1984), vol. 52: pp. 1583–1586 (cit. on p. 23).

[29] B. I. Halperin, P. A. Lee, and N. Read: 'Theory of the half-filled Landau level'. *Phys Rev B* (12 Mar. 1993), vol. 47: pp. 7312–7343 (cit. on p. 24).

[30] V. Goldman and M. Shayegan: 'Fractional quantum Hall states at v=711 and 913'. *Surface Science* (1990), vol. 229(1–3): pp. 10–12 (cit. on p. 24).

[31] C.-C. Chang and J. K. Jain: 'Microscopic Origin of the Next-Generation Fractional Quantum Hall Effect'. *Phys Rev Lett* (19 May 2004), vol. 92: p. 196806 (cit. on p. 24).

[32] E. Rezayi and N. Read: 'Fermi-liquid-like state in a half-filled Landau level'. *Phys Rev Lett* (6 Feb. 1994), vol. 72: pp. 900–903 (cit. on p. 24).

[33] W. Pan, J.-S. Xia, V. Shvarts, D. E. Adams, H. L. Stormer, D. C. Tsui, L. N. Pfeiffer, K. W. Baldwin, and K. W. West: 'Exact Quantization of the Even-Denominator Fractional Quantum Hall State at $^{\circ} = 5/2$ Landau Level Filling Factor'. *Phys Rev Lett* (17 Oct. 1999), vol. 83: pp. 3530–3533 (cit. on pp. 25, 110).

[34] J. P. Eisenstein, K. B. Cooper, L. N. Pfeiffer, and K. W. West: 'Insulating and Fractional Quantum Hall States in the First Excited Landau Level'. *Phys Rev Lett* (7 Jan. 2002), vol. 88: p. 076801 (cit. on p. 25).

[35] D. R. Luhman, W. Pan, D. C. Tsui, L. N. Pfeiffer, K. W. Baldwin, and K. W. West: 'Observation of a Fractional Quantum Hall State at $\nu = 1/4$ in a Wide GaAs Quantum Well'. *Phys Rev Lett* (26 Dec. 2008), vol. 101: p. 266804 (cit. on p. 25).

[36] J. P. Eisenstein, R. Willett, H. L. Stormer, D. C. Tsui, A. C. Gossard, and J. H. English: 'Collapse of the Even-Denominator Fractional Quantum Hall Effect in Tilted Fields'. *Phys Rev Lett* (8 Aug. 1988), vol. 61: pp. 997–1000 (cit. on p. 25).

[37] F. D. M. Haldane and E. H. Rezayi: 'Spin-singlet wave function for the half-integral quantum Hall effect'. *Phys Rev Lett* (10 Mar. 1988), vol. 60: pp. 956–959 (cit. on p. 25).

[38] G. S. Canright and S. M. Girvin: 'Fractional Statistics: Quantum Possibilities in Two Dimensions'. *Science* (1990), vol. 247(4947): pp. 1197–1205 (cit. on p. 25).

[39] P. R. Wallace: 'The Band Theory of Graphite'. *Phys Rev* (9 May 1947), vol. 71: pp. 622–634 (cit. on p. 27).

[40] A. H. Castro Neto, F. Guinea, N. M. R. Peres, K. S. Novoselov, and A. K. Geim: 'The electronic properties of graphene'. *Rev Mod Phys* (1 Jan. 2009), vol. 81: pp. 109–162 (cit. on p. 28).

[41] M. O. Goerbig: 'Electronic properties of graphene in a strong magnetic field'. *Rev Mod Phys* (4 Nov. 2011), vol. 83: pp. 1193–1243 (cit. on pp. 28, 109).

[42] J.-N. Fuchs and M. Goerbig: 'Introduction to the physical properties of graphene'. Lecture Notes. 2008 (cit. on p. 28).

[43] J. C. Slonczewski and P. R. Weiss: 'Band Structure of Graphite'. *Phys Rev* (2 Jan. 1958), vol. 109: pp. 272–279 (cit. on p. 29).

[44] Y. Barlas, K. Yang, and A. H. MacDonald: 'Quantum Hall effects in graphene-based two-dimensional electron systems'. *Nanotechnology* (2012), vol. 23(5): p. 052001 (cit. on p. 31).

[45] T. Ando, T. Nakanishi, and R. Saito: 'Berry's phase and absence of back scattering in Carbon nanotubes'. *J Phys Soc Jpn* (8 Aug. 1998), vol. 67: pp. 2857–2862 (cit. on p. 32).

[46] Y. Zhang, Z. Jiang, J. P. Small, M. S. Purewal, Y.-W. Tan, M. Fazlollahi, J. D. Chudow, J. A. Jaszczak, H. L. Stormer, and P. Kim: 'Landau-Level Splitting in Graphene in High Magnetic Fields'. *Phys Rev Lett* (13 Apr. 2006), vol. 96: p. 136806 (cit. on pp. 34, 39, 42).

[47] X. Du, I. Skachko, F. Duerr, A. Luican, and E. Y. Andrei: 'Fractional quantum Hall effect and insulating phase of Dirac electrons in graphene'. *Nature* (Nov. 2009), vol. 462(7270): pp. 192–195 (cit. on pp. 34, 40, 42, 43).

[48] C. R. Dean, A. F. Young, I. Meric, C. Lee, L. Wang, S. Sorgenfrei, K. Watanabe, T. Taniguchi, P. Kim, K. L. Shepard, and J. Hone: 'Boron nitride substrates for high-quality graphene electronics'. *Nature Nanotech* (Oct. 2010), vol. 5(10): pp. 722–726 (cit. on pp. 34, 40, 80, 83).

[49] F. F. Fang and P. J. Stiles: 'Effects of a Tilted Magnetic Field on a Two-Dimensional Electron Gas'. *Phys Rev* (3 Oct. 1968), vol. 174: pp. 823–828 (cit. on p. 36).

[50] R. J. Nicholas, R. J. Haug, K. v. Klitzing, and G. Weimann: 'Exchange enhancement of the spin splitting in a GaAs-$Ga_xAl_{1-x}As$ heterojunction'. *Phys Rev B* (3 Jan. 1988), vol. 37: pp. 1294–1302 (cit. on p. 36).

[51] A. F. Young, C. R. Dean, L. Wang, H. Ren, P. Cadden-Zimansky, K. Watanabe, T. Taniguchi, J. Hone, K. L. Shepard, and P. Kim: 'Spin and valley quantum Hall ferromagnetism in graphene'. *Nat Phys* (July 2012), vol. 8(7): pp. 550–556 (cit. on pp. 36–38, 40, 41, 73, 106, 133).

[52] J. F. JANAK: 'g Factor of the Two-Dimensional Interacting Electron Gas'. *Phys Rev* (3 Feb. 1969), vol. 178: pp. 1416–1418 (cit. on p. 37).

[53] J. Alicea and M. P. A. Fisher: 'Graphene integer quantum Hall effect in the ferromagnetic and paramagnetic regimes'. *Phys Rev B* (7 Aug. 2006), vol. 74: p. 075422 (cit. on pp. 37, 38).

[54] M. Kharitonov: 'Phase diagram for the $\nu = 0$ quantum Hall state in monolayer graphene'. *Phys Rev B* (15 Apr. 2012), vol. 85: p. 155439 (cit. on pp. 37, 40).

[55] C.-Y. Hou, C. Chamon, and C. Mudry: 'Deconfined fractional electric charges in graphene at high magnetic fields'. *Phys Rev B* (7 Feb. 2010), vol. 81: p. 075427 (cit. on p. 37).

[56] K. Nomura and A. H. MacDonald: 'Quantum Hall Ferromagnetism in Graphene'. *Phys Rev Lett* (25 June 2006), vol. 96: p. 256602 (cit. on pp. 38, 39, 106).

[57] K. Yang, S. Das Sarma, and A. H. MacDonald: 'Collective modes and skyrmion excitations in graphene $SU(4)$ quantum Hall ferromagnets'. *Phys Rev B* (7 Aug. 2006), vol. 74: p. 075423 (cit. on p. 38).

[58] D. A. Abanin, P. A. Lee, and L. S. Levitov: 'Randomness-Induced XY Ordering in a Graphene Quantum Hall Ferromagnet'. *Phys Rev Lett* (15 Apr. 2007), vol. 98: p. 156801 (cit. on p. 38).

[59] V. P. Gusynin, V. A. Miransky, S. G. Sharapov, and I. A. Shovkovy: 'Excitonic gap, phase transition, and quantum Hall effect in graphene'. *Phys Rev B* (19 Nov. 2006), vol. 74: p. 195429 (cit. on pp. 38, 39).

[60] I. F. Herbut: 'Theory of integer quantum Hall effect in graphene'. *Phys Rev B* (16 Apr. 2007), vol. 75: p. 165411 (cit. on p. 38).

[61] A. Schmeller, J. P. Eisenstein, L. N. Pfeiffer, and K. W. West: 'Evidence for Skyrmions and Single Spin Flips in the Integer Quantized Hall Effect'. *Phys Rev Lett* (23 Dec. 1995), vol. 75: pp. 4290–4293 (cit. on p. 38).

[62] M. Ezawa: 'Intrinsic Zeeman Effect in Graphene'. *J Phys Soc Jpn* (2007), vol. 76(9): p. 094701 (cit. on p. 40).

[63] Z. Jiang, Y. Zhang, H. L. Stormer, and P. Kim: 'Quantum Hall States near the Charge-Neutral Dirac Point in Graphene'. *Phys Rev Lett* (10 Sept. 2007), vol. 99: p. 106802 (cit. on p. 39).

[64] E. V. Gorbar, V. P. Gusynin, V. A. Miransky, and I. A. Shovkovy: 'Dynamics in the quantum Hall effect and the phase diagram of graphene'. *Phys Rev B* (8 Aug. 2008), vol. 78: p. 085437 (cit. on p. 40).

[65] E. V. Gorbar, V. P. Gusynin, and V. A. Miransky: 'Toward a theory of the quantum Hall effect in graphene'. *Low Temperature Physics* (2008), vol. 34(10): pp. 790–793 (cit. on p. 40).

[66] E. V. Gorbar, V. P. Gusynin, V. A. Miransky, and I. A. Shovkovy: 'Coulomb interaction and magnetic catalysis in the quantum Hall effect in graphene'. *Phys Scr* (2012), vol. 2012(T146): p. 014018 (cit. on p. 40).

[67] V. A. Miransky and I. A. Shovkovy: 'Quantum field theory in a magnetic field: From quantum chromodynamics to graphene and Dirac semimetals'. *Physics Reports* (2015), vol. 576: pp. 1–209 (cit. on p. 40).

[68] D. A. Abanin, K. S. Novoselov, U. Zeitler, P. A. Lee, A. K. Geim, and L. S. Levitov: 'Dissipative Quantum Hall Effect in Graphene near the Dirac Point'. *Phys Rev Lett* (19 May 2007), vol. 98: p. 196806 (cit. on pp. 41, 42).

[69] K. I. Bolotin, F. Ghahari, M. D. Shulman, H. L. Stormer, and P. Kim: 'Observation of the fractional quantum Hall effect in graphene'. *Nature* (July 2011), vol. 475(7354) (cit. on pp. 40, 42, 43).

[70] J. G. Checkelsky, L. Li, and N. P. Ong: 'Zero-Energy State in Graphene in a High Magnetic Field'. *Phys Rev Lett* (20 May 2008), vol. 100: p. 206801 (cit. on pp. 40, 42).

[71] J. G. Checkelsky, L. Li, and N. P. Ong: 'Divergent resistance at the Dirac point in graphene: Evidence for a transition in a high magnetic field'. *Phys Rev B* (11 Mar. 2009), vol. 79: p. 115434 (cit. on pp. 40, 42).

[72] L. Zhang, J. Camacho, H. Cao, Y. P. Chen, M. Khodas, D. E. Kharzeev, A. M. Tsvelik, T. Valla, and I. A. Zaliznyak: 'Breakdown of the $N = 0$ quantum Hall state in graphene: Two insulating regimes'. *Phys Rev B* (24 Dec. 2009), vol. 80: p. 241412 (cit. on pp. 40, 42).

[73] D. A. Abanin, P. A. Lee, and L. S. Levitov: 'Spin-Filtered Edge States and Quantum Hall Effect in Graphene'. *Phys Rev Lett* (17 May 2006), vol. 96: p. 176803 (cit. on p. 42).

[74] J. Jung and A. H. MacDonald: 'Theory of the magnetic-field-induced insulator in neutral graphene sheets'. *Phys Rev B* (23 Dec. 2009), vol. 80: p. 235417 (cit. on p. 42).

[75] M. König, S. Wiedmann, C. Brüne, A. Roth, H. Buhmann, L. W. Molenkamp, X.-L. Qi, and S.-C. Zhang: 'Quantum Spin Hall Insulator State in HgTe Quantum Wells'. *Science* (2007), vol. 318(5851): pp. 766–770 (cit. on p. 42).

[76] A. F. Young, J. D. Sanchez-Yamagishi, B. Hunt, S. H. Choi, K. Watanabe, T. Taniguchi, R. C. Ashoori, and P. Jarillo-Herrero: 'Tunable symmetry breaking and helical edge transport in a graphene quantum spin Hall state'. *Nature* (Jan. 2014), vol. 505(7484): pp. 528–532 (cit. on p. 42).

[77] B. E. Feldman, B. Krauss, J. H. Smet, and A. Yacoby: 'Unconventional Sequence of Fractional Quantum Hall States in Suspended Graphene'. *Science* (2012), vol. 337(6099): pp. 1196–1199 (cit. on p. 43).

[78] B. E. Feldman, A. J. Levin, B. Krauss, D. A. Abanin, B. I. Halperin, J. H. Smet, and A. Yacoby: 'Fractional Quantum Hall Phase Transitions and Four-Flux States in Graphene'. *Phys Rev Lett* (7 Aug. 2013), vol. 111: p. 076802 (cit. on p. 43).

[79] X. Lin, R. Du, and X. Xie: 'Recent experimental progress of fractional quantum Hall effect: 5/2 filling state and graphene'. *National Science Review* (2014), vol. 1(4): pp. 564–579 (cit. on p. 43).

[80] Z. Papi ć, M. O. Goerbig, and N. Regnault: 'Atypical Fractional Quantum Hall Effect in Graphene at Filling Factor 1/3'. *Phys Rev Lett* (17 Oct. 2010), vol. 105: p. 176802 (cit. on p. 43).

[81] Z. Papić, M. Goerbig, and N. Regnault: 'Theoretical expectations for a fractional quantum Hall effect in graphene'. *Solid State Commun* (2009), vol. 149(2728). Recent Progress in Graphene Studies: pp. 1056–1060 (cit. on p. 44).

[82] M. O. Goerbig and N. Regnault: 'Theoretical aspects of the fractional quantum Hall effect in graphene'. *Phys Scr* (2012), vol. 2012(T146): p. 014017 (cit. on p. 45).

[83] B. J. van Wees, L. P. Kouwenhoven, H. van Houten, C. W. J. Beenakker, J. E. Mooij, C. T. Foxon, and J. J. Harris: 'Quantized conductance of magnetoelectric subbands in ballistic point contacts'. *Phys Rev B* (5 Aug. 1988), vol. 38: pp. 3625–3627 (cit. on p. 52).

[84] K. Bolotin, K. Sikes, Z. Jiang, M. Klima, G. Fudenberg, J. Hone, P. Kim, and H. Stormer: 'Ultrahigh electron mobility in suspended graphene'. *Solid State Commun* (2008), vol. 146(9–10): pp. 351–355 (cit. on p. 56).

[85] B. Hunt, J. D. Sanchez-Yamagishi, A. F. Young, M. Yankowitz, B. J. LeRoy, K. Watanabe, T. Taniguchi, P. Moon, M. Koshino, P. Jarillo-Herrero, and R. C. Ashoori: 'Massive Dirac Fermions and Hofstadter Butterfly in a van der Waals Heterostructure'. *Science* (2013), vol. 340(6139): pp. 1427–1430 (cit. on pp. 56, 73).

[86] B. W. Alphenaar, P. L. McEuen, R. G. Wheeler, and R. N. Sacks: 'Selective equilibration among the current-carrying states in the quantum Hall regime'. *Phys Rev Lett* (6 Feb. 1990), vol. 64: pp. 677–680 (cit. on p. 58).

[87] J. Li and S.-Q. Shen: 'Disorder effects in the quantum Hall effect of graphene *p-n* junctions'. *Phys Rev B* (20 Nov. 2008), vol. 78: p. 205308 (cit. on p. 63).

[88] W. Long, Q.-f. Sun, and J. Wang: 'Disorder-Induced Enhancement of Transport through Graphene *p-n* Junctions'. *Phys Rev Lett* (16 Oct. 2008), vol. 101: p. 166806 (cit. on p. 63).

[89] J.-c. Chen, T. C. A. Yeung, and Q.-f. Sun: 'Effect of disorder on longitudinal resistance of a graphene *p-n* junction in the quantum Hall regime'. *Phys Rev B* (24 June 2010), vol. 81: p. 245417 (cit. on p. 63).

[90] J.-c. Chen, H. Zhang, S.-Q. Shen, and Q.-f. Sun: 'Dephasing effect on transport of a graphene pn junction in a quantum Hall regime'. *J Phys : Condens Matter* (2011), vol. 23(49): p. 495301 (cit. on p. 64).

[91] J. R. Williams, L. DiCarlo, and C. M. Marcus: 'Quantum Hall Effect in a Gate-Controlled p-n Junction of Graphene'. *Science* (2007), vol. 317(5838): pp. 638–641 (cit. on p. 64).

[92] D. A. Abanin and L. S. Levitov: 'Quantized Transport in Graphene p-n Junctions in a Magnetic Field'. *Science* (2007), vol. 317(5838): pp. 641–643 (cit. on p. 64).

[93] B. Özyilmaz, P. Jarillo-Herrero, D. Efetov, D. A. Abanin, L. S. Levitov, and P. Kim: 'Electronic Transport and Quantum Hall Effect in Bipolar Graphene *p-n-p* Junctions'. *Phys Rev Lett* (16 Oct. 2007), vol. 99: p. 166804 (cit. on pp. 64, 68).

[94] D.-K. Ki and H.-J. Lee: 'Quantum Hall resistances of a multiterminal top-gated graphene device'. *Phys Rev B* (19 May 2009), vol. 79: p. 195327 (cit. on pp. 64, 68, 69).

[95] S.-G. Nam, D.-K. Ki, J. W. Park, Y. Kim, J. S. Kim, and H.-J. Lee: 'Ballistic transport of graphene pnp junctions with embedded local gates'. *Nanotechnology* (2011), vol. 22(41): p. 415203 (cit. on p. 64).

[96] F. Amet, J. R. Williams, K. Watanabe, T. Taniguchi, and D. Goldhaber-Gordon: 'Selective Equilibration of Spin-Polarized Quantum Hall Edge States in Graphene'. *Phys Rev Lett* (19 May 2014), vol. 112: p. 196601 (cit. on pp. 64, 69, 71, 72, 124, 128, 133, 134).

[97] C. R. Woods et al.: 'Commensurate-incommensurate transition in graphene on hexagonal boron nitride'. *NATURE PHYSICS* (June 2014), vol. 10(6): pp. 451–456 (cit. on p. 73).

[98] S. Nakaharai, J. R. Williams, and C. M. Marcus: 'Gate-Defined Graphene Quantum Point Contact in the Quantum Hall Regime'. *Phys Rev Lett* (3 July 2011), vol. 107: p. 036602 (cit. on pp. 73–76).

[99] P. Blake, E. W. Hill, A. H. Castro Neto, K. S. Novoselov, D. Jiang, R. Yang, T. J. Booth, and A. K. Geim: 'Making graphene visible'. *Appl Phys Lett* (2007), vol. 91(6) (cit. on p. 80).

[100] T. Taniguchi and K. Watanabe: 'Synthesis of high-purity boron nitride single crystals under high pressure by using Ba-BN solvent'. *J Cryst Growth* (May 2007), vol. 303(2): pp. 525–529 (cit. on p. 81).

[101] S. Reich, A. C. Ferrari, R. Arenal, A. Loiseau, I. Bello, and J. Robertson: 'Resonant Raman scattering in cubic and hexagonal boron nitride'. *Phys Rev B* (20 May 2005), vol. 71: p. 205201 (cit. on p. 82).

[102] R. V. Gorbachev, I. Riaz, R. R. Nair, R. Jalil, L. Britnell, B. D. Belle, E. W. Hill, K. S. Novoselov, K. Watanabe, T. Taniguchi, A. K. Geim, and P. Blake: 'Hunting for Monolayer Boron Nitride: Optical and Raman Signatures'. *Small* (2011), vol. 7(4): pp. 465–468 (cit. on p. 82).

[103] A. C. Ferrari, J. C. Meyer, V. Scardaci, C. Casiraghi, M. Lazzeri, F. Mauri, S. Piscanec, D. Jiang, K. S. Novoselov, S. Roth, and A. K. Geim: 'Raman Spectrum of Graphene and Graphene Layers'. *Phys Rev Lett* (18 Oct. 2006), vol. 97: p. 187401 (cit. on p. 82).

[104] L. Wang, I. Meric, P. Y. Huang, Q. Gao, Y. Gao, H. Tran, T. Taniguchi, K. Watanabe, L. M. Campos, D. A. Muller, J. Guo, P. Kim, J. Hone, K. L. Shepard, and C. R. Dean: 'One-Dimensional Electrical Contact to a Two-Dimensional Material'. *Science* (2013), vol. 342(6158): pp. 614–617 (cit. on pp. 84, 89).

[105] R. de Picciotto, H. Stormer, L. Pfeiffer, K. Baldwin, and K. West: 'Four-terminal resistance of a ballistic quantum wire'. *Nature* (May 2001), vol. 411(6833): pp. 51–54 (cit. on p. 97).

[106] B. Huard, N. Stander, J. A. Sulpizio, and D. Goldhaber-Gordon: 'Evidence of the role of contacts on the observed electron-hole asymmetry in graphene'. *Phys Rev B* (12 Sept. 2008), vol. 78: p. 121402 (cit. on pp. 97, 98).

[107] J. Cayssol, B. Huard, and D. Goldhaber-Gordon: 'Contact resistance and shot noise in graphene transistors'. *Phys Rev B* (7 Feb. 2009), vol. 79: p. 075428 (cit. on p. 98).

[108] K. K. Kim, A. Hsu, X. Jia, S. M. Kim, Y. Shi, M. Dresselhaus, T. Palacios, and J. Kong: 'Synthesis and Characterization of Hexagonal Boron Nitride Film as a Dielectric Layer for Graphene Devices'. *ACS Nano* (2012), vol. 6(10). PMID: 22970651: pp. 8583–8590 (cit. on pp. 99, 114).

[109] P. Blake, R. Yang, S. Morozov, F. Schedin, L. Ponomarenko, A. Zhukov, R. Nair, I. Grigorieva, K. Novoselov, and A. Geim: 'Influence of metal contacts and charge inhomogeneity on transport properties of graphene near the neutrality point'. *Solid State Commun* (2009), vol. 149. Recent Progress in Graphene Studies: pp. 1068–1071 (cit. on p. 99).

[110] C. W. J. Beenakker and H. van Houten: 'Billiard model of a ballistic multiprobe conductor'. *Phys Rev Lett* (17 Oct. 1989), vol. 63: pp. 1857–1860 (cit. on pp. 101, 103).

[111] Y. Avishai and Y. B. Band: 'Quantum electronic conductance of a terminal junction'. *Phys Rev Lett* (21 May 1989), vol. 62: pp. 2527–2530 (cit. on p. 101).

[112] Y. Takagaki, K. Gamo, S. Namba, S. Ishida, S. Takaoka, K. Murase, K. Ishibashi, and Y. Aoyagi: 'Nonlocal quantum transport in narrow multibranched electron wave guide of GaAs-AlGaAs'. *Solid State Commun* (1988), vol. 68(12): pp. 1051–1054 (cit. on p. 101).

[113] G. Timp, H. U. Baranger, P. deVegvar, J. E. Cunningham, R. E. Howard, R. Behringer, and P. M. Mankiewich: 'Propagation around a Bend in a Multichannel Electron Waveguide'. *Phys Rev Lett* (20 May 1988), vol. 60: pp. 2081–2084 (cit. on p. 101).

[114] A. S. Mayorov, R. V. Gorbachev, S. V. Morozov, L. Britnell, R. Jalil, L. A. Ponomarenko, P. Blake, K. S. Novoselov, K. Watanabe, T. Taniguchi, and A. K. Geim: 'Micrometer-Scale Ballistic Transport in Encapsulated Graphene at Room Temperature'. *Nano Lett* (June 2011), vol. 11(6): pp. 2396–2399 (cit. on pp. 101, 104).

[115] T. Taychatanapat, K. Watanabe, T. Taniguchi, and P. Jarillo-Herrero: 'Electrically tunable transverse magnetic focusing in graphene'. *Nature Phys* (Apr. 2013), vol. 9(4): pp. 225–229 (cit. on pp. 102, 103).

[116] G. Kirczenow: 'Mechanism of the quenching of the Hall effect'. *Phys Rev Lett* (25 June 1989), vol. 62: pp. 2993–2996 (cit. on p. 103).

[117] M. L. Roukes, A. Scherer, S. J. Allen, H. G. Craighead, R. M. Ruthen, E. D. Beebe, and J. P. Harbison: 'Quenching of the Hall Effect in a One-Dimensional Wire'. *Phys Rev Lett* (26 Dec. 1987), vol. 59: pp. 3011–3014 (cit. on p. 103).

[118] C. J. B. Ford, T. J. Thornton, R. Newbury, M. Pepper, H. Ahmed, D. C. Peacock, D. A. Ritchie, J. E. F. Frost, and G. A. C. Jones: 'Vanishing hall voltage in a quasi-one-dimensional GaAs – $Al_xGa_{1-x}As$ heterojunction'. *Phys Rev B* (12 Oct. 1988), vol. 38: pp. 8518–8521 (cit. on p. 103).

[119] C. J. B. Ford, S. Washburn, M. Büttiker, C. M. Knoedler, and J. M. Hong: 'Influence of geometry on the Hall effect in ballistic wires'. *Phys Rev Lett* (23 June 1989), vol. 62: pp. 2724–2727 (cit. on p. 103).

[120] A. M. Chang, T. Y. Chang, and H. U. Baranger: 'Quenching of the Hall resistance in a novel geometry'. *Phys Rev Lett* (9 Aug. 1989), vol. 63: pp. 996–999 (cit. on p. 103).

[121] B. Huard, J. A. Sulpizio, N. Stander, K. Todd, B. Yang, and D. Goldhaber-Gordon: 'Transport Measurements Across a Tunable Potential Barrier in Graphene'. *Phys Rev Lett* (23 June 2007), vol. 98: p. 236803 (cit. on p. 114).

[122] N. Gu, M. Rudner, A. Young, P. Kim, and L. Levitov: 'Collapse of Landau Levels in Gated Graphene Structures'. *Phys Rev Lett* (6 Feb. 2011), vol. 106: p. 066601 (cit. on p. 134).

[123] X. G. Wen: 'Electrodynamical properties of gapless edge excitations in the fractional quantum Hall states'. *Phys Rev Lett* (18 Apr. 1990), vol. 64: pp. 2206–2209 (cit. on pp. 141, 142).

[124] X. G. Wen: 'Gapless boundary excitations in the quantum Hall states and in the chiral spin states'. *Phys Rev B* (13 May 1991), vol. 43: pp. 11025–11036 (cit. on p. 141).

[125] X.-G. Wen: 'Edge transport properties of the fractional quantum Hall states and weak-impurity scattering of a one-dimensional charge-density wave'. *Phys Rev B* (11 Sept. 1991), vol. 44: pp. 5708–5719 (cit. on p. 141).

[126] F. D. M. Haldane: ''Luttinger liquid theory' of one-dimensional quantum fluids. I. Properties of the Luttinger model and their extension to the general 1D interacting spinless Fermi gas'. *Journal of Physics C: Solid State Physics* (1981), vol. 14(19): p. 2585 (cit. on p. 141).

[127] C. Kane and M. Fisher: 'Edge State Transport'. (1997), vol. (cit. on pp. 141–144, 146, 147).

[128] F. Milliken, C. Umbach, and R. Webb: 'Indications of a Luttinger liquid in the fractional quantum hall regime'. *SOLID STATE COMMUNICATIONS* (1996), vol. (cit. on pp. 141, 143, 144).

[129] R. dePicciotto, M. Reznikov, M. Heiblum, V. Umansky, G. Bunin, and D. Mahalu: 'Direct observation of a fractional charge'. *NATURE* (Sept. 1997), vol. 389(6647): pp. 162–164 (cit. on p. 142).

[130] L. Saminadayar, D. C. Glattli, Y. Jin, and B. Etienne: 'Observation of the $e/3$ Fractionally Charged Laughlin Quasiparticle'. *Phys Rev Lett* (13 Sept. 1997), vol. 79: pp. 2526–2529 (cit. on p. 142).

[131] A. H. MacDonald: 'Edge states in the fractional-quantum-Hall-effect regime'. *Phys Rev Lett* (2 Jan. 1990), vol. 64: pp. 220–223 (cit. on p. 142).

[132] C. L. Kane and M. P. A. Fisher: 'Transport in a one-channel Luttinger liquid'. *Phys Rev Lett* (8 Feb. 1992), vol. 68: pp. 1220–1223 (cit. on p. 143).

[133] M. P. A. Fisher and L. I. Glazman: 'Mesoscopic Electron Transport'. Ed. by L. L. Sohn, L. P. Kouwenhoven, and G. Schön. Dordrecht: Springer Netherlands, 1997. Chap. Transport in a One-Dimensional Luttinger Liquid: pp. 331–373 (cit. on p. 144).

[134] I. P. Radu, J. B. Miller, C. M. Marcus, M. A. Kastner, L. N. Pfeiffer, and K. W. West: 'Quasi-Particle Properties from Tunneling in the v = 5/2 Fractional Quantum Hall State'. *Science* (2008), vol. 320(5878): pp. 899–902 (cit. on pp. 144, 148, 150).

[135] X.-G. Wen: 'Edge transport properties of the fractional quantum Hall states and weak-impurity scattering of a one-dimensional charge-density wave'. *Phys Rev B* (11 Sept. 1991), vol. 44: pp. 5708–5719 (cit. on p. 144).

[136] S. Roddaro, V. Pellegrini, F. Beltram, G. Biasiol, L. Sorba, R. Raimondi, and G. Vignale: 'Nonlinear Quasiparticle Tunneling between Fractional Quantum Hall Edges'. *Phys Rev Lett* (4 Jan. 2003), vol. 90: p. 046805 (cit. on pp. 144, 148).

[137] C. L. Kane and M. P. A. Fisher: 'Resonant tunneling in an interacting one-dimensional electron gas'. *Phys Rev B* (11 Sept. 1992), vol. 46: pp. 7268–7271 (cit. on p. 148).

[138] J. B. Miller, I. P. Radu, D. M. Zumbuehl, E. M. Levenson-Falk, M. A. Kastner, C. M. Marcus, L. N. Pfeiffer, and K. W. West: 'Fractional quantum Hall effect in a quantum point contact at filling fraction 5/2'. *NATURE PHYSICS* (Aug. 2007), vol. 3(8): pp. 561–565 (cit. on p. 148).

[139] S. Baer, C. Rössler, T. Ihn, K. Ensslin, C. Reichl, and W. Wegscheider: 'Experimental probe of topological orders and edge excitations in the second Landau level'. *Phys Rev B* (7 Aug. 2014), vol. 90: p. 075403 (cit. on pp. 148, 152, 158).

[140] M. D. Johnson and A. H. MacDonald: 'Composite edges in the ν=2/3 fractional quantum Hall effect'. *Phys Rev Lett* (15 Oct. 1991), vol. 67: pp. 2060–2063 (cit. on p. 151).

[141] X. Lin, C. Dillard, M. A. Kastner, L. N. Pfeiffer, and K. W. West: 'Measurements of quasiparticle tunneling in the $\upsilon = \frac{5}{2}$ fractional quantum Hall state'. *Phys Rev B* (16 Apr. 2012), vol. 85: p. 165321 (cit. on p. 152).